AD-A275 439

(2)

TOUGHENING MECHANISMS IN ULTRAHIGH-STRENGTH STEELS

Final Report

Prof. G. B. Olson, Principal Investigator
Prof. T. Mura, Co-Investigator

DTIC
ELECTE
FEB 03 1994
S
A

December 1, 1993

U.S. Army Research Office
Grant Number DAAL03-89-K-0152
September 1, 1989 to August 31, 1993

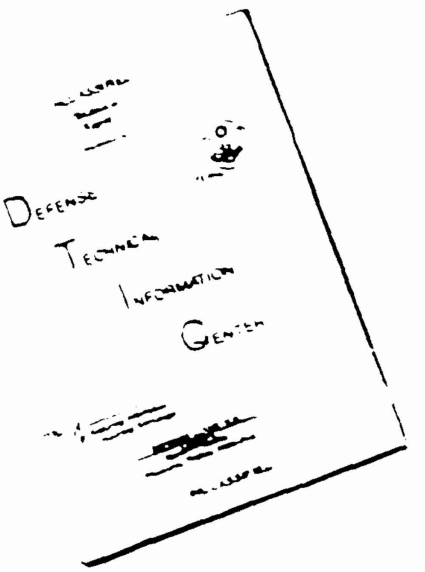
Materials Research Center
Northwestern University
Evanston, IL 60208

APPROVED FOR PUBLIC RELEASE;
DISTRIBUTION UNLIMITED

94 2 08 136

94-04436

DISCLAIMER NOTICE



THIS DOCUMENT IS BEST QUALITY AVAILABLE. THE COPY FURNISHED TO DTIC CONTAINED A SIGNIFICANT NUMBER OF PAGES WHICH DO NOT REPRODUCE LEGIBLY.

REPORT DOCUMENTATION PAGE

Form Approved
OMB No 0704-0188

Public reporting burden for this collection of information is estimated to average 1 hour per response, including the time for reviewing instructions, searching existing data sources, gathering and maintaining the data needed, and completing and reviewing the collection of information. Send comments regarding this burden estimate or any other aspect of this collection of information, including suggestions for reducing this burden, to Washington Headquarters Services, Directorate for information Operations and Reports, 1215 Jefferson Davis Highway, Suite 1204, Arlington, VA 22202-4302, and to the Office of Management and Budget, Paperwork Reduction Project (0704-0188), Washington, DC 20503.

1. AGENCY USE ONLY (Leave blank)	2. REPORT DATE	3. REPORT TYPE AND DATES COVERED
	01 December 1993	Final / Sep 89 - 31 Aug 93

4. TITLE AND SUBTITLE

Toughening Mechanisms in Ultrahigh-Strength Steels

5. FUNDING NUMBERS

DAAL03-89-K-0152

6. AUTHOR(S)

G. B. Olson and T. Mura

7. PERFORMING ORGANIZATION NAME(S) AND ADDRESS(ES)

Materials Research Center
Northwestern University
Evanston, IL 60208

8. PERFORMING ORGANIZATION REPORT NUMBER

9. SPONSORING/MONITORING AGENCY NAME(S) AND ADDRESS(ES)

U.S. Army Research Office
P.O. Box 12211
Research Triangle Park, NC 27709-2211

10. SPONSORING/MONITORING AGENCY REPORT NUMBER

APO 27163.5-MS

11. SUPPLEMENTARY NOTES

The views, opinions and/or findings contained in this report are those of the author(s) and should not be construed as an official Department of the Army position, policy, or decision, unless so designated by other documentation.

12a. DISTRIBUTION/AVAILABILITY STATEMENT

Approved for public release; distribution unlimited.

12b. DISTRIBUTION CODE

13. ABSTRACT *(Maximum 200 words)*

A systems approach to materials design is extended to adaptive microstructures undergoing a programmed dynamic evolution in both processing and service to achieve novel combinations of properties. Fundamental principles are developed to support rational design of high-toughness ultrahigh-strength martensitic steels of interest for advanced armor and high performance gear applications. Theoretical modelling and high resolution microanalytical experiments in the martensitic alloys address control of autocatalytic coherent precipitation to achieve efficient strengthening without embrittlement, and the controlled precipitation of optimal stability metastable austenite for adaptive dilatant transformation plasticity tuned to crack-tip stress states for efficient interaction with strain localization processes in ductile fracture.

DTIC QUALITY INSPECTED 5

14. SUBJECT TERMS	15. NUMBER OF PAGES
Fracture Toughness Precipitation Strengthening Transformation Toughening	172
	16. PRICE CODE

17. SECURITY CLASSIFICATION OF REPORT	18. SECURITY CLASSIFICATION OF THIS PAGE	19. SECURITY CLASSIFICATION OF ABSTRACT	20. LIMITATION OF ABSTRACT
UNCLASSIFIED	UNCLASSIFIED	UNCLASSIFIED	UL

Table of Contents

Foreword 1

Research Objectives 2

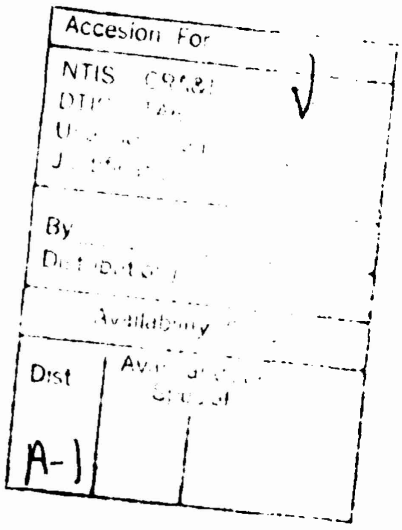
Summary of Results 2

References 7

Scientific Personnel 10

Report of Inventions 10

Appendices 11



1. Foreword: Materials as Dynamic Systems

A "systems" view of materials as hierarchical structures with properties governed by dynamic evolution in processing and in service was expounded by the late C. S. Smith [1]. This viewpoint has been developed into a general strategy for the rational design of complex materials, pioneered by the multi-institutional Steel Research Group (SRG) program centered at Northwestern University [2-4], with successful application in high toughness ultrahigh-strength alloy steels [5]. This view of a secondary-hardening martensitic alloy steel as a system is summarized in Figure 1 [2], depicting the hierarchy of microstructural subsystems controlling the required set of properties for desired performance, and the sequential processing subsystems which in turn control structure. Using this approach to focus basic research on key process/structure and structure/property relations, quantitative microstructural objectives have been expressed in thermodynamic terms (including scaling factors governing dynamic evolution), and the THERMOCALC thermochemical database and software system [6] has then been applied to the prediction of unique multicomponent alloy compositions capable of achieving desired multiphase microstructures under prescribed processing conditions. The successful application of this approach in ultrahigh strength steels has made possible the teaching of an undergraduate course in Materials Design [4], and the extension of thermodynamics-based systems design to ceramics and polymers is now being actively explored within the Department of Materials Science and Engineering at Northwestern [7].

The research described here has extended the SRG systems design approach with an increased emphasis on dynamic microstructures to establish fundamental principles supporting rational design of programmed multilevel structures achieving new combinations of properties. The research has focussed on transformation toughened secondary hardening martensites achieving novel strength/toughness combinations through control of coherent precipitation phenomena during processing, combined with tuned-stability crack-tip transformation plasticity to control fine-scale strain localization processes during fracture in service.

The research goals respond to performance needs specific to Army applications, which constitute some of the most severe requirements for high performance ferrous alloys. The martensitic ultrahigh strength steels show promise for a new generation of shatter-resistant ultrahard armor steels offering a new level of V_{50} ballistic penetration resistance with greatly improved resistance to plastic shear localization. The attendant reduction of required areal density for ballistic protection would be of particular interest for Army aircraft systems; such steels would offer advantages for ballistically tolerant structural components as well. Employing surface hardening by high temperature carburizing and/or lower temperature plasma nitriding during secondary hardening, these steels also offer potential for a new generation of higher power density gear systems exploiting the greatly increased fatigue strength of higher case hardness levels as well as the greater thermal stability of secondary hardening steels to allow both lighter weight gears and higher gear system operating temperatures desired for helicopter transmission systems.

Reprints of papers describing the SRG program [3], an overview of the scientific basis of our approach [2], and a description of the SRG-based Materials Design course [4] are attached as Appendices A, B and C. Papers describing elasticity calculations relevant to coherent precipitation [8-10], including particle self energies [8] and dislocation interaction energies [9], are attached as Appendices D, E and F. Appendix G [11] presents a thorough experimental study of carbide precipitation in the co· nercial AF1410 steel with theoretical analysis based on Appendices D and E. A theory o: precipitate coarsening rate constants for multicomponent systems [12] is presented in Appendix H.

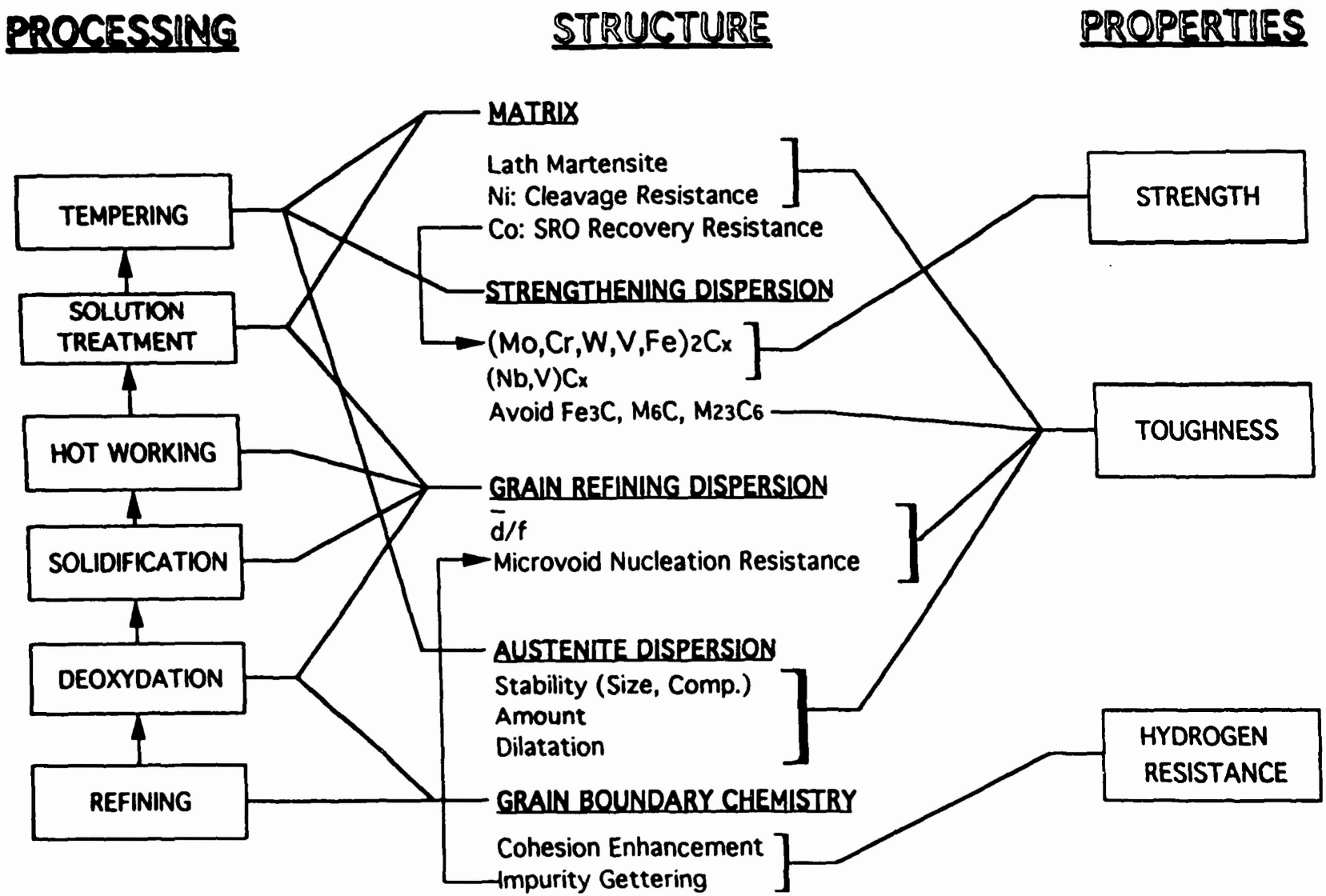


Figure 1. Flow-block diagram representing a secondary hardening martensitic steel as a system [2].

Table 1. Alloy Steel Compositions (wt.pct.)

	C	Co	Ni	Mo	Cr	V
AF1410	0.16	14.2	10.1	1.1	2.1	-
SRG2	0.24	16.0	5.0	4.0	-	-
SRG3	0.24	16.1	5.0	2.8	0.7	-
SRG4	0.24	16.1	5.0	1.5	1.4	-
Aermet100	0.24	13.5	11.0	1.1	3.0	-
MTL1	0.21	12.5	10.1	1.1	2.9	0.10
MTL2	0.30	13.5	10.6	1.2	3.0	0.11
MTL3	0.30	14.4	10.8	1.1	2.9	0.10

2. Research Objectives

While quantitative property objectives are important to obtain sufficient focus of basic research coordinated within a systems design framework, the primary objectives of this research effort are the fundamental principles and basic data necessary to support rational design. This includes the principles of microstructural evolution during coherent carbide precipitation for efficient strengthening without embrittlement and the control of metastable austenite precipitation for transformation toughening with optimal transformation stability and dilatancy. The research emphasizes the dynamics of microstructural evolution in both processing and service.

Specific property targets guiding the conceptual design of prototype materials for evaluation are a hardness level of R_c55-58 for the secondary hardening martensitic steels with K_{IC} fracture toughness of 80-120 ksi$\sqrt{in}$. This would ensure adequate critical flaw size at yield for armor steel applications as well as a suitable core material for high performance gear steels.

3. Summary of Results

3.1 Efficient Strengthening: Autocatalytic Coherent Precipitation

Our first dynamic problem of interest in the secondary hardening martensitic steels represented by Figure 1 is the evolution of coherent carbide precipitation during the final stage of processing. Here the goal is to achieve desired strength with the minimum necessary alloy carbon content and without introducing unnecessary embrittling constituents. Theory and experiment has addressed M_2C alloy carbide precipitation in the series of high Co alloy steel compositions listed in Table 1. The doctoral thesis of Dr. Jonathan Montgomery (App. G [11]) focussed on the commercial AF1410 steel and included the higher strength experimental compositions SRG 2, 3, and 4 with variations in Cr/Mo ratio. Consistent with predictions of models derived from study of these alloys, Carpenter Steel developed the commercial Aermet100 alloy which successfully extended the behavior of AF1410 to higher strength levels. The MTL1,2,3 compositions represent prototype armor steel compositions which we designed under a one-year contract from the Materials Directorate of ARL (formerly MTL) based on results of our ARO sponsored research. The MTL1 prototype successfully matches the strength/toughness combinations of Aermet100 employing significantly lower carbon content.

As first shown by the work of Speich [13] the high toughness of these Co steels derives from their resistance to overaging such that high strength can be maintained at completion of M_2C carbide precipitation, allowing full dissolution of the transient cementite that otherwise limits fracture toughness. A typical toughness/hardness trajectory during secondary hardening (at 480C) is shown in Figure 2 for the MTL1 prototype armor steel. The best strength-toughness combination is obtained in a slightly overaged condition providing cementite dissolution without excessive coarsening of the M_2C carbide strengthening dispersion. The "X" in Figure 2 shows the toughness-hardness combination achieved with optimal 1125C solution treatment and an 8 hr temper in the higher carbon MTL2 and MTL3 compositions. Preliminary testing at ARL has demonstrated excellent ballistic properties.

Strength in the overaged condition is controlled by the Orowan dislocation bypass mechanism [14] where increased strength (for a given alloy carbon content) can be achieved by refining the carbide particle size to reduce interparticle spacing. The fine carbide sizes achieved in these steels derive in part from their heterogeneous nucleation on dislocations retained during tempering as a result of an unusually high recovery resistance associated with Co short range

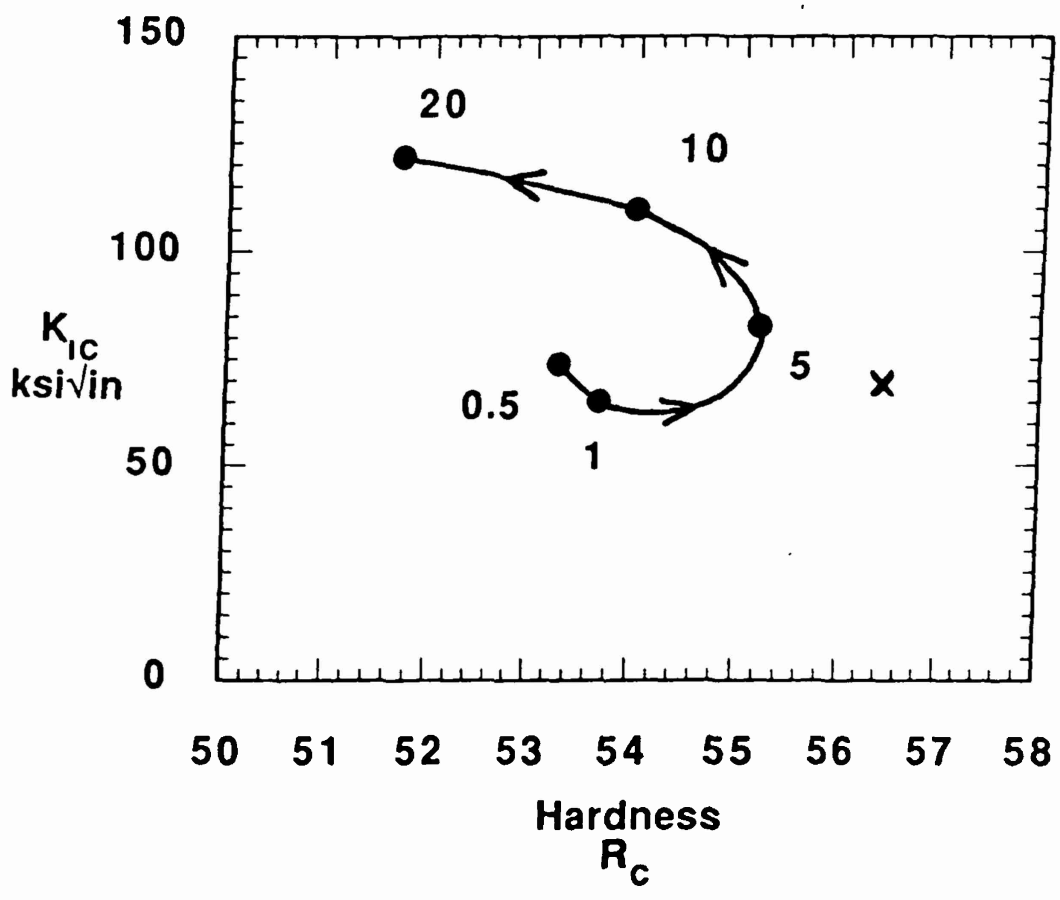


Figure 2. K_{IC} toughness vs. R_c hardness for MTL1 prototype steel solution treated 1hr at 1000C and tempered at 480C for times indicated in hours. The "X" shows properties achieved with MTL2 and MTL3 for an 8 hr temper after 1125C-1hr solution treatment.

order [2]. The thorough electron microscopy study of M_2C precipitation in AF1410 by Montgomery [11] coordinated with small angle neutron scattering (SANS) measurements by Weertman and coworkers [15] under the SRG program, demonstrated that the fine carbide size is also promoted by precipitation at high supersaturations where, as predicted by Langer and Schwartz [16] and developed further by Kampman and Wagner [17], competition between nucleation and coarsening maintains an average particle size near the critical nucleus size as supersaturation drops, thus suppressing the classical "growth" stage of precipitation. The SANS data further revealed a surprising additional contribution to particle size refinement depicted by the measured size distributions for tempering at 1 hr and 2 hr at 510C as shown in Figure 3. After 1 hr, where precipitation is half complete and nucleation has ceased due to reduced supersaturation, a second stage of nucleation occurs, greatly increasing the particle number density and reducing the average particle size measured after 2 hr. This second nucleation stage is an important contribution to the softening resistance responsible for the high strength maintained by AF1410 in the high toughness overaged state. Theoretical work in our ARO-sponsored research has focussed on the fundamental basis of these phenomena promoting particle refinement for efficient strengthening in these steels.

In the high supersaturation regime, the Langer-Schwartz theory predicts two primary scaling factors governing the evolution of the particle size distribution. One is a diffusion time factor which can be deduced from the coarsening rate constant, and another is the initial critical nucleus size setting the length scale. To predict a coarsening rate constant for multicomponent systems, our earlier studies [18] under the SRG program employed a simple model proposed by Hillert and coworkers [19]. Under our ARO-sponsored work, Kuehmann and Voorhees [20] developed a more rigorous treatment of ternary systems, and more recently Research Associate Alex Umantsev has derived a general coarsening rate constant for multicomponent systems:

$$\bar{r}^3 - \bar{r}_o^3 = Kt$$

$$K = \frac{\frac{8}{9}\sigma V_m^{\beta}}{\sum_{i=1}^{n}\sum_{j=2}^{n}\frac{\partial \mu_i^{\alpha}}{\partial x_j^{\alpha}} X_j^{\alpha q}\frac{kj-1}{D_j}}$$

where μ_i^{α} are chemical potentials in the α matrix phase, $X_j^{\alpha q}$ are matrix equilibrium solute concentrations, k_j are solute partitioning ratios, and D_j the solute diffusivities. The theory is described in Appendix H [12] and is now being tested against our AF1410 data and recent SANS data obtained on the SRG 2, 3, and 4 alloys of Table 1.

Before discussing our continuing research on the factors governing particle length scales, we note that, as depicted in Figure 1, the solution treatment prior to tempering exerts an important influence not only on the initial matrix composition, but also (along with deoxidation, solidification, and hot working conditions) on the nature of the grain refining dispersion that influences the microvoid nucleation resistance governing fracture toughness. The latter has been an important component of our prior SRG research [21-23] and under our ARO-supported effort Graduate Fellow C. Kuehmann has focussed on the optimization of solution treatment to control this important component of microstructure. In both the commercial Aermet100 alloy and the MTL1 prototype alloy extensive extraction replica electron microscopy has revealed the conditions for dissolution of Cr-Mo carbides while retaining fine (Ti, Mo)C carbides (introduced

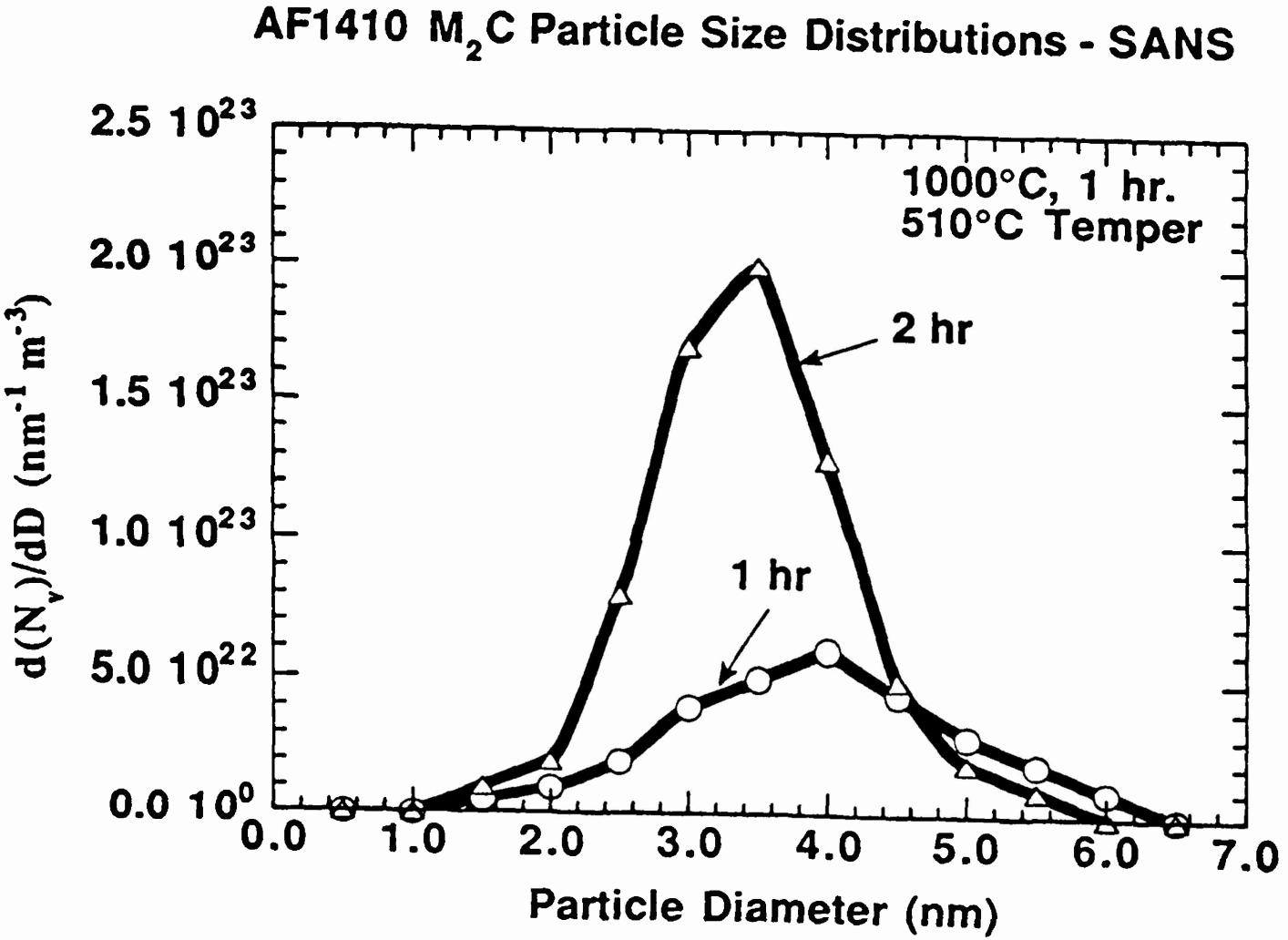


Figure 3. Size distribution of M_2C carbides measured by SANS in AF1410 steel tempered at 510C for 1hr and 2hr [15].

via melt deoxidation practice) which previous work has shown to possess the best interfacial strength for microvoid nucleation resistance [2]. Fracture toughness has been correlated with the solution treatment employing a 200C stage I temper condition to avoid cross interactions with secondary hardening behavior. In this way multi-step heat treatments are developed by sequential optimization of each processing step, focusing on the primary microstructural role of each step within the structural hierarchy of Figure 1. The toughness-hardness trajectory for increasing solution temperature in Aermet 100 is summarized in Figure 4, showing an optimum condition near 900C.

An area of continuing interest in our research is the control of the carbide initial critical nucleus size which sets the primary length scale during precipitation strengthening. This size is inversely proportional to the thermodynamic driving force for precipitation which can be estimated employing the THERMOCALC thermochemical database and software system. However, measured carbide lattice parameters [11] and carbide compositions determined by atom-probe field-ion microanalysis (APFIM) [24] suggest that precipitation initiates in a coherent state and so it is necessary to employ coherent thermodynamics to estimate the precipitation driving forces. Under ARO support we have applied linear elastic estimates described in Appendices D, E and F [8-10]as an upper bound to the elastic self energy associated with the large coherency strains operating in this system. Incorporating the composition dependence of the M_2C carbide lattice parameters, the carbide self energy has been combined with the available chemical thermodynamics to treat the thermodynamics of coherent M_2C precipitation. Reasonable agreement is obtained with precipitation composition trajectories measured in AF1410 and the SRG 2, 3, and 4 alloys when the linear elastic self energy is corrected by a factor of 1/4 to 1/2. Given the significance of the coherent thermodynamics in controlling the strengthening dispersion length scale, we will further refine our theoretical estimates of the carbide elastic self energy in continuing research.

A more stringent test of coherent thermodynamics can be sought from the predicted inhomogeneous nature of the solute distribution in the elastic field of a coherent precipitate. Generalizing the "open system elastic constant" method of Larché and Cahn [25] we have calculated the solute distribution around coherent M_2C carbides in AF1410 steel as described in Appendix D [8]. An atomic resolution test of such predictions has recently been made possible by the development of a Position-Sensitive Atom-Probe (PoSAP) at Oxford University [26] and a preliminary experiment run on an AF1410 specimen has provided three dimensional Cr distributions. In future work we will apply our theory to the prediction of model alloy compositions for enhanced solute distributions measurable by the PoSAP technique.

Employing our current level of approximation in estimating the elastic self energy, we have also examined in detail the elastic interaction of a coherent carbide in AF1410 with a dislocation, as described in Appendix E [9], in order to explore the heterogeneous nucleation that initiates precipitation during tempering. Using a reasonable coherent interfacial energy of 0.1 J/m^2, good agreement is obtained with the observed critical nucleus size and necessary nucleation barrier height to account for observed nucleation [11]. Nucleation on dislocations can not, however, account for the second stage of nucleation occurring after half completion of precipitation as depicted in Figure 3. This problem has been addressed by Research Assistant R.-H. Liarng who has examined the possibility of autocatalytic nucleation in the stress field of the first-generation coherent carbides once the average size reaches a critical level. Liarng's calculations show that the interaction energy density in the elastic field of an average-size carbide at 1 hr tempering is four times that of a dislocation, and more than sufficient to provide barrierless nucleation of a second generation of particles. The recent SANS data suggest that the second stage of nucleation also occurs in the SRG 2, 3, and 4 compositions, but not as strongly as in AF1410. Such autocatalytic nucleation is an important source of strengthening in the high toughness overaged microstructures.

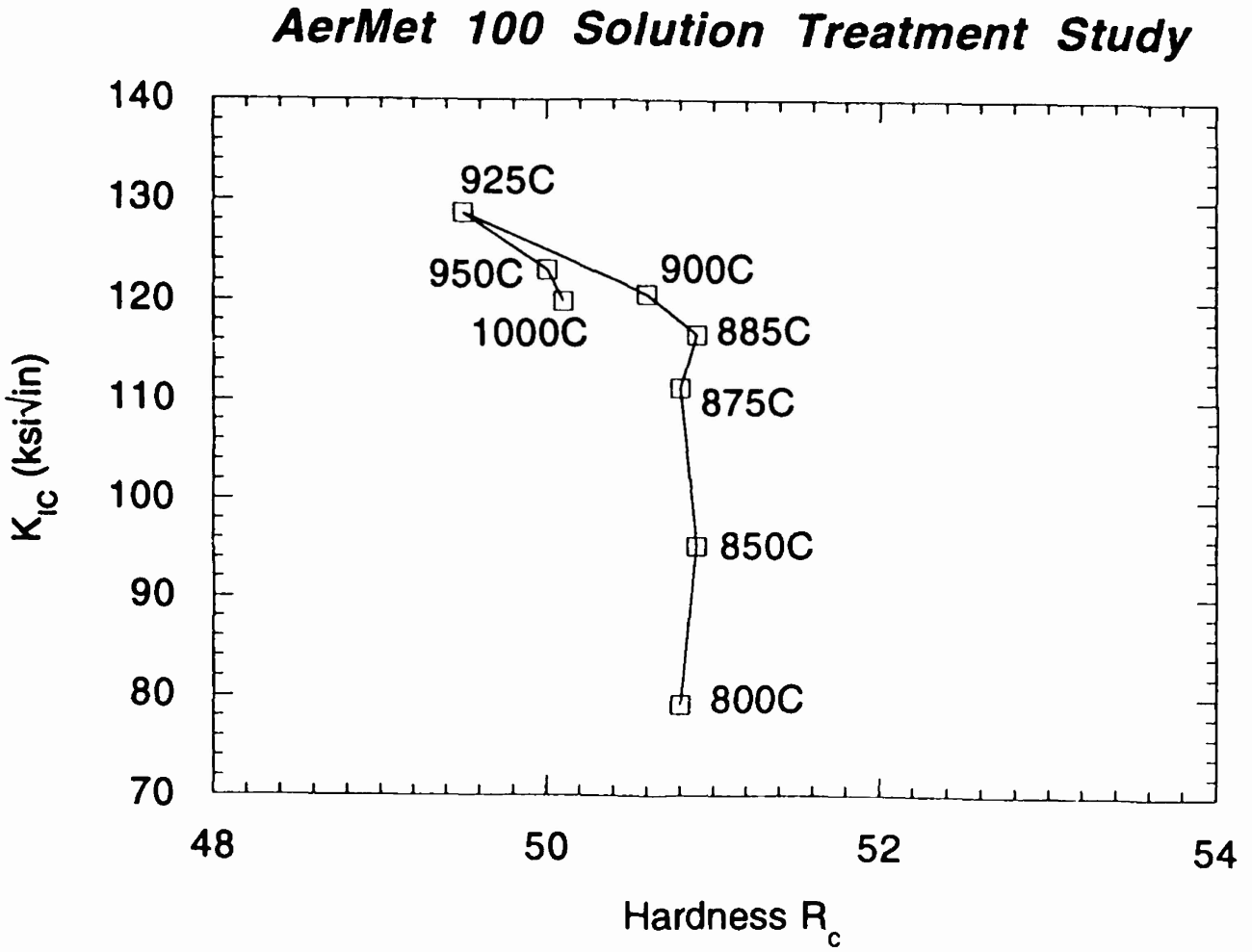


Figure 4. Toughness-Hardness trajectory with increasing solution temperature (1hr) for Aermet 100 tempered 1hr 200C.

Our current models of coherent precipitation predict that small V additions should be particularly effective in improving strengthening efficiency in these alloys. As described in Appendix C [4], this has been incorporated in the conceptual design of a R_c60 stainless matrix bearing steel which was evaluated under a NASA grant, demonstrating a doubling of K_{IC} toughness compared to conventional bearing steels. In this way principles established in AF1410 at a hardness level of R_c48 were directly applied at R_c60, achieving this hardness with a carbon content of only 0.30 wt pct. The effectiveness of V is also supported by the strength achieved in the MTL prototype alloys represented in Figure 2.

3.2 Adaptive Microstructures: Dispersed-Phase Transformation Toughening

The best examples so far of adaptive microstructures achieving programmed microstructural evolution in service are based on the exploitation of transformation plasticity associated with mechanically-induced martensitic transformations. The most well known examples are the TRIP steels [27] demonstrating enhanced ductility at ultrahigh strength levels, and more recently the transformation toughened ZrO_2 ceramics [28]. The concept of programming a change of crystal structure as an adaptive response represents a new level of sophistication in engineering materials.

Under a DOE-sponsored effort within the SRG program, we have examined the quantitative roles of phase stability and transformation dilatancy as key variables governing the efficiency of transformation toughening in ultrahigh-strength steels, using precipitation-strengthened austenitic steels as model systems. Figure 5 summarizes the J_{IC} toughness measured in two series of 200ksi yield strength alloys, employing a thermodynamic free-energy parameter to represent the phase stability [29,30]. Relative to the dashed line denoting the toughness of stable austenite, it is seen that an optimal stability with respect to strain-induced martensitic transformation gives a factor of 7 increase in J_{IC} toughness. Additional studies employing variations in transformation volume change or dilatancy show further that the toughening scales with the third power of the dilatancy [2,31]. Detailed metallographic examination of sectioned crack tips reveals a strong interaction of strain-induced transformation in delaying processes of plastic shear localization in ductile fracture. Application of recent transformation plasticity constitutive models [32] in finite element simulations of crack tip plasticity [33] reveals the toughening role of pressure-sensitive strain hardening associated with the pressure dependence of transformation kinetics arising from the transformation volume change. Optimal transformation toughening thus involves a tuning of phase stability and transformation dilatancy for adaptive response to the specific stress state of a plastic crack tip. Our ability to control phase stability is further enhanced by a new martensite kinetic model addressing solid solution strengthening effects in interfacial mobility governing the composition dependence of the critical thermodynamic driving force for martensitic nucleation [34].

Under ARO support, we have examined the exploitation of this toughening phenomenon in ultrahigh strength martensitic steels, employing a dispersion of metastable austenite particles as represented by the fourth microstructural subsystem in Figure 1. As denoted in the Figure, the roles of dilatancy and the composition dependence of stability carry over from the bulk austenitic alloys, but additional important variables in dispersed-phase systems are the amount (phase fraction) of austenite and a strong role of particle size on stability through the statistical nature of heterogeneous nucleation [35]. Achieving the very high levels of austenite stability required for optimal toughening at ultrahigh strength levels demands both particle size refinement and strong compositional enrichment. In contrast to the more conventional retained austenite produced during quenching from the solution treatment temperature, the latter compositional enrichment is made possible in secondary hardening steels via the formation of precipitated austenite during tempering, as also denoted in Figure 1. In our earlier work on the commercial AF1410 steel [36], we demonstrated that a two-step tempering treatment , in which a short-time higher temperature

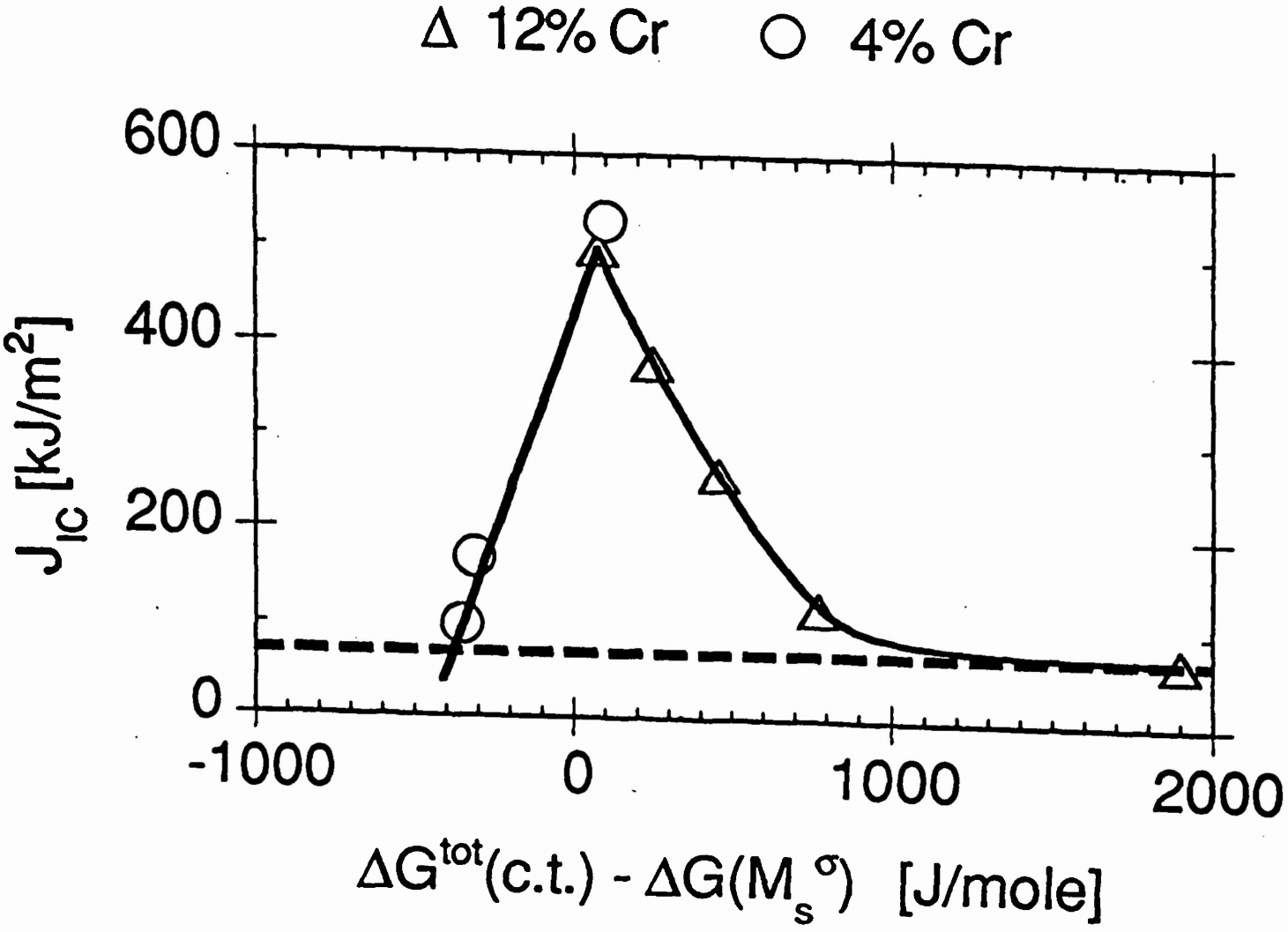


Figure 5. Measured J_{IC} fracture toughness vs. free energy parameter defining phase stability for γ'-strengthened austenitic steels with 200 ksi yield strength [29,30].

austenite nucleation step precedes final tempering to complete carbide precipitation, gives a toughening response similar to that in Figure 5 when toughness is expressed as a function of austenite precipitation time. For optimal precipitation conditions, the increased toughness obtained is represented by the band denoted AF1410-TT (for Transformation Toughened) in the toughness-hardness plot of Figure 6. Also shown is the band of properties obtained for the commercial Aermet100 alloy and our lower-carbon MTL1 prototype alloy of Figure 2, without exploiting the phenomenon of precipitated austenite transformation toughening. Thermodynamic calculations employing the THERMOCALC software and database predict that optimal precipitated austenite stability levels should be similarly achievable in these alloy compositions. The "objectives" box in Figure 6 represents the properties we believe can be achieved by a combination of further strengthening (through the refinements of coherent carbide precipitation discussed earlier) and full exploitation of precipitated-austenite transformation toughening. The dashed lines bounding the objectives denote acceptable levels of critical flaw size at yield. Such properties would represent a significant advance in the useable strength levels of steels for high performance structural applications.

As a step toward achieving such property combinations, Graduate Fellow Charles Kuehmann has tested the levels of transformation toughening achievable in the Aermet100 alloy. Employing solution treatment conditions based on the optimization study of Figure 4, the toughness-hardness trajectory during 2-step tempering is measured using an improved geometry compact-tension J_{IC} specimen, and precipitated austenite content is monitored by magnetometry. Results are presented in Figure 7, expressing toughness as K_{IC}. The open data points represent the toughness-hardness trajectory for 482C isothermal (1-step) tempering, similar to the upper branch of Figure 2. The solid points depict the properties achieved when the standard 482C-5h temper is preceded by an austenite precipitation step at 582C or 532C for times in minutes denoted in the Figure. The 2-step treatments are seen to follow a higher toughness curve compared to the standard 1-step treatments, attributed to improved stability of precipitated austenite. However, the toughening increment is not as large as indicated by the preliminary AF1410-TT experiments shown in Fig. 6. Further, compared to the behavior of AF1410, the 2-step treatments in Aermet 100 cause excessive overaging of the carbide dispersion with an associated loss of strength. Similar results were obtained in the MTL1 prototype armor steel composition. Exploitation of precipitated-austenite transformation toughening in these alloys will require precise control of the relative rate constants of austenite and carbide precipitation to achieve desired austenite stability without excessive carbide coarsening. The new coarsening rate theory of Appendix H [12] will aid the design of the required alloy compositions.

Future research will explore the synthesis of composite structures through powder processing in order to exploit transformation toughing without requiring austenite precipitation.

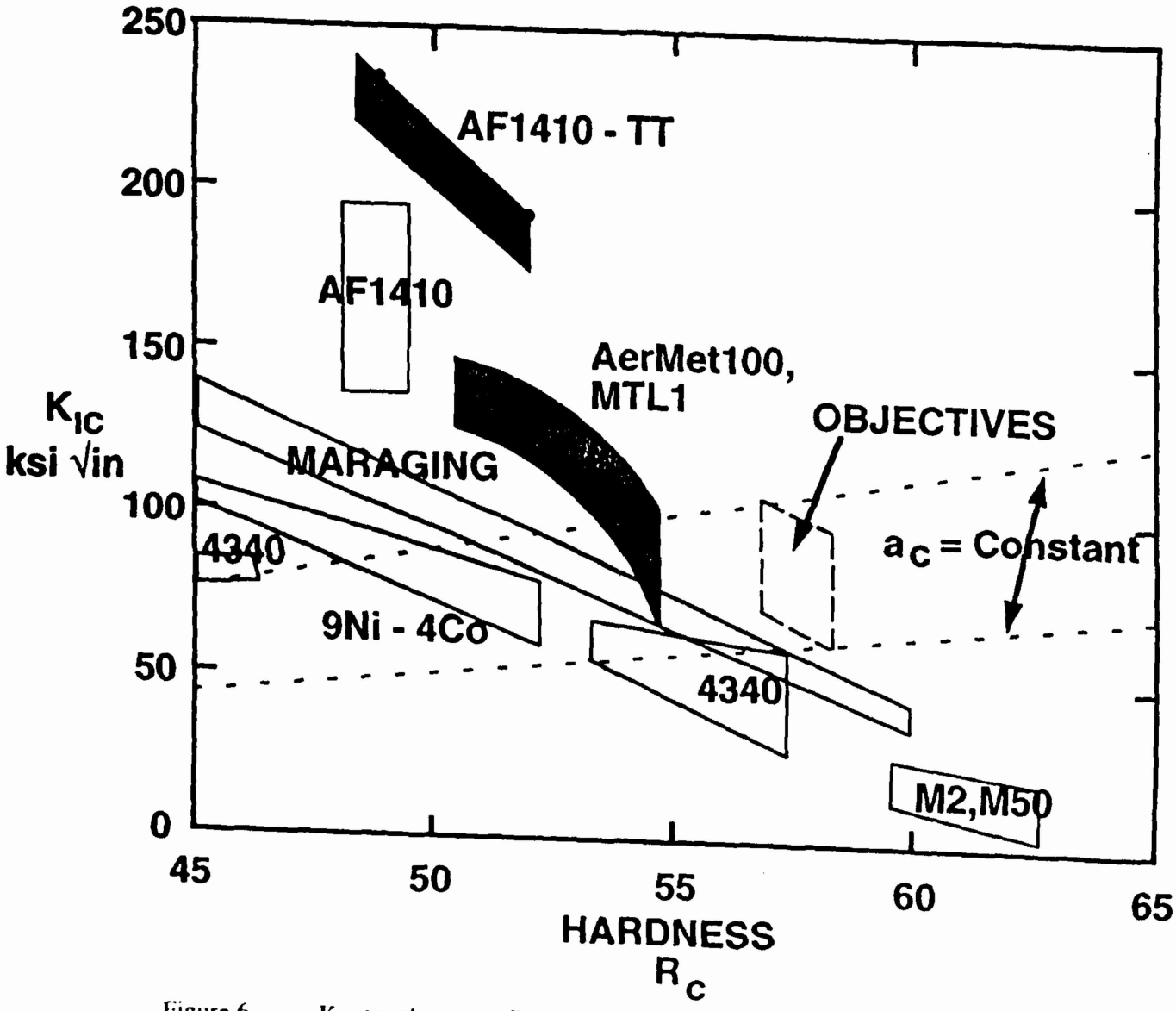


Figure 6. K_{Ic} toughness vs. R_c hardness for commercial steels (white bands). Dark bands depict transformation-toughened AF1410 (AF1410-TT) and the recently developed Aermet100 and prototype MTL1 steels.

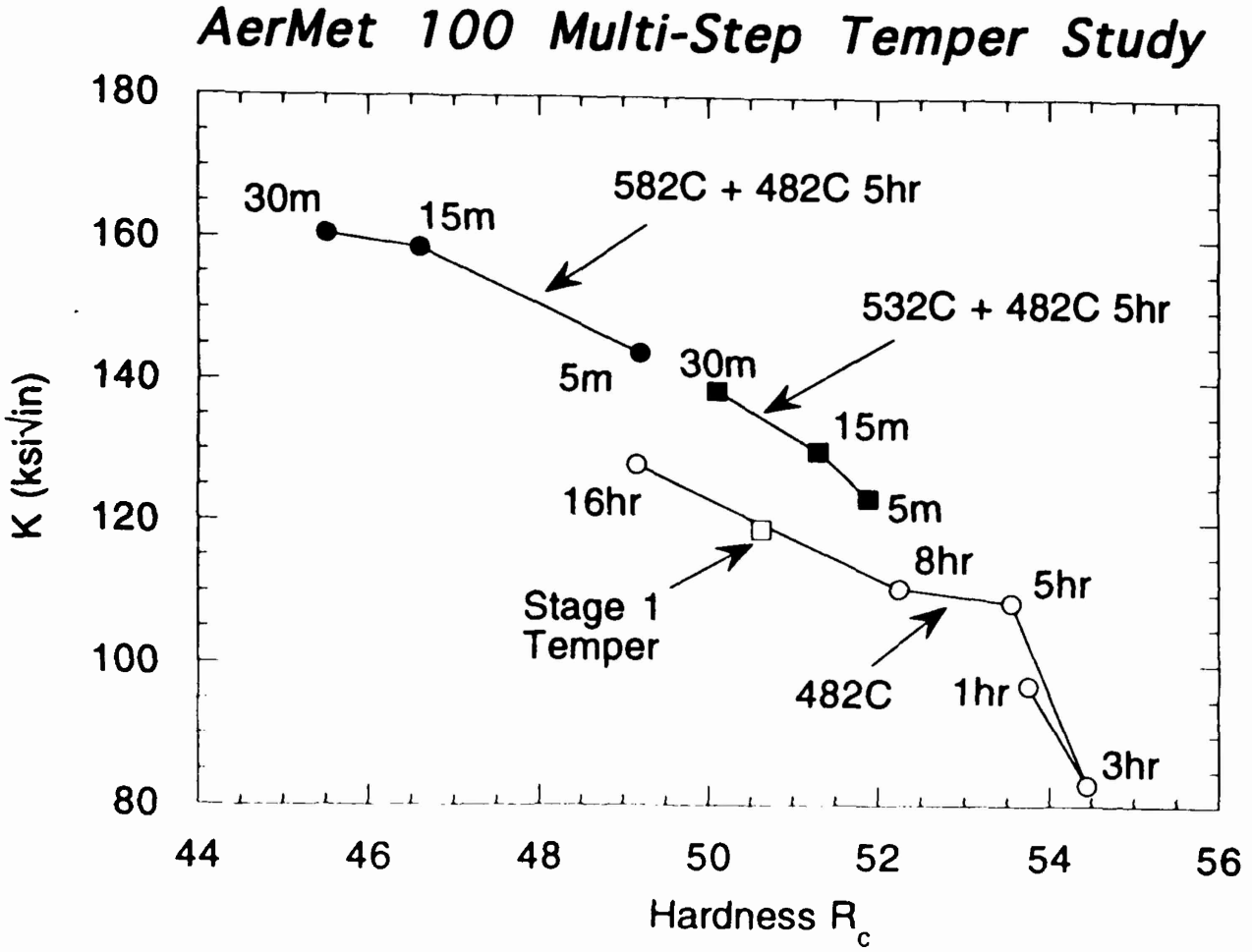


Figure 7. K_{IC} toughness vs. R_c hardness for Aermet 100 comparing isothermal 1-step tempering at 482C with 2-step tempering for times indicated in minutes at 532C or 582C followed by standard 482C, 5hr temper.

4. References (*denotes papers acknowledging ARO support)

1. C. S. Smith, A Search for Structure, (1981) MIT Press: Cambridge MA

* 2. G. B. Olson, "Science of Steel," in Innovations in Ultrahigh Strength Steel Technology, eds. G. B. Olson, M. Azrin and E. S. Wright, Sagamore Army Materials Research Conf. Proc.: 34th (1990) pp. 3-66.

* 3. G. B. Olson, "New Steel by Design," J. Materials Education 11 (1989) pp. 515-528.

* 4. G. B. Olson, "Materials Design: An Undergraduate Course," Morris E. Fine Symposium, eds. P. K. Liaw, J. R. Weertman, H. L. Markus, and J. S. Santner, TMS-AIME: Warrendale, PA (1991) pp. 41-48.

5. T. A. Stephenson, C. E. Campbell, and G. B. Olson, "Systems Design of Advanced Bearing Steels," in Advanced Earth-to-Orbit Propulsion Technology 1992, eds. R. J. Richmond and S. T. Wu, NASA Conf. Pub. 3174, Vol. II (1992) pp. 299-307.

6. B. Sundman, B. Jansson and J. O. Andersson, "THERMOCALC: a Thermochemical Databank and Software System," CALPHAD 9 (1985) 153.

7. Materials Design Initiative, Dept. Materials Science and Engineering, Northwestern University, Evanston, IL.

* 8. K. C. King, P. W. Voorhees and G. B. Olson, "Solute Distribution Around a Coherent Precipitate in a Multicomponent Alloy," Metall. Trans. A 22A (1991) 2199-2210.

* 9. K. C. King, G. B. Olson and T. Mura, "Elastic Energy of Coherent Precipitation at Dislocations in an Anisotropic Matrix," Proc. ARO Workshop, Modern Theory of Anisotropic Elasticity and Applications, Ed. J. J. Wu, T. C. T. Ting, and D. M. Barnett, SIAM: Philadelphia, PA (1991) pp. 103-121.

* 10. H. Hasegawa, R-H. Liarng and T. Mura, "Thermal Stress in a Half Space with a Cylindrical Inhomogeneous Inclusion," J. Thermal Stresses 15 (1992) pp. 295-310.

* 11. J. S. Montgomery and G. B. Olson, "M_2C Carbide precipitation in AF1410," in Gilbert R. Speich Symp. Proc.: Fundamentals of Aging and Tempering in Bainitic and Martensitic Steel Products, eds. G. Krauss and P. E. Repas, ISS-AIME: Warrendale, PA (1992) pp. 177-214.

* 12. A. Umantsev and G. B. Olson, "Ostwald Ripening in Multicomponent Alloys," Scripta Metall. Vol. 29 (1993), pp. 1135-1140.

13. G. R. Speich, "Secondary Hardening Ultrahigh-Strength Steel," in Innovations in Ultrahigh Strength Steel Technology, eds. G. B. Olson, M. Azrin and E. S. Wright, Sagamore Army Materials Research Conf. Proc.: 34th (1990) pp. 89-112.

14. E. Hornbogen, "Alloy Design for >3 GPA Steels," in Innovations in Ultrahigh Strength Steel Technology, eds. G. B. Olson, M. Azrin and E. S. Wright, Sagamore Army Materials Research Conf. Proc.: 34th (1990) pp. 113-126.

15. A. J. Allen, D. Gavillet and J. R. Weertman, "SANS and TEM Studies of Isothermal M_2C Carbide Precipitation in Ultrahigh Strength AF1410 Steels," Acta Metall. 42 No. 6 (1993) pp. 1869-1884.

16. J. S. Langer and A. J. Schwartz, Phys. Rev. A21 (1980) 948.

17. R. Wagner and R. Kampmann, "Solid State Precipitation at High Supersaturations," in Innovations in Ultrahigh Strength Steel Technology, eds. G. B. Olson, M. Azrin and E. S. Wright, Sagamore Army Materials Research Conf. Proc.: 34th (1990) pp. 209-222.

18. H. M. Lee, S. M. Allen and M. Grujicic, "Stability and Coarsening Resistance of M_2C Carbides in Secondary Hardening Steels," in Innovations in Ultrahigh Strength Steel Technology, eds. G. B. Olson, M. Azrin and E. S. Wright, Sagamore Army Materials Research Conf. Proc.: 34th (1990) pp. 127-146.

19. S. Björklund, L. F. Donaghey and M. Hillert, Acta Metall. 20 (1972) 867-874.

20. C. J. Kuehmann and P. W. Voorhees, "A Theory of Coarsening Kinetics in Ternary Systems," manuscript in preparation.

21. J. G. Cowie, M. Azrin and G. B. Olson, "Microvoid Formation During Shear Deformation of Ultrahigh-Strength Steels," in Innovations in Ultrahigh Strength Steel Technology, eds. G. B. Olson, M. Azrin and E. S. Wright, Sagamore Army Materials Research Conf. Proc.: 34th (1990) pp. 357-382.

22. M. L. Schmidt and M. J. Gore, "Solution Treatment Effects in AF1410 Steel," in Innovations in Ultrahigh Strength Steel Technology, eds. G. B. Olson, M. Azrin and E. S. Wright, Sagamore Army Materials Research Conf. Proc.: 34th (1990) pp. 407-424.

23. M. J. Gore, G. B. Olson and M. Cohen, "Grain-Refining Dispersions and Properties in Ultrahigh-Strength Steels," in Innovations in Ultrahigh Strength Steel Technology, eds. G. B. Olson, M. Azrin and E. S. Wright, Sagamore Army Materials Research Conf. Proc.: 34th (1990) pp. 425-442.

24. G. B. Olson, T. J. Kinkus and J. S. Montgomery, "APFIM Study of Multicomponent M_2C Carbide Precipitation in AF1410 Steel," Surf. Sci. 246 (1991) 238-245.

25. F. Larché and J. W. Cahn, Acta Metall. 21 (1973) 1051.

26. A. Cerezo, T. J. Godfrey and G. D. W. Smith, Rev. Sci. Instrum. 59 (1988) 862.

27. V. F. Zackay, E. R. Parker, D. Fahr, and R. Busch, Trans. ASM 60 (1967) 252.

28. R. C. Garvie, R. J. H. Hannick and C. Urbani, "Ceramic Steel," Nature (London) 258 (1975) 703.

29. F. Stavehaug, "Transformation Toughening of γ' Strengthened Metastable Austenitic Steels," Ph.D. Thesis, MIT Dept. Materials Science and Engineering, June, 1990.

30. G. B. Olson, "Mechanically Induced Phase Transformations in Solids: An Update," Encyclopedia of Materials Science and Engineering, Supp. Vol. 3 (1993) Pergamon pp. 1786-1789.

31. C-C. Young, "Transformation Toughening in Phosphocarbide-Strengthened Austenitic Steels," Ph.D. Thesis, MIT Dept. Materials Science and Engineering, June 1988.

32. R. G. Stringfellow, D. M. Parks and G. B. Olson, "A Constitutive Model for Transformation Plasticity Accompanying Strain-Induced Martensitic Transformations in Metastable Austenitic Steels," Acta Metall. 40 (1992) 1703-1760.

33. R. G. Stringfellow and D. M. Parks, "Strain-Induced Transformation Toughening in Metastable Austenitic Steels," in Fracture Behavior and Design of Materials and Structures, Vol. 1, Ed. D. Firrao, EMAS Ltd., Warley, U.K., p. 400.

34. G. Ghosh and G. B. Olson, "Solid Solution Strengthening and Kinetics of Martensitic Transformations in Fe-Base Alloys," Proc. ICOMAT-92, ed. J. Perkins, in press.

35. G. B. Olson, K. Tsuzaki, and M. Cohen, "Statistical Aspects of Martensitic Nucleation," in Turnbull Symposium: Phase Transitions in Condensed Systems, eds. G. S. Cargill, F. Spaepen, and K. N. Tu, MRS (1987) p. 129.

36. G. N. Haidemenopoulos, G. B. Olson, and M. Cohen, "Dispersed-Phase Transformation Toughening in Ultrahigh-Strength Steels," in Innovations in Ultrahigh Strength Steel Technology, eds. G. B. Olson, M. Azrin and E. S. Wright, Sagamore Army Materials Research Conf. Proc.: 34th (1990) pp. 549-596.

5. Scientific Personnel

Professor G. B. Olson, Principal Investigator
Professor T. Mura, Co-Investigator
Dr. Fu-Rong Chen, Assistant Research Professor
Dr. Gautam Ghosh, Assistant Research Professor
Dr. Alex Umantsev, Research Associate
Carol McCarus, Research Technologist
J. Van Nostrand, Director's Assistant
James Herman, Director's Assistant
Junghyun Cho, Graduate Student, M.S., December 1993
Kwang-Un King, Graduate Research Assistant, Ph.D., June 1990
Charles J. Kuehmann, Graduate Fellow
R-H. Liarng, Graduate Research Assistant
Jonathan S. Montgomery, Graduate Fellow, Ph.D., December 1990
P. O'Neill, Undergraduate Student
L. Ralya, Undergraduate Student, B.S., June 1992

6. Report of Inventions

None

APPENDICES

Appendix A "New Steels by Design," G. B. Olson, J. Mater. Educ., Vol. 11 (1989) pp. 515-528.

Appendix B "Overview: Science of Steel," G. B. Olson, in Innovations in Ultrahigh-Strength Steel Technology, eds. G. B. Olson, M. Azrin and E. S. Wright, Proc. 34th Sagamore Army Research Conf. (1990) pp. 3-66.

Appendix C "Materials Design: An Undergraduate Course," G. B. Olson, Morris E. Fine Symposium, TMS (1991) pp. 41-48.

Appendix D "Solute Distribution Around a Coherent Precipitate in a Multicomponent Alloy," K. C. King, P. W. Voorhees, G. B. Olson and T. Mura, Met. Trans. A Vol. 22A (1991) pp. 2199221C

Appendix E "Elastic Energy of Coherent Precipitation at Dislocations in an Anisotropic Matrix," K. C. King, G. B. Olson and T. Mura, in Modern Theory of Anisotropic Elasticity and Applications, eds. J. Wu, T. Ting and D. Barnett, SIAM (1991) pp. 103-121.

Appendix F "Thermal Stress in a half space with a cylindrical inhomogeneous inclusion," H. Hasegawa, R-H. Liarng and Toshio Mura, J. Them. Stresses 15 Hemisphere Publishing Corp. (1992) pp. 295-310.

Appendix G "M_2C Carbide Precipitation in AF1410," Proc. Gilbert R. Speich Symposium: Fundamentals of Aging and Tempering in Bainitic and Martensitic Steel Products, J. S. Montgomery and G. B. Olson, eds. G. Krauss and P. E. Repas, ISS-AIME, Warrendale, PA, (1992) pp. 177-214.

Appendix H "Ostwald Ripening in Multicomponent Alloys," A. Umantsev and G. B. Olson, Scripta Metall. Vol. 29 (1993) pp. 1135-1140.

J. Mater. Educ., Vol. 11, pp. 515-528, 1989.

NEW STEELS BY DESIGN*

G.B. Olson
Department of Materials Science and Engineering
Northwestern University
Evanston, IL 60208-3108

INTRODUCTION

Research presented here is part of the multi-institutional Steel Research Group program involving the participants listed in Figure 1. We will focus in particular on developments in ultrahigh-strength martensitic alloy steels (Program A) which are motivated by the ultimate mechanical property objectives shown in the plot of K_{IC} fracture toughness vs. strength level in Figure 2. Moving from the lower band of commercially available properties to the objective band shown would allow a substantial increase in the useable strength level of ultrahigh-strength steels in advanced structural applications. However, it is important as well to achieve a similar improvement in stress-corrosion resistance represented by the K_{ISCC}.

Our approach to this is not only to determine the scientific principles controlling the properties of interest, but to develop methods of integrating this understanding within an engineering systems design framework. Figure 3 represents our view of a steel as a system,

---

* This paper was presented at the Materials Research Society Annual Meeting, Symposium XTV, "New Frontiers of Materials Research," Boston, November (1989).

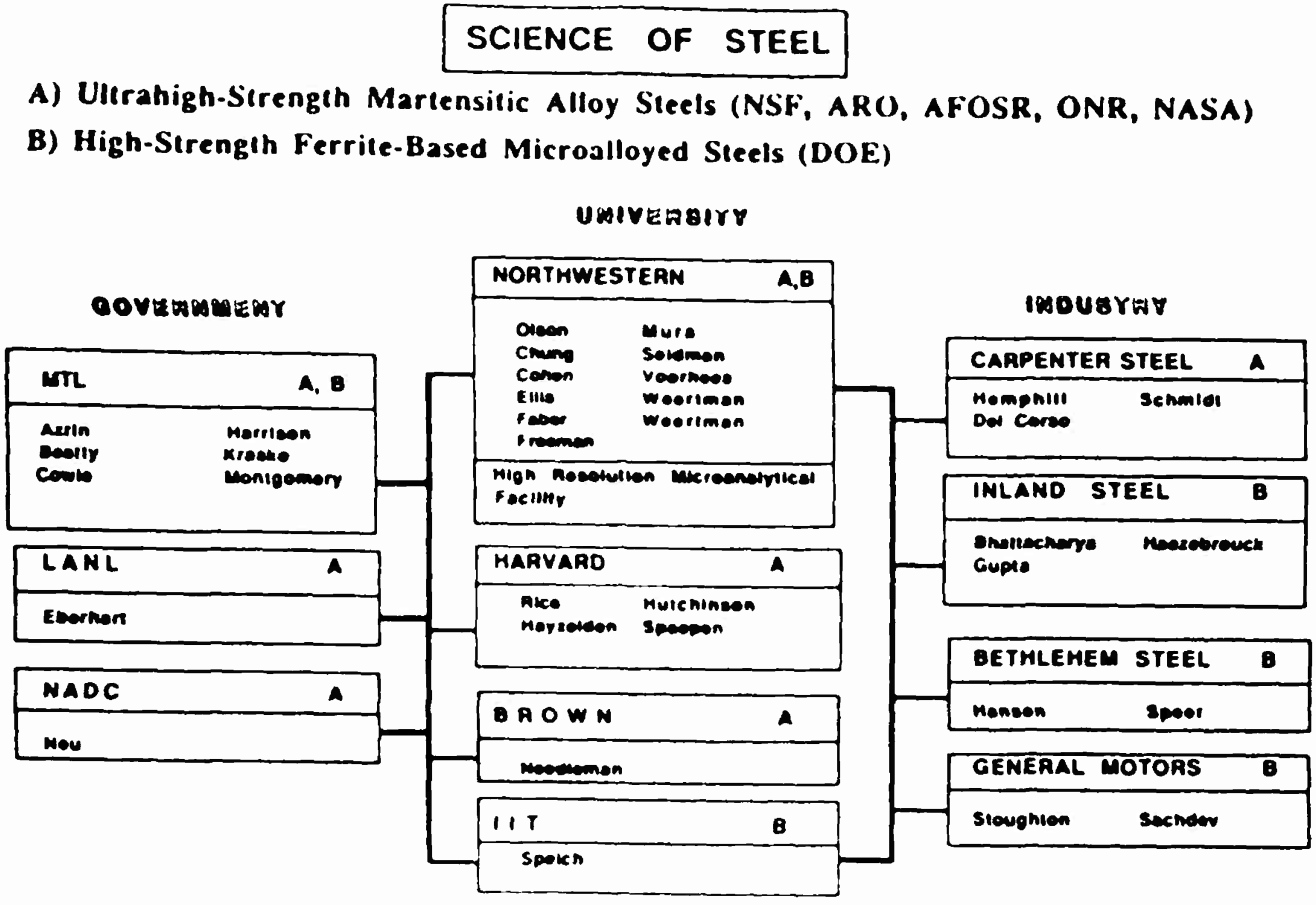


FIG. 1

Organizaton of the Steel Research Group.

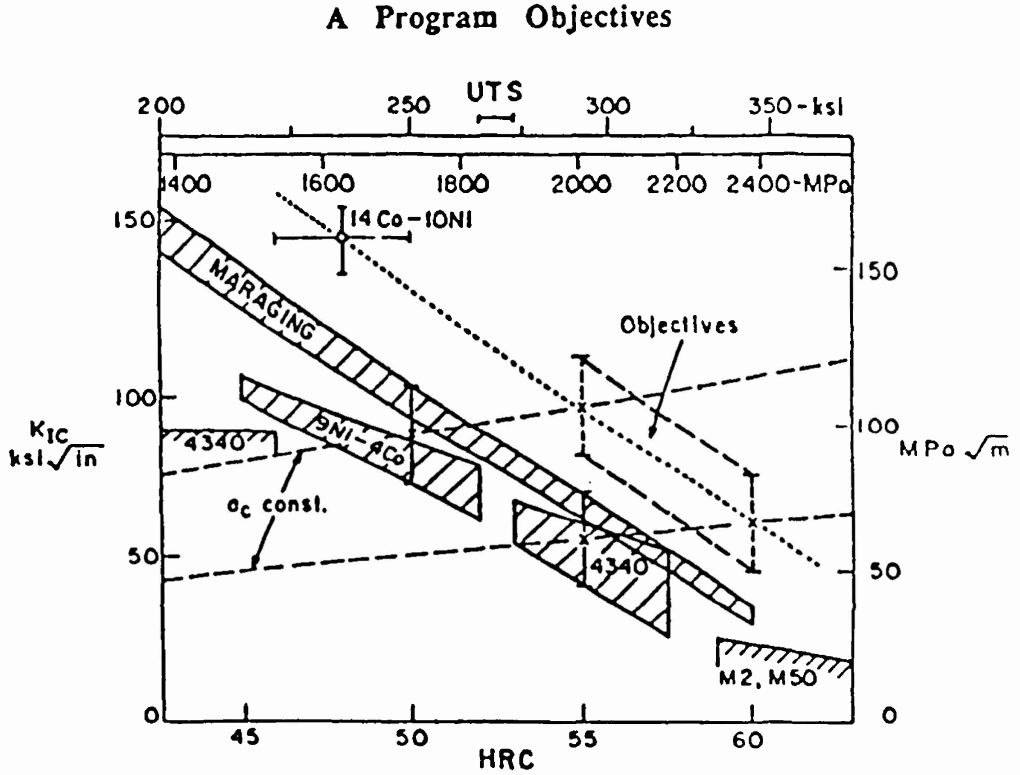


FIG. 2

Fracture toughness vs. strength (hardness) showing A program objectives relative to commercial ultrahigh-strength steels.

represented by a set of microstructural subsystems as defined from the viewpoint of the particular set of properties that we wish to control, and showing their interconnections with the stages of processing that influence them. We will here examine developments in (a) the control of kinetic phase competition for precipitation strengthening without embrittlement, (b) the control of precipitation of metastable austenite dispersions for transformation toughening, and (c) the electronic level control of intergranular cohesion for hydrogen stress-corrosion resistance.

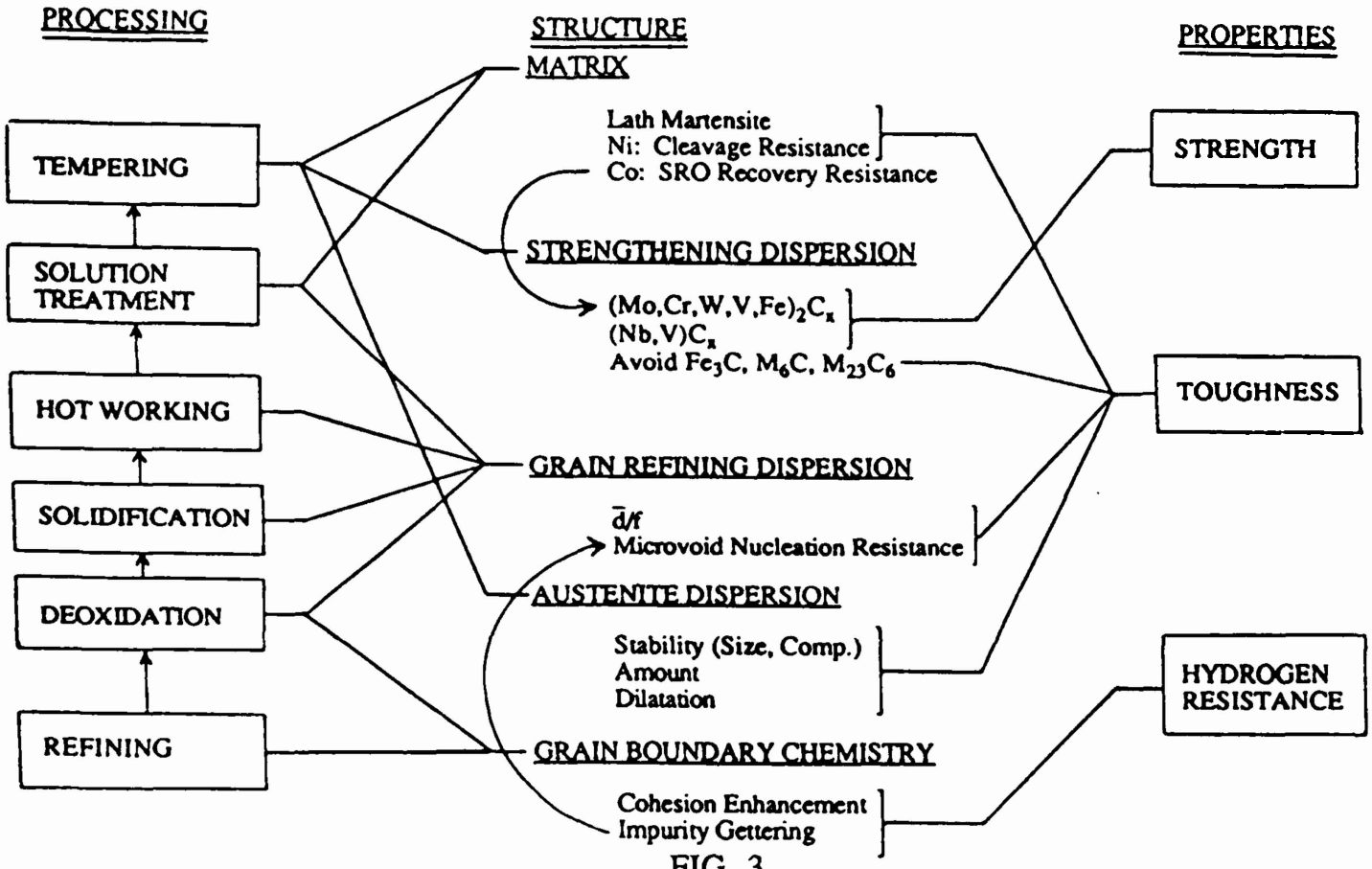


FIG. 3

Flow-block diagram representing a steel as a system of interacting processing/structure/property subsystem.

STRENGTHENING

The objective of precipitation strengthening is to achieve the finest possible dispersion of M_2C alloy carbides at completion of the precipitation reaction. Completion is important in order to eliminate the transient iron-based cementite, which limits fracture toughness[1]; and since the desired carbide is metastable, it is also important to reach that completion prior to the precipitation of equilibrium carbides such as M_6C which form on grain boundaries and limit fracture toughness (Figure 3). Toward that end we have conducted an extensive study of M_2C carbide precipitation in AF1410 steel, which is summarized by the plots vs. tempering time of Figure 4, showing the evolution of (a) particle size, number density, and volume fraction determined primarily by small-angle neutron scattering (SANS),[2] (b) the carbide lattice parameters determined by electron diffraction,[3] and (c) the carbide composition trajectory determined at short times by atom-probe microanalysis[4,5] and at longer times by STEM.[6] The overall features are consistent with theoretical predictions[7] for behavior at very high supersaturations where a competition at early times between nucleation and coarsening phenomena lead to a suppressed growth behavior, which is very useful for achieving the finest possible dispersion. Under these conditions, the scaling factor determining the size scale corresponds to the initial critical nucleus size which in turn scales inversely with the precipitation thermodynamic driving force. The composition trajectory shows major departures from equilibrium; these compositions, together with the associated lattice parameter shifts, indicate that precipitation begins in a fully coherent state. Therefore, to treat the thermodynamics we must take into account the composition-dependent elastic energy associated with particle coherency. To do this in complex multi-component alloys, we use the THERMOCALC thermochemical database and software system[8] modified to incorporate the elastic energy effects.[9]

Based on our experience with the AF1410 alloy, we have used the thermodynamics to explore possible new higher-strength compositions for this class of steel using the type of precipitation driving force map[10] shown in Figure 5. This shows for a fixed Co, Ni and C content, contours vs. Cr and Mo content, of the driving force for (a) the equilibrium M_6C carbide and (b) the desired metastable coherent M_2C carbide. Our experience with alloys along the dashed straight line in Figure 5a indicates that a threshold driving force for intergranular embrittlement by the equilibrium M_6C carbide is 15kJ/mole. This then

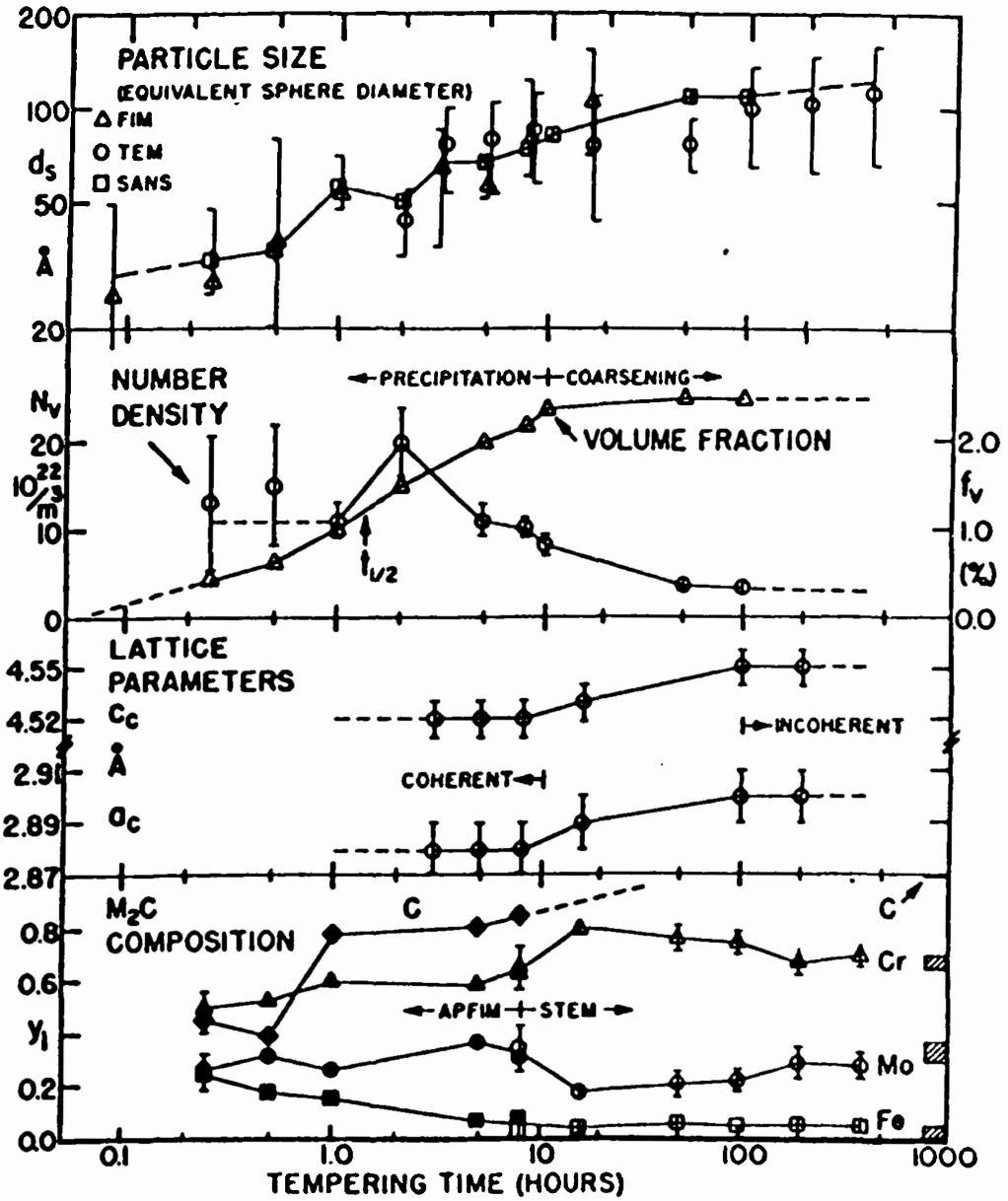


FIG. 4

M_2C precipitation behavior in AF1410 steel (Fe-14Co-10Ni-2Cr-1Mo-0.16C) at 510°C.

gives a composition constraint: we must stay to the left of this contour, which is superimposed as a dashed line in Figure 5b. Subject to this constraint, we can then find a unique composition which maximizes the driving force for the desired coherent M_2C carbide and gives the most

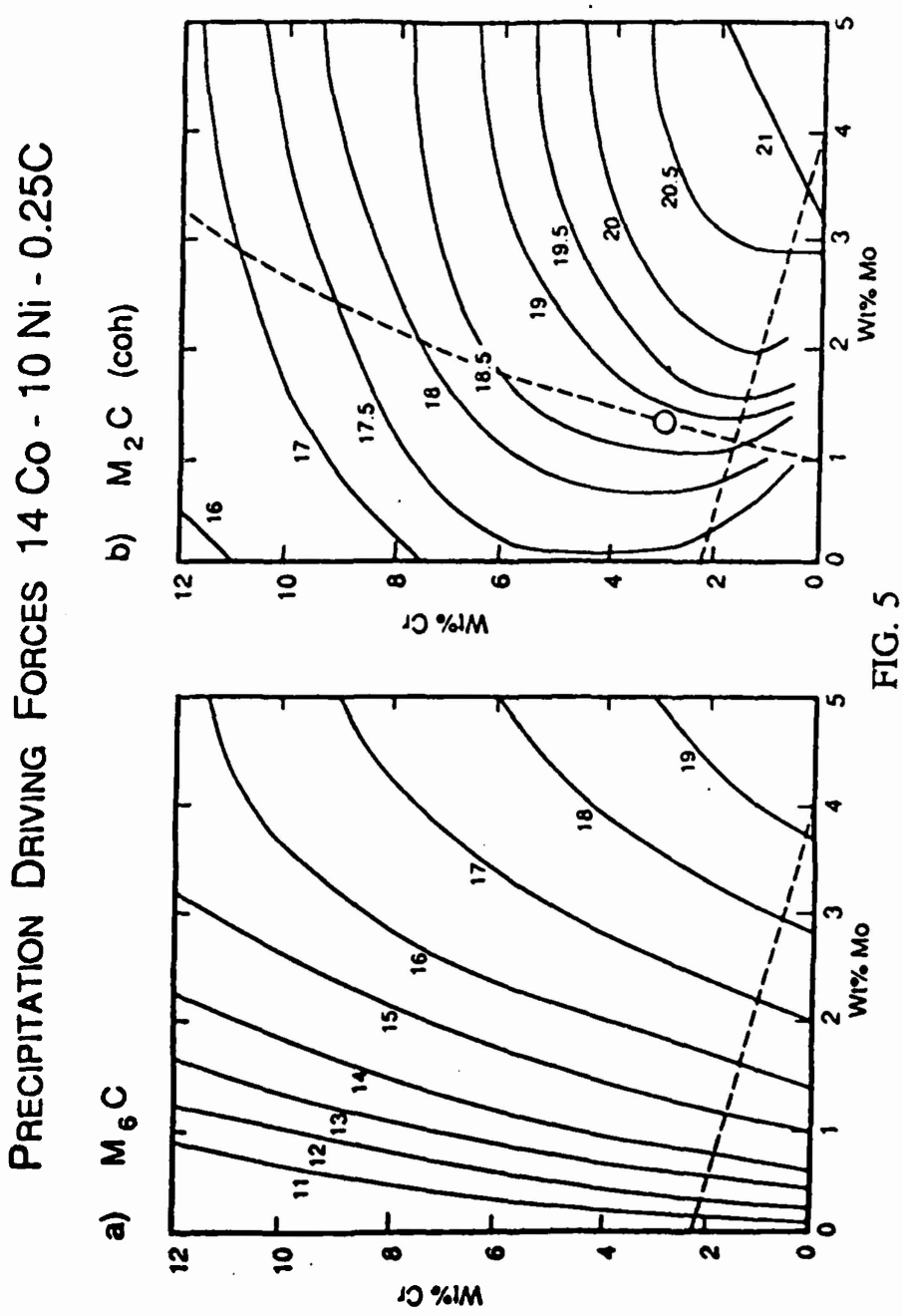


FIG. 5

Contours of precipitation thermodynamic driving force (kJ/mole) in 14Co-10Ni-0.25C steels for (a) M_6C and (b) coherent M_2C, for precipitation from fully supersaturated ferrite at 150°C.

efficient strengthening. In parallel with these thermodynamic calculations, an empirical alloy development program at Carpenter Steel has actually arrived at a composition very similar to this and shown substantially improved mechanical properties.[11]

TRANSFORMATION TOUGHENING

To achieve further enhancement of fracture toughness we can control the simultaneous precipitation of metastable austenite during tempering, in order to achieve transformation toughening phenomena. This we have studied initially in AF1410 steel as summarized in Table 1.[11] We find that standard tempering at 510°C at 5-8 hrs provides precipitation of 3-6% austenite on the lath boundaries of the martensite at a size scale of about 0.1μ, and with a composition only slightly enriched with Ni. Our experiments show that this is not sufficiently stable to give optimum transformation toughening, and our transformation kinetic models predict that we can obtain optimal stability by decreasing the particle size and further enhancing the Ni content.

TABLE 1

AF1410 precipitated-austenite transformation toughening.

	510°C/5h	510°C/8h	600°C/15 min + 510°C/8h
γ-microstructure			
Composition			
interlath (0.1-0.2μm)		14Ni-13Co-3Cr	17Ni-15Co-4Cr
intralath (100-200Å)		—	29Ni-10.5Co-4Cr
f^{γ}	0.03	0.06	0.15
Properties			
Hardness	R_c48	R_c46	R_c48
Yield strength	1550 MPa	1360 MPa	1370 MPa
J_{IC} toughness	178 kJ/m^2	201 kJ/m^2	250 kJ/m^2

In seeking ways to do this, we discovered experimentally that insertion prior to the final standard tempering of a higher temperature short time treatment (600°C, 15 min) allows the nucleation within the martensite laths of a finer 100Å dispersion of highly Ni enriched austenite which has compositions near equilibrium predictions. This

very fine, high Ni austenite is at the optimum stability giving the mechanical properties summarized in Table 1; a record level of fracture toughness (corresponding to $K_{IC} = 250$ MPa$\sqrt{m}$ at R_c48 hardness) resulting from control of this particular component of microstructure. Further experiments in model austenitic steels demonstrate that the toughening efficiency of transformation scales as the cube of the transformation dilation.[13] We are now accordingly designing compositions to further enhance the transformation toughening.

HYDROGEN STRESS-CORROSION RESISTANCE

Stress corrosion of ultrahigh-strength martensitic steels is controlled by intergranular hydrogen embrittlement invariably associated with prior segregation of embrittling impurities. Toward the control of intergranular cohesion we have recently completed our first set of all-electron total-energy calculations of the energy and electronic state of embrittling impurities, comparing the grain-boundary environment with the corresponding free surface environment. Our initial calculation for the case of P in Fe in the grain boundary configuration at the left of Figure 6 shows a surprising extent of charge transfer from P onto the adjacent Fe atoms (#1), with an attendant reduction of the magnetic moment of those Fe atoms.[14] Upon fracturing the boundary, the P atom can relax out of the plane of the first Fe atom to the configuration shown in the right figure, and in so doing the charge transfer is found to reverse to the P atom with restoration of the magnetic moment of the adjacent Fe atom.[15] This, together with some directional bonding effects,[16] gives a lower energy of the P atom in the fracture surface environment than in the initial grain boundary, contributing to reduced cohesion.[17] We have compared B, C, P, and S and shown that these electronic features correlate with the relative embrittling effects of these impurities giving an electronic basis for the embrittlement.[14] We are now going on to calculation of alloying effects in order to ultimately design grain boundary compositions for enhanced intrinsic cohesion and resistance to interaction with hydrogen.

In the meantime, we have made our most significant advances in stress corrosion resistance in these steels by finding novel ways of removing existing impurities from the boundaries.[18] Our thermodynamic calculations showed that the most effective compound for the stable gettering of P in Fe based alloys is $LaPO_4$, and that this phase should be accessible at high melt undercoolings achievable by

FIG. 6

Configurations employed in electronic calculations for P in Fe at grain boundary (left) and corresponding free surface (right) environments; free surface includes computed charge density contours.

rapid solidification. By combination of centrifugal atomization and late La additions to the melt, we successfully achieved a very fine dispersion of $LaPO_4$ which gave the remarkable increase in K_{ISCC} compared to conventional steels in Figure 7.

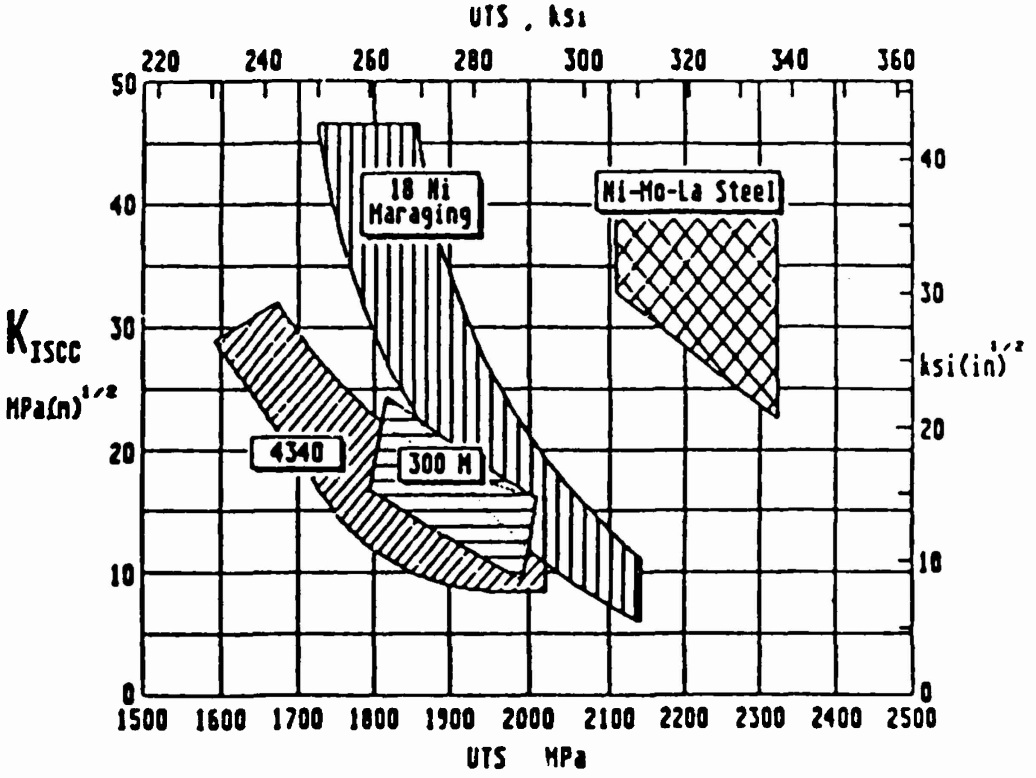


FIG. 7

Stress-corrosion resistance vs. strength comparing rapidly solidified La-Ni-Mo steel with conventional ultrahigh-strength steels.

MATERIALS DESIGN

So far our first effort to take all these developments and integrate them into the design of one steel was undertaken by a team of students in the Materials Design Course at Northwestern University,[19] who performed a conceptual design of a stainless bearing steel for the Space Shuttle Main Engine turbopumps, a demanding application requiring substantial improvements in toughness and stress-corrosion resistance. Consistent with the scheme of Figure 3, a sequence of operations was followed to arrive at an alloy composition tailored to respond to specific processing. First, the composition was constrained for compatibility with rapid solidification and the La treatment. The matrix composition was then constrained to include 12% Cr for stainless properties. THERMOCALC computations were then used to compute a line of compositions in Ni and Co that maintained a sufficiently high M_S temperature to give the desired lath martensite structure. Thereafter, a unique Ni and Co composition was found by considering the type of austenite that would precipitate during tempering, both in terms of its amount and its stability as quantified by the martensitic transformation driving force at room temperature. With that matrix composition, Mo and V contents were finally optimized to maximize the driving force for the coherent M_2C while maintaining limits on the M_6C and $M_{23}C_6$ carbides.

In this way, a computer-aided thermodynamics-based design yielded at a unique composition; if it is successful, we will have arrived at a very different way a creating new materials.

ACKNOWLEDGEMENTS

The Northwestern University component of the Steel Research Group program is sponsored by NSF/MRL, ARO, AFOSR, ONR, NASA and DOE.

REFERENCES

1. G.R. Speich, D.S. Dabkowski and L.F. Porter, Met. Trans. 4, 303 (1973).
2. A. Allen and J.R. Weertman, Northwestern University, manuscript in preparation.
3. J.S. Montgomery and G.B. Olson, Proc. 34th Army Sagamore Materials Conf., in press.
4. G.M. Carinci, M.G. Hetherinton anc G.B. Olson, J. de Physique 49, C6-311 (1988).
5. T. Kinkus and G.B. Olson, Northwestern University research in progress.
6. H-M. Lee and A.J. Garratt-Reede, MIT unpublished research (1988).
7. J.S. Langer and A.J. Schwartz, Phys. Rev. A21, 948 (1980).
8. B. Sundman, B. Jansson and J.A. Andersson, CALPHAD 9, 153 (1985).
9. M. Grujicic and G.B. Olson, CALPHAD 12, 403 (1988).
10. G. Ghosh and G.B. Olson, Northwestern University research in progress.
11. R. Hemphill, Carpenter Steel Aermet 100 alloy steel, patent pending.
12. G. Haidenmenopoulos, G.B. Olson and M. Cohen, Proc. 34th Army Sagamore Materials Conf., in press.
13. C-C. Young, Ph.D. thesis, MIT(May 1988).
14. G.L. Krasko and G.B. Olson, manuscript in preparation.
15. C. Li and A.J. Freeman, Northwestern University research in progress.
16. H. Eguchi, M.S. thesis, Northwestern University (June 1990).
17. J.R. Rice and J-S. Wang, Mat. Sci. and Eng. A107, 23 (1989).
18. G.B. Olson, J.F. Watton and M. Cohen, U.S. Patent #4,836,869.
19. A. Bilyk, T. Chen, N. Akaiwa, H. Eguchi and G.B. Olson, Northwestern University 750-C95 Materials Design Class Project Report (June 1989).

INSTRUCTIONAL USE PROFILE

1. Title - New Steels by Design
2. Author - G.B. Olson, Northwestern University
3. Correspondent - MEC Administrator, 110 Materials Research Laboratory, The Pennsylvania State University, University Park, PA 16802
4. Version - II, 1989; JME 11(5&6).
5. Classification - Materials Science; pedagogical, peer reviewed, interdisciplinary
6. Intended Audience - Senior and beginning graduate student level
7. Length - 14 pages, 7 figures
8. Recommended Support Media - None
9. Key Word List - Steel, design, martnesite, properties, composition
10. Skills and Knowledge Taught - Upon successful completion of this module, the student will be able to describe a systems approach to materials design, specifically an ultrahigh-strength martensitic steel, and prescribe multicomponent alloy compositions to achieve specified microstructural objectives.
11. Prerequisites - Completion of: elementary physics, chemistry and materials science
12. Nearest Neighbor Links - None
13. Distribution Information - Institutional subscription to JME carries unlimited reproduction rights. (See inside front cover.)

OVERVIEW: SCIENCE OF STEEL

G.B. OLSON
Department of Materials Science and Engineering, Northwestern University, Evanston, IL 60208

INTRODUCTION: STEELS AND MATERIALS DESIGN

Steel is the frontier of materials science. More is known about steels than any other class of materials. Paradoxically, despite this position in fundamental understanding, the actual process by which new steels are still developed amounts to the same empiricism which is applied to newer materials for which the alternative of science-based design is not an option. In the arena of empiricism the maturity of steels poses a severe disadvantage in that the "soft ground" has already been explored and empirical development has reached a point of diminishing returns. To compete with newer materials for which traditional empiricism can bring more rapid improvements, there is a pressing need for a better way to develop new steels. Moreover, the ultimate goal of materials science must certainly be the design of superior materials from basic understanding; our very limited ability to truly design materials calls into question the viability of this discipline. This circumstance makes the science of steel a most timely subject: no material is in a better position to be designed from scientific knowledge at the same time that no material is in more need of this approach.

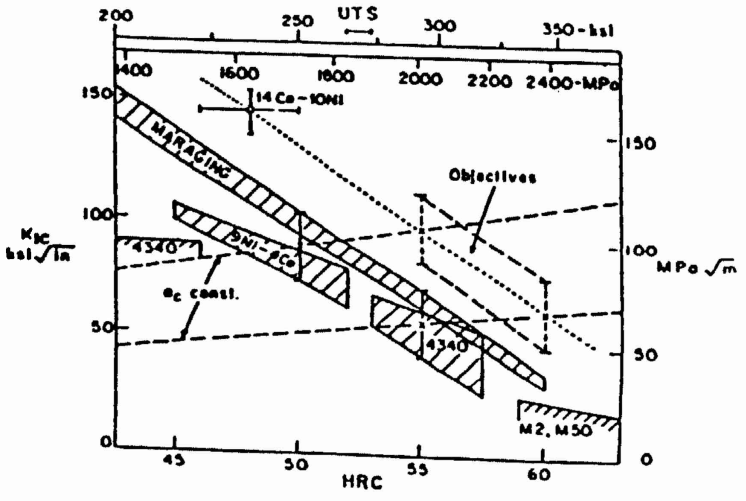
The research reviewed here is based primarily on the Steel Research Group (SRG) program, a multi-institutional university/government/industry interdisciplinary effort directed at the scientific principles for the design of new classes of steels, motivated by specific property objectives of importance to industry. Two key classes of steels have been selected. The major effort reviewed here ("A" Program) is directed at ultrahigh-strength martensitic steels for advanced structural applications, while a smaller effort ("B" Program) is directed at high-strength ferrite-based microalloyed steels for high formability automotive sheet applications. Objectives have been deliberately chosen to represent a sufficiently ambitious advance to require a more fundamental approach to materials design than ever previously attempted.

PROPERTY OBJECTIVES

The performance of a material in service is controlled by a set of properties. Surprisingly, our ability to specify the long list of properties actually required for a given application can be the weakest link in the materials design process. In searching for a model system in which to develop

new approach to design, it is helpful to examine the most emanding applications for which the list of properties one an reasonably request is relatively short. Ultrahigh trength steels for advanced structural applications are an xcellent example where primary objectives can be expressed n terms of the three properties of strength, toughness, and ydrogen resistance. If a sufficiently improved combination f these properties can be achieved, other properties such as ost and processability are secondary considerations.

Strength/toughness objectives adopted for the ultrahigh trength steels are depicted in Figure 1 which shows data ompiled at MTL representing the typical K_{IC} fracture oughness levels of commercial steels currently in use in pplications requiring hardness levels of R_c50 and above. lso indicated are the approximate ultimate tensile strength UTS) corresponding to each hardness. Marginal fracture oughness and corresponding critical flaw size limit the seable hardness level in structural applications (involving ignificant tensile loads) to R_c55, with more conservative



ig. 1 Typical plane-strain fracture toughness (K_{IC}) vs. Rockwell C hardness (HRC) for commercial ultrahigh-strength steels currently employed in advanced structural applications. Upper scale shows approximate ultimate tensile strength (UTS) with indicated scale limit. Strength/toughness objectives depicted allow a factor of 2 increase in useable strength level at K_{IC} = 100 ksi$\sqrt{in}$ and a factor of 3 at K_{IC} = 50 ksi$\sqrt{in}$.

applications demanding greater flaw tolerance limited to R_c50. The dashed lines depict contours of constant critical flaw size at a design stress proportional to hardness, identifying the objectives shown to allow a 5 R_c point increase in useable hardness level. The latter corresponds to a substantial strength increment of 50 ksi or 400 MPa. The strength levels thus defined mark the toughness "frontier" of ultrahigh-strength steels; the objectives posed demanding K_{IC} improvements by a factor of 2 at R_c55 and 3 at R_c60.

While low alloy stage-I tempered (ε-carbide strengthened) martensitic steels, exemplified by 4340, still show potential for toughness improvement and are the subject of further study under the SRG program, the new class of steels which has so far demonstrated the highest combinations of strength and toughness is the high alloy secondary-hardening (alloy carbide strengthened) martensitic steels, currently represented by the commercial HY180 and AF1410 steels. At R_c45, HY180 exhibits K_{IC} toughness levels in excess of 230 ksi$\sqrt{in}$, beyond the scale of Figure 1. The higher-strength AF1410 reliably provides a K_{IC} toughness of 140 ksi$\sqrt{in}$ at R_c48 as depicted in Figure 1, while exceptional commercial heats can show 190 ksi$\sqrt{in}$. Expanding this class of steel to the ultrahigh-strength R_c55-60 range offers the greatest potential of meeting our toughness objectives. Moreover, in extending the useable strength of structural steels to R_c60, such secondary hardening steels would overlap with tool steels (represented by M2 and M50 in Figure 1) of interest for bearing and gear applications, thus creating a class of steels with a wide range of potential applications.

Although fracture toughness is an important consideration, a more serious limitation on the reliability of ultrahigh-strength steels is their low resistance to stress-corrosion cracking, which at these strength levels occurs by a hydrogen embrittlement mechanism associated with cathodic charging at the crack tip. At R_c55, the low hydrogen resistance limits the stress corrosion threshold K_{ISCC} to ~10 ksi$\sqrt{in}$. Raising useable strength to the levels depicted in Figure 1 requires major improvements in hydrogen stress-corrosion resistance in order to maintain a K_{ISCC}/K_{IC} ratio of at least 0.5 out to R_c60. As traditional alloy development approaches have produced little change in this property of ultrahigh strength steels in the past decade, the required K_{ISCC} improvements represent the most ambitious objective of the SRG effort, warranting the most interdisciplinary and fundamental approach.

MATERIALS AS SYSTEMS: AN APPROACH TO DESIGN

The central paradigm of materials science is the sequential interrelation of processing, structure, properties, and performance. Although empirical development attempts to bypass elements of this sequence, for example correlating processing and performance without regard to structure/property relations, scientific understanding demands that each link of the sequence be known. Cause-and-effect logic gives a natural direction to this sequence of the form: processing→structure→properties→performance, and from the philosophy of scientific analysis by which we distill simple laws from natural complexity, it it tempting to imagine a materials design process in which predictive theory specifies a composition and processing producing the necessary structure providing the required properties for desired performance. In practice each of these elements and their interrelation is of infinite complexity in real materials, severely compromising our predictive abilities. To usefully synthesize available understanding, we must combine with the scientist's methods of simplifying analysis the engineer's methods for dealing with real complexity, formalized in the "systems" approach (1).

Cyril Smith (2) has expounded on the notion of materials as systems, characterized by a hierarchical structure of interacting microstructural subsystems. Processing and properties can each be likewise described as hierarchies of interactive subsystems, each such subsystem involving important cross-interactions with microstructural subsystems. Morris Cohen (3) has observed that within this interlocking network there is a "reciprocity" such that equally valid to the notion that structure controls properties is the alternative view that properties control structure: our perception of structure is a function of the properties we are attempting to explain. This yields the important principle that knowledge of the relation of a particular component (subsystem) of structure to a property can be used to improve that property without ever requiring the impossible task of characterizing the entire structure. An important aspect of the engineering science of materials is then the discrimination between microstructural components which are actively linked to properties of interest, and inert ingredients such as nonessential evolutionary vestiges which are a common feature of complex systems. As emphasized by Cohen (3,4) this will always involve a blend of predictive theory and empiricism. It is a reasonable expectation that by a combination of predicting the predictable and measuring the measurable we can identify sufficient subsystem interrelations to pose process/structure solutions to property/performance problems, tempered by a certain amount

of discouragement from "unknowables" which are beyond our current abilities to predict or measure.

The flow-block diagram of Figure 2 describes the structure of Ni-Co secondary hardening martensitic steels as a hierarchy of microstructural subsystems defined from the viewpoint of combined strength, toughness, and hydrogen resistance, and identifying the stages of processing affecting each. The multicomponent matrix of the steels consists of a lath martensitic microstructure (representing the best class of microstructure for strength/toughness) with a high Ni content for cleavage resistance. Based on the seminal research of Speich (5,6) the Co is used to retard dislocation recovery (which we will later associate with short-range order), which has an important interaction with the strengthening subsystems via heterogeneous nucleation of the M_2C (and MC) carbide strengthening dispersion on the dislocations during tempering. Speich's study of HY180 (6), which formed the basis of the AF1410 development, further showed that an optimum strength/toughness combination is achieved by bringing the alloy carbide precipitation reaction to completion in order to dissolve the relatively coarse transient θ-cementite (Fe_3C) which precipitates earlier and acts as a microvoid nucleation site limiting ductile fracture resistance. The M_2C carbide primarily responsible for secondary hardening is metastable, and high fracture toughness also demands that this metastable reaction reach completion without the nucleation of more stable carbides (M_6C, $M_{23}C_6$) which can precipitate incoherently on interfaces and degrade toughness.

Microvoid nucleation during plastic deformation accelerates ductile fracture through a process of shear localization. Once the precipitation kinetics of competing phases are controlled to achieve a fine strengthening dispersion without unnecessary coarser particles, resistance to microvoid nucleation is ultimately governed by the grain refining dispersion necessary to maintain a sufficiently fine grain size during solution treatment to inhibit competing brittle fracture modes. The grain refining ability of this dispersion is set by the ratio of average particle diameter d to the volume fraction f. Subject to this constraint, toughness enhancement can be sought from an optimization of the geometry and composition of the dispersion (set by earlier processing stages), in order to increase microvoid nucleation resistance.

Further toughening can be achieved through modification of matrix constitutive behavior, the most dramatic example being the incorporation of transformation plasticity from a dispersion of metastable austenite particles precipitated

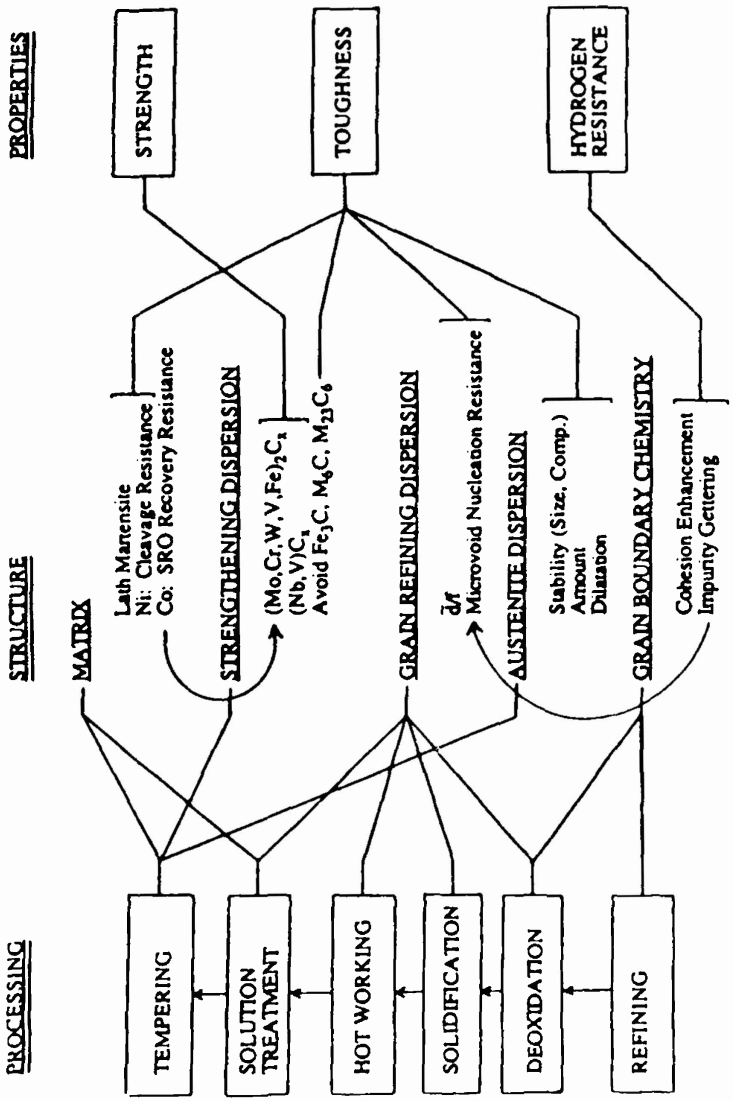


Fig. 2 Flow-block diagram illustrating the interactive hierarchical structure of a Co-Ni secondary hardening martensitic steel from the viewpoint of desired properties.

during tempering. The transformation toughening is sensitive to the particle transformation kinetic stability (controlled by particle size and composition), the amount of dispersed phase, and the magnitude of its transformation dilatation.

Hydrogen stress corrosion cracking in ultrahigh strength martensitic steels occurs by a brittle intergranular cleavage mechanism invariably associated with boundary segregation of embrittling metalloid impurities. The embrittlement appears to be controlled by the chemistry of intrinsic boundary cohesion. Under the SRG program, an interdisciplinary effort is directed at the ultimate application of an electronic-level understanding of intergranular cohesion to the design of grain boundary composition for both enhanced intrinsic cohesion and reduced interaction with hydrogen. A parallel effort explores the use of novel processing techniques to getter embrittling impurities into highly stable compounds, potentially offering the additional toughening benefit of cleaning the interphase boundaries controlling microvoid nucleation.

As is a common feature of systems, the separate optimization of each of the subsystems of Figure 2 poses conflicting objectives. Optimization of the total system demands compromise between subsystems such that local optimizations are highly constrained by the requirements of other subsystems. After reviewing progress in our understanding of the functioning of each of these subsystems, we will examine its application in conceptual designs which effect this compromise.

STRENGTHENING

The strength of overaged precipitation-hardened structures is controlled by the Orowan bypass mechanism for which strength is inversely related to the particle mean free path. For a given amount of precipitating phase, maintaining the highest possible strength at completion of precipitation requires minimization of the final particle size. This is controllable in principle through application of transformation kinetic theory, once theory is properly calibrated by appropriate experiments in the system of interest. It is a fairly recent development that available instrumentation has attained the capabilities required to adequately characterize the fine scale strengthening dispersions of ultrahigh-strength steels.

Results of an ongoing comprehensive study of M_2C carbide precipitation in AF1410 steel are summarized in Figure 3. The figure shows the M_2C carbide particle size, shape, number density, volume fraction, lattice parameters,

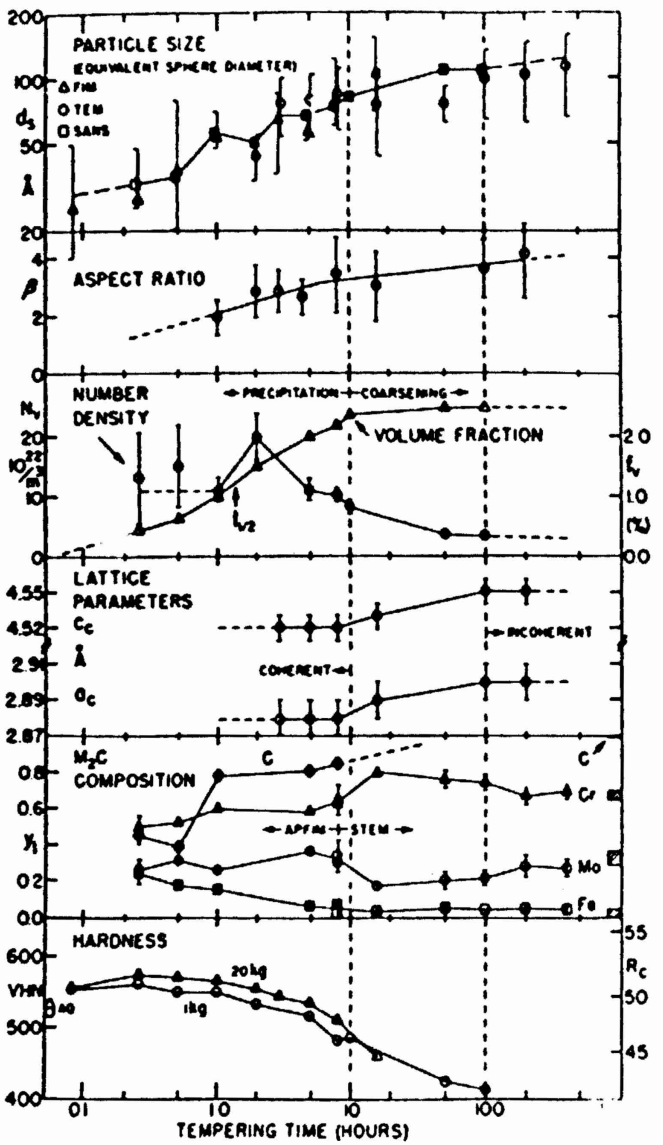


Fig. 3 M_2C carbide precipitation behavior in AF1410 steel vs. tempering time at 510C following 1 hr solution treatment at 830C.

and composition, as well as the steel hardness, all as a function of tempering time at the standard temperature of 510C, following 1 hr solution treatment at the standard austenitizing temperature of 830C. The alloy composition studied is given in Table 1. The average particle size of the rod-shaped carbides is expressed by the diameter, d_s, of a sphere of equivalent volume. While there is considerable uncertainty in the size estimates from field-ion microscopy (FIM) (7) and transmission electron microscopy (TEM) (8), the greater sampling statistics of small-angle neutron scattering (SANS) (9) give a well-defined size distribution defining an average particle size with 90% confidence limits comparable to the size of the squares plotted in Figure 3. Analysis of the SANS data incorporated the particle aspect ratio, β, determined from TEM of extracted particles, smoothly varying from near unity at initial nucleation to 4 at (near) equilibrium. The time dependence of average size suggests a smooth transition from nucleation to coarsening with suppressed growth characteristic of precipitation at high supersaturations as predicted by recent theories (10-12) based on the model of Langer and Schwartz (13). Nucleation in the ~0.1-0.5h regime is followed by a short growth regime between 0.5 and 1.0h, increasing average particle size from 36 to 56 Å. This is followed between 1 and 2h (bracketing the reaction half-time $t_{1/2}$ indicated by the volume fraction f_v curve) by a surprising second stage of nucleation which reduces the average particle size through an increased number of finer particles, bringing the total particle number density N_v (determined by SANS) to a maximum. This may represent an extreme form of a phenomenon encountered in the numerical modelling of precipitation at high supersaturation by Kampmann and Wagner (11) in which oscillations in nucleation rate are associated with crossovers between the average and critical particle sizes. Overall, the observations are consistent with the general features of high supersaturation behavior in which the major portion of solute depletion is associated with nucleation rather than growth, and the average particle size never differs greatly from the critical size. This constitutes a highly useful phenomenon for maintaining the finest possible particle size at completion of precipitation.

The volume fraction curve, determined from SANS, shows that precipitation is virtually complete after 10h tempering and very nearly complete after the standard 5 to 8h temper employed in practice. This is consistent with nearly complete dissolution of transient cementite for optimal toughness as emphasized by Speich (5,6).

TABLE 1

Alloy Steel Compositions (wt. pct.)

Commercial	C	Co	Ni	Mo	Cr	other
HY 180	0.11	8.0	10.2	1.0	2.0	0.18Mn
AF1410	0.16	14.25	10.15	1.05	2.10	--
Experimental						
1) 1410-4Mo	0.23	14.17	10.24	3.96	0.06	--
2) 1605-4Mo	0.24	15.99	4.96	4.03	0.02	--
3) 1605-MoCr	0.24	16.08	4.97	2.82	0.71	--
4) 1605-CrMo	0.24	16.06	4.98	1.52	1.40	--
5) 1605-4Mo(Nb)	0.24	16.02	4.97	4.03	0.02	0.029Nb
6) 1605-4Mo(NbV)	0.25	16.10	4.97	4.03	0.02	0.013Nb 0.006V
7) .1605-4Mo(Au)	0.23	15.92	5.03	4.10	0.02	0.07Au

Information on the state of interfacial coherency of the carbide particles can be deduced from the lattice parameters of extracted carbides measured by electron diffraction (8), also shown in Figure 3. In a coherent state the carbides will tend to reduce elastic energy by adopting a modified composition which reduces the overall magnitude of the orthorhombic lattice deformation relating the coherent HCP carbide to the BCC matrix. The smaller lattice parameters at shorter tempering times, observed here and in similar alloys (8), are consistent with such a reduction in the large positive BCC→HCP transformation strains in this system. The observed lattice parameter shifts suggest that the particles are coherent below 10 hr tempering and reach a fully incoherent state beyond 100 hr.

Measurement of the composition trajectories of the M_2C carbides presented in Figure 3 is made possible by the atom-probe field-ion microscope (APFIM) providing the necessary microanalytical resolution at the atomic scale (14-16); microanalysis of the coarser particles obtained beyond 10 hr tempering (17,18) is performed by scanning transmission electron microscopy (STEM). Compositions are represented as M_2C site fractions, with the bars at the right depicting the range of equilibrium compositions predicted by available thermodynamic databases (17). Although the carbide composition appears to ultimately reach equilibrium in the incoherent state, major departures from equilibrium exist at early stages of precipitation. Based on available data for the composition dependence of the M_2C lattice parameters (8), the depletion of C and enrichment in Fe are consistent with the observed lattice parameter shifts. In addition to elastic coherency effects, particle composition at small

sizes will also be strongly influenced by capillarity. If the interfacial energy is not strongly composition dependent, the first particles will tend to adopt a composition corresponding to the maximum precipitation driving force; thermodynamic calculations of this composition suggest a reduced Cr/Mo ratio consistent with observation (19). The lattice parameter shifts and volume fraction measurements further suggest that the carbides achieve completion of precipitation in the coherent state, and are therefore close to a state of coherent equilibrium after 8 hr tempering of this steel.

The hardness curve in Figure 3 demonstrates that the completion of M_2C precipitation (and elimination of cementite) at 8-10 hrs tempering corresponds to an overaged condition. As mentioned earlier, strength in this regime is controlled by the Orowan bypass mechanism for which the strength achieved from a given volume fraction of precipitate can be increased by refining the particle size. Employing the information obtained from Figure 3, improved alloy compositions for more efficient strengthening can be sought from precipitation kinetic theory through control of appropriate scaling factors. In current theory of precipitation at high supersaturations (10-13), the principal scaling factors are (a) a diffusion time factor, which can be deduced from particle coarsening behavior, and (b) the initial critical nucleus size, inversely related to the precipitation thermodynamic driving force.

A rate constant for multicomponent particle coarsening, defining a diffusion time factor for multicomponent precipitation, has been derived by an extension (17,20) of the model of Bjorklund, Donaghey, and Hillert (21). The model has been tested (17, 20) by comparison of the relative $(Cr,Mo)_2C$ carbide coarsening rates in the experimental alloys 1 to 4 listed in Table 1. This series of alloys has a total Cr and Mo content balanced to 0.25 w/o C in the stoichiometry of the M_2C carbide, representing the minimum alloy content for complete replacement of cementite by M_2C. Alloy 1 (1410-4Mo) has the 14Co-10Ni matrix composition of AF1410, while alloys 2 through 4 (1605 series) have a 16Co-5Ni matrix which eliminates interference from austenite precipitation at long tempering times (17). Figure 4 plots the computed rate constant K defined in ref. 20, as well as the relative value (k/k_1) normalized to alloy 1. Despite the higher diffusivity of Cr relative to Mo and the lower thermodynamic stability of Cr_2C compared to Mo_2C, the model predicts a relatively low coarsening rate for the mixed $(Cr,Mo)_2C$ carbides (in part due to the stabilizing contribution of the entropy of mixing in the M_2C phase), as indicated in the lower curves for the 1605-.25C and 1410-.25C series. These stoichiometric

compositions are predicted to have generally low coarsening rates (due to reduced Cr and Mo in matrix solution) as shown by comparison with the upper dashed curve representing 1410-.16 alloys with the lower carbon content of AF1410. Experimentally observed relative coarsening rates, k/k_1 as defined by the time dependence of average particle volume in 10 to 100 hrs tempering at 510C (17) are also plotted for alloys 1 to 4 and AF1410 in Figure 4. Apart from an anomalously high rate for alloy 2, the comparison supports the predicted lower coarsening rate of the stoichiometric alloys (by a factor of 20) compared to the non-stoichiometric AF1410, and supports the predicted multicomponent effects giving the mixed $(Cr,Mo)_2C$ carbides of alloys 3 and 4 coarsening rates comparable to the (more stable) Mo_2C carbide of alloy 1. These data must be viewed with some caution, however, as the alloys experienced some degree of decarburization during heat treatment. Overall, the coarsening model appears reasonable and could be applied to design of alloys with lower coarsening rates for thermal softening resistance (as in tool steels); in structural steels for room temperature applications it is more desirable to enhance the diffusional rate factor to accelerate secondary hardening at lower tempering temperatures.

The most important scaling factor governing the size scale of the precipitate dispersion (as well as the rate of nucleation) is the initial critical nucleus size. This in turn scales directly with the precipitate interfacial energy, and inversely with the precipitation thermodynamic driving force. The alloy composition dependence of the latter can be predicted from solution thermodynamics as conveniently treated by available computer software such as the THERMOCALC thermochemical database and software system (22). In order to treat coherent precipitation, however, it is necessary to modify the solution thermodynamics to incorporate the effects of elastic energy. The composition dependence of the M_2C carbide coherency strains (as described by the BCC→HCP lattice deformation accompanying coherent precipitation) can be prescribed from the composition dependence of the carbide lattice parameters (8). Using a simple isotropic homogeneous spherical inclusion model, it has been shown that the coherency elastic energy (in the limit of small carbide volume fractions) can be expressed in a form compatible with the solution free-energy functions employed in the THERMOCALC system allowing a simple modification of the database to treat the thermodynamics of coherent precipitation (19,23). Newer elastic calculations for anisotropic inhomogeneous ellipsoidal inclusions (using observed aspect ratios as represented in Figure 3) have been further refined to incorporate the effects of the redistribution of matrix substitutional solutes in the stress field of the coherent particle (24). This has been performed by an extension to

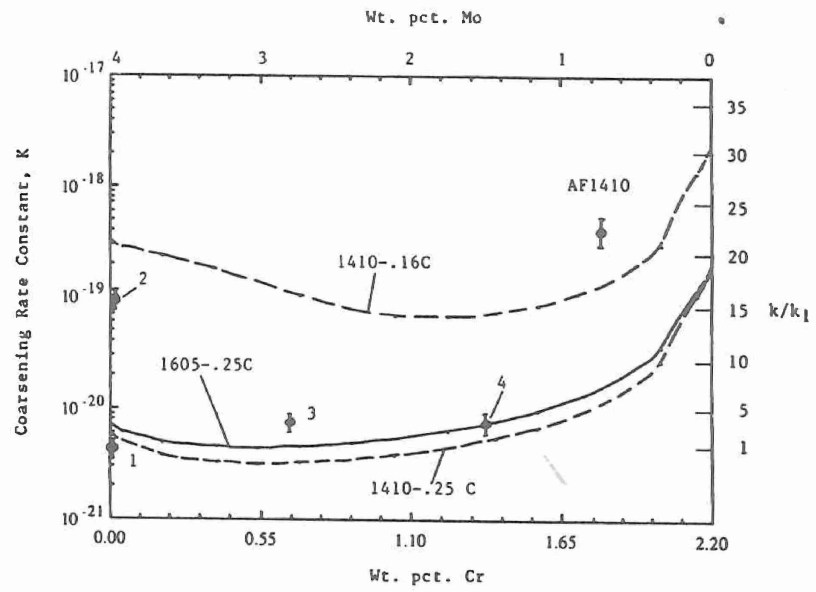


Fig. 4 Rate constants for $(Cr,Mo)_2C$ carbide coarsening in Ni-Co alloy steels with Cr and Mo contents stoichiometrically balanced to 0.24 w/o C.

multicomponent systems of the "open system" elastic constants method of Larché and Cahn (25) in which effective matrix elastic constants (incorporating solute redistribution) are defined from the solution chemical thermodynamics and the composition dependence of the matrix lattice parameters. Application to ferrite-M_2C coherent equilibrium in AF1410 is represented by Figure 5, depicting computed contours of constant hydrostatic stress and composition in the matrix surrounding a coherent M_2C carbide viewed along the matrix $[100]_\alpha$ direction corresponding to the habit direction of the rod-shaped particle (24). Dashed contours depict compressive stress and solute depletion, while solid contours represent tensile stress and solute enrichment. The predicted solute distribution (particularly for Ni and Co) should be measurable by high resolution microanalysis for the coherent particle size achieved after 8 hr tempering. Elastic energies computed from such linear elastic calculations represent an upper bound estimate. Assuming a composition-independent interfacial energy, reasonable agreement is obtained with measured M_2C composition trajectories in AF1410

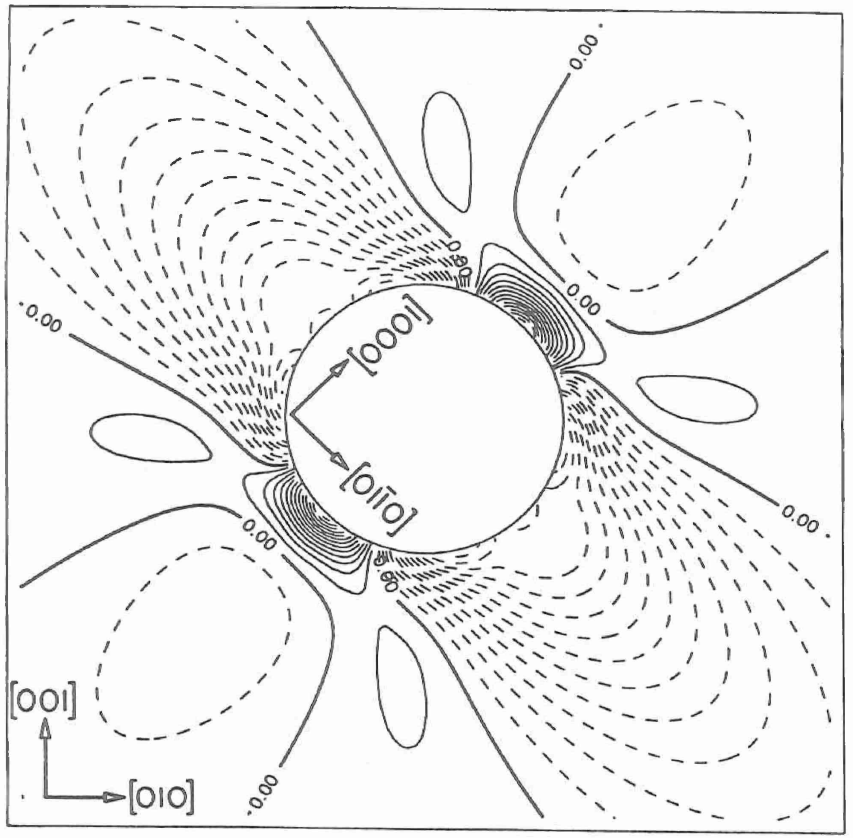


Fig. 5 Computed contours of constant hydrostatic stress and composition surrounding M_2C carbide in coherent equilibrium in AF1410 steel. Carbide viewed along $[100]_\alpha$ rod axis. Crystal axes of BCC α matrix and HCP M_2C carbide are indicated (24).

(Figure 3) and alloys 1-4 of Table 1 (17,18) when a correction factor of 0.25 is applied to the composition dependent elastic energy function defined by these calculations (26). This factor likely compensates for neglect of particle interaction with matrix dislocations to be discussed later.

A quantitative model for the thermodynamics of coherent M_2C precipitation allows prediction of alloy compositions capable of more efficient strengthening through refinement of the particle size. As mentioned in discussion of Figure 2,

however, optimization of the metastable M_2C dispersion is constrained by kinetic phase competition with equilibrium phases such as M_6C and $M_{23}C_6$ which can precipitate incoherently on interfaces degrading toughness. This competition should also be amenable to control through alloy thermodynamics. Figure 6 shows a precipitation driving force map, constructed via THERMOCALC computations, showing contours of constant driving force (in kJ/mole) at 510C for precipitation of incoherent M_6C (Figure 6a) and coherent M_2C (Figure 6b) as a function of Cr and Mo content in alloys containing 14Co-10Ni-0.25C (26). The dashed straight lines represent stoichiometrically balanced compositions (as for the experimental alloys of Table 1) again corresponding to the minimum alloy content for complete elimination of cementite by M_2C precipitation. Intergranular embrittlement during 510C tempering of the experimental alloys (27), tentatively ascribed to M_6C precipitation, suggests a threshold driving force for M_6C nucleation under the tempering conditions of interest of 15 kJ/mole. The contour corresponding to this limit is superimposed as a dashed curve on the coherent M_2C driving force plot of Figure 6b. Through the competing influences of the chemical and mechanical thermodynamic contributions, the coherent M_2C driving force is nonmonotonic with Cr content, but increases with Mo. Maximization of the coherent M_2C driving force subject to the M_6C driving force constraint gives a unique optimum composition represented by the open point in Figure 6b. In parallel with these studies, an empirical alloy development program at Carpenter Steel (28) has arrived at a very similar composition demonstrating an excellent strength/toughness combination at a significantly higher strength than AF1410, supporting plausibility of the suggested thermodynamic design approach. It should be noted that the reference state for the driving force calculations of Figure 6 was fully supersaturated ferrite, while alloy carbide precipitation is in practice preceded by cementite precipitation which lowers the carbon potential. The effect can be estimated by adopting an initial state of ferrite-cementite paraequilibrium in which the cementite is constrained to inherit the substitutional composition of the alloy (29). The lower carbon potential reduces the M_6C driving force by ~0.7kJ/mole and the coherent M_2C driving force by ~2.7 kJ/mole with a slight distortion of the contour shapes of Figure 6 (26).

The influence of the high Co recovery-resistant matrix on M_2C secondary hardening behavior is shown in Figure 7 comparing 1 hr isochronal tempering hardness curves for a simple 4Mo-.23C steel (30) and for alloy 1 of Table 1, with the same Mo and C content but containing 14Co-10Ni (17). In

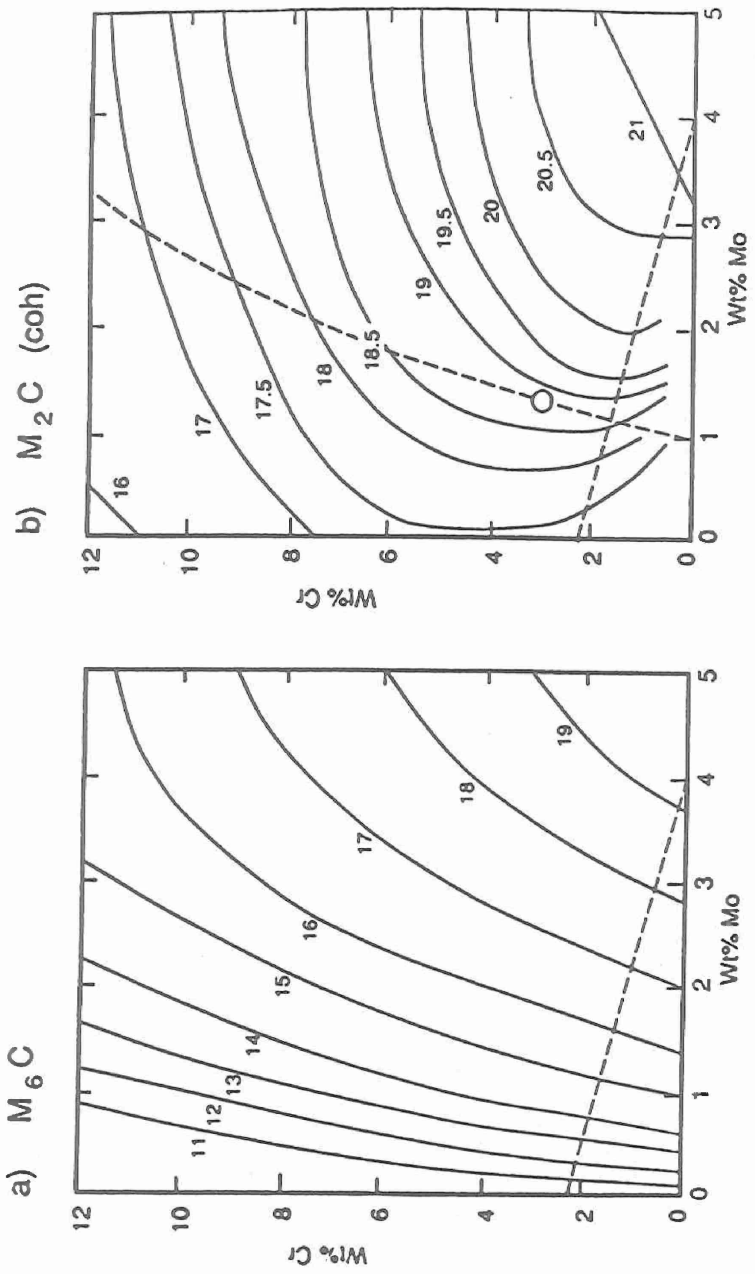


Fig. 6 Computed precipitation driving force (kJ/mole) at 510C for alloys containing 14Co-10Ni-0.25C: (a) incoherent M_6C, (b) coherent M_6C (26).

the latter steel the secondary hardening peak temperature is moved down 100°C with a 10R_c point increase in peak hardness. Comparison of the isothermal hardening behaviors at 500°C (31,32) shows an acceleration of secondary hardening in the Co-Ni steel by 2 to 3 orders of magnitude. Such a strong acceleration allowing a substantial reduction in secondary hardening temperature (with an attendant increase in precipitation driving force) is consistent with a switch to heterogeneous nucleation on dislocations in the recovery-resistant Co-Ni steels as proposed by Speich (5,6).

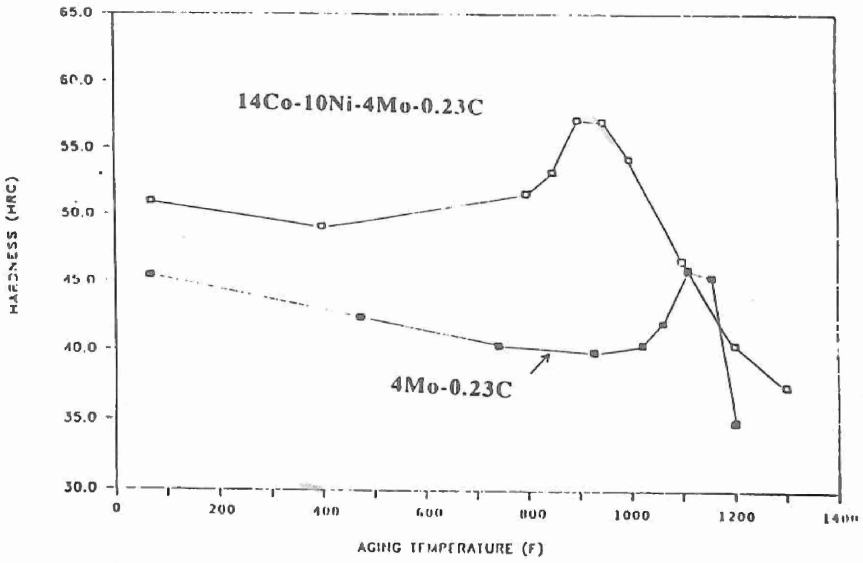


Fig. 7 Isochronal tempering hardness curves (1 hr) for 4Mo-0.23C steels with and without 14Co-10Ni.

The observed acceleration and enhancement of secondary hardening is similar to the nucleation effects of small additions of MC carbide formers (e.g. Nb,V) and GP-zone formers (e.g. Au) to simple Mo-C steels studied by Honeycombe and coworkers (31,33). To investigate the possibility of superimposing the two types of nucleation phenomena, the effect of Nb, V, and Au additions on the secondary hardening response of the Co-Ni alloy 2 of Table 1 was studied in the series of alloys represented by alloys 5 to 7 (15). Observed hardening enhancement was limited to the level of ~1 R_c point, and extensive atom-probe microanalysis indicated preferential acceleration of M_2C nucleation by the high

dislocation density such that there was little interaction with either MC precipitation or GP zone formation which required a longer time scale. Although some Au clustering was observed both in the matrix and M_2C suggestive of some degree of M_2C nucleation on Au zones, the Nb and V were found only in the M_2C phase with no indication of separate MC formation in near-peak-hardness microstructures. The measured compositions of M_2C carbides in alloys 5 to 7 are listed in Table 2. Following this demonstration of Nb and V solubility in M_2C, subsequent coherent thermodynamic calculations have indicated that V can be a very effective alloy addition to enhance the precipitation driving force for coherent M_2C (26).

TABLE 2

M_2C Compositions in Trace-Addition Alloys
(510°C/100hr temper)

Alloy	Carbide Formula
#5) 1605-4Mo (Nb)	$(Mo_{0.94\pm0.04}Fe_{0.04\pm0.01}Nb_{0.02\pm0.01})_2C_{0.88\pm0.02}$
#6) 1605-4Mo (NbV)	$(Mo_{0.95\pm0.04}Fe_{0.03\pm0.01}Nb_{0.01\pm0.01}V_{0.01\pm0.01})_2C_{0.92\pm0.03}$
#7) 1605-4Mo (Au)	$(Mo_{0.98\pm0.03}Fe_{0.018\pm0.01}Au_{0.002\pm0.001})_2C_{0.90\pm0.02}$

The strong effect of heterogeneous nucleation at dislocations on the M_2C carbide precipitation behavior emphasizes the important role of Co in retarding dislocation recovery so that a high dislocation density can be retained at secondary hardening temperatures. Neutron diffraction has revealed the presence of short-range order (SRO) in precipitation-hardening high Co martensitic steels (34), and field-ion microscopy has indicated SRO in AF1410 (35). Based on the hypothesis that the recovery resistance is associated with SRO, recovery behavior has been investigated by TEM (36) in the simple ferritic binary Fe-Co and Fe-Al alloy systems where previous studies have demonstrated SRO by neutron diffraction (37) and TEM (38), respectively. The recovery behavior in the temperature range of 400 to 600C was also compared with that of Fe-Ni and Fe-Ni-Co martensitic alloys (36). Figure 8 shows the retarded softening behavior at 527C for cold-worked Fe-14Co and Fe-6Al compared to Fe as expressed by the hardness decrease ΔH relative to the decrease for full recrystallization ΔH_{REX}. As indicated in the figure, a preliminary neutron diffraction measurement (39) confirmed the existence of SRO in the Fe-14Co alloy after 1 hr at 527C. The heavily cold-worked initial structure of

these alloys showed a deformation microband substructure very similar in character and size scale (~0.25 μm width) to the lath structure of the martensitic alloys, and showed similar stages of recovery consisting of (a) reduced general dislocation density, (b) sharpening of dislocation walls, and (c) polygonization and subgrain coarsening. The measured parabolic rate constant for subgrain coarsening at 527C showed an order of magnitude reduction for Fe-14Co (2.2×10^{-7} $\mu m^2/s$) compared to Fe ($2.8 \times 10^{-6} \mu m^2/s$). While the Fe-Ni martensites showed monotonic softening behavior, the Fe-Ni-Co martensites showed hardening similar to previous observations interpreted as SRO strengthening (40). After full recrystallization at 800 to 830C, the ferritic Fe-Co and Fe-Al alloys also showed some hardening with aging at 420 to 575C. Although some preliminary Mossbauer spectroscopy on the Fe-Co and X-ray diffractometry on the Fe-Al did not yield supporting evidence for SRO (36), the bulk of the literature observations (34,37,38) and the neutron diffraction evidence (39) suggest that SRO is the most plausible basis for both the hardening and recovery resistance. In addition to increased dislocation glide resistance indicated by the observed hardening, dislocation climb processes important to recovery may be inhibited through a reduction of diffusivity by SRO as has been demonstrated in Cu-Zn (41). A more quantitative understanding of the mechanism of recovery resistance could allow both the more effective use of Co and some degree of substitution of other ordering elements such as Al in secondary hardening steels.

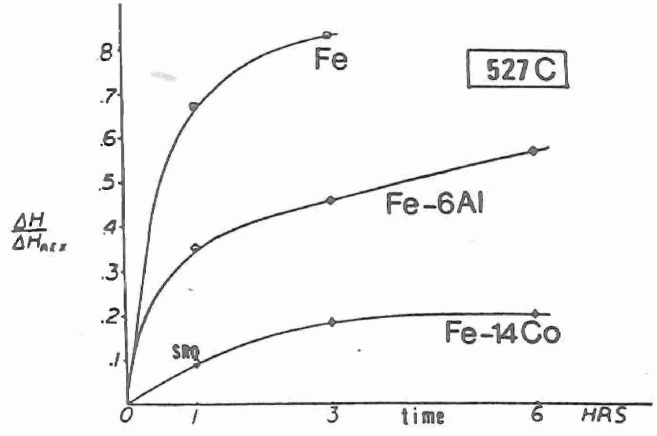


Fig. 8 Relative hardness decrease ΔH, normalized to full hardness decrease with recrytallization ΔH_{REX}, during 527C isothermal recovery of heavily cold-worked ferritic Fe, Fe-6Al, and Fe-14Co, showing retarded softening with alloying (36).

A longer-range issue regarding the achievement of maximum carbide strengthening for a given alloy carbon content concerns the properties of the carbide phase itself. In overaged structures characteristic of the completion of precipitation, size refinement will increase strength until a critical size is reached below which strength is controlled by particle shearing rather than the Orowan bypass mechanism. As discussed by Hornbogen (42) the critical particle size for this transition, and alloy strength in this regime, is controlled by the mechanical behavior of the dispersed phase; the high elastic modulus of alloy carbides compared to intermetallic phases makes them efficient obstacles capable of Orowan strengthening at smaller particle sizes. The ultimate design of optimal carbide strengthening dispersions will require information on the mechanical properties of the M_2C phase which can be obtained by synthesis of the multicomponent M_2C carbides of interest in bulk form. Such an investigation is currently underway (43).

TOUGHENING AND SHEAR LOCALIZATION

The role of primary void formation at inclusion particles in ductile fracture is well established. Major improvements in the fracture toughness of high-strength steels in the past two decades have accompanied improved processing technology providing "clean" steels with reduced inclusion volume fractions; more recent work has demonstrated the importance of inclusion spacing in ductile fracture (44). Less well understood is the role of finer ~0.1μm scale secondary particle dispersions which nucleate microvoids promoting shear localization, accelerating the process of primary void coalescence (45). In clean steels, the shear localization can dominate ductile fracture causing a mode I-loaded crack to locally adopt a mixed mode I and II "zig-zag" form of crack propagation. In addition to its microscopic role in mode I fracture toughness, shear localization also represents an important macroscopic failure mode limiting ballistic performance of ultrahigh-strength steels in armor and ballistically-tolerant structural applications (46). Not only are the structure/property relations governing shear localization currently poorly defined, but due to experimental difficulties associated with the finer particle size relative to the well-studied ~1 μm-scale primary inclusions, the microvoid nucleating particle dispersions are generally poorly characterized, constituting one of the least controlled components of steel microstructures. Control of shear localization represents the current frontier in the enhancement of ductile fracture resistance of ultrahigh-strength steels. As depicted in Figure 2, efforts to control shear localization behavior focus on (a) the role of secondary particle dispersions (primarily grain refining dispersions) in microvoid nucleation and associated softening, and (b) the role of matrix constitutive behavior, as most effectively controlled through application of transformation plasticity provided by finely dispersed metastable austenite.

Shear Instability and Particle Dispersions

Shear localization behavior in ultrahigh-strength martensitic steels has been effectively investigated using shear tests conducted with and without compressive loading superimposed normal to the shear plane (47-49). Not only do the shear test specimen geometries allow relatively large amounts of material to be uniformly deformed to the point of shear instability, but the operating stress states provide no driving force for primary void growth, forcing the materials to fail entirely by the macroscopic shear localization mode. The experiments thus selectively study behavior associated with the microstructural component of interest: the microvoid nucleating particle dispersions. Tests are conducted using both thin-wall torsion and a linear-shear geometry allowing superimposed compressive loading. The critical shear instability strain, γ_i, is measured as the imposed uniform strain beyond which deformation localizes in shear bands, and corresponds to a maximum stress in the shear stress-strain (τ-γ) curve. The γ_i values measured in an air-melted 4340 steel with and without an applied normal compressive stress of 1/3 σ_y are plotted versus R_c hardness level in Figure 9 (47,48). Hardness is varied by 1-hr tempering at temperatures corresponding to Stage I (ε-carbide strengthening, R_c56), Stage II (retained austenite decomposition, R_c 49-51), and Stage III (Θ-cementite strengthening, R_c 30-40) tempering. The instability strain generally decreases with increasing hardness level with an anomalous dip in Stage II tempering corresponding to "tempered-martensite embrittlement" associated with interlath cementite precipitation via austenite decomposition. The large increase in γ_i with compressive stress is consistent with a pressure-sensitive microvoid softening mechanism of shear instability. The role of microvoid formation in driving the instability is supported by TEM and SEM observations of microvoids in material deformation just to γ_i (47,58) but such observations of fine voids associated with ~0.1 μm scale particles are not easily reproduced. Some preliminary experiments performed on the same material suggest that small-angle X-ray scattering measurements may allow detection of early stage microvoid formation in thin sections of deformed shear-test specimen gage sections (50).

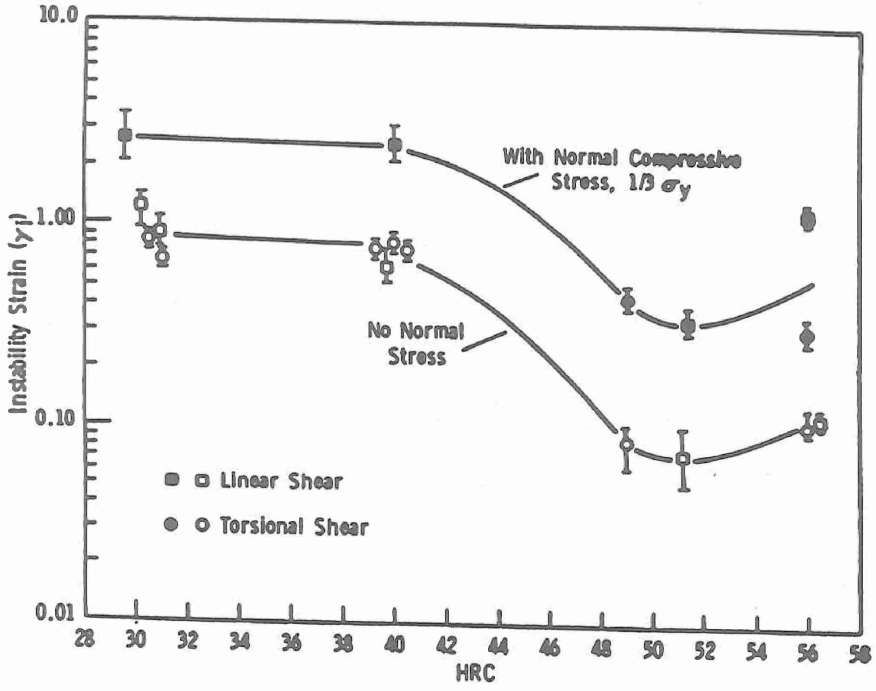


Fig. 9 Measured shear instability strain γ_i for 4340 steel as a function of hardness with and without normal compressive stress of 1/3 σ_y (48).

Comparison of the instability strain measured in high-hardness 4340 under isothermal conditions at a strain rate of $10^{-3}s^{-1}$ and under adiabatic conditions at $10^{2}s^{-1}$ gives the surprising result that γ_i is unchanged (47,48). While thermal softening under adiabatic deformation conditions may well contribute to shear localization in the highly compressive stress states associated with ballistic performance (46), it does not appear to significantly contribute to localization under pure shear stress. This would presumably also apply in tensile stress states such that improved resistance to microvoid formation should improve localization-controlled fracture toughness in ultrahigh-strength steels under both quasistatic and dynamic conditions.

An abrupt nature of shear localization observed in steels at ultrahigh strength levels together with the small degrees of microvoiding observed just prior to its onset implies that the microvoid softening is nucleation controlled rather than growth controlled at these strength levels. A

crucial tool for the theoretical investigation of structure/property relations governing microvoid nucleation and its associated softening has been the finite-element cohesive zone void nucleation model of Needleman (51,52). Prescribing a local force-distance law for interfacial separation defining a characteristic length scale, the complete process of interfacial decohesion of a rigid spherical particle in an isotropically hardening elastic viscoplastic matrix is modelled as a function of particle diameter, d, particle volume fraction, f, and interfacial cohesive characteristics (separation work $\Delta\gamma$ and interaction range δ). The predicted nature of nucleation is depicted in Figure 10 showing a quadrant of a cell with a particle centered at its lower left corner; equivalent strain contours in the matrix and interfacial configurations during separation are depicted for four applied remote strain levels $\varepsilon_1<\varepsilon_2<\varepsilon_3<\varepsilon_4$ in axisymmetric tensile deformation. Abrupt decohesion at the top of the particle is followed by spreading along the interface. The macroscopic stress-strain response associated with these processes in a material with a periodic array of such cells is summarized in Figure 11 comparing materials with three particle sizes $d_1<d_2<d_3$. The upper dashed curve represents the rigidly bonded case while the lower dashed curves correspond to replacement of the particles with voids of the same volume fraction, f. The largest particle size (d_3) shows the earliest nucleation with severe (brittle) softening behavior. Reduced particle size not only delays nucleation, but reduces softening via a more gradual (ductile) process of interfacial decohesion. Identical effects are observed by reducing f at fixed d. Fitting the model to measured microvoid nucleation conditions in steels for which d and f data are available allows an estimate of interfacial cohesive properties (52), with which the model can then predict quantitative benefits of variations in d and f. Stress states of the shear test experiments have been simulated by superimposing hydrostatic compressive stress, while retaining the axisymmetric deformation approximation (53).

Analytical modelling by Hutchinson and Tvergaard (54,55) has elucidated both the nature of void/particle interactions promoting void growth in shear deformation, and the strong strain softening influence of void nucleation. Matrix plastic flow associated with load shedding from the decohering interface is shown to give stronger strain softening than had previously been expected. Further analyses (56) have gone beyond isolated particle and periodic cell models to explore the influence of nonuniformity of particle spatial distributions, demonstrating the manner in which clustering can further accelerate nucleation. As the basis of a more detailed accounting of the directional

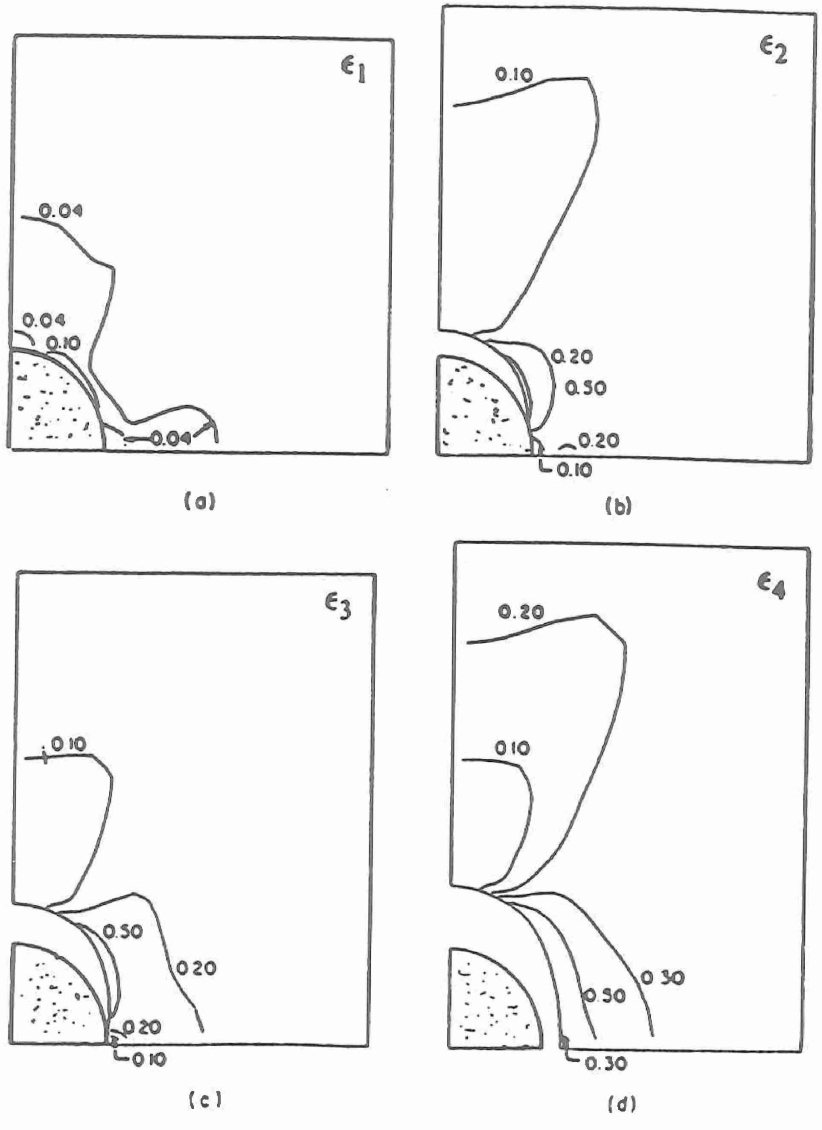


Fig. 10 Quadrant of cell model showing matrix strain contours and interface geometry during particle interfacial debonding at increasing applied strain levels (51).

particle pair interactions underlying local cluster behavior, Tracey and Perrone (57,58) have performed three-dimensional finite-element calculations of the deformation fields between pairs of spherical voids and particles in a plastic matrix undergoing the plane-strain shear deformation imposed in the shear test experiments, adopting constitutive relations appropriate to carbide particles in high hardness 4340 steel. Pairs of voids lying in the shear plane are found to exhibit the strongest interaction in a direction normal to the shear direction, while particle pairs exhibit strongest interaction when aligned parallel to the shear direction. Such analyses should ultimately allow control of anisotropic shear localization behavior in wrought alloys with anisotropic particle distributions.

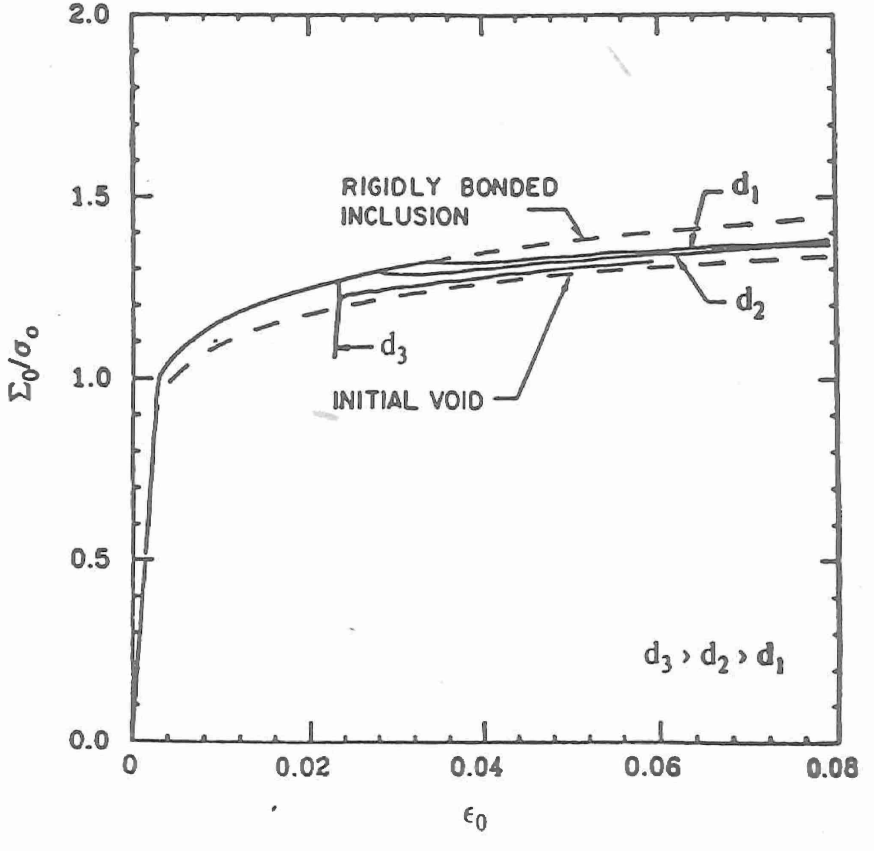


Fig. 11 Computed macroscopic stress-strain response during void nucleation at different size particles (51).

To experimentally examine the influence of particle dispersion variations on shear localization behavior, the same shear tests performed on the air-melted (AM) 4340 of Figure 9 have been extended to 4340 steels processed by vacuum-arc remelting (VAR) and rapid solidification processing (RSP) by centrifugal atomization and hot consolidation (48,49,59) and the particle dispersions quantitatively characterized by TEM and STEM analysis of thin foils and extraction replicas (49,59,60). In the stage III tempered condition, shear localization is found to be dominated by the cementite dispersion precipitated on tempering and is relatively insensitive to earlier stages of processing. In contrast, the much finer ε-carbide strengthening dispersion precipitated in Stage I tempering does not participate in microvoid nucleation, and shear localization is controlled by the grain refining particle dispersion which remains undissolved during austenitizing, and which is sensitive to solution treatment and melt practice. After conventional 1 hr. solution treatment at 840C, the AM4340 contains a large number of 50nm AlN particles and the distribution of MnS particles (predominantly 10-20 μm stringers) includes a small component of spherical 0.16 μm particles (60). Raising the solution temperature to 1100C dissolves the small sulfides and reduces the apparent number density of AlN particles by an order of magnitude (60). This is accompanied by an increase in the shear instability strain at R_c55 hardness from ~0.15 to 0.23 (47). In contrast to the AM4340, a more detailed study of the effect of solution temperature on the VAR4340 in the range 870 to 1200C shows a monotonic decrease of γ_i with increasing solution temperature (49). In this case the dominant component of the grain refining dispersion at 870C is 0.17μm diameter $M_{23}C_6$ carbides of composition $(Fe_{.74}Cr_{.25}Mo_{.01})_{23}C_6$ determined by STEM (60), with a total dispersion volume fraction of f=0.44% estimated from SEM metallography (49). After 1200°C treatment the estimated volume fraction of fine particles is reduced to f=.05%, consisting mainly of 80nm Ti(C,N) and a small amount of 50 nm Al_2O_3 (49). Compared to the AM4340, the VAR4340 shows greater high temperature grain coarsening, with a grain diameter of 17 μm at 870C coarsening to 280 μm at 1200C. In Stage III tempered material where cementite is the predominant microvoid nucleation site, γ_i decreases by the same factor on increasing solution temperature from 870C to 1200C as for the Stage I tempered material, suggesting the γ_i decrease is a feature of grain coarsening rather than the changing particle distribution. The RSP 4340 exhibits a highly stable grain refining dispersion of 0.27 mm Al_2O_3 with f=.26%; the dispersion, grain size, and γ_i are not significantly changed

on increasing the solution temperature from 870° to 1200C (49).

Comparison of shear tests, slow-bend Charpy tests, and K_{IC} tests in the Stage I tempered (R_c53) VAR4340 (49) revealed a correlation between γ_i and Charpy energy consistent with the demonstration by metallographic sectioning of bend specimens that failure in the blunt notch initiates by shear localization for both coarse and fine grained microstructures. Sectioning of K_{IC} specimens loaded to 90% K_{IC} showed that sharp crack propagation in the fine grained 870C treated material occurs by "zig-zag" shear localization with a 10μm wavelength, while an anomalous increase in K_{IC} in the 1200C-treated coarse-grained material is associated with intergranular microcracking which increases the fracture process zone by more than an order of magnitude. This peculiar effect of grain coarsening does not appear to represent a practical toughening mechanism in view of the associated degradation in shear localization resistance revealed in other test geometries. Accelerated shear localization in the coarse structures may be related to texture softening effects associated with crystal slip behavior (61).

Comparative shear, Charpy, and K_{IC} testing of fine-grained VAR processed AF1410 steel shows strong correlations indicative of a dominant role of microvoid nucleation and shear localization in all three geometries. With a standard 830C solution treatment, comparison of underaged and overaged materials of the same hardness shows the accelerated microvoid nucleation effect of undissolved cementite in the underaged material as revealed in a reduction of both γ_i and K_{IC}. The results indicate a direct scaling between γ_i and the critical crack opening displacement (COD) for propagation (47). In the standard 510C 5h tempered condition (slightly overaged), a modest increase in solution temperature from 830C to 885C is found to produce a significant improvement in strength/Charpy toughness combination without excessive grain coarsening (62). Examination of the particle dispersions present at these two temperatures demonstrates that the temperature increase greatly simplifies the dispersion from a list of 6 phases to a single (Ti,Mo)(C,N) phase as summarized in Table 3 (49). Although the strength is slightly reduced by the higher solution treatment, a lower temperature post-age treatment for enhanced Co ordering is found to restore a normal strength level while maintaining a 40% enhancement in Charpy toughness (49, 62). These experiments demonstrate how, for a fixed melt practice, fine-tuning of solution treatment to eliminate unnecessary particles can provide an optimal grain refining dispersion maintaining a sufficiently

fine grain size while enhancing toughness through improved microvoid nucleation resistance.

TABLE 3

Particles in AF1410

Solution Temp.		Particle Type	Size Range
1525°F	(830°C)	$(Ti,Mo)_xC,N$	10 - 180 nm
		$(Cr,Fe,Mo)_{23}C_6$	50 - 125 nm
		$(Fe,Cr,Mo)_{23}C_6$	75 - 105 nm
		$(Mo,Cr)_xC$	30 - 65 nm
		$(Mo,Fe)_xC$	40 - 50 nm
		Mo_xC	5 - 10 nm
1625°F	(885°C)	$(Ti,Mo)_xC,N$	20 - 35 nm

Information on interfacial cohesion for phase selection for grain refining dispersions can be derived from nucleation experiments on well characterized microstructures. Interpreting the measured shear localization strains as microvoid nucleation strains in the fine-grained 870C-treated VAR4340 and RSP4340, a fit of the Needleman numerical nucleation model using the measured $\bar{d}$ and f for the $M_{23}C_6$ and Al_2O_3 dispersions has provided an estimate of the interfacial strength (or work of separation) indicating superior interfacial cohesion for $M_{23}C_6$ compared to Al_2O_3 (53). The intrinsic work of interfacial separation per unit area, $\Delta\gamma$, can be expressed by:

$$\Delta\gamma = \gamma_P + \gamma_M - \gamma_{IPB}$$

where γ_P and γ_M are the particle and matrix free surface energies and γ_{IPB} is the particle/matrix interphase boundary energy. While γ_{IPB} is difficult to anticipate, phases with high cohesive energy (which also promotes high stability and coarsening resistance to maintain fine dispersions) will tend to have higher free surface energy γ_P promoting higher $\Delta\gamma$. Such simple considerations imply Al_2O_3 should be superior to $M_{23}C_6$, contrary to experiment. In practice, interfacial cohesion will likely be strongly influenced by impurity segregation through mechanisms to be addressed in our discussion of grain boundary cohesion. High resolution microanalysis of these interfaces will likely play an important role in the full characterization of the structural basis of microvoid nucleation resistance. In the meantime,

quantitative estimates allowed by currently available nucleation experimental data indicate that TiC possesses the highest interfacial cohesion in steels (63). The observation of the closely related (Ti,Mo)(C,N) phase in an optimally solution-treated (Table 3) commercial AF1410 composition which is the product of an empirically optimized melt practice, further supports the merit of this compound for intrinsic nucleation resistance. Experiments to quantify the interfacial cohesion of this phase in AF1410 are underway (64).

While nucleation models can prescribe the dependence of microvoid nucleation resistance on average particle size, $\bar{d}$, and volume fraction, f, optimization of a grain refining dispersion requires a description of the dependence of grain refinement on these same variables. Based on an extensive quantitative study of grain refinement in VAR and RSP matrix tool steels, Hsu (65) has synthesized boundary pinning models of Gladman (66) and Hellman-Hillert (67) to define the average grain diameter $\bar{D}$ stabilized by the boundary pinning interaction of a dispersion of stable (static) particles of distributed size:

$$\bar{D} = \frac{4}{3\alpha}\left(\frac{3}{2} - \frac{2}{Z}\right)\left(\Sigma\frac{f_i}{d_i}\right)^{-1} .$$

Here, f_i is the volume fraction of particles of diameter d_i, Z is a grain size distribution parameter defined by the ratio of the largest grain to the average grain size, and α represents the range of boundary/particle interaction normalized to the particle size. In the approximation of monodispersed particles of diameter, $\bar{d}$, and total volume fraction, f, the expression simplifies to:

$$\bar{D} = \frac{4}{3\alpha}\left(\frac{3}{2} - \frac{2}{Z}\right)\frac{\bar{d}}{f} .$$

Figure 12 summarizes the observed correlation (with $\alpha = 1$) between $\bar{D}$ and $(\Sigma f_i/d_i)^{-1}$ for VAR and RSP processed M-2 and M-50 matrix tool steels over a wide range of solution temperatures, and includes available literature data (68-70) relating $\bar{D}$ and $\bar{d}/f$ in other steels. The beneficial grain refining effect of fine particle sizes in hot-consolidated RSP material is partly offset by a broader grain size distribution represented by a higher Z. The ability of RSP processing to disperse highly stable, coarsening resistant

compounds such as oxides and oxysulfides on a fine size scale for efficient boundary pinning has allowed achievement of remarkable high temperature grain coarsening resistance in a wide range of steels (71); the phenomenon offers the potential for practical exploitation of high solution treatment temperatures in the high toughness secondary hardening steels of concern here.

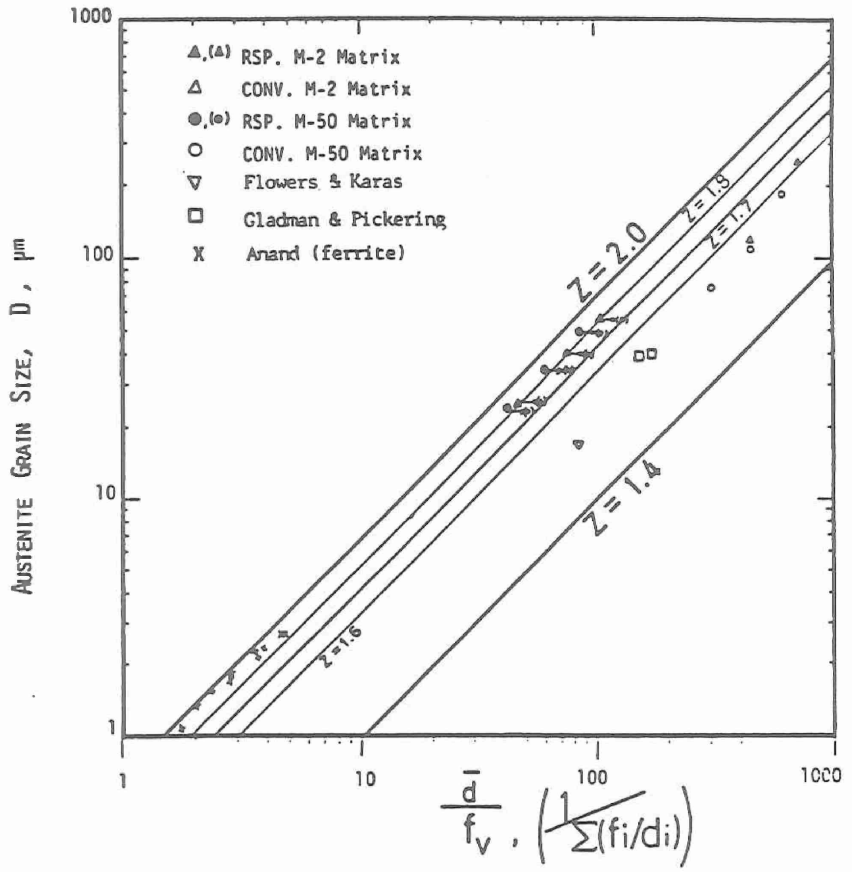


Fig. 12 Comparison of grain size data for steels with average particle size and volume fraction. Arrows show shift associated with summation over particle size distribution. Straight lines depict model predictions for various values of grain size distribution parameter, Z (65)

Since maintaining a desired grain size requires a fixed ratio of d to f, and nucleation resistance (as in Figure 11) depends monotonically on both variables, geometric optimization of the grain refining dispersion then requires minimization of both d and f at fixed d/f. However, it can be anticipated that at sufficiently small particle size the Gladman type of static particle/boundary interaction just discussed will no longer apply as thermally activated boundary unpinning reduces the net interaction force exerted by the particles. Modelling such unpinning behavior by an adaptation of thermally activated deformation theory gives the effective pinning behavior described in Figure 13 (72). Figure 13a depicts the required f to maintain a 10μm grain size in a steel after 1 hr at 870C and 1200C as a function of particle size d. The straight line corresponds to the Gladman-type static interaction. Below a critical particle size, higher f is required for boundary pinning to compensate the effect of thermal activation. Adopting the f-d curve for 1200C solution treatment as inputs to the Needleman nucleation model, preliminary calculations of microvoid nucleation strain vs. particle size (with f constrained to maintain constant D) for R_c53 VAR 4340 with an $M_{23}C_6$ dispersion give the behavior depicted in Figure 13b (53). Although thermal activation ultimately limits improvements achievable at very small particle sizes, the model predicts that modest size refinement below the current level of d = 0.17μm can yield substantial improvement in microvoid nucleation resistance. Maintaining the desired finer particle sizes during solution treatment will require more stable coarsening resistant phases such as those accessible through rapid solidification processing.

While experiments have already demonstrated substantial toughness enhancement in AF1410 through improved solution treatment to eliminate unnecessary dispersed particles, evolving theoretical guidelines and preliminary quantitative estimates indicate that even greater improvements in microvoid nucleation resistance await the design of optimal grain refining dispersions via combined phase selection and process control to achieve prescribable dispersion geometries.

Transformation Toughening

As emphasized by Krauss (45), equally important to shear localization as the role of particle dispersions is the role of the constitutive behavior of the matrix in which the particles reside. The most dramatic means of altering matrix constitutive behavior to delay shear localization and ductile fracture is the transformation plasticity that can be obtained from a dispersion of metastable austenite, as also represented in Figure 2. Transformation plasticity resulting

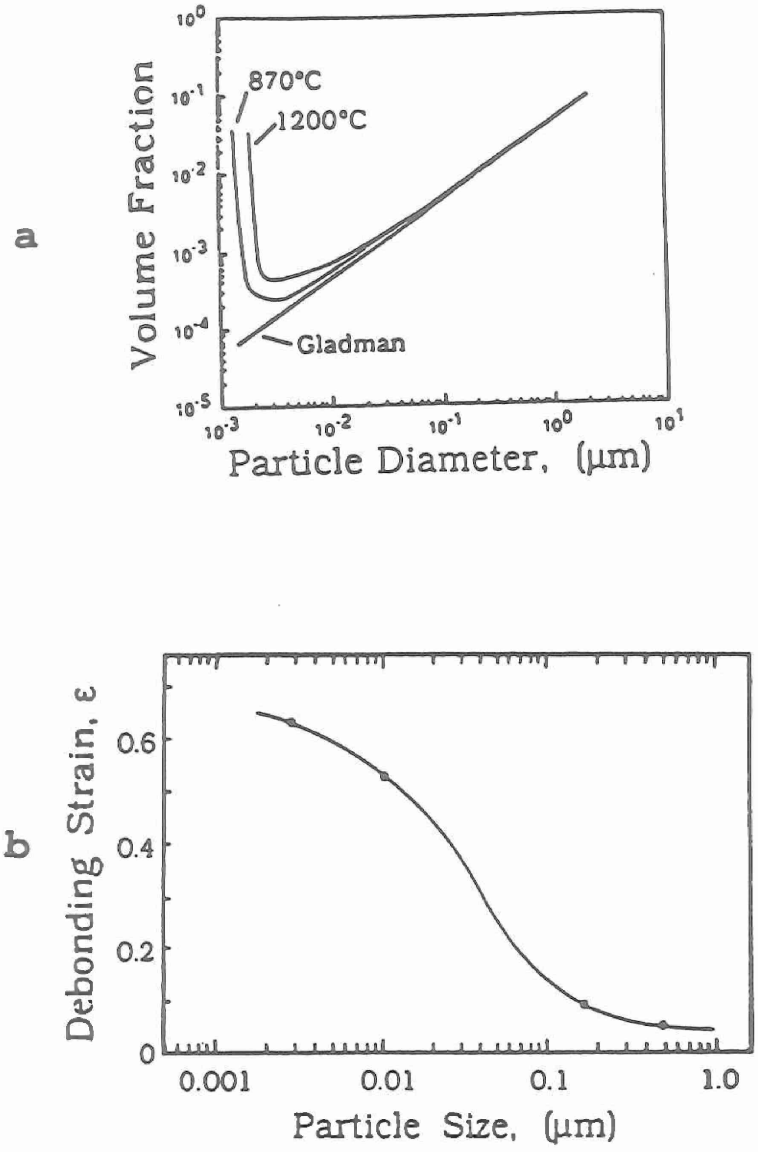


Fig. 13 Void nucleation on grain refining dispersion. (a) Necessary particle volume fraction vs. particle diameter to maintain 10μm grain size after 1 hr at 870C and 1200C accounting for thermal activation, (b) Particle debonding strain vs. particle diameter employing volume fractions of (a) in Needleman model.

from martensitic transformation during deformation has been most thoroughly investigated in fully austenitic steels (73), identifying two basic modes of transformation. Stress-assisted transformation involves the same nucleation sites as the spontaneous transformation on cooling, but assisted by the thermodynamic effect of applied stress, while strain-induced transformation is controlled by the production of new nucleation sites by plastic deformation. Different transformation product morphologies tend to be associated with these two modes: stress-assisted transformation giving relatively coarse plates, while the strain-induced transformation develops as fine laths typically formed at intersections of shear microbands. Kinetic models and quantitative constitutive relations for associated transformation plasticity have been developed for both the stress-assisted (74) and strain-induced (75,76) modes. Both modes promote sigmoidal stress-strain (σ-ε) curves with an initial upward curvature deriving from the combined influence of a softening contribution of the transformation as a deformation mechanism and a hardening contribution of the transformation product. Stress-assisted transformation gives plastic flow at stresses lower than the normal slip-controlled yield stress, and produces a reverse (positive) temperature dependence of the yield stress. The temperature where the transformation yield stress and slip yield intersect, characterized by a reversal in the yield-stress temperature dependence, is designated M_s^σ, and its value measured in uniaxial tension serves as a convenient measure of overall austenite stability with respect to mechanically induced transformation. As the transformation volume change interacts with the hydrostatic component of stress, the austenite stability and M_s^σ temperature vary significantly with stress state.

The upward σ-ε curvature associated with transformation plasticity imparts high stability to plastic flow behavior which is found to retard not only tensile necking but shear localization both within tensile necks and at crack tips. Figure 14 summarizes the measured effect of austenite stability (controlled by test temperature) on the relative change in a) uniform ductility, ε_u, b) tensile fracture ductility, ε_f, and c) J_{IC} fracture toughness, in high-strength (1300 MPa σ_y) γ'-strengthened austenitic steels (77,78). The stability variable θ represents a normalized temperature defined by $\theta = (T-M_s^\sigma)/(M_d-M_s^\sigma)$ such that $\theta = 0$ corresponds to M_s^σ, and $\theta = 1$ corresponds to $T = M_d$, the highest temperature for which strain-induced transformation occurs. Here the M_s^σ temperature corresponds to that for the particular stress state controlling the property of interest. In addition to

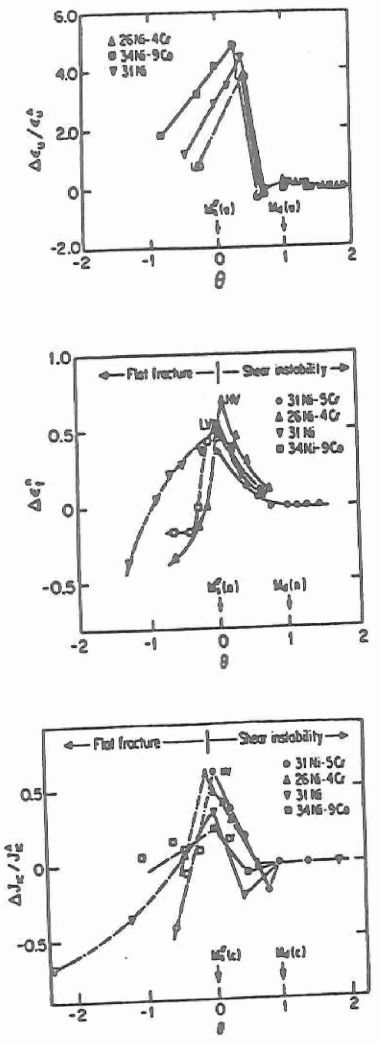


Fig 14. Relative mechanical property enhancement vs. transformation stability represented by normalized temperature, θ, for precipitation-strengthened metastable austenite steels. (a) increase in uniform ductility $\Delta\varepsilon_u$ relative to stable austenite value ε_u^A, (b) increase in true fracture strain ε_f^n in axisymmetric tension, (c) increase in fracture toughness ΔJ_{IC} relative to stable austenite value J_{IC}^A, with LV and HV denoting low and high volume-change alloys, respectively (77, 78).

the well known effect of transformation on uniform tensile ductility, the results of Figure 14 demonstrate strong enhancement of ε_f and J_{IC} in materials where both failure initiation in the tensile neck and sharp-crack propagation are controlled by shear localization. Property enhancement is extremely sensitive to stability, with optimum properties achieved near the M_s^σ temperature. Hence, efficient use of transformation plasticity to improve a property at a given temperature requires placement of M_s^σ (for the stress state governing that property) at the temperature of interest. The precise mechanism by which transformation plasticity enhances J_{IC} toughness is being investigated by detailed metallographic observations of crack tip shear localization and transformation behavior (79) coupled with finite-element modelling of crack-tip transformation plasticity based on the transformation-kinetics-based constitutive models (80).

Composite systems with metastable austenite dispersions can exhibit essentially the same transformation plasticity features as fully austenitic alloys. The stability and transformation plasticity behavior of dispersed austenite in high strength steels has been most thoroughly investigated in the case of retained austenite in Stage I tempered 4340 steel (32,81-83). For both 870C and 1200C austenitizing temperatures, controlled experiments varying austenite content with high magnetic field cryogenic treatments prior to 200C tempering have separated the role of the austenite in mechanical behavior. Microyielding experiments have quantified the retained austenite stability by measuring its M_s^σ temperature in uniaxial tension and compression, and revealed microyield σ-ε behavior consistent with transformation plasticity model predictions (82). The measured stress-state dependence of M_s^σ revealed an M_s^σ near room temperature for pure shear, and room temperature shear tests confirmed a significant increase in the shear instability strain, γ_i, from transformation plasticity interaction. The measured stability also indicated too low a stability level for optimum toughening interaction at a mode I crack tip, and controlled experiments confirmed that there was no significant effect of the retained austenite on K_{IC} toughness (81). The high stress levels operating in such high-strength steels contribute a large mechanical driving force for transformation. Achieving sufficiently high stability against transformation to obtain optimal toughening interaction is likely beyond the capabilities of the simple carbon-partitioning-based stabilization operative in the conventional retained austenite of Stage I tempered martensitic steels.

Martensitic nucleation theory (84) prescribes the manner in which particle size and composition control the stability of dispersed austenite. Size influences stability through the statistical behavior of heterogeneous nucleation sites. In metals and ceramics, a universal form of nucleation site potency distribution (85,86) defines the manner in which characteristic defect potency diminishes with decreasing particle size. Composition affects stability in the same manner as for bulk materials, through the transformation chemical driving force and through a solid solution hardening effect on interfacial mobility (85). The high levels of austenite stability necessary for optimal transformation toughening in ultrahigh strength steels can thus be attained by a combination of particle size refinement and enrichment in stabilizing solutes. The precipitation of austenite during tempering of secondary hardening steels offers the means to achieve this microstructural objective.

Multistep tempering treatments have demonstrated the ability to effect the desired microstructural control. Austenite stabilization also forms the central concept of "triple phase" ferrite/martensite/austenite low-alloy sheet steels designed to achieve sufficient plane-strain uniform ductility (20-25%) for adequate stretch formability at high strength levels (100ksi 3% flow strength) desired for automotive applications (87). Short-time intercritical tempering after a low temperature temper which enriches cementite in Mn can produce a paraequilibrium carbide→austenite conversion, trapping a higher-than-equilibrium Mn content in the austenite (88). While this austenite normally forms at martensite lath boundaries where rapid growth ensues, thermodynamic calculations employing the paraequilibrium constraint can predict optimal cementite Mn contents and intercritical tempering temperatures to promote intragranular carbide conversion in recrystallized structures to achieve finer dispersions with higher stabilizing Mn contents (87). Similarly, in the high alloy AF1410 secondary hardening steel, solute enrichment of cementite at 420C prior to 510C tempering has been shown to provide a finer, more solute enriched (intralath) austenite compared with the interlath austenite which precipitates during conventional single-step 510C tempering (83).

While optimal austenite stabilization in the low alloy steels requires trapping of Mn levels higher than equilibrium, the interlath austenite that precipitates during conventional tempering of high alloy steels like AF1410 involves incomplete partitioning such that the austenite solute content is lower than the equilibrium level, and further stabilization can be achieved by moving closer to equilibrium. In this case, more effective than cementite nucleation of austenite is the use of a short high

temperature treatment prior to 510C tempering, which is found to nucleate a fine intralath dispersion of near-equilibrium austenite (83). The open symbols in Figure 15 show Charpy toughness/hardness combinations achieved by various temperature(°C)/time(minutes) treatments prior to 510C/8 hr tempering in AF1410; also shown are the properties (solid symbols) for conventional 510C tempering for 5 and 8hrs. The curves represent contours of a quality parameter reflecting the normal hardness dependence of Charpy toughness. At R_c48 hardness, the 600C/15min. treatment provides a 24% toughness increase, while 570C treatments offer even better hardness/toughness combinations. Figure 16 shows a transmission electron micrograph of the microstructure produced using the 600C/15min treatment (83). While relatively coarse interlath austenite (similar to that formed with single-step 510C tempering) is present, a fine intralath dispersion of 10-20nm austenite particles is also evident throughout the structure. Austenite compositions determined by STEM microanalysis of this structure are compared with

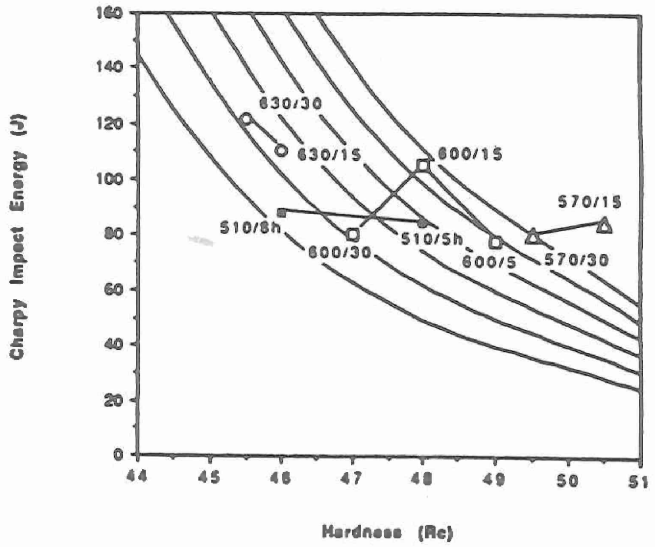


Fig. 15 Charpy V-notch impact toughness vs. hardness achieved by multistep heat treatment to form high stability austenite in AF1410 steel. Open symbols denote properties for indicated temperature (°C)/time (minutes) treatments prior to 510C/8 hr tempering. Closed symbols denote properties for conventional 510C tempering for 5 and 8 hrs (83).

those for single-step 510C (5 and 8hr) in Table 4, together with associated mechanical properties. In addition to the substantial size refinement, it is evident that the Ni content is much increased in the fine austenite nucleated at 600C, and is close to the predicted equilibrium composition (82). Whether compared to single-step 510C tempered materials on the basis of constant hardness (510C/5hr) or yield strength (510C/8hr), it is clear from the properties listed in Table 4 that the achievement of an optimal austenite stability level has produced a substantial improvement in J_{IC} fracture toughness; equivalent to a K_{IC} of 230 ksi$\sqrt{in}$, this corresponds to a record toughness for a steel of R_c48 hardness.

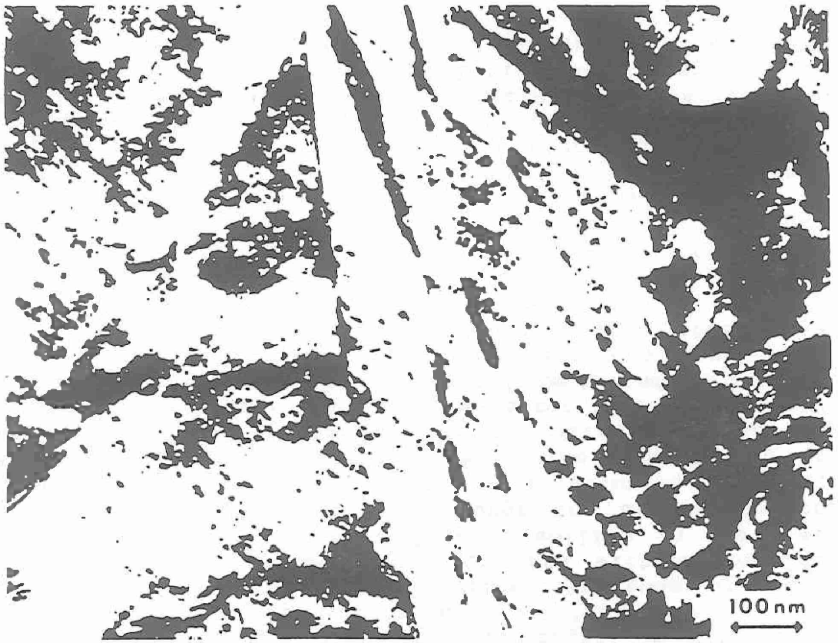


Fig. 16 TEM micrograph showing fine dispersion of intralath austenite formed by multistep heat treatment (600°C/15 min + 510°C/8 hr); larger interlath austenite is also evident (83).

TABLE 4

AF1410
PRECIPITATED-AUSTENITE TRANSFORMATION TOUGHENING

	510C/5h	510C/8h	600C/15min+510C/8h
γ MICROSTRUCTURE			
Composition			
interlath: (0.1-0.2mm)		14Ni-13Co-3Cr	17Ni-15Co-4Cr
intralath: (100-200Å)		---	29Ni-10.5Co-4Cr
f^{γ}	0.03	0.06	0.15
PROPERTIES			
Hardness	R_c48	R_c46	R_c48
Yield Strength	1550 MPa	1360 MPa	1370 MPa
J_{IC} Toughness	178 kJ/m^2	201 kJ/m^2	250 kJ/m^2

Experiments in two series of model high-strength (R_c45) austenitic alloys strengthened by γ' precipitation and phosphocarbide precipitation have allowed a separation of the relative roles of transformation strain hardening and transformation dilatation in transformation toughening under condition of shear-localization-controlled ductile fracture (89). In the phosphocarbide-strengthened material, comparison of underaged and overaged material of the same hardness allows variation of transformation strain hardening behavior by altering the austenite/martensite hardenss difference. Due to preferential martensite hardening by dissolved carbon, the underaged material has an austenite/martensite Vickers hardness difference of ΔH_v=88±2 while the overaged material has ΔH_v=47±2 identical to the γ'-strengthened alloys. Variations in Ni and Cr content provide variations in transformation dilatation. Figure 17 shows the transformation toughening efficiency determined in these alloys as the ΔJ_{IC} toughening increment per amount of crack-tip transformation measured as the transformation half-zone height, H/2. The curves indicated for the two ΔH_v levels suggest that higher transformation strain hardening enhances toughening, but a more dramatic effect is that toughening increases as the third power of the transformation dilatation; this behavior of transformation toughening in ductile solids contrasts with a second power dependence of crack-tip shielding-based transformation toughening in brittle solids (90). The strong dilatation dependence suggests that much more toughening can be achieved from precipitated austenite in secondary hardening martensitic steels by designing the austenite for maximum dilatation.

Although the composition dependence of the transformation dilatation is highly nonlinear due to magnetic anomalies in austenite, magnetic models have been applied to its prediction (91). Such models are being calibrated by precision lattice parameter measurements in key compositions, to be applied in the design of optimal precipitated austenite for transformation toughening (92).

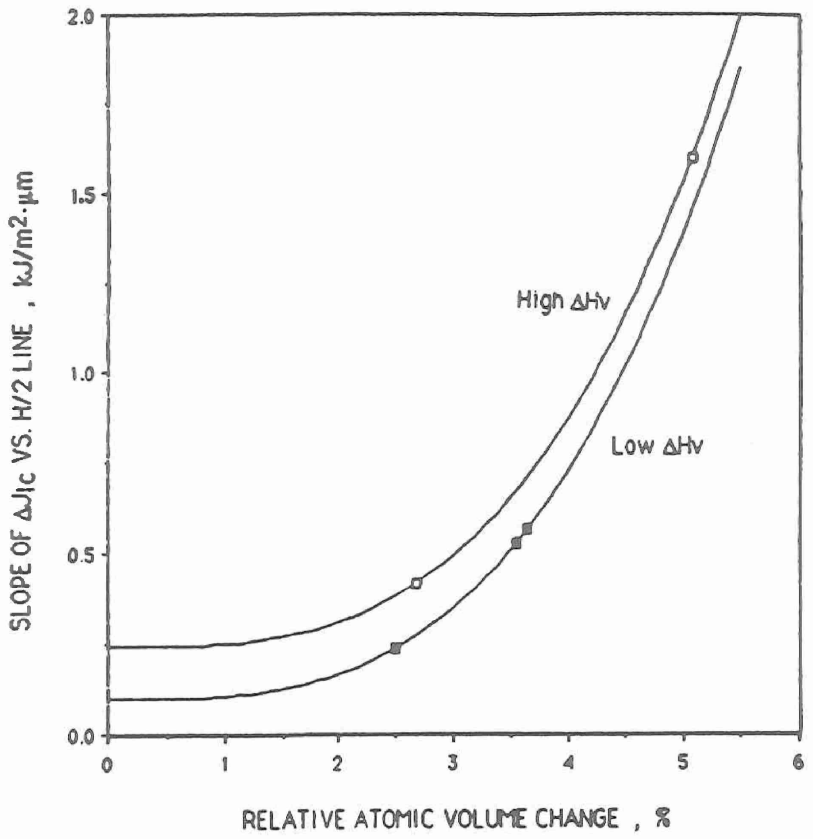


Fig. 17 Transformation toughening efficiency (slope of ΔJ_{IC} vs. transformation zone half-height, H/2) vs. transformation volume change for precipitation-hardened metastable austenitic steels with two levels of austenite-martensite hardness difference, ΔHV (89).

HYDROGEN RESISTANCE AND INTERFACIAL COHESION

The stress corrosion cracking of ultrahigh-strength martensitic steels in aqueous environments, as quantified in standard K_{Iscc} tests, is known to occur by a hydrogen embrittlement mechanism associated with cathodic charging at the crack tip. Typical of hydrogen-assisted cracking at extreme strength levels, the fracture generally follows an intergranular path and is commonly associated with prior intergranular segregation of embrittling impurities. As discussed by McMahon (93), these are the same impurities responsible for the phenomenon of intergranular temper embrittlement, and extensive studies have revealed the relative embrittling potencies of impurities (e.g. P, S, Sn, Sb) and embrittling alloying elements (e.g. Mn, Si), as well as separating the role of cosegregating alloying elements which can alter the degree of impurity segregation. Thusfar, the embrittling effect of hydrogen and prior segregants appear to be additive, and a common mechanistic basis can be sought for interfacial embrittlement by chemical segregants including hydrogen.

A general theoretical framework for treating the chemical embrittlement of interfaces has been developed by Rice and coworkers (94, 95) who have modelled the competition between brittle interfacial cleavage separation and crack-tip blunting by dislocation emission. Considering a flat crack in a bicrystal interface, the conditions for ductile vs. brittle crack advance are determined by comparison of (a) the critical crack extension force (strain energy release rate) G_{disl} for crack-tip dislocation emission, as governed by crystal plasticity, and (b) the Griffith work of interfacial cleavage, $2\gamma_{int}$, as influenced by chemical segregation. Brittle propagation prevails when $G_{disl}>2\gamma_{int}$, and ductile when $G_{disl}<2\gamma_{int}$. For fixed $2\gamma_{int}$, model calculations predict that G_{disl} will depend on the direction of crack advance, such that brittle fracture can occur for one direction while ductile behavior occurs for the opposite direction. The prediction has been confirmed in critical bicrystal experiments on Cu embrittled by Bi (95).

While the precise manner in which chemical segregants might modify G_{disl} for dislocation emission remains unclear, a definite role of segregation in determining the Griffith work of interfacial cleavage $2\gamma_{int}$ has emerged from application of surface thermodynamics. Further, arguments have also been developed that $2\gamma_{int}$ is not only of crucial importance in governing the transition between ductile and brittle response, but even under conditions of substantial crack-tip plasticity the critical crack-extension force G_{Ic} for

intergranular fracture can be a monotonic function of $2\gamma_{int}$ (94). Control of $2\gamma_{int}$ would thus appear the most effective means of enhancing interfacial fracture resistance. The thermodynamic analysis (94, 95) reveals that for interfacial separation at fixed boundary solute coverage, Γ, nonlinear entropy contributions can be neglected such that $2\gamma_{int}$ changes linearly with Γ according to the relation:

$$2\gamma_{int} = (2\gamma_{int})_o - (\Delta g_b^o - \Delta g_s^o)\Gamma$$

where $(2\gamma_{int})_o$ is the work of separation of the clean interface, and Δg_b^o and Δg_s^o are the free energies of segregation of the solute to the boundary and free surface, respectively, evaluated at the temperature of fracture, taken as 300K. The analysis clearly predicts that a segregating solute with a greater (more negative) segregation energy at a free surface compared to an internal boundary will embrittle (reduced $2\gamma_{int}$), while one with a lower energy at a boundary compared to the free surface will enhance interfacial cohesion (increased $2\gamma_{int}$). The embrittling potency of a segregant scales with the quantity $\Delta g_b^o - \Delta g_s^o$. The model further predicts that an embrittling solute which is mobile during fracture such that it can maintain a constant potential μ during separation will be far more embrittling than for the case of separation at fixed Γ (immobile solute).

The relative wealth of surface thermodynamic data (determined primarily from Auger electron spectroscopy studies) available for iron and steels compared to other materials make iron-based alloys the best case to test thermodynamic theory of interfacial cohesion. Unfortunately, nowever, both the grain boundary and free surface quantities are anisotropic, and insufficient data is available to either compare Δg_b^o and Δg_s^o at a fixed orientation or to apply consistent directional averaging procedures. Nevertheless, chemical trends are evident when $\Delta g_b^o - \Delta g_s^o$ is estimated from the available data for embrittling impurities. The best current measure of embrittling potency is the shift of the intergranular ductile-brittle transition temperature per amount of segregated solute (expected to depend linearly on $2\gamma_{int}$) and available measurements of this quantity are plotted vs. $\Delta g_b^o - \Delta g_s^o$ in Figure 18 (94). Despite considerable uncertainty associated with the available mix of polycrystalline and single crystal data, the predicted trend represented by the solid line is supported, particularly for the more well-defined cases of P and S. More recent

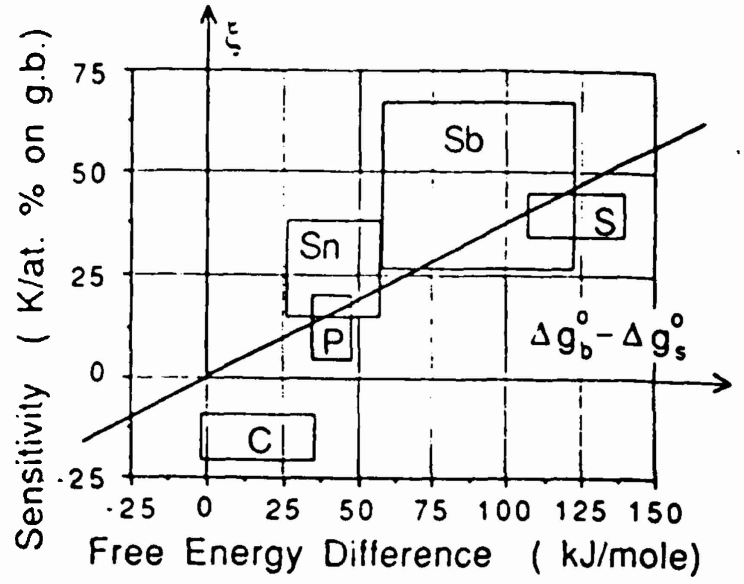


Fig. 18 Embrittling potency of impurity segregants in iron and steel (shift of transition temperature per amount of segregant) vs. difference in segregation free energies to grain boundaries Δg_b^o and free surfaces Δg_s^o (94).

thermodynamic data for B also correlate with its measured cohesion-enhancing effect (96). Estimates of $\Delta g_b^o - \Delta g_s^o$ for H indicate an intrinsic embrittling potency less than or equal to that of P (95). The high mobility of H can allow separation at constant μ, however, and calculations for this case (95) predict substantial reduction of $2\gamma_{int}$ even for equilibrium matrix concentrations of $X_H \approx 10^{-9}$; the model is thus consistent with the extreme effectiveness of H as an embrittler (93).

A plausible thermodynamic description of the chemical embrittlement of interfaces opens the way to a more fundamental approach whereby first-principles quantum-mechanical calculations of the electronic state of impurities in grain boundary and corresponding fracture surface environments can provide insight into the origins of

$\Delta g_b^o - \Delta g_s^o$ in chemical bond behavior, offering the potential for design of boundary composition for both enhanced intrinsic cohesion and reduced hydrogen interaction. The relatively low intrinsic embrittling potency represented by $\Delta g_b^o - \Delta g_s^o$ for P and H, which are the most common embrittlers of the highest strength steels, offers hope of neutralizing their embrittlement or even reversing their role to cohesion enhancement through appropriate boundary doping to achieve desired boundary electronic structure. While the most advanced techniques such as the Full-Potential Linearized Augmented Plane Wave (FLAPW) method (97) now appear capable of computing the relatively small energy differences governing metallurgical phenomena, the crucial first step in applying such techniques is to obtain realistic atomic positions for the structures of interest.

As reviewed by Harrison et al (98), simple hard-sphere models of grain boundary structure have revealed a striking similarity between the special polyhedral packing units present in grain boundary cores and the local coordination environments adopted by the light metalloid elements (e.g. B, C, P, S) in metal-rich transition metal compounds such as Fe_3P, as well as their coordination environments in metallic glasses. Specifically, these elements adopt the nine-fold coordination of a capped trigonal prism which is a common structural unit in tilt boundaries. Harrison et al (98) have simulated the core structures of several high coincidence tilt boundaries chosen to allow relatively short-period supercells appropriate for band-theory-based electronic calculations. To examine local atomic relaxations, a simple interatomic potential for Fe was derived based on the embedded atom method (EAM) and tested against observed free surface relaxations in Fe*. The model was initially applied to a $\Sigma 5$ [100] tilt boundary on (031). Full occupancy of the trigonal prism sites of this boundary by P, however, would involve a minimum P-P spacing of 2.87Å which is shorter than the minimum P-P distance of 3.48Å exhibited in Fe_3P.

*Although the ability to predict observed oscillitory variations in interplanar spacings at free surfaces is often used as an assessment of the validity of these potentials, they found such variations to be relatively insensitive to details of the potential, and found no better agreement with the observed surface relaxations of Fe than could be predicted from a simple model based on electrostatic effects neglected in the EAM approximations.

Furthermore, chemisorption of P on a (100) Fe surface, where the minimum site spacing is 2.87Å, is observed to involve a c(2x2) surface reconstruction maintaining a minimum P-P spacing of 4.05Å. A survey of possible boundaries allowing a minimum period supercell with full P site occupancy led to selection of the $\Sigma 3[1\bar{1}0]$ "incoherent" twin boundary on (111); the P site spacing of 4.05Å is greater than the minimum P-P distance in Fe_3P, and P chemisorption on the corresponding (111) Fe free surface involves a simple p(1x1) structure with full site occupancy. The relaxed structure for this boundary computed with the Fe EAM potential is shown in the supercell of Figure 19. Viewed along the $[1\bar{1}0]$ tilt axis, the two sizes of open circles represent the two stacking positions of $(1\bar{1}0)$ planes. The solid rectangles outline the projected positions of BCC units cells in the two grain orientations, and the capped trigonal prism 9-fold coordination sites are outlined in solid and dashed lines with solid circles depicting schematically the position of P sites. Repetition of supercells such as that outlined in Figure 19 provides the necessary periodic structure for band-theory-based electronic calculations.

As a first assessment of the ability of band calculations to treat the chemical aspects of brittle fracture in transition metals, Krasko (99) has applied the Linear Muffin Tin Orbitals-Atomic Spheres Approximation (LMTO-ASA) method to the classical problem of the effect of Ni on the resistance of Fe alloys to (100) cleavage fracture, using a simple periodic supercell in which vacuum is represented by empty atomic spheres to simulate (100) free surfaces. Using unrelaxed surface structures in which bulk interplanar spacings are rigidly maintained, the calculations overestimate the magnitude of the free surface energy, but clearly demonstrate that Ni at positions both on the free surface and one plane below substantially raise the (100) surface energy and therefore increase the Griffith work of separation. A decomposition of the surface energy change into magnetic and chemical contributions shows that while the strong effect of Ni below the surface is chemical in nature, the effect of Ni on the surface plane is entirely a magnetic effect arising from suppression of the normally enhanced magnetic moment of Fe atoms on a (100) surface which significantly reduces the surface energy and (100) cleavage resistance of pure Fe.

An initial application by Krasko (100) of the LMTO-ASA method to the Fe grain boundary of Figure 19 has indicated that the near neighbor Fe atom separations across the boundary predicted by the EAM potential are unrealistically small. A modified EAM potential incorporating an explicit magnetic energy function is being developed (101) using

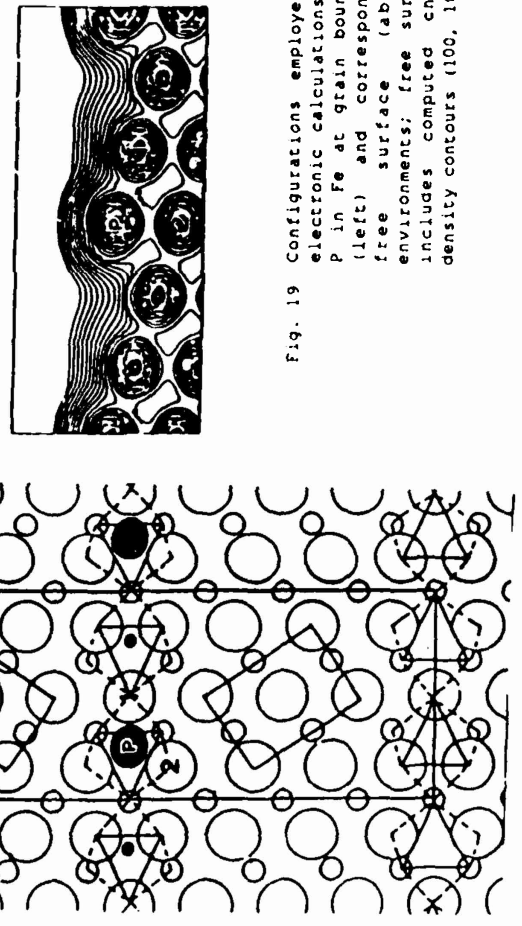


Fig. 19 Configurations employed in electronic calculations for P in Fe at grain boundary (left) and corresponding free surface (above) environments; free surface includes computed charge density contours (100, 103).

results of LMTO-ASA calculations for large strain deformation of Fe between BCC and FCC structures (102). Preliminary LMTO-ASA calculations have been performed for the $\Sigma 3[1\bar{1}0](111)$ Fe tilt boundary containing P using a smaller 6-layer supercell in which the interplanar spacing of the first two (111) planes at the boundary core are adjusted to maintain the Fe-P bond distances of the Fe_3P structure (100). The energy and electronic structure have been compared with and without P, holding the Fe atom configurations fixed. Comparison with the state of P on the corresponding (111) fracture surface is made possible by a preliminary FLAPW calculation performed for this case by Li and Freeman (103). Upon fracturing the boundary, the P atom can relax out of the plane of the grain boundary central Fe atoms (#1 in Figure 19) to a position like that represented in the computed charge density plot at the right of Figure 19. In this preliminary calculation, the Fe-P distance was arbitrarily set equal to the Fe-Fe near neighbor distance.

Consistent with the expected electronegativity difference, the FLAPW calculation indicates charge transfer from Fe to P on the (111) free surface. In contrast, the LMTO-ASA calculation for P in the confined environment of the grain boundary indicates that the P atom (as defined by its Wigner-Seitz sphere volume) is charge deficient, and integration over this volume of the charge density difference relative to the superimposed charge densities of the clean Fe boundary and a pure P monolayer indicates a net transfer of ~0.1 electron from P. Such reverse charge transfer is consistent with the findings of other calculations for metalloid impurities in solid metallic environments and runs counter to the proposal of Briant and Messmer (104) based on simple cluster calculations that impurity-induced embrittlement is associated with weakened Fe-Fe bonding through charge transfer from Fe to the impurity. As is typical of free surfaces, the FLAPW calculations indicate the outer Fe atoms on the clean free surface are deficient 0.24 electron. Adsorption of a P monolayer restores 0.2 electron to these Fe atoms, and increases the Fe work function from 4.7 to 5.5 eV indicative of strong Fe-P bonding. The reversal of Fe-P charge transfer to a more natural state on the free surface and the restoration of surface Fe charge through P interaction may contribute to a lower energy of P on the free surface compared to the grain boundary. Energy comparisons will require relaxations of the surface P configuration, and a meaningful assessment of the role of charge transfer will require a more detailed analysis of the spatial redistribution of charge.

In analogy to the findings for the effect of Ni on Fe (100) cleavage resistance, an assessment of possible magnetic contributions to P embrittlement can be sought from the

calculated Fe magnetic moments in the grain boundary and free surface environments. In both environments, Fe atom #1 of Figure 19 in the absence of P shows an enhanced magnetic moment of ~2.8μ_B compared to 2.2μ_B for bulk BCC Fe. Segregated P lowers the moment of this Fe atom in both environments, but more so in the grain boundary (~1.1μ_B) than on the free surface (~2.2μ_B). A lower magnetic free energy might thus contribute to the lower energy of P on the free surface vs. the grain boundary.

Holding the Fe atom configuration the same as that adopted for the Fe-P case, a preliminary comparison of the states of B, C, P, and S in the grain boundary environment has been conducted with the LMTO-ASA method (100). The reverse charge transfer and strongly reduced Fe magnetic moment are similar for P and S, while weaker effects are found for B and C. Projected density of states (DOS) curves for the Fe atom adjacent to the boundary in Figure 19 are directly compared with reflected (negative) DOS plots for the impurity atoms in Figure 20. Overlap between the B and C 2p bands and the Fe 3d band in the region ~0.3 R_y below the Fermi level, E_F, allows for strong Fe-impurity bonding, while such overlap with the 3p bands of P and S is virtually absent. These features, together with the relative magnetic moments and charge transfers, are in line with the greater boundary segregation energies for B and C compared to P and S. The relatively poorer bonding of P and S to the grain boundary offers the potential for a more profound change of bonding character on moving to the less constrained free surface environment.

An application of the simpler layer Korringa-Kohn-Rostoker (LKKR) technique to the Fe-P $\Sigma3[1\bar{1}0](111)$ boundary reproduces qualitative features of the more rigorous LMTO-ASA results, including the relative reduction of the boundary Fe magnetic moment by P (105). Some preliminary calculations (106) using the Discrete Variational-X_α (DV-X_α) embedded cluster technique (107) have allowed direct comparison of the state of P in the Fe grain boundary and free surface configurations using the same atomic positions employed in the LMTO-ASA and FLAPW calculations. While the 3p component of the P DOS shows a similar shape to that in Figure 20 for the grain boundary case, the shape distorts in the free surface case favoring energies near E_F which may reflect enhanced Fe-P interaction. Once essential electronic features of embrittlement are determined using the more rigorous LMTO-ASA and FLAPW methods, these simpler techniques may allow a quicker investigation of alloying effects as the basis of alloy design for enhanced interfacial cohesion.

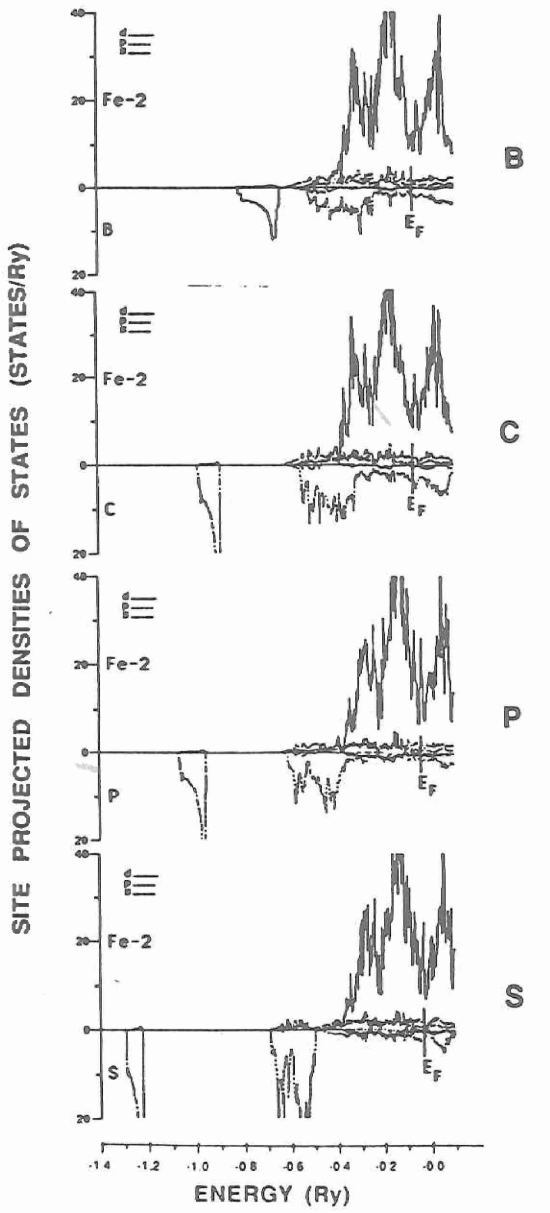


Fig. 20 Density of states (DOS) curves for the Fe atom adjacent to boundary of Figure 19, directly compared to reflected (negative) DOS plots for B, C, P, and S in impurity site (100).

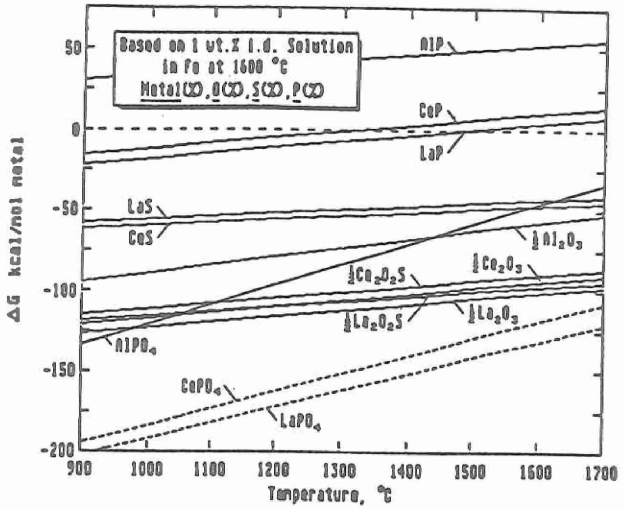


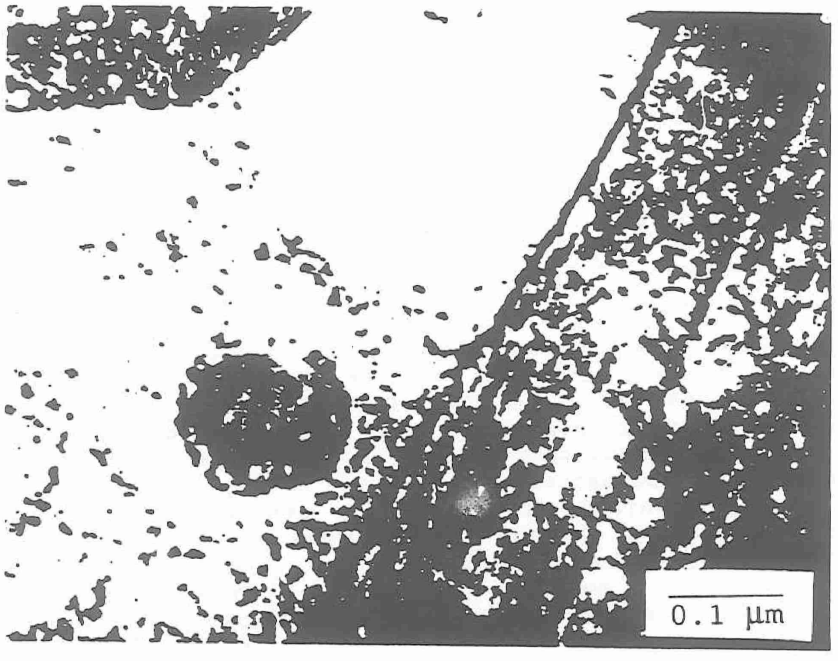
Fig. 21 Estimated free energy of formation (from solution in Fe) of potential impurity gettering phases (108).

While an electronic level understanding of interfacial embrittlement offers the greatest potential for property improvements in the long term, more immediate improvements based on empirical knowledge have been achieved through novel techniques for gettering of known embrittling impurities, and through constraint of alloy composition to exclude known embrittling alloying elements. Studies of rapid solidification phenomena in steels mentioned earlier (65, 71) have revealed that in addition to a substantial refinement in the particle size of "inclusion" phases, the normal sequential formations of oxides and sulfides is replaced by complex oxysulfide formation at the high melt undercoolings achievable by rapid solidification. Compared to sulfides, these phases getter sulfur in a much more stable form which resists dissolution at extreme temperatures. Phosphorus is normally very difficult to getter in conventionally processed steels due to the much lower stability of phosphides relative to sulfides. To explore the possibility of extending the rapid solidification effect to the formation of stable oxygen-phosphorus compounds, a thermodynamic survey was conducted of the potentially most stable phosphorus and sulfur gettering compounds in steels (108). Figure 21 summarizes the estimated free energy of formation of such compounds from dilute solution in Fe, plotted vs. temperature in the range 900-1700°C, identifying lanthanum as the most promising alloy addition to getter P as $LaPO_4$ and S as La_2O_2S.

Thermodynamic and kinetic modelling further indicated feasibility of forming the metastable $LaPO_4$ phase at high melt undercoolings in compositions with the P and S contents of typical high quality steels, provided oxygen is kept sufficiently low (108). The high stability of such compounds should also provide the necessary coarsening resistance for an effective grain refining dispersion (once finely dispersed by rapid solidification) while their high cohesive energy should also in principle contribute interfacial cohesion (and microvoid nucleation resistance) through a high particle-phase free surface energy.

A simple stage I tempered martensitic steel composition was then designed as a substitute for 4340 steel capable of equivalent strength and toughness, but excluding Mn, Si and Cr for enhanced interfacial cohesion. Carbon was maintained at 0.40C for strength, a comparable nickel content of 2.0Ni was held for cleavage resistance, and molybdenum (a possible cohesion enhancer) was increased to 1.5Mo for equivalent hardenability. Rapid solidification processing was performed by remelting a well-deoxidized billet of this composition, followed by a late addition of $LaNi_5$ (balanced to the melt P and S content with an empirical loss factor) just prior to rapid solidification via centrifugal atomization. A modest quantity of powder was produced and consolidated by hot extrusion at 1100°C. STEM microanalysis employing a windowless Xray detector revealed particles of the type shown in Figure 22 with an Xray fluorescence spectrum confirming the presence of La, O, and P; finer particles containing La, O, and S and presumed to be La_2O_2S were also observed. The presence of the La-O-P phase after 1100°C consolidation and its relatively fine ~0.1μm size attests to a high stability of the compound. Observations on as-solidified powder by Hayzelden (60) confirms the presence of similar particles, but quantitative STEM microanalysis reveals a much higher O/P ratio than that of $LaPO_4$ suggesting an "oxyphosphide" phase rather than phosphate.

Despite serious powder cross-contamination, the experimental steels exhibited K_{IC} toughness superior to conventional 4340 and a reduced degree of quasicleavage fracture. Due to a higher-than-specified carbon content, a hardness of R_c57 was achieved with stage I tempering at 200°C, and the grain coarsening resistance associated with the stable particle dispersions was also demonstrated. Although the small amount of material did not allow adequate K_{Iscc} determination, a rising-load K_{Iscc} screening test for which 4340 steel failed at 10 ksi$\sqrt{in}$ indicated a K_{Iscc} of 40 ksi$\sqrt{in}$, and a standard K_{Iscc} specimen survived 10^3 hr at 20 ksi$\sqrt{in}$ without failure. The K_{Iscc} levels indicated by these



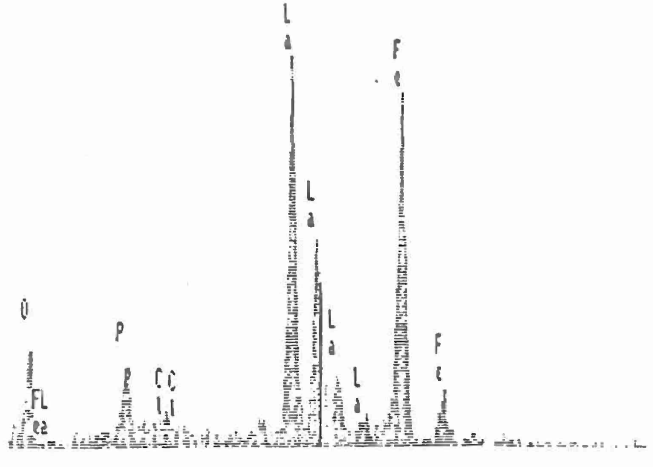


Fig. 22 STEM micrograph and associated X-ray fluorescence spectrum of La-O-P particle in rapidly solidified LaNiMo steel after consolidation at 1100C (108).

preliminary experiments are compared against conventional ultrahigh-strength steels in Figure 23, indicating a major property advance associated with achievement of the designed microstructure.

A larger heat of the experimental steel has been produced by gas atomization (109), but STEM microanalysis revealed the presence of lanthanum silicates attributed to a crucible reaction, with no evidence of the desired P and S gettering phases. Strength and toughness equivalent to 4340 was obtained, with good ballistic properties, but a measured 10^3 hr K_{ISCC} of only 7 ksi$\sqrt{in}$ confirms the necessity of the impurity gettering to achieve the remarkable stress corrosion resistance (110). Another gas-atomized heat produced with appropriate processing modifications is currently being evaluated (110).

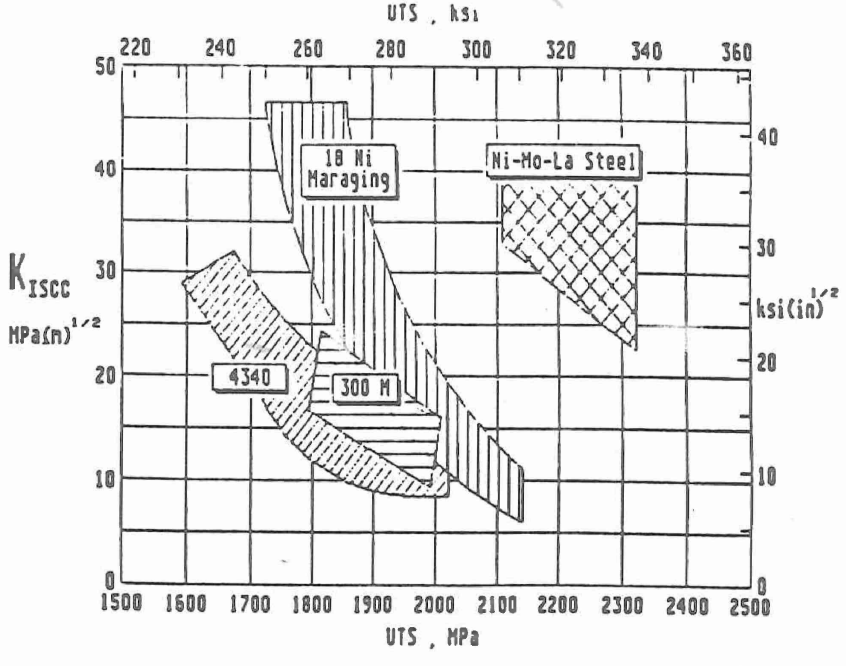


Fig. 23 Stress-corrosion resistance vs. strength comparing rapidly solidified LaNiMo steel with conventional ultrahigh-strength steels (108).

MATERIALS DESIGN: STAINLESS BEARING STEEL

Our first effort to integrate these developments into the design of one alloy was undertaken by a team of students in the Materials Design Course at Northwestern University (111), who performed a conceptual design of a stainless bearing steel for the Space Shuttle Main Engine turbopumps, a demanding application requiring substantial improvements in toughness and stress-corrosion resistance. Maintaining a R_c60 hardness level required for rolling contact fatique resistance and wear resistance, property objectives consisted of a doubling of K_{IC} and K_{ISCC} relative to the current alloy 440C employed in this application. Consistent with the system framework of Figure 2, a sequence of calculations was devised to arrive at a unique alloy composition tailored to achieve quantitative microstructural objectives under specific processing conditions. For stress corrosion resistance, the overall composition was first constrained for compatability with rapid solidification processing and La treatment, with exclusion of Mn and Si for interfacial cohesion. An Orowan strengthening analysis was applied to the available hardness and particle size data from the experimental steels of Table 1, defining the necessary particle spacing for R_c60 hardness, and a minimum carbon content of 0.30C was estimated to achieve this condition. Matrix composition was constrained to include 12Cr for stainless properties. THERMOCALC computations were then employed to compute a line of compositions in Ni and Co that maintained a sufficiently high M_s temperature to give the desired lath martensite structure. To incorporate transformation toughening, a unique Ni and Co composition was determined by the nature of the austenite that would precipitate during tempering near 500C, both in terms of its amount and its transformation stability as quantified by the martensitic transformation driving force at room temperature. To achieve maximum strengthening efficiency without embrittlement following the considerations of Figure 6, V and Mo contents were then optimized to maximize the driving force for coherent M_2C at 500C while maintaining limits on the M_6C and $M_{23}C_6$ carbide driving forces, subject to a maximum allowed solution treatment temperature. A second iteration of this complete sequence was then followed to achieve self consistency.

In this manner, a computer-aided thermodynamics-based design yielded a unique seven component alloy composition which is thermodynamically (and kinetically) capable of achiéving a desired multiphase microstructure under fairly well prescribed processing conditions. A small heat of this composition has been prepared and is currently undergoing evaluation. If this prototype alloy is successful, we will have arrived at a very different way of creating new materials.

SUMMARY

Advances in theory and instrumentation focused on the principles underlying control of strength, toughness, and hydrogen resistance in ultrahigh-strength steels have achieved a level of fundamental understanding allowing true materials design. A comprehensive combined SANS, TEM, APFIM, STEM investigation of M_2C carbide precipitation has demonstrated important predicted features of precipitation at high supersaturation, and identified major effects of particle coherency. Recent theory of coherent thermodynamics and multicomponent diffusional kinetics calibrated by nanoscale experimental measurements has allowed application of the THERMOCALC thermochemical database and software system to predict the alloy composition dependence of basic scaling factors governing precipitation behavior. The thermodynamics-based control of competing precipitation reactions then allows design of optimal compositions for efficient strengthening without embrittlement.

Novel shear tests conducted in materials with well characterized particle dispersions have quantified the pressure-dependent resistance to microvoid-nucleation-induced shear localization which accelerates ductile fracture. Continuum mechanical models show the role of dispersion geometry (size, fraction, spatial inhomogeneity) and interfacial properties on microvoid nucleation and softening behavior. The models predict improved geometries for grain refining dispersions and allow estimates of particle interfacial properties from measured nucleation behavior as a basis of phase selection for optimal grain refining dispersions with maximum resistance to microvoid nucleation. For a given alloy composition and melt practice, procedures for optimization of solution treatment to eliminate unnecessary particles have demonstrated substantial toughness enhancement.

Controlled experiments defining austenite stability and critically testing the role of austenite in mechanical behavior show that conventional retained austenite is too unstable to enhance fracture toughness in ultrahigh-strength steels. Transformation kinetic theory prescribing the particle-size and composition dependence of dispersed austenite stability predicts that optimal stability for transformation toughening is achievable through austenite precipitation in high alloy steels. Guided by thermodynamic predictions, novel heat treatments and STEM microanalytical studies in AF1410 steel have demonstrated precipitation of

optimally stable ultrafine intralath austenite of near-equilibrium composition, yielding a record level of fracture toughness in this steel. Critical experiments in model austenitic alloys have identified an important role of transformation dilatation in the transformation toughening of ductile solids, providing a basis for design of superior alloy compositions for maximum dispersed-phase transformation toughening.

Thermodynamic and continuum mechanical modelling of the competition between intergranular separation and crack-tip blunting predicts a thermodynamic basis for intergranular hydrogen stress corrosion with support from available surface thermodynamic data. Directed at the electronic basis of the governing thermodynamic quantities, band theoretic and cluster model calculations for embrittling impurities in grain boundary and corresponding fracture surface environments show charge transfer, magnetic moment, and band structural changes which correlate with embrittlement potency. The emerging understanding of the electronic basis of embrittlement will allow design of grain boundary composition for both enhanced intrinsic cohesion and reduced hydrogen interaction, offering the greatest potential for property improvements. Substantial advances in hydrogen stress corrosion resistance through cleaning of impurities from grain boundaries have already been achieved by design of novel metastable impurity-gettering compounds accessible through rapid solidification processing.

Integration of these concepts within a systems engineering framework has led to the first demonstration of computer-aided thermodynamics-based design of a complex multicomponent alloy directed at specific property and microstructural objectives. The frontier of materials design defined by this research constitutes both a new concept of materials science and the advent of true materials engineering.

ACKNOWLEDGEMENTS

An initial phase of the Steel Research Group effort was conducted at MIT under NSF sponsorship. The expanded program now underway at Northwestern University is funded by NSF, ONR, NASA, ARO, AFOSR, and DOE, supplemented by industrial fellowship support. Coordinated efforts at Harvard and Brown Universities are supported by NSF.

REFERENCES

1. G.M. Jenkins, "The Systems Approach," in Systems Behavior, ed. J. Beishon and G. Peters, Open University Press, 1972.

2. C.S. Smith, A Search for Structure, MIT Press, Cambridge, MA, 1981.

3. M. Cohen, "Unknowables in the Essence of Materials Science and Engineering," Mat. Sci. and Eng. 25 (1976) 3.

4. M. Cohen, "Metallurgy and the Evolution of Materials Science and Engineering," these proceedings.

5. G.R. Speich, "Secondary Hardening Ultrahigh-Strength Steels," these proceedings.

6. G.R. Speich, D.S. Dabkowski, and L.F. Porter, Metall Trans. 4 (1973) 303.

7. J.A. Liddle, G.D.W. Smith, and G.B. Olson, "Alloy Carbide Precipitation in a High Cobalt-Nickel Secondary Hardening Steel," Proc. 33rd Int'l Field-Emission Symposium, J. de Physique, 47 (1986) C7-223.

8. J.S. Montgomery, and G.B. Olson, "Kinematics of M_2C Carbide Precipitation," these proceedings.

9. A.J. Allen, D. Gavillet, and J.R. Weertman, "SANS and TEM Studies of Isothermal M2C Carbide Precipitation in Ultrahigh-Strength AF1410 Steel," manuscript in preparation.

10. H. Wendt and P. Haasen, Acta Metall. 31 (1983) 1649.

11. R. Kampmann and R. Wagner, in Decomposition of Alloys, ed. P. Haasen et al., Pergamon Press, NY (1984) p. 91.

12. R. Wagner and R. Kampmann, "Solid State Precipitation at High Supersaturations," these proceedings.

13. J.S. Langer and A.J. Schwartz, Phys. Rev. A21 (1980) 948.

14. G.M. Carinci, G.B. Olson, J.A. Liddle, L. Chang, and G.D.W. Smith, "APFIM Study of Multicomponent Precipitation," these proceedings.

15. G.M. Carinci, "Precipitation of Multicomponent Carbides in Co-Ni Martensitic Steels," Ph.D. thesis, MIT, February 1989.

16. T. Kinkus and G.B. Olson, Northwestern University research in progress.

17. H.M. Lee, "Stability and Coarsening Resistance of M_2C Carbides in the Secondary Hardening Reaction," Ph.D. thesis, MIT, February 1989.

18. A.J. Garratt-Reed and H.M. Lee, MIT unpublished research, 1988.

19. M. Grujicic and G.B. Olson, CALPHAD 12 (1988) 405.

20. H.M. Lee, S.M. Allen, and M. Grujicic, "Stability and Coarsening Resistance of M_2C Carbides in Secondary Hardening Steels," these proceedings.

21. S. Bjorklund, L.F. Donaghey, and M. Hillert, Acta Met. 20 (1972) 867.

22. B. Sundman, B. Jansson, and J.O. Andersson, CALPHAD, 9 (1985) 153.

23. M. Grujicic, "Design of M_2C Carbides for Secondary Hardening," these proceedings.

24. K-U. King, P.W. Voorhees, T. Mura, and G.B. Olson, Northwestern University research in progress.

25. F. Larché and J.W. Cahn, Acta Metall. 21 (1973) 1051.

26. G. Ghosh and G.B. Olson, Northwestern University research in progress.

27. M. Schmidt and R. Hemphill, "Characterization of 4% Molybdenum SRG Experimental Steel," these proceedings.

28. R. Hemphill, Carpenter Steel alloy AerMet100, patent pending.

29. M. Grujicic and G.N. Haidemenopoulos, CALPHAD 12 (1988) 219.

30. J.L. Goss, "Austenitic Grain Growth and Precipitation Strengthening in Rapidly Solidified Alloys," M.S. thesis, MIT, August 1980.

31. J.J. Irani and R.W.K. Honeycombe, J. Iron and Steel Inst., 203 (1965) 826.

32. G.N. Haidemenopoulos, "Dispersed-Phase Transformation Toughening in Ultrahigh-Strength Steels," Ph.D. thesis, MIT, May 1988.

33. A.T. Davenport and R.W.K. Honeycombe, Metal Science, 9 (1975) 201.

34. S. Spooner, H.J. Rack, and D. Kalish, Metall. Trans. 2A (1971) 2306.

35. L. Chang, G.D.W. Smith, and G.B. Olson, J. de Physique 47 (1986) C2-265.

36. I. Aslanidis, "Softening and Recovery Resistance in Fe, Fe-Co, Fe-Al, Fe-Ni, and Fe-Ni-Co Alloys," Ph.D. thesis, MIT, September 1989.

37. V. Pierron-Bohnes, M.C. Cadeville, and G. Parette, J. Phys. F: Met. Phys., 15 (1985) 1441.

38. H. Warlimont and G. Thomas, Metal Sci. 4 (1972) 47.

39. S. Spooner, Oak Ridge National Laboratory, unpublished research.

40. A.F. Yedneral, O.P. Zhukov, M.A. Kablukovskaya, B.M. Mogutnov, and M.D. Perkas, Fiz. Metal. Metalloved, 36 (1974) 727.

41. A.B. Kuper, D. Lazarus, J.R. Manning, and C.T. Tomizuka, Phys. Rev., 104 (1956) 1536.

42. E. Hornbogen, "Alloy Design for >3GPa Steels," these proceedings.

43. C. Knepfler, K.T. Faber, and J. Weertman, Northwestern University, research in progress.

44. W.M. Garrison, Jr., and K.J. Handerhan, "Fracture Toughness: Particle-Dispersion Correlations," these proceedings.

45. G. Krauss, "Shear Fracture of Ultrahigh-Strength Low Alloy Steels," these proceedings.

46. J. Mescall and H. Rogers, "The Role of Shear Instability in Ballistic Penetration," these proceedings.

47. J.G. Cowie, M. Azrin, and G.B. Olson, "Microvoid Formation During Shear Deformation of Ultrahigh-Strength Steels," these proceedings.

48. J.G. Cowie, M. Azrin, and G.B. Olson, Metall. Trans. 20A (1989) 143.

49. M.J. Gore, "Grain Refining Dispersions and Mechanical Properties in Ultrahigh-Strength Steels," Ph.D. thesis, MIT, May 1988.

50. A. Benedetti and J.B. Cohen, Northwestern University, unpublished research, 1989.

51. A. Needleman, J. Applied Mechanics, 54 (1987) 525.

52. A. Needleman, "A Numerical Study of Void Nucleation at Carbides," these proceedings.

53. M.J. Gore, A. Needleman, and G.B. Olson, unpublished research, 1988.

54. J.W. Hutchinson and V. Tvergaard, "Effect of Particle-Void Interaction on Void Growth in Tension and Shear," these proceedings.

55. J.W. Hutchinson and V. Tvergaard, "Softening Due to Void Nucleation in Metals," in Fracture Mechanics: Perspectives and Directions ed. R.P. Wei and R.P Gangloff, ASTM STP 1020 (1989) p.61.

56. Y. Huang and J.W. Hutchinson, "A Model Study of the Role of Nonuniform Defect Distribution on Plastic Shear Localization," in Role of Modelling in Materials Design, ed. J.D. Embury, TMS-AIME (1990).

57. D.M. Tracey and P.J. Perrone, "Modelling of Interactions in Void Nucleation and Growth," these proceedings.

58. D.M. Tracey and P.J. Perrone, "Stress Distributions Near Microstructural Inhomogeneities," Trans. 6th Army Conf. Applied Math. and Computing ARO Report #89-1 (1989).

59. M.J. Gore, G.B. Olson, and M. Cohen, "Grain-Refining Dispersions and Properties in Ultrahigh-Strength Steels," these proceedings.

60. C. Hayzelden, "Secondary Particle Dispersions and Impurity Gettering in Ultrahigh-Strength Steels," these proceedings.

61. R.J. Asaro and J.R. Rice, J. Mech. Phys. Solids 25 (1977) 309.

62. M. Schmidt and M.J. Gore, "Solution Treatment Effects in AF1410 Steel," these proceedings.

63. A.S. Argon and J. Im, Metall Trans., 6A (1975) 839.

64. J.H. Beatty and M. Azrin, MTL research in progress.

65. C-Y. Hsu, "Grain-Growth Mechanisms in Rapidly Solidified Matrix Steels," Ph.D. thesis, MIT, February 1984.

66. T. Gladman, Proc. R. Soc. A294 (1966) 298.

67. P. Hellman and M. Hillert, Scandinavian Journal of Metallurgy, 4 (1975) 211.

68. J.W. Flowers, Jr., and S.P. Karas, J. Appl. Phys. 38 (1967) 163.

69. T. Gladman and F.B. Pickering, JISI 205 (1967) 653.

70. L. Anand and J. Gurland, Metall Trans. 6A (1975) 928.

71. G.B. Olson and R.G. Bourdeau, "Rapidly Solidified Ferrous Alloys," in Rapidly Solidified Alloys, ed. S.K. Das, B.H. Kear, and C.M. Adam, TMS-AIME, Warrendale, PA (1985) p.185.

72. M.J. Gore, M. Grujicic, G.B. Olson, and M. Cohen, Acta Metall, 37 (1989) 2849.

73. G.B. Olson, "Transformation Plasticity and the Stability of Plastic Flow," in Deformation, Processing and Structure, chpt. 9, ed. G. Krauss, ASM (1984) p. 391.

74. G.B. Olson and M. Cohen, Metall. Trans. 13A (1982) 1907.

75. G.B. Olson and M. Cohen, Metall. Trans. 6A (1975) 791.

76. T. Narutani, G.B. Olson, and M. Cohen, J. de Physique 43 (1982) C4-429.

77. R.H. Leal, "Transformation Toughening of Metastable Austenitic Steels," Ph.D. thesis, MIT, June 1984.

78. G.B. Olson and M. Cohen, "Martensitic Transformation as a Deformation Process," in Mechanical Properties and Phase Transformations in Engineering Materials," ed.

S.D. Antalovich, R. O. Ritchie, and W.W. Gerberich, TMS-AIME (1986) p.367.

79. F. Stavehaug, "Transformation Toughening of γ'-Strengthened Metastable Austenitic Steels," Ph.D. thesis, MIT, June 1990.

80. R.G. Stringfellow and D.M. Parks, MIT research in progress.

81. G.N. Haidemenopoulos, G.B. Olson, M. Cohen, and K. Tsuzaki, Scripta Metall. 23 (1989) 207.

82. G.N. Haidemenopoulos, M. Grujicic, G.B. Olson, and M. Cohen, Acta Metall. 37 (1989) 1677.

83. G.N. Haidemenopoulos, G.B. Olson, and M. Cohen, "Dispersed-Phase Transformation Toughening in Ultrahigh-Strength Steels," these proceedings.

84. G.B. Olson and M. Cohen, "Dislocation Theory of Martensitic Transformations," in Dislocations in Solids, Vol. 7 ed. F.R.N. Nabarro, North-Holland, Amsterdam (1986) p. 295.

85. G.B. Olson, K. Tsuzaki, and M. Cohen, "Statistical Aspects of Martensitic Nucleation," Turnbull Symposium: Phase Transitions in Condensed Systems, ed. G.S. Cargill, F. Spaepen, and K.N. Tu, MRS (1987) p. 129.

86. I-W. Chen, Y-H. Chiao, and K. Tsuzaki, Acta Metall. 33 (1985) 1847.

87. M. Grujicic, M. Buonanno, S.M. Allen, G.B. Olson, and M. Cohen, "Heterogeneous Precipitation of Austenite for Stabilization," these proceedings.

88. B.V.N. Rao, "Ferrite-Austenite Dual Phase Steel," U.S. Patent 4,544,422, October 1, 1985.

89. C-C. Young, "Transformation Toughening in Phosphocarbide-Strengthened Austenitic Steels," Ph.D. thesis, MIT, May 1988.

90. B. Budiansky, J.W. Hutchinson, and J.C. Lambropoulos, Intl J. Solids and Structures, 19 (1983) 337.

91. G.N. Haidemenopoulos, M. Grujicic, G.B. Olson, and M. Cohen, CALPHAD 13 (1989) 215.

92. C. Kuehmann and G.B. Olson, Northwestern University research in progress.

93. C.J. McMahon, Jr., "Hydrogen Embrittlement of High-Strength Steels," these proceedings.

94. J.R. Rice and J-S. Wang, Mat. Sci. and Eng. A107 (1989) 23.

95. P.M. Anderson, J-S. Wang, and J.R. Rice, "Thermodynamic and Mechanical Models of Interfacial Embrittlement," these proceedings.

96. J-S. Wang, private communication.

97. E. Wimmer, C.L. Fu, and A.J. Freeman, Phys. Rev. Lett., 55 (1986) 2618.

98. R.J. Harrison, F. Spaepen, A.F. Voter, and S-P. Chen, "Structure of Grain Boundaries in Iron," these proceedings.

99. G.L. Krasko and G.B. Olson, "Evaluation of Decohesion Mechanisms by LMTO-ASA-Stoner Cohesive Energy Calculations," these proceedings.

100. G.L. Krasko and G.B. Olson, "The Effect of Boron, Carbon, Phosphorus and Sulfur on Intergranular Cohesion in Iron," submitted to Phys. Rev. B.

101. R.J. Harrison and G.L. Krasko, MTL research in progress.

102. G.L. Krasko and G.B. Olson, Phys. Rev B 40 (1989) 11536.

103. C. Li and A.J. Freeman, Northwestern University research in progress.

104. C.L. Briant and R.P. Messmer, Phil. Mag. B, 42 (1980) 569.

105. M.E. Eberhart and J.M. MacLaren, "Mechanisms for Cleavage and Intergranular Embrittlement in Fe," these proceedings.

106. H. Eguchi, "Electronic Basis of Phosphorus Embrittlement of Iron Grain Boundaries," M.S. thesis, Northwestern University, June 1990.

107. D.E. Ellis, "Molecular Clusters," in Handbook on the Physics and Chemistry of the Actinides, ed. A.J. Freeman and G.H. Lander, North-Holland, Amsterdam (1985) p.1.

108. J.F. Watton, G.B. Olson, and M. Cohen, "A Novel Hydrogen-Resistant UHS Steel," these proceedings.

109. G. Del Corso and G.B. Olson, unpublished research.

110. J.H. Graves and A.A. Anctil, MTL research in progress.

111. A. Bilyk, T. Chen, N. Akaiwa, H. Eguchi, and G.B. Olson, Northwestern University 750-C95 Materials Design Class Project Report, June 1989.

MATERIALS DESIGN: AN UNDERGRADUATE COURSE

G.B. Olson
Northwestern University
Department of Materials Science and Engineering
Evanston, Illinois 60208

Abstract

General principles of systems engineering are applied to the design of materials to meet specific performance objectives. Results of ongoing research on processing/structure and structure/property relations in ultrahigh-strength steels are used to illustrate the formulation of quantitative microstructural objectives to achieve required property combinations, and the computer thermodynamics-based design of compositions responding to prescribed processing conditions. A class project addresses the conceptual design of a 7-component stainless bearing steel for a critical Space Shuttle application.

Introduction

On the suggestion of Professor Morris Fine, this paper, rather than presenting the usual discussion of research results, will instead focus on teaching and its interrelation with research. In the late 1960's and early 1970's, Professor Fine taught a pioneering course at Northwestern on Materials Development which in part responded to the concerns of accreditation boards regarding the declining design component of engineering undergraduate curricula. Twenty years later, the concerns are more valid than ever. In the spirit of Professor Fine's innovations, a new course at Northwestern (1) directly addressing Materials Design has been made possible by a multi-institutional research program; centered at Northwestern, the interdisciplinary Steel Research Group (SRG) program focusses on the quantitative scientific principles allowing design of new classes of advanced steels.

To approach materials design in the broadest context, a survey of instructors of Systems Engineering courses at Northwestern identified a concise review of the systems approach by G.M. Jenkins (2), presenting an excellent overview that could be readily translated to materials problems. A recent review by Ashby (3) effectively describes the process of materials selection in the various stages of engineering design, and provides an excellent framework for the specification of material property objectives to achieve desired performance. To provide materials science students with sufficiently quantitative design tools, computer laboratory sessions were found effective in developing proficiency in available thermodynamic and kinetic software, most notably the ThermoCalc system (4) that has formed the cornerstone of our materials design research. Applications to control of both constrained equilibria and thermodynamics-based kinetic scaling factors provided the basis of student team design projects during the second half of the course.

Materials as Systems

The central paradigm of materials science is the sequential interrelation of processing, structure, properties, and performance as depicted in the linear structure of Figure 1. While the notion of materials as systems has been well developed by Cyril Smith (5) in the context of material *structure* as a hierarchy of interacting microstructural subsystems, the concept can be further broadened to regard each of the blocks of Figure 1 as a primary subsystem, each of which can itself be further subdivided into a hierarchy of interacting subsystems. Although "cause and effect" logic suggests a sequence of interrelations from left to

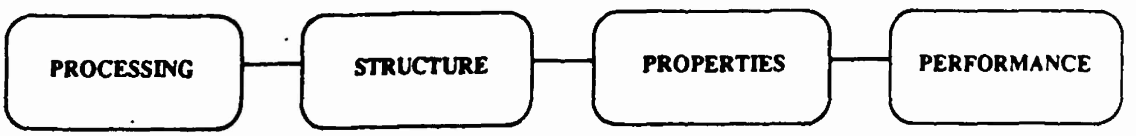


Figure 1: Linear structure of materials science, defining primary material subsystems.

Morris E. Fine Symposium
Edited by Peter K. Liaw, J. R. Weertman,
Harris L. Marcus and Joseph S. Santner
The Minerals, Metals & Materials Society, 1991

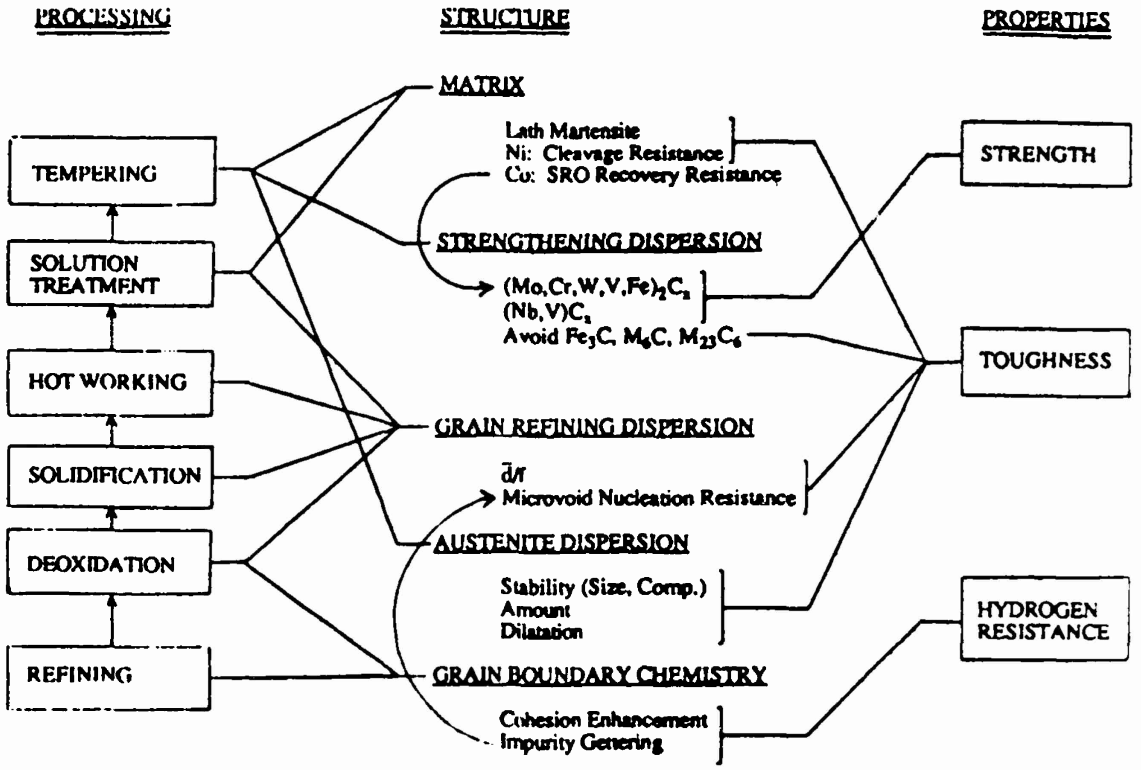


Figure 2: Flow-block diagram illustrating the structure of Co-Ni secondary hardening steels as a system.

right in Figure 1 (e.g. structure controls properties), Morris Cohen (6,7) has observed there is a "reciprocity" whereby it is equally valid to regard our perception of *structure* as controlled by the *properties* we wish to explain. This reciprocal view is particularly useful in materials design.

As outlined by Jenkins (2) a system in general is a complex grouping of components which is divisible into a hierarchy of interacting subsystems, usefully represented by a flow-block diagram. Figure 2 illustrates such a diagram, expanded from the general structure of Figure 1, representing the ultrahigh-strength martensitic alloy steels addressed by the SRG research program. Shown are the key microstructural subsystems controlling the three primary properties of interest, together with the stages (subsystems) of processing affecting each. While further details will be discussed later, it is evident from Figure 2 that in addition to the horizontal primary subsystem interactions reflected in Figure 1, important vertical subsystem interactions also exist such as the effect of recovery resistance on carbide precipitation, and the effect of impurity gettering on microvoid nucleation resistance. As is also a universal feature of systems, the material of Figure 2 is part of a hierarchy of larger systems, strongly influenced by higher levels, particularly in the formulation of its objectives. It is the application of the steel as a load-bearing component in an engineering structure that defines its performance objective quantifying the required three primary properties of strength, toughness, and hydrogen resistance. Further, as for all systems, the ultimate system objective of a *combination* of properties demands a compromise between conflicting objectives of property subsystems (e.g. strength vs. toughness), and to function at maximum efficiency the system must be *designed*.

Systems Design of Materials

Stages of Systems Engineering

The sequential stages of the general systems design approach described by Jenkins (2) are depicted in Figure 3. We here briefly examine each of these in the context of materials.

Analysis

The basic steps of systems analysis consist of problem formulation, definition of the system and the wider system in which it functions, and definition of the system objectives. In the case of materials, problem formulation consists of identification of a broad materials performance need. The materials system is then defined in terms of class of material and microstructure, and important subsystems and

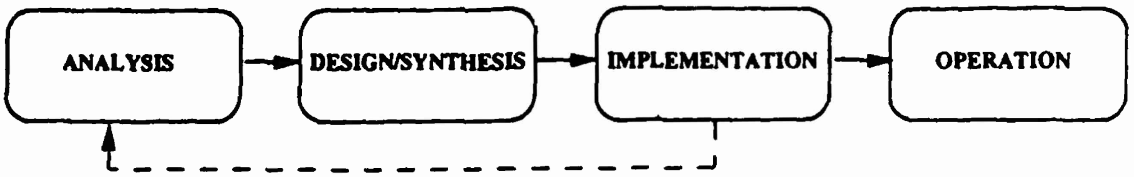


Figure 3: Stages of systems engineering (2).

interactions are identified and represented in a flow-block diagram as in Figure 2. While Figure 2 reflects a fairly advanced stage of analysis, an initial stage would emphasize simplicity and flexibility of approach. Consideration of the wider system then defines the function of the material in a device, which in turn prescribes performance requirements.

The manner in which property/performance relations can be used to set quantitative property objectives for a material is well described in the review by Ashby (3). Using the examples of table legs, bicycle fo[illegible] springs, and pressure vessels, a series of combine property parameters superimposed on property cross-plots is used to compare competing materials. Such an analysis is not only useful to the design engineer selecting materials from those available, but also serves to define property objectives for the materials scientist designing an improved material to better compete with available alternative materials. For the ultrahigh strength steels of Figure 2, property objectives were defined by choosing a significant strength increment beyond that which can be reliably used in current commercial steels for advanced structural applications such as aircraft landing gear. This defines an ultimate tensile strength range of 2000-2400 MPa corresponding to a hardness of R_c55 to 60. Quantitative K_{IC} toughness objectives are then defined by the toughness/strength ratio required for a desired minimum critical flaw size. Hydrogen resistance, quantified in these steels by the stress corrosion threshold K_{ISCC}, is then specified by a desired minimum K_{ISCC}/K_{IC} ratio.

Another important early step in analysis is the organization of an interdisciplinary design team for which Jenkins (2) gives useful general guidelines. It is particularly noteworthy that the required breath of knowledge demands that the materials design team leader must be a materials scientist, but necessarily one well suited to interaction with related disciplines.

Design/Synthesis

The first step in the synthesis of understanding in design is modelling. Ideally, quantitative models should be developed for each of the important structure/property and property/structure relations depicted in Figure 2, spanning a hierarchy of structural scales. While empiricism at some level is inevitable, the most useful models, particularly for the generally nonlinear phenomena at play in materials, are as fundamentally mechanistic as possible. Jenkins (2) cautions however, that modelling for design must be purposeful, with the goal of optimization rather than subsuming facts. In this regard it is useful to prioritize phenomena and decide the necessary accuracy of required models.

It should perhaps be acknowledged at this point that materials science is a relatively young field for which quantitative models are not abundant. Even in the most scientifically advanced area of high strength steels, relations for toughness and hydrogen resistance remain quite qualitative. The kinetic theory of phase transformations has provided a reasonably quantitative basis for the microstructural evolution underlying process/structure relations, however, and recent progress indicates that quantitative microstructural objectives can be formulated and achieved to provide specified strength with desired qualitative changes in toughness and hydrogen resistance (8,9).

The second stage of synthesis is the actual application of models in simulation of material behavior on both the local scale of microstructural subsystems and ultimately the global scale of the entire system. Simulation is then applied to system optimization. As emphasized by Jenkins (2) it is here crucial to avoid "sub-optimization" whereby a subsystem is optimized at the expense of the total system. The total system must be optimized as a whole, recognizing constraints imposed by competing subsystems. Again material performance demands a combination of properties, such that major increases in one property can be useless if other necessary properties are degraded.

Another important aspect of system optimization is the application of simulations to the identification of sensitive variables (in material composition and processing) in order to minimize sensitivity for controllability; i.e. "sharp" optima are to be avoided. Control and reliability also demand that control systems be built into the design, ideally allowing for process monitoring and readjustment. Reliability also requires some tolerance for the unpredictable, such that statistical variations can not cause an excessive fraction of processed material to fall below final specifications.

Implementation and Operation

As depicted in Figure 3, the next step in systems engineering is *implementation*, which here corresponds to the production of a prototype material. The testing of model predictions via characterization of prototypes allows refinement of the system models through an iterative process denoted by the dashed line in the figure.

When sufficient optimization is achieved, the *operation* stage is entered corresponding to the setting of materials specifications in terms of composition and processing.

It should be recognized at this point that the actual practice by which new materials are currently developed consists of the simultaneous evaluation of a set of materials with variations in composition and processing to allow optimization via empirical process/ structure correlations with minimal involvement of structural details. Experience in other engineering systems would strongly indicate that, once mechanistic models are sufficiently mature, the true design of materials through the deliberate approach of Figures 2 and 3, involving the sequential characterization of a small number of prototype materials, will ultimately lead to greater and more rapid advances. The general principles reviewed here offer a glimpse of the future of materials design. Recent progress suggests that, for steels at least, that future may be close at hand.

The Example of Ultrahigh-Strength Steels

Specific examples giving meaning to the development and application of mechanistic models for design just discussed are obtained from results of SRG research on ultrahigh-strength martensitic steels. Detailed theoretical and experimental results defining process/structure and structure/property relations for each of the microstructural subsystems listed in Figure 2 are reviewed elsewhere (8,9). Examples concerning behavior of the alloy matrix include the electronic basis of Ni-enhancement of cleavage resistance (10) and the mechanism of Co-enhancement of dislocation recovery resistance (9). We will here highlight advances in the mechanistic modelling of these subsystems, emphasizing examples which serve to illustrate key points.

Control of competing precipitation reactions in secondary hardening martensitic steels offers an excellent example of quantitative processing/ structure relations. Achieving optimum strength/toughness combinations in these steels requires near completion of M_2C alloy carbide precipitation to eliminate Fe-base Fe_3C carbides which precipitate earlier in a coarse form limiting toughness through microvoid nucleation (11). Completion results in an overaged microstructure where strength is controlled by the Orowan bypass mechanism. In this regime M_2C particle size refinement governs strengthening. Hence the desired microstructural objectives is to achieve the finest particle size at completions of precipitation. Extensive study (9) of M_2C precipitation behavior by a range or experimental techniques in the 14Co-10Ni steel AF1410 shows nucleation and coarsening behavior with suppressed growth consistent with theory of precipitation at high supersaturations (12), and shows a particle composition trajectory indicative of coherent precipitation. The primary size scaling factor in the high supersaturation regime is the initial critical nucleus size which scales inversely with the driving force for coherent precipitation. Incorporating the elastic contribution of particle coherency, the latter can be computed as a function of alloy composition using the ThermoCalc software and database. However, an important constraint enters because the M_2C phase is typically metastable, and completion of its precipitation must be achieved before the embrittling incoherent interfacial precipitation of equilibrium carbides such as M_6C. Toward design of optimal alloy compositions for strength/toughness, Figure 4 depicts computed contours of precipitation driving force for (a) the M_6C carbide and (b) the coherent M_2C carbide, as functions of Cr and Mo content in 14Co-10Ni-0.25C steels (13). Experience from experimental alloys with Cr and Mo contents along the dashed line in Figure 4a indicates interfacial embrittlement during secondary hardening for M_6C driving forces beyond 15 kJ/mole. This then provides the constraint that alloy composition must lie to the left of the dashed curve superimposed in Figure 4b. Subject to this constraint, maximizing the coherent M_2C driving force for efficient strengthening defines the alloy composition denoted by the open point. This point lies very close to a recently developed alloy with excellent strength/toughness properties (14).

An example of analysis of structure/property relations involving interdisciplinary collaboration with applied mechanics, introducing materials science students to the capabilities of numerical finite-element methods, is the investigation of the role of particle dispersion geometry on microvoid nucleation resistance. Once unnecessary particles such as Fe_3C are eliminated by optimal processing, the microvoid nucleation resistance governing ductile fracture toughness becomes controlled by the grain refining dispersion necessary to limit grain coarsening during solution treatment. The geometric requirements in terms of particle diameter d and volume fraction f for grain refinement are well established. Combining this with the predicted role of these variables from the numerical modelling of microvoid nucleation (15) has allowed an assessment of the toughening benefits of particle size refinement while maintaining a fixed grain size (9). Dispersions

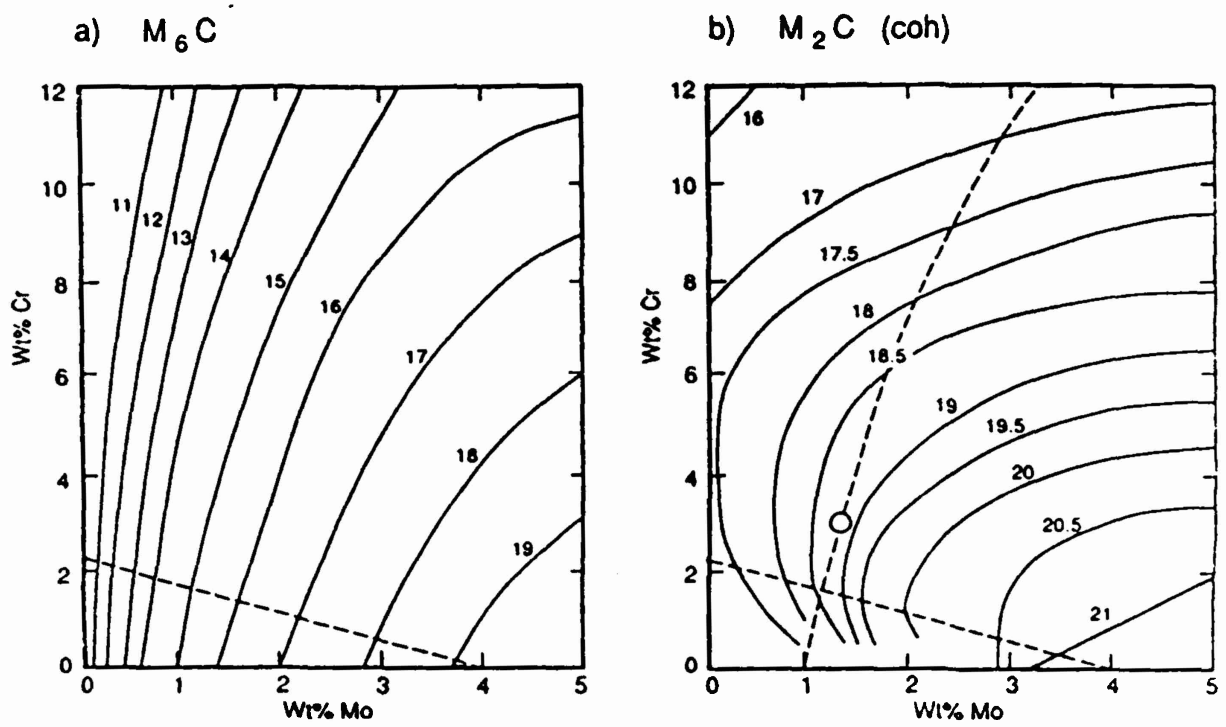


Figure 4: Computed precipitation driving force (kJ/mole) at 510C for alloys containing 14Co-10Ni-0.25C: (a) incoherent M_6C, (b) coherent M_2C (13).

with the desired finer size and required coarsening resistance may be achievable by rapid solidification processing.

A unique example of a structure/property relation amenable to rather direct control through thermodynamics is the transformation toughening from a dispersion of precipitated austenite. Experiments in model austenitic steels identify the optimal thermodynamic stability for maximum transformation toughening and isolate the important role of transformation dilatation (9). Transformation kinetic theory predicts the roles of particle composition and size on the transformation stability of dispersed austenite, and experiments employing multi-step heat treatments in AF1410 steel demonstrate the toughening benefit of optimal stability austenite dispersions (16). Constrained equilibrium calculations employing ThermoCalc predict the amount, composition, and thermodynamic stability of austenite that can be precipitated during secondary hardening treatment, and models for the composition dependence of the austenite and martensite lattice parameters can allow prediction of alloy compositions for increased transformation dilatation for enhanced toughening.

Our best example of an interdisciplinary approach to a structure/property relation involving collaboration of metallurgy, mechanics, and quantum physics explores the ultimate electronic origin of intergranular cohesion underlying the hydrogen resistance of ultrahigh strength steels. Intergranular hydrogen stress corrosion in these steels is invariably associated with prior interfacial segregation of impurities which reduce intergranular cohesion (17). Modelling the thermodynamics and mechanics of the competition between crack-tip blunting and brittle interfacial separation has predicted a correlation between the embrittling potency of a segregant (including hydrogen) and the difference between the free energy of segregation to grain boundaries and free surfaces, consistent with available data (18). The resulting thermodynamic description of embrittlement gives a well defined physics problem being addressed by total energy electronic calculations employing suitable models of grain boundary and free surface atomic structures (9,19,20). While these calculations are only now revealing features of electronic structures which correlate with the thermodynamic quantities underlying embrittlement, and have yet to reveal new principles of interfacial cohesion enhancement, the approach introduces materials students to the capabilities of total electronic calculations, illustrates the manner in which materials-related problems can be formulated to be addressed by allied disciplines, and emphasizes the effectiveness of thermodynamics as a medium of communication across disciplines.

A more direct means of applying thermodynamics to the improvement of hydrogen resistance, while providing an example of composition design for optimal process interactions, is the design of novel gettering compounds to remove embrittling residual impurities such as phosphorus from grain boundaries (21). A thermodynamic survey identified lanthanum phosphate as potentially the most stable gettering phase for phosphorus in steels, and further calculations indicated the metastable phase could be accessible at high melt undercooling achievable by rapid solidification. Preliminary rapid solidification experiments performed on a simple NiMo steel confirmed formation of such a phase and revealed a major improvement in hydrogen stress corrosion resistance as represented by K_{ISCC}. The fine coarsening resistant dispersion of the stable compound further provides stable grain refinement at relatively high solution treatment temperatures.

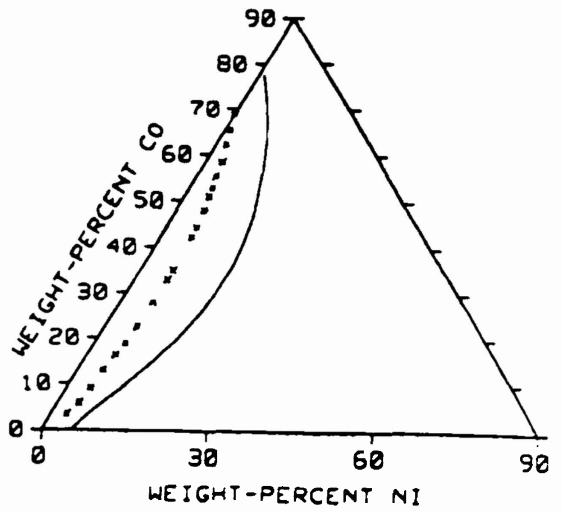


Figure 5: Composition diagram for 12Cr-1Mo-0.3C steels representing Co and Ni contents giving equal FCC and BCC free energies at T_o = 940K. Solid line is equilibrium FCC/FCC+BCC phase boundary (22).

Class Project: Design of a Stainless Bearing Steel

From the viewpoint of undergraduate materials students, research examples just cited serve to not only convey an important sense of the nature of interdisciplinary research for purposeful modelling, but many of the final outputs of these activities are expressible in terms of undergraduate thermodynamics and kinetics, yielding principles compatible with the available tools of the ThermoCalc system. These then provided the basis for student design projects, the most intricate example of which was a team project directed at a stainless bearing steel for the Space Shuttle Main Engine (SSME) turbopumps (22).

Mechanical property objectives adopted for this demanding application of a martensitic stainless steel were a minimum hardness level of R_c60 for wear and fatigue resistance, with a doubling of K_{IC} and K_{ISCC} relative to the 440C alloy steel currently employed, in order to achieve the desired level of reliability. Applying the approach represented in Figures 2 and 3, composition was first constrained by available knowledge (17) of alloying effects on intergranular cohesion (primarily excluding Mn and Si) and compatibility with rapid solidification and lanthanum treatment for impurity gettering and stable grain refinement. Matrix composition was then constrained to include 12Cr for stainless properties. Applying an Orowan strengthening analysis to available dispersion hardening data from experimental high-Co secondary hardening steels, (9), a minimum carbon level of 0.30 wt.pct. was estimated to achieve the desired R_c60 hardness in this class of alloy. A rough initial estimate of Mo content of 1.0 wt.pct. was then adopted, based on previous results such as those of Figure 4.

At this point, an approximate constraint was introduced to maintain a sufficiently high martensitic transformations temperature (Ms) to achieve the desired lath martensitic microstructure. Lacking suitable martensitic kinetic parameters for the high alloy range of interest, the FCC-BCC To partitionless equilibrium temperature was set equal to that of AF1410 steel (940K). This then defined the range of alloy Ni and Co contents represented by the X-curve in Figure 5. A unique Ni and Co content along this line was then selected by consideration of the amount and stability of austenite that could precipitate at secondary hardening temperatures near 500C for subsequent transformation toughening in service at and below room temperature. Stability was assessed by the FCC-BCC free energy difference at room temperature and set slightly higher than the optimally stable dispersed austenite studied in AF1410. This stability level could be achieved with a total austenite amount of 20 pct. A secondary objective was to maintain a high Ni content in the BCC matrix for cleavage resistance.

Optimization of carbide forming elements was then examined employing driving force calculations like those of Figure 4, holding Cr at 12 wt.pct. and varying Mo and V. For this high Cr content the M_6C driving force was easily maintained below the critical level of Figure 4. The driving force for $M_{23}C_6$ was

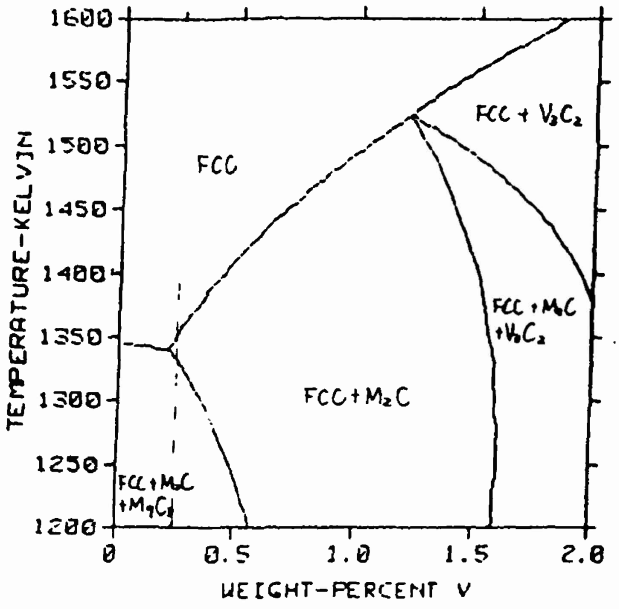


Figure 6: Phase diagram section vs. V content for Fe-30Co-12Cr-6Ni-0.3Mo-0.3C (22).

significantly higher but corresponding experimental information regarding embrittlement behavior associated with this carbide is currently lacking, thus identifying a need for further experiment. In this range of composition, the coherent thermodynamic model prediction of the driving force for the desired coherent M_2C was rather insensitive to Mo content, but strongly increased with V as desired for partide size refinement for efficient strengthening. Maintaining a Mo level of 0.3 wt.pct. to provide pitting corrosion resistance, the V level was then set by considering solution treatment requirements defined by the computed phase diagram section of Figure 6. A selected level of 0.25 wt.pct. corresponds to the onset of a steep rise in solution temperature with further increase of V. The final alloy composition thus defined can be solution treated at 1100C where the grain refining dispersions formed by rapid solidification should remain quite stable.

By this sequence of thermodynamic calculations, a unique 7-component alloy composition has been defined which is predicted to be thermodynamically capable of generating the desired set of microstructural features defined in Figure 2 under fairly well prescribed conditions of solidification, solution treatment, and tempering. Following a second iteration of the calculational sequence for improved self consistency, a prototype of such an alloy has been prepared and is currently being evaluated under NASA sponsorship.

Closure

A systems approach to materials design has been outlined based on general principles of systems engineering. Employing quantitative relations developed from ongoing research on ultrahigh-strength steels, the feasibility of computer-aided thermodynamics-based design of alloy compositions capable of achieving prescribed microstructural objectives under specified processing conditions has been demonstrated with the conceptual design of a stainless bearing steel uniquely combining a set of phenomena with high potential for substantial property improvements.

It is noteworthy that, while the ongoing research program made a materials design course possible, the scheduling of the course greatly catalyzed the process of integrating results within a well-defined design approach, and profoundly altered the direction of the research program. The first complete materials design exercises occurred in fact in the class projects. This synergism between teaching and research provided an exhilarating experience for all who participated in it.

Acknowledgments

Professor Morris Fine's enthusiasm for materials design, steel research, and the bridging of teaching and research have been a great inspiration since the author's arrival to the stimulating environment of Northwestern University. The author is also grateful to Professors W. J. Hopp, C. W. N. Thompson, and G. V. Rath of Northwestern for helpful discussions and provision of useful text materials on systems engir ring. The Steel Research Group program is spon. red by NASA, ONR, DOE, ARO, AFOSR, and NSF with industrial fellowship support.

References

1. Materials Design, Northwestern University course MSc-C95, Spring Quarter, 1989.

2. G.M. Jenkins, "The Systems Approach," in Systems Behavior, ed. J. Beishon and G. Peters, Open University Press, 1972.

3. M.F. Ashby, "Materials Selection in Conceptual Design," in Ashby Symposium on Materials Design ed. D. Embury, ASM, Metals Park, Ohio (1989).

4. B. Sundman, B. Jansson, and J.O. Andersson, CALPHAD, 9 (1985) 153.

5. C.S. Smith, A Search for Structure, MIT Press, Cambridge, MA, 1981.

6. M. Cohen, "Unknowables in the Essence of Materials Science and Engineering," Mat. Sci. and Eng. 25 (1976) 3.

7. M. Cohen, "Metallurgy and the Evolution of Materials Science and Engineering," in Innovations in Ultrahigh-Strength Steel Technology, ed. G.B. Olson, M. Azrin, and E.S. Wright, Sagamore Army Materials Research Conference Proceedings: 34th (1987) p. 67.

8. G.B. Olson, "New Steels By Design," J. Materials Ed., in press.

9. G.B. Olson, in Innovations in Ultrahigh-Strength Steel Technology, ed. G.B. Olson, M. Azrin, and E.S. Wright, Sagamore Army Materials Research Conference Proceedings: 34th (1987) p. 3.

10. G.L. Krasko and G.B. Olson, in Innovations in Ultrahigh-Strength Steel Technology, ed. G.B. Olson, M. Azrin, and E.S. Wright, Sagamore Army Materials Research Conference Proceedings: 34th (1987) p.677.

11. G.R. Speich, in Innovations in Ultrahigh-Strength Steel Technology, ed. G.B. Olson, M. Azrin, and E.S. Wright, Sagamore Army Materials Research Conference Proceedings: 34th (1987) p. 89.

12. R. Wagner and R. Kampmann, in Innovations in Ultrahigh-Strength Steel Technology, ed. G.B. Olson, M. Azrin, and E.S. Wright, Sagamore Army Materials Research Conference Proceedings: 34th (1987) p. 209.

13. G. Ghosh and G.B. Olson, Northwestern University, research in progress.

14. R. Hemphill, Carpenter Steel alloy AerMet100, patent pending.

15. A. Needleman, in Innovations in Ultrahigh-Strength Steel Technology, ed. G.B. Olson, M. Azrin, and E.S. Wright, Sagamore Army Materials Research Conference Proceedings: 34th (1987) p. 331.

16. G.N. Haidemenopoulos, G.B. Olson, and M. Cohen, in Innovations in Ultrahigh-Strength Steel Technology, ed. G.B. Olson, M. Azrin, and E.S. Wright, Sagamore Army Materials Research Conference Proceedings: 34th (1987) p.549.

17. C.J. MacMahon, Jr., in Innovations in Ultrahigh-Strength Steel Technology, ed. G.B. Olson, M. Azrin, and E.S. Wright, Sagamore Army Materials Research Conference Proceedings: 34th (1987) p. 597.

18. P.M. Anderson, J.S. Wang, and J. R. Rice, in Innovations in Ultrahigh-Strength Steel Technology, ed. G.B. Olson, M. Azrin, and E.S. Wright, Sagamore Army Materials Research Conference Proceedings: 34th (1987) p. 619.

19. G.L. Krasko, C. Li, R. Wu, A.J. Freeman, and G.B. Olson, research in progress.

20. M.E. Eberhart and J. M. MacLaren in Innovations in Ultrahigh-Strength Steel Technology, ed. G.B. Olson, M. Azrin, and E.S. Wright, Sagamore Army Materials Research Conference Proceedings: 34th (1987) p. 693.

21. J.F. Watton, G.B. Olson, and M. Cohen, in Innovations in Ultrahigh-Strength Steel Technology, ed. G.B. Olson, M. Azrin, and E.S. Wright, Sagamore Army Materials Research Conference Proceedings: 34th (1987) p. 705.

22. A. Bilyk, T. Chen, N. Akaiwa, H. Eguchi, and G.B. Olson, Northwestern University 750-C95 Materials Design Class Project Report, June 1989.

Solute Distribution Around a Coherent Precipitate in a Multicomponent Alloy

APPENDIX D

K.C. KING, P.W. VOORHEES, G.B. OLSON, and T. MURA

The open system elastic constants for a multicomponent alloy are derived and used to determine the equilibrium solute concentration profile surrounding an isolated coherent M_2C carbide precipitate with a transformation strain with three unequal eigenstrains in an elastically anisotropic AF1410 steel. The open system bulk modulus was found to vary with stress in this alloy, indicating that the chemical thermodynamics of AF1410 in an open system can result in the material becoming nonlinearly elastic. However, the open system shear moduli are identical to their usual constant composition values as a result of the cubic symmetry of the solute expansion tensor. We find that the nonuniform stress field surrounding the misfitting precipitate will induce significant nonuniformities in the concentration of the chemical components in this alloy. At certain positions in the matrix, the change in the concentration of Cr and Mo due to the elastic stresses, relative to their average concentrations in the alloy, can be as large as 100 to 250 pct. Although the solute redistribution reduces the matrix effective bulk modulus by 12 pct, the coherent carbide elastic self-energy is reduced by only 0.45 pct, reflecting a large contribution of shear distortions to the elastic self-energy, which are relatively unaffected by the dilating solutes.

I. INTRODUCTION

STRESS fields induced by material defects can influence the equilibrium distribution of solute in crystalline solids. For example, nonuniform distributions of solute atoms are possible in the vicinity of a dislocation[1,2,3] and inclusions.[4,5] Enhancement of the concentration of impurities can have major effects on materials properties; for example, increased solute concentration can initiate the growth of a void[6] and increase the corrosion rate of an alloy.[7]

To obtain the equilibrium solute concentration field in a nonuniformly stressed crystalline solid, both the chemical and mechanical equilibrium conditions must be satisfied at all points in the system. These equilibrium conditions require that in addition to the diffusion potential being uniform throughout the system,[8] the stress induced by the nonuniform solute distribution should be accounted for in a self-consistent fashion. Although it is possible to modify the constitutive law to relate the stress to the concentration to account for this stress, Larché and Cahn found that this approach does not necessarily yield thermodynamically self-consistent solute concentration fields.

Larché and Cahn further found that it was possible to determine the equilibrium solute concentration field in a stressed crystalline solid in a simple manner through the use of "open system" elastic constants.[8] The idea is to modify the usual elastic constants, which are measured at constant composition, to account for both the stress induced by the nonuniform solute field and the effect this redistribution has on the chemical thermodynamics of the system. Thus, the stresses are determined in the usual fashion *via* linear elasticity, using the open system elastic constants instead of the usual elastic constants.

Larché and Cahn have employed this approach to determine the solute distributions in a binary alloy surrounding dislocations[8,9] in the linear elastic approximation and concentration fields in uniaxially stressed nonlinearly elastic solids.[10] Johnson and Voorhees[11] determined the concentration profiles surrounding two elastically interacting uniformly dilating precipitates in a binary alloy using the open system elastic constant approach. They found that elastic stress induced by those precipitates can induce a significant nonuniform solute concentration.

Once the elastic stress has been determined, the composition field follows at once by requiring that the diffusion potential be constant throughout the system.[8] Since the diffusion potential is related to the usual chemical potentials of the chemical components in the alloy (measured in the absence of stress) and the calculated stress at a point in the solid, it is possible to use existing thermodynamic databases to determine the solute concentration field without performing any other experiments and with no adjustable parameters.

In contrast to the extensive work on binary alloys, the effects of elastic stress on the equilibrium solute distribution in a multicomponent alloy has received little attention. For example, the form of the open system elastic constants in a multicomponent alloy is not known. In addition, the diffusion potential approach has not been used to determine the equilibrium solute distribution in a multicomponent alloy.

Here we extend the Larché and Cahn[8] open system elastic constants and diffusion potential approach to multicomponent alloys and apply it to the more general case of a coherent system involving three unequal eigenstrains. We chose as our example the multicomponent secondary hardening alloy steel AF1410 which has

K.C. KING, Research Associate, P.W. VOORHEES, Associate Professor, and G.B. OLSON, Professor, Department of Materials Science and Engineering, and T. MURA, Professor, Department of Civil Engineering, are with Northwestern University, Evanston, IL 60208.

Manuscript submitted November 26, 1990.

been the subject of an extensive theoretical and experimental investigation aimed at the principles for design of a new class of ultrahigh-strength steels.[12] In this effort, the control of thermodynamic driving forces for coherent precipitation is crucial to the desired refinement of carbide dispersions for efficient strengthening. The stress in this case is generated by a coherent ellipsoidal M_2C carbide precipitate which has different elastic constants from the matrix. The eigenstrain method was used to calculate the stress field. The composition field in the matrix surrounding the precipitate was then determined using available thermochemical data from the Thermocalc alloy database.[13]

II. THEORY

A. *Thermodynamics*

Here the thermodynamic relationships necessary to couple the elastic stress and the equilibrium composition fields in a multicomponent alloy are derived. We extend the approach used by Larché and Cahn[10] for a binary substitutional alloy to a multicomponent alloy.

The matrix is in equilibrium when the diffusion potential, $M_{IK} = M_{IK}(\boldsymbol{\rho}, T_{kl})$, and temperature are constant, where $\boldsymbol{\rho} = \rho_1, \ldots, \rho_{K-1}, \rho_{K+1}, \ldots, \rho_N$ and ρ_J is the molar density of chemical component J measured per unit volume of the reference or stress-free state, T_{kl} is the stress tensor, and N is the total number of chemical components, of which $(1, \ldots, K-1)$ are interstitial components and $(K+1, \ldots, N)$ are substitutional components. The molar density of the Kth substitutional component is not an independent variable in the diffusion potential, since in the absence of any vacancies, the sum of the molar densities of each number of substitutional components must be equal to a constant, ρ_0, the molar density of lattice points in the system in the reference state for strain. The molar density of vacancies can be included explicitly, but here we choose to neglect vacancies as they are normally in sufficiently low concentrations to negligibly effect the equilibrium thermodynamics. The diffusion potential is different from the usual chemical potential in that it is a function of both the composition of the alloy and stress. Thus, if the elastic stress is a function of position in the matrix and since M_{IK} must be a constant at equilibrium, this implies that the composition must also be a function of position. We will assume that the temperature is constant.

The stress-free matrix will be taken as the reference state for strain. Consistent with this choice, all changes in composition will be measured with respect to this state. The independent variables will be taken to be the stress components T_{kl} and molar densities of all of the chemical components, except component K. Hence, the total strain E_{ij} and the diffusion potential M_{IK} can be expressed as a function of these variables as follows:

$$E_{ij} = E_{ij}(\boldsymbol{\rho}, T_{kl}) \qquad [1]$$

$$M_{IK} = M_{IK}(\boldsymbol{\rho}, T_{kl}) \qquad [2]$$

The total differentials of E_{ij} and M_{IK} are

$$dE_{ij} = \left.\frac{\partial E_{ij}}{\partial T_{kl}}\right|_{\rho} dT_{kl} + \sum_{I} \left.\frac{\partial E_{ij}}{\partial \rho_I}\right|_{T_{kl},\rho} d\rho_I \qquad [3]$$

$$dM_{IK} = \left.\frac{\partial M_{IK}}{\partial T_{kl}}\right|_{\rho} dT_{kl} + \sum_{J} \left.\frac{\partial M_{IK}}{\partial \rho_J}\right|_{T_{kl},\rho} d\rho_J \qquad [4]$$

where the subscript ρ denotes that all of the other independent molar densities of each component are held constant, except that component used in the partial derivatives, and the summations in the above and in the following are defined as, for example,

$$\sum_{J} \equiv \sum_{\substack{J=1 \\ J \neq K}}^{N} \qquad [5]$$

The dependence of the diffusion potential M_{IK} on stress T_{kl} can be expressed in terms of a Maxwell relation as[18]:

$$\left.\frac{\partial M_{IK}}{\partial T_{kl}}\right|_{\rho} = -\left.\frac{\partial E_{kl}}{\partial \rho_I}\right|_{T_{kl},\rho} \qquad [6]$$

Substituting Eq. [6] into Eq. [4], we obtain

$$\sum_{J} \left.\frac{\partial M_{IK}}{\partial \rho_J}\right|_{T_{kl},\rho} d\rho_J = dM_{IK} + \left.\frac{\partial E_{kl}}{\partial \rho_I}\right|_{T_{kl},\rho} dT_{kl} \qquad [7]$$

Equation [7] is a linear system of equations of the order $(N-1)$, and thus, $d\rho_J$ can be found using Cramer's rule as follows:

$$d\rho_J = \frac{1}{J_\rho} \sum_{n} \left[dM_{nK} + \left.\frac{\partial E_{kl}}{\partial \rho_n}\right|_{T_{kl},\rho} dT_{kl} \right] A_{nJ} \qquad [8]$$

where J_ρ is the Jacobian,

$$J_\rho = \frac{\partial(M_{1K}, \ldots, M_{(K-1)K}, M_{(K+1)K}, \ldots, M_{NK})}{\partial(\rho_1, \ldots, \rho_{(K-1)}, \rho_{(K+1)}, \ldots, \rho_N)} \qquad [9]$$

and A_{nJ} is the cofactor found by eliminating the nth row and Jth column of the matrix and calculating the determinant:

$$\begin{bmatrix} \frac{\partial M_{1K}}{\partial \rho_{(1)}} & \cdots & \frac{\partial M_{1K}}{\partial \rho_{(K-1)}} & \frac{\partial M_{1K}}{\partial \rho_{(K+1)}} & \cdots & \frac{\partial M_{1K}}{\partial \rho_{(N)}} \\ \vdots & & & & & \\ \frac{\partial M_{(K-1)K}}{\partial \rho_{(1)}} & & & & & \\ \frac{\partial M_{(K+1)K}}{\partial \rho_{(1)}} & & & \ddots & & \vdots \\ \vdots & & & & & \\ \frac{\partial M_{NK}}{\partial \rho_{(1)}} & & & & \cdots & \frac{\partial M_{NK}}{\partial \rho_{(N)}} \end{bmatrix} \qquad [10]$$

The first term of the right-hand side of Eq. [8] is zero in the case we are considering, for the diffusion potential is constant throughout the system at equilibrium. Hence, Eq. [8] becomes

$$d\rho_J = \frac{1}{J_\rho} \sum_{n} \left[\left.\frac{\partial E_{kl}}{\partial \rho_n}\right|_{T_{kl},\rho} dT_{kl} \right] A_{nJ} \qquad [11]$$

Substituting Eq. [11] into Eq. [3], yields

$$dE_{ij} = \left\{ \left.\frac{\partial E_{ij}}{\partial T_{kl}}\right|_{\rho} + \frac{1}{J_\rho} \sum_l \sum_n \left.\frac{\partial E_{ij}}{\partial \rho_l}\right|_{T_{kl},\rho} \left.\frac{\partial E_{kl}}{\partial \rho_n}\right|_{T_{kl},\rho} A_{nl} \right\} dT_{kl} \quad [12]$$

The inverse of the constant composition isothermal elastic constant tensor, C^{-1}_{ijkl}, is defined as follows:

$$C^{-1}_{ijkl} \equiv \left.\frac{\partial E_{ij}}{\partial T_{kl}}\right|_{\rho} \quad [13]$$

Similarly, the inverse of the open system elastic constant tensor C^{o-1}_{ijkl} can be found from Eq. [12] as

$$C^{o-1}_{ijkl} \equiv \frac{1}{J_\rho} \sum_l \sum_n \eta^l_{ij} \eta^n_{kl} A_{nl} + C^{-1}_{ijkl} \quad [14]$$

where η^l_{ij} is the solute expansion coefficient for component l and is defined by

$$\eta^l_{ij} = \rho_0 \left.\frac{\partial E^c_{ij}}{\partial c_l}\right|_{T_{kl},\rho} \quad [15]$$

where E^c_{ij} is the strain due to a change in composition and c_l is the mole fraction of component l. For a system with cubic symmetry, we have

$$\eta^l_{ij} = \eta^l \delta_{ij} \quad [16]$$

Under these conditions, only the diagonal components of C^{o-1}_{ijkl} are altered in an open system, since

$$C^{o-1}_{ijkl} \equiv \left[\frac{1}{J_\rho} \sum_l \sum_n \eta^l \eta^n A_{nl} \right] \delta_{ij}\delta_{kl} + C^{-1}_{ijkl} \quad [17]$$

Although the general expression for the open system elastic constants, Eq. [14], in a multicomponent alloy differs from that found by Larché and Cahn[9], we are now in agreement that Eq. [14] is correct.[14] The elastic constants C_{ijkl} are measurable for a wide variety of systems. Thus, the open system elastic constants C^o_{ijkl} can be calculated once the dependence of M_{lK} on composition is determined. The derivatives appearing in Eqs. [9] and [10] can be evaluated at any particular composition and stress. The open system elastic constants evaluated in the reference state, *i.e.*, the stress-free state, are used in the following elasticity calculations.

In order to calculate the solute distribution around the precipitate, it is necessary to determine the dependence of the diffusion potential on concentration and stress. Here, the Maxwell relation, Eq. [6], is integrated with respect to T_{kl} while holding ρ constant to obtain

$$M_{lK}(\rho, 0) = M_{lK}(\rho, T_{kl}) + \eta^l_{ij} T_{ij} \quad [18]$$

where repeated subscripts imply summation from 1 to 3.

The diffusion potential in the absence of stress is given by[18]

$$M_{lK}(\rho, 0) = \rho_0(\mu_l(\mathbf{c}) - \mu_K(\mathbf{c})) \quad [19]$$

for substitutional components and by

$$M_{lK}(\rho, 0) = \rho_0 \mu_l(\mathbf{c}) \quad [20]$$

for interstitial components, where, $\mathbf{c} = c_1, \ldots, c_{K-1}, c_{K+1}, \ldots, c_N$, c_J is the molar fraction of component J and c_J and ρ_J are related as follows:

$$\rho_J = \rho_0 c_J \quad [21]$$

Since the diffusion potential has to be constant throughout the matrix to insure thermodynamic equilibrium and we assume that the system is open thermodynamically, *i.e.*, the diffusion potential is fixed at its reference state value of zero stress and molar densities $\bar{\rho}$, the diffusion potential in the reference state must be equal to the diffusion potential at some stress and concentration

$$M_{lK}(\rho, T_{kl}) = M_{lK}(\bar{\rho}, 0) \quad [22]$$

Equation [22] is substituted into Eq. [18] to yield

$$M_{lK}(\rho, 0) = M_{lK}(\bar{\rho}, 0) + \eta^l_{ij} T_{ij} \quad [23]$$

Using the expressions for the relationship between the diffusion potential in the absence of stress and the chemical potential, we obtain the equations which need to be solved to determine the concentration field in a nonuniformly stressed multicomponent alloy,

$$\mu_l(\mathbf{c}) - \mu_K(\mathbf{c}) = \mu_l(\bar{\mathbf{c}}) - \mu_K(\bar{\mathbf{c}}) + \eta^l_{ij} T_{ij}/\rho_0 \quad [24]$$

for substitutional components and

$$\mu_l(\mathbf{c}) = \mu_l(\bar{\mathbf{c}}) + \eta^l_{ij} T_{ij}/\rho_0 \quad [25]$$

for interstitial components. Here, $\bar{\mathbf{c}}$ denotes the reference state molar fraction. In a crystal with cubic symmetry, $\eta^l_{ij} = \eta^l \delta_{ij}$ for substitutional solutes, and thus, Eqs. [24] becomes

$$\mu_l(\mathbf{c}) - \mu_K(\mathbf{c}) = \mu_l(\bar{\mathbf{c}}) - \mu_K(\bar{\mathbf{c}}) + \eta^l T_{kk}/\rho_0 \quad [26]$$

If we similarly assume the interstitial solutes produce isotropic dilatations, Eq. [25] becomes

$$\mu_l(\mathbf{c}) = \mu_l(\bar{\mathbf{c}}) + \eta^l T_{kk}/\rho_0 \quad [27]$$

In such cases, the concentration couples only to the hydrostatic component of the stress tensor.

Equations [24] and [25], which determine the concentration of the substitutional components, constitute $N - 1$ nonlinear equations in the $N - 1$ unknown concentrations. They can be solved numerically for a given magnitude of the stress.

A linearized solution can be obtained by taking a first-order Taylor's series expansion of the stress-free diffusion potentials about the reference state compositions $\bar{c}$, *i.e.*,

$$M_{lK}(\rho, 0) = M_{lK}(\bar{\rho}, 0) + \rho_0 \sum_J \left.\frac{\partial M_{lK}}{\partial \rho_J}\right|_{\rho} \Delta c_J \quad [28]$$

where

$$\Delta c_J = c_J - \bar{c}_J$$

The linearized relation that expresses the change in concentration due to stress is obtained by substituting Eq. [28] into Eq. [23] and using Cramer's rule to obtain

$$\Delta c_J = \frac{1}{J_\rho} \left\{ \frac{1}{\rho_0} \sum_l \eta^l_{ij} A_{lJ} \right\} T_{ij} \quad [29]$$

Where $\eta^l_{ij} = \eta^l \delta_{ij}$, we have

$$\Delta c_J = \frac{1}{J_\rho} \left\{ \frac{1}{\rho_0} \sum_l \eta^l A_{lJ} \right\} T_{kk} \quad [30]$$

and as before, only the hydrostatic component of the stress affects the composition field.

B. *Elastic Field Surrounding an Ellipsoidal Precipitate*

The stress field surrounding an inhomogeneous coherent precipitate in an elastically anisotropic system can be determined through the use of the eigenstrain method. Here, "inhomogeneous" means that the elastic constants inside the precipitate are different from those of the matrix, and "homogeneous" implies that the elastic constants are the same for both precipitate and matrix. We assume that the elastic constants inside the precipitate and the matrix are independent of position. As shown by Eshelby,[15] the elastic field surrounding an inhomogeneous ellipsoidal precipitate can be found by solving the corresponding homogeneous problem with equivalent eigenstrains. This procedure is discussed briefly below.

As shown by Mura,[16] the displacement field can be represented as

$$u_i(\mathbf{x}) = -\int_\Omega C_{jlmn}\varepsilon^p_{mn}(\mathbf{x}')G_{ij,l}(\mathbf{x}-\mathbf{x}')\,d\mathbf{x}' \quad [31]$$

where the Fourier transform of the Green's function $G_{ij}(\mathbf{x}-\mathbf{x}')$ is defined as

$$G_{ij}(\mathbf{x}-\mathbf{x}') = (2\pi)^{-3}\int_{-\infty}^{+\infty} N_{ji}(\xi)D^{-1}(\xi) \cdot \exp\left[i\xi\cdot(\mathbf{x}-\mathbf{x}')\right]d\xi \quad [32]$$

where

$$\int_{-\infty}^{+\infty} d\xi \equiv \int\int_{-\infty}^{+\infty}\int d\xi_1\,d\xi_2\,d\xi_3 \quad [33]$$

$$K_{ik}(\xi) = C_{ijkl}\xi_l\xi_j \quad [34]$$

and $N_{ji}(\xi)$ are the cofactors of the matrix $K_{ik}(\xi)$, and $D(\xi)$ is the determinant of the matrix $K_{ik}(\xi)$; ε^p_{mn} is the eigenstrain. The displacement gradients can be obtained by taking the derivative of Eq. [31] as

$$u_{i,j}(\mathbf{x}) = -\int_\Omega C_{klmn}\varepsilon^p_{mn}(\mathbf{x}')G_{ik,lj}(\mathbf{x}-\mathbf{x}')\,d\mathbf{x}' \quad [35]$$

The stress field can be obtained once the strain field is found. As noted first by Eshelby,[15] the stress and strain fields become uniform inside the precipitate if the eigenstrains are constant inside the ellipsoidal domain Ω. This is valid for both isotropic and anisotropic systems. Since the eigenstrains are constant, the linear relation between total strain ε_{ij} and eigenstrain inside the precipitate can be expressed as

$$\varepsilon_{ij} = S_{ijlk}\varepsilon^p_{kl} \quad [36]$$

where S_{ijlk} is the Eshelby's tensor (Eq. [41]).

The elastic field in the inhomogeneous case can be determined using the homogeneous case by replacing the eigenstrain ε^p_{mn} with the new eigenstrains ε^{**}_{mn}. The new eigenstrain ε^{**}_{mn}, which is defined as the sum of the eigenstrain ε^p_{mn} and the equivalent eigenstrain ε^*_{ij}, can be calculated from the following equations:[15]

$$C^o_{ijkl}(S_{klmn}\varepsilon^{**}_{mn} - \varepsilon^{**}_{kl}) = C^o_{ijkl}(S_{klmn}\varepsilon^{**}_{mn} - \varepsilon^p_{kl}) \quad [37]$$

where C^o_{ijkl} are open system elastic constants (for the matrix) derived in the previous section and C^p_{ijkl} are the elastic constants of the precipitate. The displacement gradient field can then be obtained by replacing ε^p_{mn} with ε^{**}_{mn} in Eq. [35]. The following transformations of variables are used to carry out the integration in Eq. [35]:

$$\frac{x_i}{a_i} = y_i$$

$$\frac{x'_i}{a_i} = y'_i \quad \text{(no summation)} \quad [38]$$

$$a_i\bar{\xi}_i = \zeta_i$$

where $2a_1$, $2a_2$, and $2a_3$ are the three principal lengths of the ellipsoidal inclusion Ω and the bars denote that the components of a vector are divided by the magnitude of the vector. After the integration is carried out,[17] the displacement gradients are

$$u^{in}_{i,j} = \frac{1}{4\pi}C^o_{pqmn}\varepsilon^{**}_{mn}\int_s \bar{\xi}_j\bar{\xi}_q N_{ip}(\bar{\xi})D^{-1}(\bar{\xi})\,dS(\bar{\zeta}) \quad [39]$$

$$u^{out}_{i,j} = \frac{1}{4\pi}C^o_{klmn}\varepsilon^{**}_{mn}\int_{s^*} N_{ik}(\bar{\xi})D^{-1}(\bar{\xi})\bar{\xi}_l\bar{\xi}_j\,ds(\bar{\zeta}) + \frac{1}{2\pi}\varepsilon^{**}_{mn}C^o_{klmn}\oint_{L^+}|\mathbf{y}|^{-1}N_{ik}(\bar{\xi})D^{-1}(\bar{\xi})\bar{\xi}_l\bar{\xi}_j\,d\theta(\bar{\zeta}) \quad [40]$$

Here, "in" refers to the interior of the inclusion and "out" refers to the exterior of the inclusion. The integration area S is the whole surface of the unit sphere in the ζ domain, and S^* is the subdomain of S, satisfying the condition

$$|\bar{\zeta}\cdot\mathbf{y}| < 1$$

L^+ is one of the lines which satisfies

$$|\bar{\zeta}\cdot\mathbf{y}| = 1$$

Eshelby's tensor can be obtained by comparing Eqs. [36] and [39] and using the definition of the total strain in terms of displacement gradients, as

$$S_{ijmn} = \frac{1}{8\pi}C^o_{pqmn}\int_s \{(\bar{\xi}_j\bar{\xi}_q N_{ip}(\bar{\xi}) + \bar{\xi}_i\bar{\xi}_q N_{jp}(\bar{\xi}))/D(\bar{\xi})\}\,dS(\bar{\zeta}) \quad [41]$$

Finally, the stress field can be determined as

$$T^{in}_{ij} = C^p_{ijkl}(S_{klmn}\varepsilon^{**}_{mn} - \varepsilon^p_{kl}) = C^o_{ijkl}(S_{klmn}\varepsilon^{**}_{mn} - \varepsilon^{**}_{kl}) \quad [42]$$

$$T^{out}_{ij} = C^o_{ijkl}u^{out}_{k,l} \quad [43]$$

The elastic self-energy per volume of the coherent particle can be computed as

$$\bar{W} = -\frac{1}{2}T^{in}_{ij}\varepsilon^p_{ij} \quad [44]$$

Employing the open system elastic constants accounts for the effect of solute redistribution on the elastic energy.

C. *Application to an Iron-Based Alloy*

We now apply the above relationships to determine the solute distribution surrounding a misfitting coherent precipitate in an iron-based alloy. The solute distribution surrounding the coherent precipitate is determined first by finding the appropriate open system elastic constants. These elastic constants are then used in the elasticity calculation to determine the stress field in the matrix. Finally, we assume an open system to determine the matrix concentration field. In this case, we insist that only the matrix phase be in thermodynamic equilibrium. Thus, the interface between the precipitate and matrix may not be in equilibrium for the assumed ellipsoidal shape of the precipitate.[5]

The particular iron-based alloy we consider is the secondary hardening AF1410 steel of weight percent composition Fe-14Co-10Ni-2Cr-1Mo-0.16C. The properties of the ellipsoidal precipitate are chosen to model a coherent hexagonal close-packed M_2C carbide under conditions of near completion of coherent precipitation corresponding to tempering of the alloy for 8 hours at 783 K. Based on electron microscopy observations, the precipitate is taken to be a prolate ellipsoid with an aspect ratio of 3, oriented along the direction of the minimum principal transformation strain. The precipitate is assumed to be elastically isotropic with a Young's modulus of $E = 2.5 \times 10^{11}\ N/m^2$ and an estimated Poisson's ratio of $\nu = 0.19$.[18] Based on lattice parameters determined by X-ray and electron diffraction, the misfit strains between the precipitate and matrix are $\varepsilon^p_{[1,0,0]} = 0.003484$, $\varepsilon^p_{[0,1,1]} = 0.1136$, and $\varepsilon^p_{[0,1,-1]} = 0.229$,[18] where the subscript denotes the direction of the eigenstrain referred to the body-centered cubic (bcc) ferrite matrix. The constant composition elastic constants used to determine the open system elastic constants of the matrix are assumed to be those of pure bcc iron with $C_{11} = 2.42 \times 10^{11}\ N/m^2$, $C_{12} = 1.465 \times 10^{11}\ N/m^2$, and $C_{44} = 1.12 \times 10^{11}\ N/m^2$. Because of the difference in elastic constants between the precipitate and matrix, the equivalent eigenstrains must be used for the elasticity calculation. The principal equivalent eigenstrains in this case are determined to be $\varepsilon^{**}_{[1,0,0]} = -0.0442$, $\varepsilon^{**}_{[0,1,1]} = 0.1277$, and $\varepsilon^{**}_{[0,-1,1]} = 0.2399$. In the stress-free state, the matrix is composed of Fe, Co, Cr, Mo, and Ni of the following mole fractions Co = 0.1395, Cr = 0.0136, Mo = 0.0006, Ni = 0.0997, and Fe = 0.7466 computed for incoherent ferrite-M_2C equilibrium at 783 K employing the Thermocalc database and software.[13] All of these components are substitutional and the mole fraction of Fe is chosen as the dependent variable (K). The interstitial C content of the matrix is taken to be negligible. The value of the solute expansion coefficients in the cubic material used are $\eta^{Co} = 0.017094$, $\eta^{Cr} = 0.04849$, $\eta^{Mo} = 0.12785$, and $\eta^{Ni} = 0.01828$.[18]

The open system elastic constants are determined using Eq. [17]. The derivatives of M_{IK} required to determine A_{IJ} and J_ρ can be calculated from the representation of μ_I used in the Thermo-calc alloy database, as shown in the Appendix. The parameters used to determine the coefficients in these expressions are listed in Tables I and II. We have chosen to evaluate A_{IJ} and J_ρ at zero stress, the reference state, to determine C^o_{ijkl} for use in the elasticity calculation. Thus, we evaluate these determinants at the bulk alloy composition. We have also evaluated the open system elastic constants at a nonzero stress in order to obtain some information on nonlinear elastic effects which result from the chemical thermodynamics of this particular alloy. In this case, the A_{IJ} and J_ρ are evaluated at the equilibrium matrix compositions at that chosen nonzero stress.

The stress field in the matrix surrounding the precipitate was calculated through Eq. [40] with the equivalent eigenstrains obtained from Eq. [37], using the C^o_{ijkl} of the reference state. Gauss-Legendre quadrature was used to numerically integrate Eqs. [40] and [41]. The difference between the components of the displacement gradient tensor on either side of the interface was compared with the analytical values[19] and found to be in good agreement. In addition, the value of $u_{i,j}$ was in good agreement with the analytical results for an isotropic spherical misfitting precipitate.[20]

The equilibrium matrix composition at a particular level of the trace of the stress was determined using Eqs. [26] and [27]. Since the composition is only related to the trace of the stress, a scalar, one can easily determine the equilibrium composition independent of the elasticity or open system elastic constant calculation by simply choosing various values of T_{kk} and then solving for concentration $\mathbf{c}$. The reference or stress-free matrix compositions were again used to define $\bar{\mathbf{c}}$. This implies that at an infinite distance from the precipitate, the value of the diffusion potential is fixed at $M_{IK}(\bar{\mathbf{c}})$. The representation of the stress-free chemical potentials used by the Thermo-calc database were again used to determine $M_{IK}(\bar{\mathbf{c}})$ and $M_{IK}(\mathbf{c})$. The resulting coupled nonlinear equations were solved using a Levenberg-Marquardt algorithm from the IMSL library.[21] The derivatives of M_{IK} with respect to $\mathbf{c}$ required for Eqs. [8] and [10] were determined by the expressions shown in the Appendix. By comparing the concentrations at a given value of the trace of the stress determined by Eq. [26] with those found from Eq. [27] , it is possible to determine the importance of the nonlinear relationship between T_{kk} and $\mathbf{c}$.

Since the equilibrium solute concentration at a particular T_{kk} has been determined and has been found using the open system elastic constants, the equilibrium solute distribution around the precipitate can now be determined by finding the alloy composition for each point

Table I. Thermo-calc Alloy Database—I

I	1 (Co)	2 (Cr)	3 (Mo)	4 (Ni)	5 (Fe)
${}^0G^\Phi_I$	-0.2538×10^{12}	-0.2125×10^{12}	-0.2239×10^{12}	-0.2461×10^{12}	-0.2043×10^{12}
β^0_I	0.1350×10^{1}	-0.8000×10^{-2}	0.2220×10^{1}	0.0	0.8500×10^{0}
T^0_I	0.1450×10^{4}	-0.3115×10^{3}	0.1043×10^{4}	0.0	0.5750×10^{3}

Table II. Thermo-calc Alloy Database—2

	J/I	1 (Co)	2 (Cr)	3 (Mo)	4 (Ni)	5 (Fe)
L^0_{IJ}	1	0.0	0.8856×10^{12}	-0.8987×10^{11}	0.0	0.2000×10^{11}
	2	0.0	0.0	0.1292×10^{12}	0.2266×10^{12}	0.1062×10^{12}
	3	0.0	0.0	0.0	0.2966×10^{12}	-0.1965×10^{11}
	4	0.0	0.0	0.0	0.0	0.4642×10^{12}
	5	0.0	0.0	0.0	0.0	0.0
L^1_{IJ}	1	0.0	-0.2010×10^{11}	0.0	0.0	0.0
	2	0.0	0.0	0.0	0.4073×10^{11}	0.1962×10^{12}
	3	0.0	0.0	0.0	-0.4844×10^{11}	0.2785×10^{10}
	4	0.0	0.0	0.0	0.0	0.0
	5	0.0	0.0	0.0	0.0	0.0
β^0_{IJ}	1	0.0	0.0	0.2413×10^{1}	0.0	0.4740×10^{0}
	2	0.0	0.0	-0.8500×10^{0}	0.0	0.4000×10^{1}
	3	0.0	0.0	0.0	0.0	0.0
	4	0.0	0.0	0.0	0.0	0.0
	5	0.0	0.0	0.0	0.0	0.0
β^1_{IJ}	1	0.0	0.0	0.2418×10^{0}	0.0	0.0
	2	0.0	0.0	0.0	0.0	0.0
	3	0.0	0.0	0.0	0.0	0.0
	4	0.0	0.0	0.0	0.0	0.0
	5	0.0	0.0	0.0	0.0	0.0
T^0_{IJ}	1	0.0	0.0	0.5900×10^{3}	0.0	0.5560×10^{3}
	2	0.0	0.0	0.1650×10^{4}	0.0	0.2373×10^{4}
	3	0.0	0.0	0.0	0.3350×10^{3}	0.0
	4	0.0	0.0	0.0	0.0	0.0
	5	0.0	0.0	0.0	0.0	0.0
T^1_{IJ}	1	0.0	0.0	0.0	0.0	0.0
	2	0.0	0.0	0.5500×10^{3}	0.0	-0.2880×10^{3}
	3	0.0	0.0	0.0	0.5260×10^{3}	0.6170×10^{3}
	4	0.0	0.0	0.0	0.0	0.0
	5	0.0	0.0	0.0	0.0	0.0

in the matrix corresponding to the value of T_{kk} at that point.

1. *Results*

Figure 1 shows the mole fraction of each component as a function of the trace of the stress. The dashed lines are the results of the linearized calculation, and the curved lines are the results of the nonlinear calculation. The trace of the stress has been chosen as the independent variable, since the concentration change is just related to the trace of the stress in this cubic material. The linearized solutions, which are based upon a Taylor's expansion about $T_{kk} = 0$, are tangent to the curved lines at the point $T_{kk} = 0$ for each chemical component, confirming the results of the nonlinear calculation. Figure 1 also shows that the equilibrium concentration of each component is increased by tensile stress. This is because η^I is positive for all of the components. These components expand the lattice, and thus, the equilibrium concentration can be enhanced by lattice expansion. For sufficiently large compressive stresses, contents of Cr and Mo based upon the linearized solution are negative, which is nonphysical. This is an artifact of the linearization process, for negative mole fractions are not predicted when the full nonlinear solution is used.

Figure 2(a) shows the open system elastic constants as a function of the trace of the stress. The constant composition elastic constants of bcc Fe are shown by the arrows. The open system elastic constants at zero stress, denoted by the closed circles, are those used in the elasticity calculations. Evident is a significant ~10 to 20 pct change in these zero stress elastic constants from the usual constant composition elastic constants. Also shown in Figure 2(a) is the dependence of the elastic constants on the magnitude of T_{kk}. Specifically, the equilibrium matrix compositions determined from the nonlinear calculation shown in Figure 1 at a particular level of T_{kk} were used to determine the A_{IJ} and J_ρ appearing in the expression for the open system elastic constants. Thus, one can determine the dependence of $C^{\sigma^{-1}}_{ijkl}$ on T_{kk}, which is solely a result of composition changes induced by a nonzero T_{kk}. Clearly evident is the nonlinear elastic behavior for large values of T_{kk}.

Shown in Figure 2(b) are the equivalent bulk modulus and shear moduli, where μ is the shear modulus along the (100) plane and μ' is the shear modulus for the (110) [1$\bar{1}$0] system. Evident in Figure 2(b) is that both shear moduli are independent of T_{kk} and equal to their constant composition values, whereas the bulk modulus changes with T_{kk} and, in the reference state, is reduced by 12.17 pct from its constant composition value. This is because the solute expansion tensors only have dilatational components.

Figures 3(a) through (c) illustrate contour plots for constant T_{kk} on planes normal to the principal axes, where

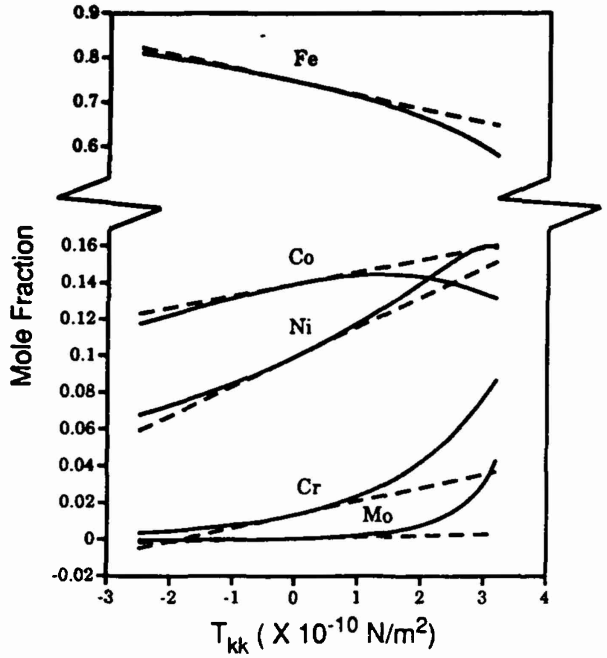
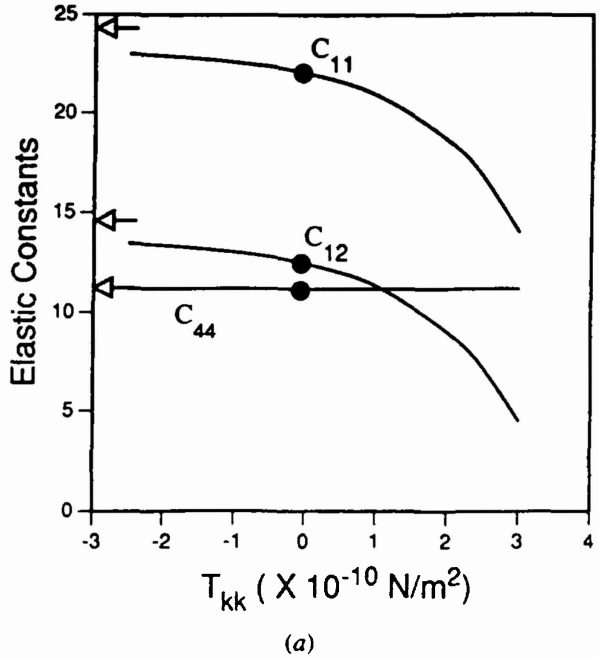
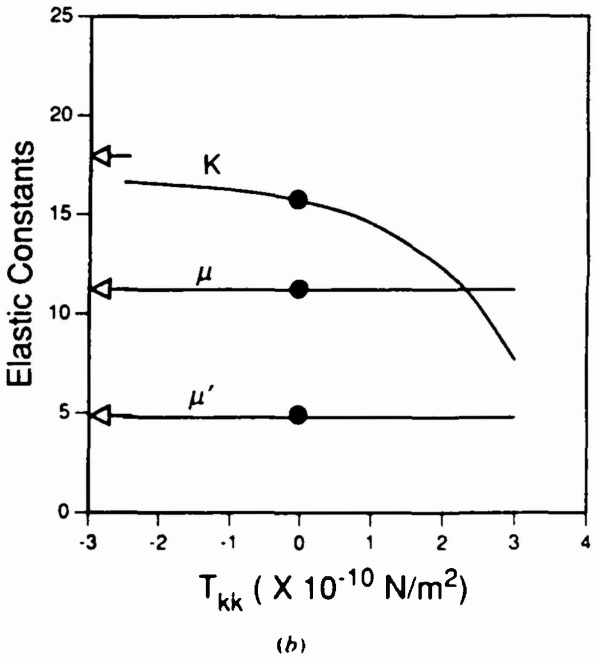


Fig. 1 — Mole fraction of each component *vs* the trace of the stress.



(*a*)



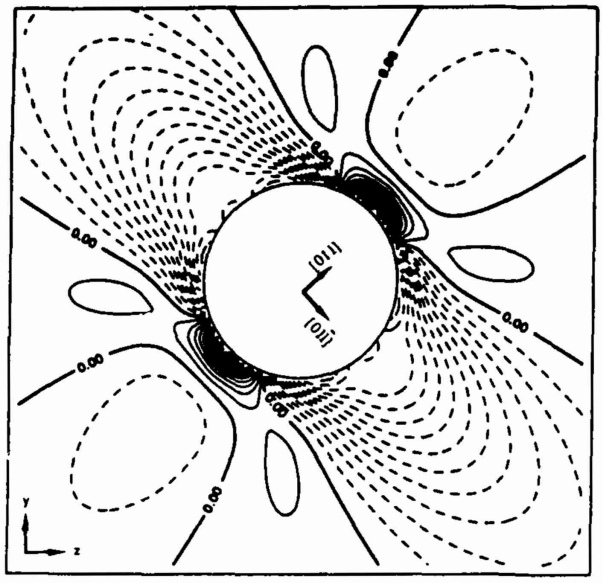
(*b*)

Fig. 2 — (*a*) Open system elastic constants *vs* the trace of the stress (alloy composition) The arrows represent the constant composition elastic constants and the solid circles represent the stress-free open system elastic constants — Voigt elastic constants (*b*) Open system elastic constants *vs* the trace of the stress (alloy composition) The arrows represent the constant composition elastic constants and the solid circles represent the stress-free open system elastic constants — Bulk modulus and shear modulus

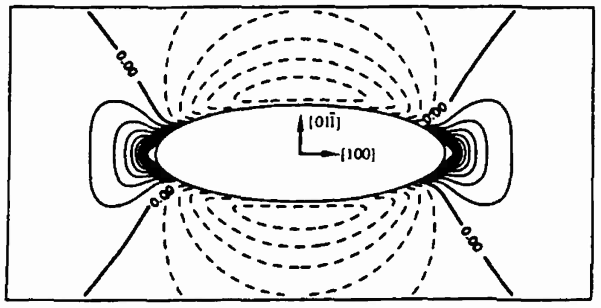
Figure 3(a) depicts the contours on the (100) plane (normal to the precipitate axis), Figure 3(b) depicts the contours on the (011) plane, and Figure 3(c) depicts the contours on the (01$\bar{1}$) plane. Solid lines in these figures represent the positive or tensile T_{kk}, and dotted lines represent the negative or compression T_{kk}. The bold lines in these figures are the nodal lines where $T_{kk} = 0$. The contour lines in Figure 3(a) are in intervals of 1.5×10^9 N/m^2, and the contour lines in Figures 3(b) and (c) are in intervals of 3×10^9 N/m^2. The elastic constants used for the elasticity calculation are the open system elastic constants at $T_{kk} = 0$, consisting of $C_{11} = 2.203 \times 10^{11}$ N/m^2, $C_{12} = 1.248 \times 10^{11}$ N/m^2 and $C_{44} = 1.12 \times 10^{11}$ N/m^2.

These T_{kk} contour lines in Figure 3 can be interpreted as the isoconcentration lines for each of the components. Within the linearized approximation, the change in the mole fraction of a particular component can be obtained by multiplying the trace of the stress T_{kk} by a factor $f_i = (1/\rho_0 J_e) \sim \eta' A_{jj}$ (Eq [30]). These factors are the slopes of the straight lines in Figure 1 and are $f_{Co} = 6.56 \times 10^{-14}$, $f_{Cr} = 7.33 \times 10^{-14}$, $f_{Mo} = 7.99 \times 10^{-15}$, $f_{Ni} = 1.62 \times 10^{-11}$, and $f_{Fe} = -3.09 \times 10^{-11}$. Thus, for example, for those elements for which $f > 0$, the solid lines represent regions of enhanced concentration, relative to the bulk alloy composition, and the dotted lines represent negative regions of depleted concentration. The mole fraction value for each contour line can then be obtained by the sum, $c_i + \Delta c_i$.

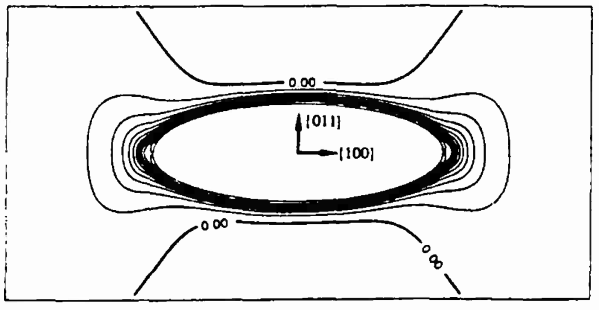
Figures 4(a) through (e) illustrate the change of the mole fraction for each of the components relative to its value in the unstressed matrix in different directions. In this case, the coordinate system is located at the center of the ellipsoid and distances are measured from the precipitate interface. Distances are scaled to the length of the minor axis of the ellipsoid. The concentration change of each element differs in different directions. For the solutes (Co, Cr, Mo, Ni), there exists a local maximum in the [100] direction near the interface and a local minimum in the [01$\bar{1}$] direction near the interface. In other



(*a*)



(*b*)



(*c*)

Fig. 3—(*a*) Contour lines for constant σ_{zz} on the (100) plane with intervals of 1.5×10^9 N/m^2. The bold lines depict the node lines where $\sigma_{zz} = 0$. (*b*) Contour lines for constant σ_{zz} on the (011) plane with intervals of 3×10^9 N/m^2. The bold lines depict the node lines where $\sigma_{zz} = 0$. (*c*) Contour lines for constant σ_{zz} on the (01$\bar{1}$) plane with intervals of 3×10^9 N/m^2. The bold lines depict the node lines where $\sigma_{zz} = 0$.

directions, local extrema still exist but not as close to the interface, and they are not as significant. It is easiest to locate these extreme points in the [010], [001], and [011] directions in Figure 3(a) by finding the closely spaced contours in these directions. For the iron, the change of the concentration is opposite to those for the solutes. Therefore, a depletion of Fe will occur in the regions with the enhanced solute concentration. The percentage change of the mole fraction of Mo is high in the vicinity of the precipitate; this is because the bulk mole fraction for Mo is relatively low and η is large. Finally, the change of concentration of all the elements approaches zero far from the precipitate. This agrees with the initial assumption that the stress and concentration field will have the reference state values at an infinite distance from the precipitate. Employing the open system elastic constants in a calculation of the coherent carbide elastic self-energy per volume gives an estimate of 3.576×10^9 J/m^3. This compares to a value of 3.592×10^9 J/m^3 when the normal constant composition elastic constants are employed.

IV. DISCUSSION

We have found that the presence of more than two chemical components in an alloy does not alter significantly the procedure used to determine the open system elastic constants from that used in a binary alloy. All of the data necessary to determine the open system elastic constants follow from measured thermodynamic and crystallographic properties of the alloy. The advantage of using the open system elastic constants is that the stress generated by the nonuniform concentration field does not have to be included explicitly in the elasticity calculation and that the stresses computed using the open system elastic constants are guaranteed to be consistent with the chemical thermodynamics of the alloy. Once the open system elastic constants are used to determine the stress field, the composition field follows in a very similar fashion as that in a binary alloy. The complications in finding the open system elastic constants and the equilibrium composition field in a multicomponent alloy lie mainly in the large thermodynamic database required to define the chemical potentials J_ρ and A_{nJ}.

In the alloy we have examined, the equilibrium concentration of each chemical component can be a strong function of the magnitude of the trace of the stress. There is no coupling to the shear components of the stress field, because the solute expansion tensor only has dilatational components. Figure 1 shows that at large values of the trace of the stress, the equilibrium concentration no longer varies linearly with stress. In fact, the equilibrium concentration of Co begins to decrease with increasing stress despite the positive solute expansion coefficient. Both of these effects are due to the nondilute, nonideal thermodynamics of the AF1410 alloy. The relationship between the equilibrium chemical concentration and magnitude of the trace of the stress shown in Figure 1 follows directly from the Maxwell relation (Eq. [6]). As a result, these calculations can be applied to an AF1410 alloy in any state of stress, which is consistent with the mechanical equilibrium equations. However, the state of stress must be determined using the open system elastic constants.

The open system elastic constant calculation indicates that at large levels of stress, the elastic constants will not be constant but will vary with the trace of the stress. The variation in the elastic constants with stress is due

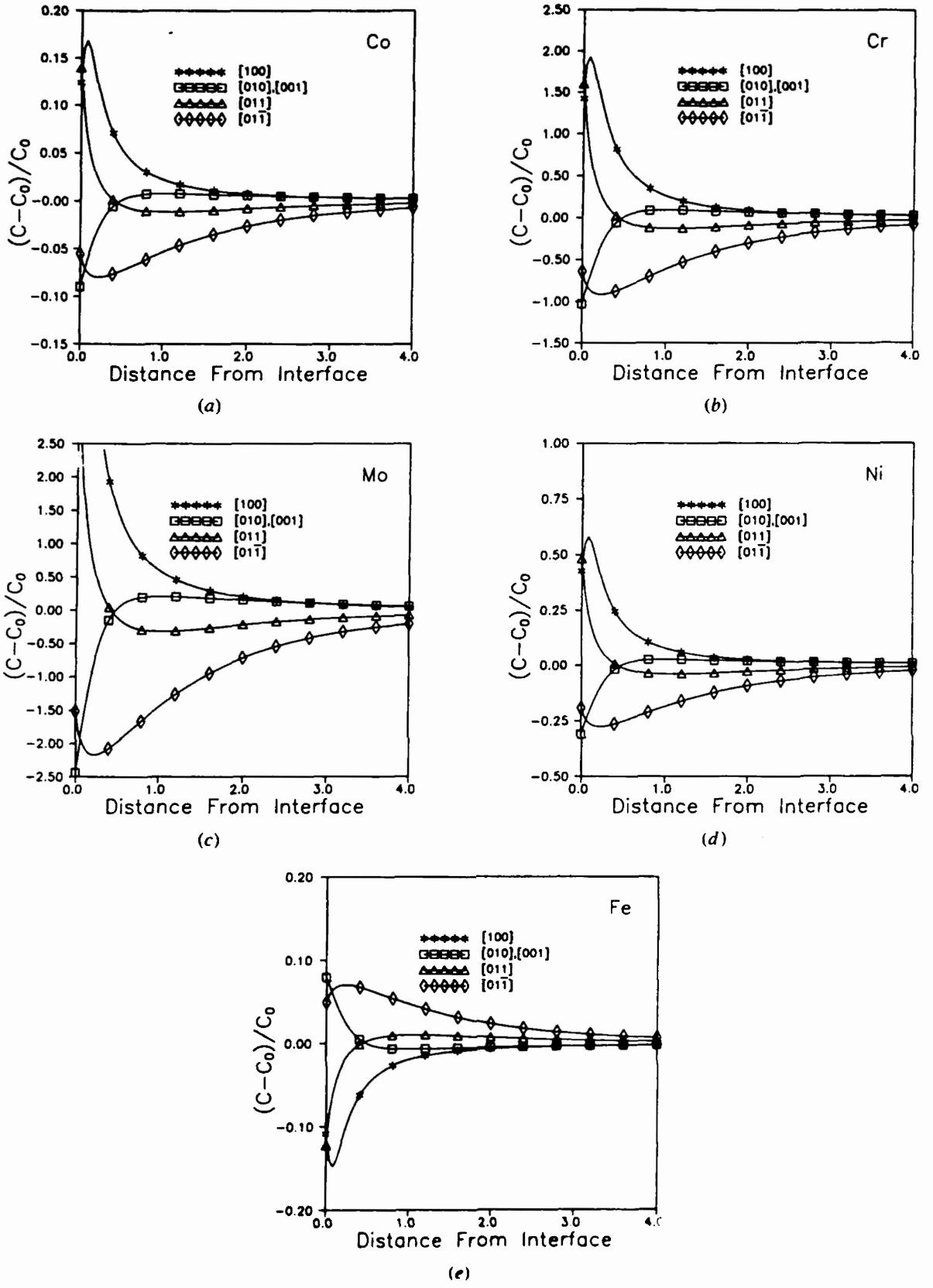


Fig. 4 — Relative change of (*a*) Co, (*b*) Cr, (*c*) Mo, (*d*) Ni, and (*e*) Fe in different directions from the precipitate. Distance, relative to the minor axis of the ellipsoid, is measured from the interface for each direction, oriented from the center of the ellipsoid.

solely to the composition dependence of J_c and A_{nJ} which appears in the expression for the open system elastic constants (Eq. [14]). This is because at equilibrium, J_c and A_{nJ} are implicit functions of the trace of the stress, since the trace of the stress and composition are related by the condition that the diffusion potential must be constant at equilibrium and, in an open system, have a specified value. Thus, Figures 2(a) and (b) were constructed by using the compositions at a given value of the trace of the stress shown in Figure 1 to evaluate J_c and A_{nJ}. The greatest change in the elastic constants is at large positive values of the trace of the stress where the equivalent bulk modulus decreases by about 50 pct from its value at zero stress. Therefore, the chemical thermodynamics can cause a material to become nonlinearly elastic at large but realistic values of the stresses in a commercially important multicomponent alloy. However, as noted by Larché and Cahn,[10] there are other factors which may also contribute to the nonlinear elastic behavior of the material which were not included in this calculation. These other factors are the usual constant composition higher order elastic constants and the composition dependence of both the solute expansion coefficient and the constant composition elastic constants. As the open system elastic constants evaluated at the stress-free state are used to determine the stresses surrounding the coherent precipitate, the decrease in the equivalent open system bulk modulus at high levels of stress implies that stresses we have calculated in the regions of large tensile stress are larger than the actual stresses expected in the material.

Figures 3(a) through (c) show the contours of constant T_{ii} on different planes. The principal eigenstrains are along [100], [011], and [01$\bar{1}$] directions. The principal equivalent eigenstrains in both [011] and [01$\bar{1}$] directions are the major eigenstrains, and both of them are positive. Therefore, the stress field far from the precipitate in these two directions is compressive (Figure 3(a)). However, it is clear that a narrow region of large tensile stress exists in the [011] direction near the interface. This is because the strength of the principal eigenstrain in the [01$\bar{1}$] direction is almost twice as large as that in the [011] direction and the expansion in the [01$\bar{1}$] direction results in the region of tensile stress in the [011] direction. The principal equivalent eigenstrain in the [100] direction is negative but quite small compared to the other principal eigenstrains. It follows that the stress field in the [100] direction is tensile (Figures 3(b) and (c)).

From the stress distribution surrounding the precipitate, the concentration profile can be determined by using either the full nonlinear solution to the diffusion potential condition, as shown in Figure 1, or the linearized solution (Eq. [30]) evaluated at zero stress. Since the trace of the stress is directly proportional to the change in concentration from its reference value in the linearized approximation, the traces of the stress fields shown in Figures 3(a) through (c) are identical to the equilibrium concentration fields. This is not the case with the full nonlinear solution to the equilibrium conditions shown in Figure 1. However, the full nonlinear solution relating to the equilibrium conditions cannot be used in this case, for in solving for the elastic field, we have assumed that the elastic constants are independent of stress, and consistent with this assumption, we can only use the linearized solution for the relationship between the trace of the stress and concentration. The difference between the linearized and nonlinear solutions is only of concern when large tensile stresses are present, for the concentrations predicted by the linear and nonlinear solutions are quite close for compressive stresses. Although the nonlinear solution cannot be employed with our linear elasticity calculations, it is helpful in determining the stresses at which nonlinear effects become important.

Figures 4(a) through (e) illustrate the fractional change of the mole fraction for each of the components in different directions. As mentioned earlier, the calculated stress field may be overestimated in the region of high tensile stress. Therefore, the concentrations in the region of large tensile stress may not be accurate. In the [01$\bar{1}$] direction, a significant local minimum for the solutes is found at a distance of 20 pct of the minor radius of the ellipsoid away from the interface. The solutes are strongly enhanced near the interface in the [100] and [011] directions, and depletion of the solutes is significant at the interface in [010] and [001] directions. All of the enhancement and depletion of the solutes are consistent with the tension and compression regions and follow from the factor f_i and the bulk concentration of the various elements. The percentage change of the mole fraction for Mo, more than 250 pct, stems from its low bulk concentration. Similar results are also discussed by Johnson and Voorhees for a binary alloy system.[11]

From an alloy design viewpoint, an important consequence of particle coherency is its influence on the thermodynamic driving force for precipitation. The important elastic energy contributions involved cannot be experimentally tested by direct measurement but must be inferred from resultant composition shifts which, for the extremely fine scale structures of interest here, require the highest resolution microanalytical techniques. The compositions of the carbides, which are ~3 nm in minor diameter in the AF1410 microstructure modeled here, have been directly measured by atom-probe field-ion microscopy, and preliminary plane-by-plane analysis of the adjacent matrix has indicated composition nonuniformity similar to that predicted here.[22] Further experiments are underway to more precisely test these important features of the thermodynamics of stressed solids.

The linear calculations performed here indicate that although the bulk modulus is reduced by 12.17 pct, the carbide elastic self-energy is reduced by only 0.45 pct as a consequence of solute redistribution. Apparently, a substantial portion of the elastic energy is contributed by shear distortions which are not greatly influenced by the solute dilatations.

V. CONCLUSIONS

On the basis of this work, we can conclude the following.

1. Open system elastic constants in multicomponent alloys can be used in much the same way as in binary

alloys to determine the thermodynamically self-consistent equilibrium stress field in a system with a nonzero solute expansion tensor.
2. At large but realistic positive values of the trace of the stress, the open system bulk modulus in a commercially important multicomponent alloy, AF1410, is a function of the trace of the stress, indicating that AF1410 can become nonlinearly elastic as a result of its chemical thermodynamics.
3. The open system shear moduli are identical to their constant composition values as a result of the cubic symmetry of the solute expansion tensors.
4. The elastic stresses surrounding an ellipsoidal precipitate in an elastically anisotropic medium can induce significant, and potentially measurable, nonuniformities in the equilibrium matrix concentration field.
5. The redistribution of matrix solute due to elastic stress provides a relatively modest decrease in the coherent carbide self-energy. This is attributable to a large shear distortion contribution to the self-energy which is insensitive to the purely dilatational solute expansion tensors of the solutes.

APPENDIX

The relation between chemical potential and Gibbs free energy can be expressed as

$$\mu_I = G_m^{\Phi} + \sum_{\substack{M=1 \\ M \neq K}}^{N} (\delta_{IM} - c_M) \frac{\partial G_m^{\Phi}}{\partial c_M}\bigg|_{c \neq c_M} \qquad [A1]$$

where the component K is assumed to be the dependent variable and δ_{IM} is the Kronecker delta, $\delta_{IM} = 1$ as $I = M$, otherwise $\delta_{IM} = 0$. The Gibbs free energy model in the Thermo-calc database is expressed as the sum of chemical and magnetic contributions:

$$G_m^{\Phi} = G_m^{\Phi,ch} + G_m^{\Phi,mo} \qquad [A2]$$

where

$$G_m^{\Phi,ch} = \sum_{I=1}^{N} c_I {}^0G_I^{\Phi} + RT \sum_{I=1}^{N} c_I \ln c_I + \sum_{I=1}^{N} \sum_{J=1}^{N} \{c_I c_J [L_{IJ}^0 + (c_I - c_J) L_{IJ}^1]\} \qquad [A3]$$

$$G_m^{\Phi,mo} = RT \ln (\beta + 1) f(\tau) \qquad [A4]$$

and with β, the magnetic moment, and T_c, the Curie temperature, expressed by

$$\beta = \sum_{I=1}^{N} c_I \beta_I^0 + \sum_{I=1}^{N} \sum_{J=1}^{N} \{c_I c_J [\beta_{IJ}^0 + (c_I - c_J) \beta_{IJ}^1]\} \qquad [A5]$$

$$T_c = \sum_{I=1}^{N} c_I T_I^0 + \sum_{I=1}^{N} \sum_{J=1}^{N} \{c_I c_J [T_{IJ}^0 + (c_I - c_J) T_{IJ}^1]\} \qquad [A6]$$

and

$$\tau = T/T_c \qquad [A7]$$

$$f(\tau) = -6.417 \times 10^{-2} \tau^{-5} - 2.037 \times 10^{-3} \tau^{-15} - 4.278 \times 10^{-4} \tau^{-25} \qquad [A8]$$

All the parameters in Eqs. [A3] through [A7] can be determined from the Thermo-calc database. For the alloy (Co,Cr,Mo,Ni,Fe) used in this work, the parameters are given in Tables I and II for $T = 783$ K.

In order to carry out the derivative in Eq. [A1], the following formulae are used:

$$\frac{\partial c_I}{\partial c_M} = \delta_{IM} \quad (\text{for } I \neq K) \qquad [A9]$$

$$\frac{\partial c_I}{\partial c_M} = -1 \quad (\text{for } I = K) \qquad [A10]$$

The following are the necessary derivatives to calculate the chemical potential in Eq. [A1]:

$$\frac{\partial}{\partial c_M}(G_m^{\Phi,ch}) = \sum_{\substack{I=1 \\ I \neq K}}^{N} \delta_{IM} {}^0G_I^{\Phi} + RT \sum_{\substack{I=1 \\ I \neq K}}^{N} (\delta_{IM} \ln c_I + \delta_{IM}) - {}^0G_K^{\Phi} - RT(\ln c_K + 1) + \sum_{\substack{I=1 \\ I \neq K}}^{N} \sum_{\substack{J=1 \\ J \neq K}}^{N} [L_{IJ}^0 (c_J \delta_{IM} + c_I \delta_{JM}) + 2 L_{IJ}^1 c_I c_J (\delta_{IM} - \delta_{JM}) + L_{IJ}^1 (c_I^2 \delta_{JM} - c_J^2 \delta_{IM})] + \sum_{\substack{I=1 \\ I \neq K}}^{N} \{(L_{IK}^0 + L_{KI}^0)(\delta_{IM} c_K - c_I) + (L_{IK}^1 - L_{KI}^1)[\delta_{IM} c_K (c_I - c_K) + c_I c_K (\delta_{IM} + 1) - c_I (c_I - c_K)]\} \qquad [A11]$$

$$\frac{\partial}{\partial c_M}(G_m^{\Phi,mo}) = \frac{RT}{\beta + 1} f(\tau) \frac{\partial \beta}{\partial c_M} - \frac{RT^2}{T_c^2} \ln (\beta + 1) \frac{\partial f}{\partial \tau} \frac{\partial T_c}{\partial c_M} \qquad [A12]$$

$$\frac{\partial}{\partial c_M}(\beta) = \sum_{\substack{I=1 \\ I \neq K}}^{N} \delta_{IM} \beta_I^0 - \beta_I^0 + \sum_{\substack{I=1 \\ I \neq K}}^{N} \sum_{\substack{J=1 \\ J \neq K}}^{N} [\beta_{IJ}^0 (c_J \delta_{IM} + c_I \delta_{JM}) + 2\beta_{IJ}^1 c_I c_J (\delta_{IM} - \delta_{JM}) + \beta_{IJ}^1 (c_I^2 \delta_{JM} - c_J^2 \delta_{IM})] + \sum_{\substack{I=1 \\ I \neq K}}^{N} \{(\beta_{IK}^0 + \beta_{KI}^0)(\delta_{IM} c_K - c_I) + (\beta_{IK}^1 - \beta_{KI}^1)[\delta_{IM} c_K (c_I - c_K) + c_I c_K (\delta_{Im} + 1) - c_I (c_I - c_K)]\} \qquad [A13]$$

$$\frac{\partial}{\partial c_M}(T_c) = \sum_{\substack{I=1 \\ I\neq K}}^{N} \delta_{IM} T_I^0 - T_I^0$$
$$+ \sum_{\substack{I=1 \\ I\neq K}}^{N} \sum_{\substack{J=1 \\ J\neq K}}^{N} [T_{IJ}^0 (c_J \delta_{IM} + c_I \delta_{JM})$$
$$+ 2T_{IJ}^1 c_I c_J (\delta_{IM} - \delta_{JM})$$
$$+ T_{IJ}^1 (c_I^2 \delta_{JM} - C_J^2 \delta_{IM})]$$
$$+ \sum_{\substack{I=1 \\ I\neq K}}^{N} \{(T_{IK}^0 + T_{KI}^0)$$
$$\cdot (\delta_{IM} c_K - c_I) + (T_{IK}^1 - T_{KI}^1)$$
$$\cdot [\delta_{IM} c_K (c_I - c_K)$$
$$+ c_I c_K (\delta_{IM} + 1)$$
$$- c_I (c_I - c_K)]\} \qquad [A14]$$

ACKNOWLEDGMENTS

We are grateful to Professor T. Mori for many helpful and stimulating discussions, to Dr. Jonathan Montgomery for his determinations of the important structural and mechanical input parameters for the ferrite-M_2C system in AF1410, and to Dr. Gautam Ghosh for his help in applying the Thermo-calc database to this problem. This research is sponsored by the Army Research Office under Grant No. DAAL03-89-K-0152 as part of the Steel Research Group program of the Materials Research Center of Northwestern University.

REFERENCES

1. T. Mura, E.A. Lautenschlager, and J.O. Brittain: *Acta Metall.*, 1961, vol. 9, pp. 453-58.
2. A.H. Cottrell and M.A. Jaswon: *Proc. R. Soc.*, 1949, vol. A199, pp. 104-14.
3. D.M. Barnett, G. Wang, and W.D. Nix: *Acta Metall.*, 1982, vol. 30, pp. 2035-41.
4. J.C.M. Li: *Metall. Trans. A*, 1978, vol. 9A, pp. 1353-80.
5. P.W. Voorhees and W.C. Johnson: *J. Chem. Phys.*, 1989, vol. 90 (5), pp. 2793-2801.
6. J.P. Hirth: *Metall. Trans. A*, 1980, vol. 11A, p. 861.
7. Y. Hirose and T. Mura: *Eng. Fract. Mech.*, 1984, vol. 19, pp. 1057-67.
8. F. Larché and J.W. Cahn: *Acta Metall.*, 1973, vol. 21, pp. 1051-63.
9. F. Larché and J.W. Cahn: *Acta Metall.*, 1985, vol. 33, pp. 331-57.
10. F. Larché and J.W. Cahn: *Acta Metall.*, 1978, vol. 26, pp. 53-60.
11. W.C. Johnson and P.W. Voorhees: *Metall. Trans. A*, 1985, vol. 16A, pp. 337-47.
12. G.B. Olson: *Innovations in Ultrahigh-Strength Steel Technology*, G.B. Olson, M. Azrin, and E.S. Wright, eds., 34th Sagamore Army Materials Research Conference Proceedings, 1990, pp. 3-66.
13. B. Sundman, B. Jansson, and J.O. Andersson: *CALPHAD*, 1985, vol. 9, p. 153.
14. F. Larché: Université de Montpellier, Montpellier-Cedex, France, private communication, 1990.
15. J.D. Eshelby: *Proc. R. Soc.*, 1957, vol. A241, pp. 376-96.
16. T. Mura: *Micromechanics of Defects in Solids*, Martinus Nijhoff, Dordrecht, The Netherlands, 1987, pp. 129-57.
17. T. Mura and P.C. Cheng: *J. Appl. Mech.*, 1977, vol. 44, pp. 591-94.
18. J.S. Montgomery: Ph.D. Thesis, Northwestern University, Evanston, IL, 1990.
19. J.N. Goodier: *Phil. Mag.*, 1937, vol. 23, pp. 1017-32.
20. S. Timoshenko and J.N. Goodier: *Theory of Elasticity*, McGraw-Hill, New York, NY, 1951.
21. IMSL MATH/LIBRARY, Ver 1.1, IMSL Inc., Houston, TX, 1989.
22. G.B. Olson, T.J. Kinkus, and J.S. Montgomery: *Surf. Sci.*, 1991, vol. 246, pp. 238-45.

CHAPTER 7

Elastic Energy of Coherent Precipitation at Dislocations in an Anisotropic Matrix*

K. C. King†
G. B. Olson†
T. Mura†

ABSTRACT The elastic strain energy is calculated for a single coherent precipitate particle nucleated heterogeneously in the vicinity of a dislocation. The precipitate is assumed to be ellipsoidal in shape. The elastic constants are allowed to differ between the precipitate and the matrix and both can be anisotropic. The equivalent eigenstrain method is used to overcome the difficulty of inhomogeneity, and equivalent eigenstrains are treated by the Taylor's series to second order. Experimental data provide the inputs for the calculation of M_2C carbide precipitation in the ultrahigh-strength steel AF1410. The results show that the elastic strain energy is sensitive to the size and the shape of the precipitate at small size, and provide the basis for a quantitative treatment of the heterogeneous nucleation, growth and coarsening in this system.

1. INTRODUCTION. The total free energy for precipitation is given by the sum of the chemical free energy, surface energy and elastic strain energy[1, 2]. For a coherent precipitate, the nucleation, growth and coarsening processes can be understood with the knowledge of this total free energy[3]. The goal of this work is to study the elastic strain energy for a single precipitate with misfit strains interacting with a dislocation in an anisotropic matrix during heterogeneous nucleation.

*This Research is sponsored by the Army Research office under Grant DAAL03-89-K-0152

†Materials Research Center, Northwestern University, Evanston, IL 60208

The elastic strain energy for heterogeneous precipitate nucleation can be obtained by the superposition of the self-energy and the interaction energy. The self energy is due to the misfit strains of the precipitate, and the interaction energy is due to the strain field of the precipitate interacting with the stress field of a defect. The defect in this case is taken to be a straight dislocation, and a screw dislocation is used as an example for numerical calculation. The precipitate is assumed to be ellipsoidal in shape and formed in the vicinity of the dislocation. The elastic constants for both the matrix and the precipitate can be anisotropic. However, a cubic symmetric matrix with an isotropic precipitate is assumed for the numerical calculations presented here.

Equivalent eigenstrains are used to overcome the difficulty of inhomogeneity, i. e. differing elastic constants of the matrix and the precipitate. Since the stress field due to the dislocation is not constant, the equivalent eigenstrains are not uniform. It has been proved that the equivalent eigenstrains can be chosen as polynomials of order N when applied stress fields are polynomials of order N[4, 5]. Therefore a Taylor's series expansion is used for both the equivalent eigenstrain and the dislocation stress field at the center of the inhomogeneity. A similar approach has been taken for the interaction between two ellipsoidal inhomogeneous inclusions[6], the interaction between a spherical inclusion and a screw dislocation[7, 8], and the interaction between an ellipsoidal inhomogeneity and a edge dislocation for the isotropic case[9]. The stress field due to the dislocation can be obtained from both Mura's formula[10] and the sextic formulation[11, 12, 13, 14, 15, 16].

Numerical calculations illustrate the elastic behavior for the case of M_2C carbide nucleation in the ultrahigh-strength steel AF1410. Experimental data[17] from a collaborative study provide the essential inputs for this work.

2. PROBLEM FORMULATION. The eigenstrain method is used to determine the elastic strain energy as a coherent precipitate forms in the vicinity of a dislocation. It is assumed that the dislocation is imbedded in the matrix before the precipitate nucleation. Therefore, the self-energy of the dislocation[18] is not considered. During the nucleation process, a uniform distribution of misfit strain is induced inside the precipitate, and the shape of the nucleated precipitate is assumed to be ellipsoidal. The elastic constants used for the matrix are cubic symmetric and those used for the precipitate are isotropic. Since the elastic constants differ between the precipitate and the matrix, the equivalent eigenstrains have to be determined to replace the misfit strain for energy calculations. However, since the stress field caused by the dislocation is not uniform in the matrix, it follows that the equivalent eigenstrain is not uniform inside the precipitate. This equivalent eigenstrain can be obtained by taking a Taylor's series expansion of the dislocation stress field at the center of the ellipsoidal precipitate. The second order approximation is applied in this work.

The elastic strain energy for the precipitate nucleation will be formulated first. Then the equations necessary to obtain the equivalent eigenstrain are derived. The stress field due to the dislocation are obtained from both Mura's formula[10] and the sextic formulation[11, 12, 13]. They are given in Appendix A.

2.1 ELASTIC STRAIN ENERGY. The dislocation in the matrix and the misfit strain inside the inclusion are the two sources of energy change in the system. In the following derivation, the elastic constants used for the matrix are denoted by C_{ijkl} and those used for the precipitate are denoted by C^{*}_{ijkl}. The infinite domain is denoted by V_{∞} and the precipitate domain is denoted by Ω. The elastic strain energy change accompanying precipitation can be expressed in the following[19]

$$\Delta W = \frac{1}{2}\int_{V_\infty}\left(\sigma^{\wedge}_{ij}+\sigma^{B}_{ij}\right)\left(u^{\wedge}_{i,j}+u^{B}_{i,j}-\varepsilon^{P}_{ij}\right)dV - \int_{V_\infty}\sigma^{D}_{ij}u^{D}_{i,j}dV \qquad (1)$$

where $\sigma^{\wedge}_{ij}$ and $u^{\wedge}_{i,j}$ are the stress and strain fields induced by the misfit between the precipitate and the matrix in the absence of the dislocation, σ^{B}_{ij} and $u^{B}_{i,j}$ are the stress and elastic strain fields of the dislocation in the presence of the precipitate (inhomogeneity) without the misfit strains, σ^{D}_{ij} and $u^{D}_{i,j}$ are the stress and strain fields of the dislocation in a homogeneous domain, and ε^{P}_{ij} are the misfit strains (see Fig. 1). By using the self-stress condition, $\sigma_{ij,j} = 0$

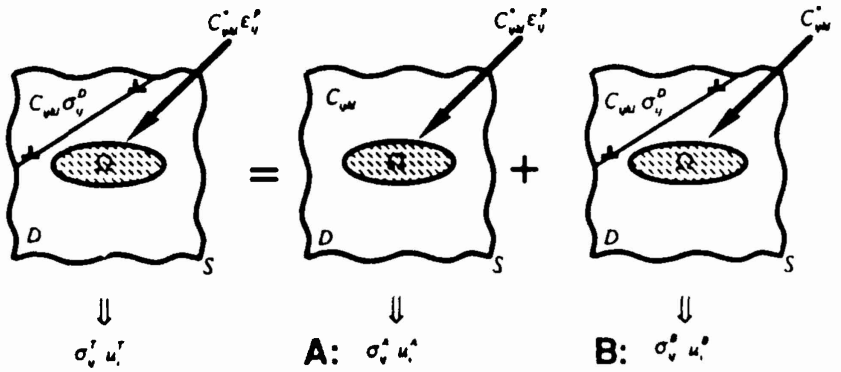


Figure 1 Schematic illustration for the decomposition of the total stress and displacement

inside domain V_- and the fact that all stresses decay sufficiently rapidly at infinity, the following equations are obtained

$$\int_{V_-} \sigma_{ij}^{A} u_{i,j}^{A} dV = 0 \tag{2}$$

$$\int_{V_-} \sigma_{ij}^{B} u_{i,j}^{B} dV = \int_{V_-} \sigma_{ij}^{D} u_{i,j}^{D} dV - \int_{\Omega} \sigma_{ij}^{D} \varepsilon_{ij}^{\beta} dV \tag{3}$$

$$\int_{V_-} \sigma_{ij}^{A} u_{i,j}^{B} dV = -\int_{\Omega} \sigma_{ij}^{D} \varepsilon_{ij}^{**} dV \tag{4}$$

$$\int_{V_-} \sigma_{ij}^{B} u_{i,j}^{A} dV = 0 \tag{5}$$

$$\int_{\Omega} \sigma_{ij}^{B} \varepsilon_{ij}^{p} dV = \int_{\Omega} \sigma_{ij}^{D} \varepsilon_{ij}^{**} dV \tag{6}$$

where $\varepsilon_{ij}^{**} = \varepsilon_{ij}^{*} + \varepsilon_{ij}^{p}$; ε_{ij}^{*} are the equivalent eigenstrains for case A (see Fig. 2);

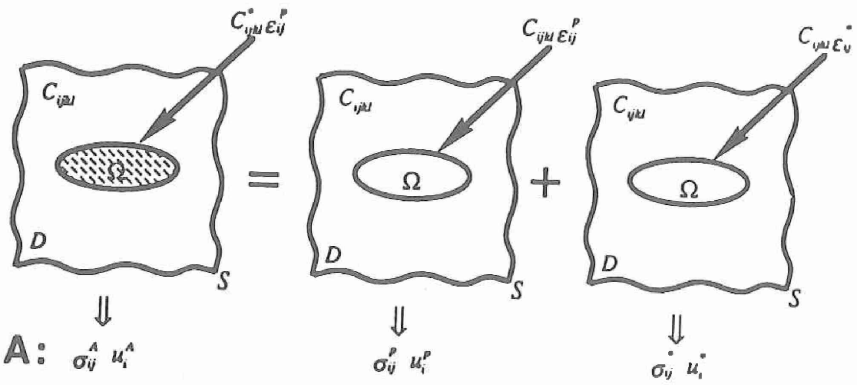


Figure 2 Schematic illustration for the decomposition of the stress and displacement caused by the misfit strain.

ε_{ij}^{β} are the equivalent eigenstrains for case B (see Fig. 3). Substituting Eqs. (2)~(6) into Eq. (1), the elastic strain energy change accompanying nucleation can be written as

$$\Delta W = -\frac{1}{2}\int_{\Omega} \sigma_{ij}^{A} \varepsilon_{ij}^{p} dV - \int_{\Omega} \sigma_{ij}^{D} \varepsilon_{ij}^{**} dV - \frac{1}{2}\int_{\Omega} \sigma_{ij}^{D} \varepsilon_{ij}^{\beta} dV \,. \tag{7}$$

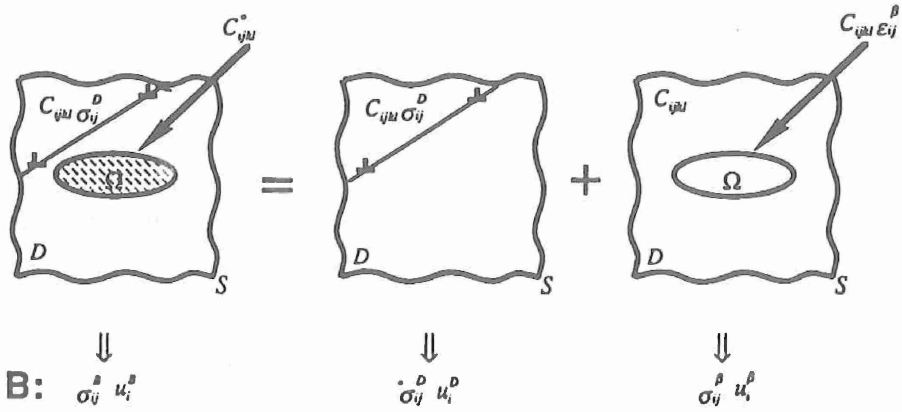


Figure 3 Schematic illustration for the decomposition of the stress and displacement caused by the dislocation.

An equivalent expression differing in form from (7) has been obtained by Barnett[9] using results obtained previously by Eshelby[20, 21]. The method used to solve these equivalent strains is discussed in the next section. The stressed σ^D_{ij} caused by dislocation can be obtained in Appendix A and the stress tensor σ^Λ_{ij} in Eq. (7) can be solved from the following equations

$$\sigma^\Lambda_{ij} = C_{ijkl}\left(S^0_{klmn}\varepsilon^{**}_{mn} - \varepsilon^{**}_{kl}\right) \tag{8}$$

where S^0_{klmn} are the Eshelby's tensors, which are available in Appendix B.

The first term in Eq. (7) is the self energy, which is the elastic strain energy due to formation of the precipitate without the dislocation, and this self-energy is considered as parts of the nucleation energy. The second and the third terms are due to the misfit and the modulus effect, and they are caused by the interaction of misfit strain and inhomogeneity with the dislocation. The nucleation energy can then be calculated after the equivalent eigenstrains ε^β_{ij} and ε^*_{ij} are obtained.

The elastic nucleation energy for the homogeneous problem, where the elastic constants of the precipitate are assumed to be same as those of the matrix, can be derived in a similar way as

$$\Delta W = -\frac{1}{2}\int_\Omega \sigma^\Lambda_{ij}\varepsilon^p_{ij}dV - \int_\Omega \sigma^D_{ij}\varepsilon^p_{ij}dV \tag{9}$$

where σ_{ij}^{A} can be determined by

$$\sigma_{ij}^{A} = C_{ijkl}\left(S_{klmn}^{0}\varepsilon_{mn}^{p} - \varepsilon_{kl}^{p}\right) \tag{10}$$

The equation (9) can be integrated directly since no equivalent eigenstrains need be determined.

2.2 EQUIVALENT EIGENSTRAIN METHOD. In this section, the necessary equations to solve the equivalent eigenstrains ε_{ij}^{p} and ε_{ij}^{**} for each case are derived by use of the equivalent eigenstrain method. It is assumed in this method that the disturbance of the stress and strain fields due to the inhomogeneity can be simulated by an extra fictitious strain field inside the inhomogeneity domain, and this fictitious strain is called the equivalent eigenstrain. It follows that the inhomogeneous problem can be solved by the superposition of the stress and strain fields of: (i) the solution of the stress and strain fields caused by the same source of force (dislocation and misfit strain) in a homogeneous matrix, and (ii) the solution of the stress and strain fields caused by the equivalent eigenstrain in a homogeneous matrix. Therefore, the equivalent eigenstrain can be solved by using the stress equivalency condition between the original problem (inhomogeneous problem) and the homogeneous problem with the same source and the equivalent eigenstrain. However, the equivalency condition is automatically satisfied in the matrix $(V_m - \Omega)$ such that the necessary equations to obtained the equivalent eigenstrain are derived from the equivalency condition inside the precipitate (Ω) only.

For case A, the misfit strain is constant inside the precipitate. It follows that the total strains are constant inside the precipitate, and they can be obtained by multiplying Eshelby's tensors with the equivalent eigenstrain ε_{mn}^{**}. The equivalency conditions for this case are as follows

$$C_{ijkl}^{*}\left(S_{klmn}^{0}\varepsilon_{mn}^{**} - \varepsilon_{kl}^{p}\right) = C_{ijkl}\left(S_{klmn}^{0}\varepsilon_{mn}^{**} - \varepsilon_{kl}^{**}\right) \tag{11}$$

where Eshelby's tensors are shown in Appendix B. The six unknown equivalent eigenstrains ε_{mn}^{**} can be solved from the six equations represented by Eq. (11).

For case B, the stress field inside the precipitate is not uniform since the stress field in the matrix caused by the dislocation is not uniform. It was proved[4, 5] that the total strain inside the precipitate has a polynomial form if the eigenstrain is given in a polynomial form, i.e., both the polynomials are of the same degree. The eigenstrain can be solved through the use of this quantity. The strain field caused by the dislocation is expanded by the

Taylor's series to the second order at the center of the precipitate x_c, and the following equations are obtained

$$\varepsilon_{ij}^{D} = \varepsilon_{ij}^{0} + \varepsilon_{ij}^{1,L} x_L + \varepsilon_{ij}^{2,MN} x_M x_N \tag{12}$$

where

$$\varepsilon_{ij}^{0} = \varepsilon_{ij}^{D}(\mathbf{x})\Big|_{\mathbf{x}=\mathbf{x}_c}$$

$$\varepsilon_{ij}^{1,L} = \frac{\partial \varepsilon_{ij}^{D}(\mathbf{x})}{\partial x_L}\Bigg|_{\mathbf{x}=\mathbf{x}_c}$$

$$\varepsilon_{ij}^{2,MN} = \frac{1}{2}\frac{\partial \varepsilon_{ij}^{D}(\mathbf{x})}{\partial x_M \partial x_N}\Bigg|_{\mathbf{x}=\mathbf{x}_c} \tag{13}$$

The equivalent eigenstrains are expanded by the Taylor's series to the second order as

$$\varepsilon_{ij}^{\beta} = \varepsilon_{ij}^{\beta^0} + \varepsilon_{ij}^{\beta^1,L} x_L + \varepsilon_{ij}^{\beta^2,MN} x_M x_N \tag{14}$$

where the coefficients of this equation ($\varepsilon_{ij}^{\beta^0}$, $\varepsilon_{ij}^{\beta^1,L}$, $\varepsilon_{ij}^{\beta^2,MN}$) are the unknown quantities. Because of the symmetry conditions of the subscript "ij" and superscript "MN", there are six unknowns $\varepsilon_{ij}^{\beta^0}$, eighteen unknowns $\varepsilon_{ij}^{\beta^1,L}$ and thirty-six unknowns $\varepsilon_{ij}^{\beta^2,MN}$ to be determined. The necessary equations to solve these unknown quantities are next derived.

The total displacement gradient field ε_{ij} inside the precipitate for the given eigenstrain in Eq. (14) can be expressed as

$$\varepsilon_{ij} = \left(S_{ijmn}^{0}\varepsilon_{mn}^{\beta^0} + S_{ijmn}^{**,MN}\varepsilon_{mn}^{\beta^2,MN}\right) + \left(S_{ijmn}^{*,PL}\varepsilon_{mn}^{\beta^1,P}\right)x_L + \left(S_{ijmn}^{**,MNRS}\varepsilon_{mn}^{\beta^2,MN}\right)x_R x_S \tag{15}$$

where Eshelby's tensors are given in Appendix B .

These equivalent eigenstrains for this case can be solved by using the equivalency condition as mentioned before. Therefore, there are six equations for the leading order term

$$C_{ijkl}^{*}\left(\varepsilon_{kl}^{0} + S_{klmn}^{0}\varepsilon_{mn}^{\beta^0} + S_{klmn}^{**,MN}\varepsilon_{mn}^{\beta^2,MN}\right) = C_{ijkl}\left(\varepsilon_{kl}^{0} + S_{klmn}^{0}\varepsilon_{mn}^{\beta^0} + S_{klmn}^{**,MN}\varepsilon_{mn}^{\beta^2,MN} - \varepsilon_{kl}^{\beta^0}\right) \tag{16}$$

eighteen equations for the first order term

$$C^{*}_{ijkl}\left(\varepsilon^{1,L}_{kl} + S^{*,PL}_{klmn}\varepsilon^{\beta^1,P}_{mn}\right) = C_{ijkl}\left(\varepsilon^{1,L}_{kl} + S^{*,PL}_{klmn}\varepsilon^{\beta^1,P}_{mn} - \varepsilon^{\beta^1,L}_{kl}\right) \tag{17}$$

and thirty-six equations for the second order term

$$C^{*}_{ijkl}\left(\varepsilon^{2,RS}_{kl} + S^{**,MNRS}_{klmn}\varepsilon^{\beta^2,MN}_{mn}\right)$$
$$= C_{ijkl}\left(\varepsilon^{2,RS}_{kl} + S^{**,MNRS}_{klmn}\varepsilon^{\beta^2,MN}_{mn} - \varepsilon^{\beta^2,RS}_{kl}\right) \tag{18}$$

where Eshelby's tensors are given in Appendix B.

The coefficients obtained from Eqs. (16),(17) and (18) are substituted into Eq. (14), and the equivalent eigenstrains ε^{β}_{ij} are obtained in the second order approximation.

Finally, the elastic nucleation energy of the precipitate for the inhomogeneous case can be obtained by substituting the solved equivalent eigenstrains (ε^{**}_{ij} and ε^{β}_{ij}) into Eq. (7) and integrating.

3. NUMERICAL CALCULATIONS AND DISCUSSION. This energy calculation method is applied to the nucleation of a coherent M_2C carbide in AF1410 steel. It is assumed that the carbide is nucleated in the vicinity of a screw dislocation lying in the [111] direction. The nearest distance between the boundary of the carbide and the dislocation is set equal to half the magnitude of the Burgers vector. The magnitude of the Burgers vector of the screw dislocation is 2.485 Å[17]. The shape of the carbide is assumed to be a prolate spheroid with the major axis in the [100] direction. During the precipitation process, the aspect ratio and the principal misfit strains change at different stages, and the experimental data[17] is shown in Table 1. The elastic constants of the carbide are: Young's modulus $E = 25 \times 10^{10}\ N/m^2$ and Poisson's ratio $\nu = 0.19$[17]. The "open system elastic constants" of the matrix are: $C_{11} = 22.03 \times 10^{10}\ N/m^2$, $C_{12} = 12.48 \times 10^{10}\ N/m^2$, $C_{44} = 11.2 \times 10^{10}\ N/m^2$[17]. The latter constants take into account the redistribution of substitutional solutes under stress[22].

The Gauss-Legendre quadrature method is used to calculate these Eshelby's tensors in Appendix B for different aspect ratios. These Eshelby's tensors are independent of the size of the inclusion but depend on its shape. Then the coefficients for the Taylor's series expansion of the strain field, which is caused by the dislocation, in Eq. (12) are calculated by using the equations in Appendix A. The numerical results are calculated by both Mura's formula and the sextic equations; the two results are in good

Table 1 Experimental data and the calculated self-energy.

Tempering Time (510 ^{0}C)	5 min	1.5 hr	8 hr
Relative Fraction Transformed	f=0	f=0.5	f=0.99
Aspect Ratio	1.0	2.0	3.0
Minor Radius, R (Å)	14.46	18.18	25.18
misfit strain $\varepsilon^p_{[100]}$	-0.027	-0.001	0.003
misfit strain $\varepsilon^p_{[0\bar{1}1]}$	0.192	0.224	0.229
misfit strain $\varepsilon^p_{[011]}$	0.091	0.114	0.117
Self-energy/volume (10^{10}J/m^3) H.	0.2882	0.3740	0.3686
Self-energy/volume (10^{10}J/m^3) IH.	0.3041	0.3704	0.3619

agreement. It follows that the equivalent eigenstrains, ε^{**}_{ij} and ε^{β}_{ij}, can be determined through the use of Eqs. (11), (14) and (16)~(18). Therefore, the elastic strain energy can be calculated by integrating Eq. (7). The integration domain in Eq. (7) is reduced to a unit sphere first, then the Gauss-Legendre quadrature method is used to carry out the integration in the spherical coordinate system. The energy under the homogeneous assumption is also calculated by using Eq. (9).

The elastic strain energy is calculated for different relative orientations between the precipitate and dislocation. The observed average size and the misfit strains of the precipitate with different aspect ratios, given in Table 1, is used for the calculation. The procedure to determine the relative position is as follows: (i) the precipitate is fixed and a plane is imagined to be located at the center of the precipitate with the normal direction [111], (ii) then a starting direction vector [$1\bar{1}0$], which lies on the (111) plane, is arbitrarily chosen, (iii) the direction vector is rotated counter-clockwise normal to [111], (iv) and the location of the dislocation line is set by keeping the nearest distance between the boundary of the precipitate and the dislocation equal to 1.243 Å. The interaction energy results are shown in Fig. 4(a) and 4(b) (also, Table 2) for the homogeneous and inhomogeneous assumptions, respectively. The self-energy per volume is only a function of aspect ratio. Therefore, the self-energy per volume is constant for different dislocation orientations and given in Table 1. The results for the elastic strain energy for precipitation can be obtained by the superposition of the interaction energy and the self-energy. It can be found in these figures that the minimum of the calculated energy per volume is located near the angle of 300 degrees, corresponding to the [$0\bar{1}1$] direction. This is the most important direction because it will provide the lowest energy barrier for the nucleation of the precipitate.

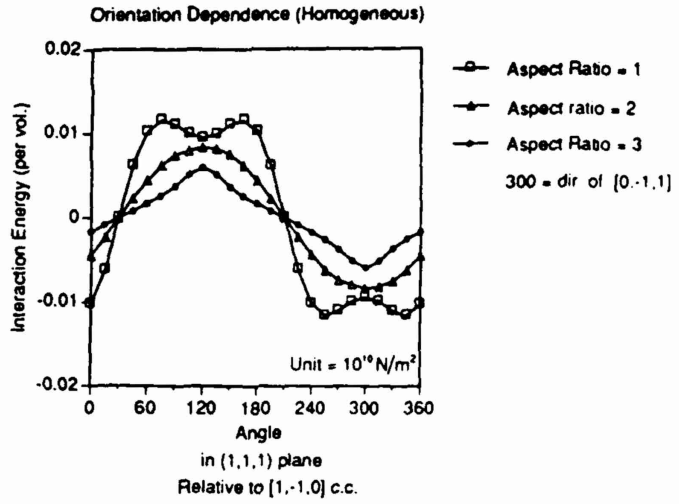


Figure 4 (a) The orientation dependence of the elastic strain energy (per unit volume precipitate). --- Homogeneous assumption.

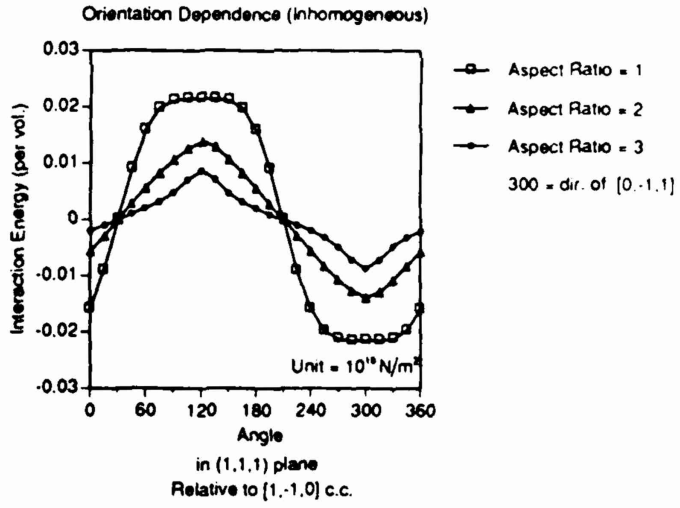


Figure 4 (b) The orientation dependence of the elastic strain energy (per unit volume precipitate). --- Inhomogeneous assumption.

Table 2 Calculations for the interaction energy orientation dependence.

Angle	f=1 H.	f=1 IH.	f=2 H.	f=2 IH.	f=3 H.	f=3 IH.
0	-0.0102	-0.0159	-0.0044	-0.0056	-0.0017	-0.0020
15	-0.0061	-0.0091	-0.0023	-0.0029	-0.0008	-0.0010
30	0.0000	0.0000	0.0000	0.0000	0.0000	0.0000
45	0.0061	0.0091	0.0023	0.0028	0.0008	0.0010
60	0.0102	0.0159	0.0044	0.0056	0.0017	0.0020
75	0.0116	0.0198	0.0062	0.0083	0.0026	0.0032
90	0.0110	0.0212	0.0074	0.0107	0.0037	0.0048
105	0.0100	0.0216	0.0079	0.0126	0.0051	0.0071
120	0.0094	0.0215	0.0084	0.0139	0.0059	0.0087
135	0.0099	0.0215	0.0082	0.0129	0.0051	0.0071
150	0.0110	0.0212	0.0075	0.0108	0.0037	0.0048
165	0.0116	0.0197	0.0062	0.0083	0.0026	0.0032
180	0.0102	0.0159	0.0044	0.0056	0.0017	0.0020
195	0.0061	0.0091	0.0023	0.0029	0.0008	0.0010
210	0.0000	0.0000	0.0000	0.0000	0.0000	0.0000
225	-0.0061	-0.0091	-0.0023	-0.0028	-0.0008	-0.0010
240	-0.0102	-0.0159	-0.0044	-0.0056	-0.0017	-0.0020
255	-0.0116	-0.0198	-0.0062	-0.0083	-0.0026	-0.0032
270	-0.0110	-0.0212	-0.0074	-0.0107	-0.0037	-0.0048
285	-0.0100	-0.0216	-0.0079	-0.0126	-0.0051	-0.0071
300	-0.0094	-0.0215	-0.0084	-0.0139	-0.0059	-0.0087
315	-0.0099	-0.0215	-0.0082	-0.0129	-0.0051	-0.0071
330	-0.0110	-0.0212	-0.0075	-0.0108	-0.0037	-0.0048
345	-0.0116	-0.0197	-0.0062	-0.0083	-0.0026	-0.0032
360	-0.0102	-0.0159	-0.0044	-0.0056	-0.0017	-0.0020

f = Aspect Ratio
H. = Interaction Energy for Homogeneous Assumption
IH. = Interaction Energy for Inhomogeneous Assumption
Unit = $10^{10}\ J/m^3$

To model nucleation, holding the orientation at the optimum, the elastic strain energy is next calculated for different sizes of the precipitate. During this calculation, the misfit strains and aspect ratios are fixed at the values in Table 1. The results for the interaction energy are illustrated in Fig. 5(a) and 5(b) (also, Table 3). Again, the results for the self-energy per volume are independent of the size of the particle, and are given in Table 1. In these figures, the effect of the interaction energy (the misfit effect and the modulus effect) is more significant for smaller precipitates, such that the elastic strain energy per volume is smaller as the size of the precipitate becomes smaller, while the self-energy of the precipitate is size independent. This comes from the fact that the field of the dislocation governing the interaction decays as 1/r, and thus, the percentage of highly stressed volume for large precipitates is smaller.

The above results are based on the assumption of linear elasticity. For martensite, the nonlinear behavior of the stress-strain relation is significant in high stress regions. Therefore, the stresses may be overestimated in these

regions under the linear assumption. It follows that the calculated elastic self energy for precipitate nucleation represents an upper bound estimate.

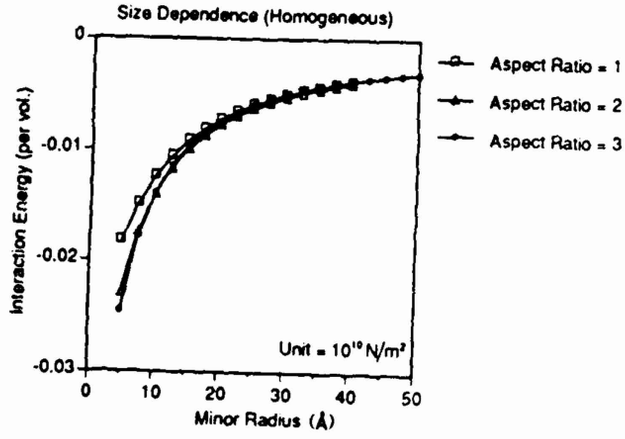


Fig. 5 (a) The size dependence of the elastic strain energy (per unit volume precipitate). --- Homogeneous assumption.

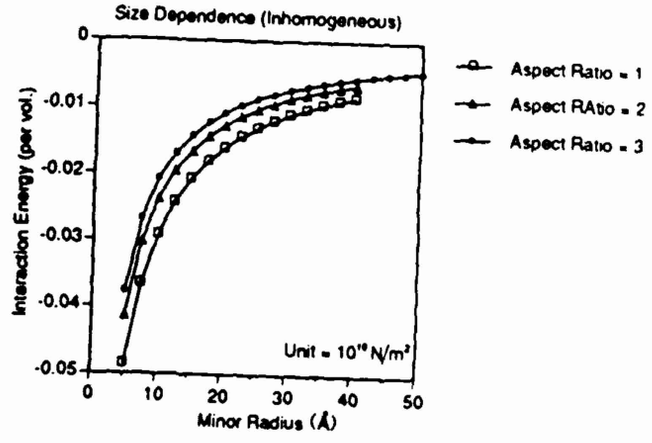


Fig. 5 (b) The size dependence of the elastic strain energy (per unit volume precipitate). --- Inhomogeneous assumption.

Table 3 Calculations for the interaction energy size dependence.

Minor radius	f=1 H	f=1 IH	f=2 H	f=2 IH	f=3 H	f=3 IH
5.0	-0.0183	-0.0487	-0.0229	-0.0414	-0.0245	-0.0376
5.8	-0.0172	-0.0441	-0.0209	-0.0371	-0.0219	-0.0333
6.6	-0.0161	-0.0402	-0.0191	-0.0335	-0.0198	-0.0298
7.4	-0.0151	-0.0370	-0.0176	-0.0306	-0.0180	-0.0270
8.2	-0.0142	-0.0342	-0.0163	-0.0281	-0.0165	-0.0247
9.0	-0.0133	-0.0318	-0.0152	-0.0260	-0.0153	-0.0228
9.8	-0.0126	-0.0297	-0.0142	-0.0242	-0.0142	-0.0211
10.6	-0.0119	-0.0279	-0.0133	-0.0226	-0.0132	-0.0196
11.4	-0.0113	-0.0263	-0.0125	-0.0212	-0.0124	-0.0184
12.2	-0.0108	-0.0248	-0.0119	-0.0200	-0.0117	-0.0173
13.0	-0.0103	-0.0235	-0.0112	-0.0189	-0.0110	-0.0163
13.8	-0.0098	-0.0224	-0.0107	-0.0179	-0.0104	-0.0154
14.6	-0.0094	-0.0213	-0.0102	-0.0170	-0.0099	-0.0146
15.4	-0.0090	-0.0203	-0.0097	-0.0162	-0.0094	-0.0139
16.2	-0.0086	-0.0194	-0.0093	-0.0155	-0.0090	-0.0133
17.0	-0.0083	-0.0186	-0.0089	-0.0148	-0.0086	-0.0127
17.8	-0.0080	-0.0179	-0.0085	-0.0142	-0.0083	-0.0121
18.6	-0.0077	-0.0172	-0.0082	-0.0137	-0.0079	-0.0116
19.4	-0.0075	-0.0166	-0.0079	-0.0131	-0.0076	-0.0112
20.2	-0.0072	-0.0160	-0.0076	-0.0127	-0.0073	-0.0108
21.0	-0.0070	-0.0154	-0.0074	-0.0122	-0.0071	-0.0104
21.8	-0.0068	-0.0149	-0.0071	-0.0118	-0.0068	-0.0100
22.6	-0.0065	-0.0144	-0.0069	-0.0114	-0.0066	-0.0097
23.4	-0.0064	-0.0140	-0.0067	-0.0110	-0.0064	-0.0093
24.2	-0.0062	-0.0136	-0.0065	-0.0107	-0.0062	-0.0090
25.0	-0.0060	-0.0132	-0.0063	-0.0104	-0.0060	-0.0088
25.8	-0.0058	-0.0128	-0.0061	-0.0101	-0.0058	-0.0085
26.6	-0.0057	-0.0124	-0.0059	-0.0098	-0.0056	-0.0083
27.4	-0.0055	-0.0121	-0.0058	-0.0095	-0.0055	-0.0080
28.2	-0.0054	-0.0118	-0.0056	-0.0093	-0.0053	-0.0078
29.0	-0.0053	-0.0115	-0.0055	-0.0090	-0.0052	-0.0076
29.8	-0.0051	-0.0112	-0.0053	-0.0088	-0.0051	-0.0074
30.6	-0.0050	-0.0109	-0.0052	-0.0086	-0.0049	-0.0072
31.4	-0.0049	-0.0107	-0.0051	-0.0084	-0.0048	-0.0070
32.2	-0.0048	-0.0104	-0.0050	-0.0082	-0.0047	-0.0069
33.0	-0.0047	-0.0102	-0.0048	-0.0080	-0.0046	-0.0067
33.8	-0.0046	-0.0099	-0.0047	-0.0078	-0.0045	-0.0065
34.6	-0.0045	-0.0097	-0.0046	-0.0076	-0.0044	-0.0064
35.4	-0.0044	-0.0095	-0.0045	-0.0075	-0.0043	-0.0063
36.2	-0.0043	-0.0093	-0.0044	-0.0073	-0.0042	-0.0061
37.0	-0.0042	-0.0091	-0.0043	-0.0072	-0.0041	-0.0060
37.8	-0.0042	-0.0089	-0.0043	-0.0070	-0.0040	-0.0059
38.6	-0.0041	-0.0088	-0.0042	-0.0069	-0.0039	-0.0057
39.4	-0.0040	-0.0086	-0.0041	-0.0067	-0.0039	-0.0056

Table 3 (continued)

Minor radius	f=1 H	f=1 IH	f=2 H	f=2 IH	f=3 H	f=3 IH
40.2	-0.0039	-0.0084	-0.0040	-0.0066	-0.0038	-0.0055
41.0	-0.0039	-0.0083	-0.0039	-0.0065	-0.0037	-0.0054
41.8	-0.0038	-0.0081	-0.0039	-0.0064	-0.0036	-0.0053
42.6	-0.0037	-0.0080	-0.0038	-0.0062	-0.0036	-0.0052
43.4	-0.0037	-0.0078	-0.0037	-0.0061	-0.0035	-0.0051
44.2	-0.0036	-0.0077	-0.0037	-0.0060	-0.0035	-0.0050
45.0	-0.0035	-0.0076	-0.0036	-0.0059	-0.0034	-0.0049
45.8					-0.0033	-0.0049
46.6					-0.0033	-0.0048
47.4					-0.0032	-0.0047
48.2					-0.0032	-0.0046
49.0					-0.0031	-0.0045
49.8					-0.0031	-0.0045
50.6					-0.0030	-0.0044
51.4					-0.0030	-0.0043
52.2					-0.0029	-0.0043
53.0					-0.0029	-0.0042

f = Aspect Ratio
H. = Interaction Energy for Homogeneous Assumption
IH. = Interaction Energy for Inhomogeneous Assumption
Unit = $10^{10}\ J/m^3$

The elastic energy calculated from this work can next be combined with the chemical energy and the surface energy to calculate the Gibbs free energy for nucleation. The results of such a calculation, fitting the surface energy to observed nucleation rates and critical nucleus size, will be discussed elsewhere.

4. CONCLUSIONS. The elastic strain energy for the coherent heterogeneous nucleation of M_2C carbides in AF1410 steel has been calculated. The results show the difference between the homogeneous and inhomogeneous assumptions. For a given screw dislocation lying in the [111] direction, the minimum energy is obtained when the precipitate is oriented in the $[0\bar{1}1]$ direction. The elastic strain energy is sensitive to the size and the shape of the precipitate at small size, i.e., during the nucleation stage. For the larger sizes relevant to coarsening, the interaction energy is negligible and the self-energy dominates the elastic strain energy. The self-energy per unit volume of precipitate is independent of the size, and therefore, the elastic strain energy per unit volume of precipitate is almost a constant for a large precipitate.

APPENDIX A

The solution for the dislocation displacement gradient is given as follows[11, 12, 13]

$$u^{0}_{i,j}(\mathbf{x}) = \frac{1}{2\pi i}\sum_{\alpha=1}^{6} \pm A_{i\alpha} L_{i\alpha} B_j \frac{m_j + p_\alpha n_j}{\mathbf{m}\cdot\mathbf{x} + p_\alpha \mathbf{n}\cdot\mathbf{x}} \qquad \text{(A1)}$$

where **m** and **n** are the unit vectors orthogonal to each other and are also orthogonal to the direction of the dislocation line. In this notation p_α represents the eigenvalues, and $A_{i\alpha}$ and $L_{s\alpha}$ represent the eigenvectors. The solution is obtained by summation over α, which is the label for the eigenvectors and eigenvalues. The positive (negative) sign in this summation is used according to whether p_α has a positive (or negative) imaginary part. The Burgers vector is denoted by B_s. The eigenvalues and eigenvectors can be determined from the following equation

$$\begin{bmatrix} (nm) & I \\ (mm) & 0 \end{bmatrix} \begin{bmatrix} \mathbf{A}_\alpha \\ \mathbf{L}_\alpha \end{bmatrix} = p_\alpha \begin{bmatrix} -(nn) & 0 \\ -(mn) & I \end{bmatrix} \begin{bmatrix} \mathbf{A}_\alpha \\ \mathbf{L}_\alpha \end{bmatrix} \tag{A2}$$

where I is the unit matrix and 0 is the matrix with all zero components. The notation (ab) is defined as

$$(ab)_{jk} = a_i C_{ijkl} b_l \tag{A3}$$

and

$$\begin{bmatrix} \mathbf{A}_\alpha \\ \mathbf{L}_\alpha \end{bmatrix} = \begin{bmatrix} A_{1\alpha} \\ A_{2\alpha} \\ A_{3\alpha} \\ L_{1\alpha} \\ L_{2\alpha} \\ L_{3\alpha} \end{bmatrix} \tag{A4}$$

The derivative of the displacement gradient (A1) is given in the following

$$\frac{\partial}{\partial x_M} u^D_{i,j}(\mathbf{x}) = \frac{-1}{2\pi i} \sum_{\alpha=1}^{6} \pm A_{i\alpha} L_{s\alpha} B_s (m_M + p_\alpha n_M) \frac{m_j + p_\alpha n_j}{(\mathbf{m}\cdot\mathbf{x} + p_\alpha \mathbf{n}\cdot\mathbf{x})^2} \tag{A5}$$

$$\frac{\partial}{\partial x_M \partial x_N} u^D_{i,j}(\mathbf{x}) = \frac{1}{\pi i} \sum_{\alpha=1}^{6} \pm A_{i\alpha} L_{s\alpha} B_s (m_M + p_\alpha n_M)(m_N + p_\alpha n_N) \frac{m_j + p_\alpha n_j}{(\mathbf{m}\cdot\mathbf{x} + p_\alpha \mathbf{n}\cdot\mathbf{x})^3} \tag{A6}$$

The other solution for the dislocation displacement gradient is obtained by using Mura's formula[110], the solution is given as follows

$$u^D_{i,j}(\mathbf{x}) = -(2\pi)^{-2} \varepsilon_{jmn} C_{klmn} B_m \nu_k r^{-1} I_{ik}(\mathbf{t},\mathbf{s}) \tag{A7}$$

where ε_{jmk} is the permutation tensor. In this notation ν is the unit vector in the direction of the dislocation line, $\mathbf{t}$ is the unit vector normal to ν and it lies on a plane which contains the dislocation and the observing point $\mathbf{x}$, and the unit vector $\mathbf{s}$ is defined as $\mathbf{s} = \mathbf{t} \times \nu$. The definition of $I_{ik}(\mathbf{t},\mathbf{s})$ is as follows (Mura 1987: "Micromechanics of Defects in Solids" p. 332)

$$I_{ik}(\mathbf{t},\mathbf{s}) = \int_0^{2\pi} \left[\frac{t_l N_{ik}(-\mathbf{t}\sin\Phi + \mathbf{s}\cos\Phi)}{D(-\mathbf{t}\sin\Phi + \mathbf{s}\cos\Phi)} - \frac{\cos\Phi}{\sin\Phi} s_l \right. \left. \left\{ \frac{N_{ik}(-\mathbf{t}\sin\Phi + \mathbf{s}\cos\Phi)}{D(-\mathbf{t}\sin\Phi + \mathbf{s}\cos\Phi)} - \frac{N_{ik}(\mathbf{s})}{D(\mathbf{s})} \right\} \right] d\Phi \tag{A8}$$

where $N_{ik}(\xi)$ and $D(\xi)$ are the cofactor and determinant of the matrix $K_{ik}(\xi)$, which is given as

$$K_{ik}(\xi) = C_{ijkl}\xi_j\xi_l \tag{A9}$$

As explained in Mura's book[19] Eq. (A1) can be derived directly from Eq. (A7).

APPENDIX B

The displacement inside an ellipsoidal inclusion with a distributed eigenstrain $\varepsilon^*_{mn}(\mathbf{x})$ is given as[23]

$$u_i(\mathbf{x}) = \frac{-a_1a_2a_3}{8\pi^2} \int_0^{2\pi} d\Phi \left[\int_0^R r dr \frac{\partial}{\partial z} \varepsilon^*_{mn}(\mathbf{x}') - (\bar{\zeta}\cdot\mathbf{y}) \{\varepsilon^*_{mn}(\mathbf{x}')\}_{r=R} \right]_{z=\bar{\zeta}\cdot\mathbf{y}}$$
$$\times \int_{s^2} C_{kimn} N_{ik}(\bar{\xi}) D^{-1}(\bar{\xi}) \bar{\xi}_l \zeta^{-2} dS(\bar{\xi}) \tag{B1}$$

where

$$\frac{x_i}{a_i} = y_i$$

$$\frac{x_i'}{a_i} = y_i' \qquad (\textit{no summation})$$

$$a_i\bar{\xi}_i = \zeta_i$$

$$y_i' = z\bar{\zeta}_i + r(m_i\cos\Phi + n_i\sin\Phi) \tag{B2}$$

and $2a_1, 2a_2, 2a_3$ are the three principal lengths of the ellipsoidal inclusion and the bars denote that the components of a vector are divided by the magnitude of the vector. The integration domain S^2 is the surface of a unit sphere. The unit vector m and n are arbitrarily chosen vectors satisfying the condition that m, n and $\bar{\zeta}$ have to be mutually orthogonal. The total strain inside the inclusion can be obtained by using the following equation as

$$\varepsilon_{ij} = \frac{1}{2}\left(u_{i,j} + u_{j,i}\right) \tag{B3}$$

Therefore, Eshelby's tensors can be obtained by substituting a given eigenstrain into Eq. (B1). They are presented according to the order of the polynomial in the following.

Case 1. $\varepsilon^*_{mn}(\mathrm{x}) = \varepsilon^0_{mn}$

$$\varepsilon_{ij} = S^0_{ijmn}\varepsilon^0_{mn} \tag{B4}$$

$$S^0_{ijmn} = \frac{1}{8\pi} C_{klmn} \int_{S^2} \left[N_{ik}\left(\bar{\xi}\right)\bar{\xi}_j\bar{\xi}_l + N_{jk}\left(\bar{\xi}\right)\bar{\xi}_i\bar{\xi}_l \right] D^{-1}\left(\bar{\xi}\right) dS\left(\bar{\zeta}\right) \tag{B5}$$

Case 2. $\varepsilon^*_{mn}(\mathrm{x}) = \varepsilon^{1,L}_{mn} x_L$

$$\varepsilon_{ij} = S^{*,PL}_{ijmn}\varepsilon^{1,L}_{mn} x_P \tag{B6}$$

$$S^{*,PL}_{ijmn} = \frac{3}{8\pi} C_{klmn} \frac{a_{\bar{L}}}{a_{\bar{P}}} \int_{S^2} \left[N_{ik}\left(\bar{\xi}\right)\bar{\xi}_j\bar{\xi}_l + N_{jk}\left(\bar{\xi}\right)\bar{\xi}_i\bar{\xi}_l \right] D^{-1}\left(\bar{\xi}\right)\bar{\zeta}_L\bar{\zeta}_P dS\left(\bar{\zeta}\right) \tag{B7}$$

Case 3. $\varepsilon^*_{mn}(\mathrm{x}) = \varepsilon^{2,MN}_{mn} x_M x_N$

$$\varepsilon_{ij} = S^{**,MN}_{ijmn}\varepsilon^{2,MN}_{mn} + S^{**,MNRS}_{ijmn}\varepsilon^{2,MN}_{rs} x_R x_S \tag{B8}$$

$$S^{**,MN}_{ijmn} = \frac{1}{16\pi} C_{klmn} a_{\bar{M}} a_{\bar{N}} \int_{S^2} \left[\left(N_{ik}\left(\bar{\xi}\right)\bar{\xi}_j\bar{\xi}_l + N_{jk}\left(\bar{\xi}\right)\bar{\xi}_i\bar{\xi}_l \right) \left(\delta_{NM} - 3\bar{\zeta}_N\bar{\zeta}_M \right) \right] D^{-1}\left(\bar{\xi}\right) dS\left(\bar{\zeta}\right) \tag{B9}$$

$$S^{**,MNRS}_{ijmn} = \frac{1}{16\pi} C_{klmn} \frac{a_{\bar{M}} a_{\bar{N}}}{a_{\bar{R}} a_{\bar{S}}} \int_{S^2} \left[\left(N_{ik}\left(\bar{\xi}\right)\bar{\xi}_j\bar{\xi}_l + N_{jk}\left(\bar{\xi}\right)\bar{\xi}_i\bar{\xi}_l \right) \left(15\bar{\zeta}_N\bar{\zeta}_M - 3\delta_{NM} \right) \right] D^{-1}\left(\bar{\xi}\right)\bar{\zeta}_R\bar{\zeta}_S dS\left(\bar{\zeta}\right) \tag{B10}$$

with no summation for the barred subscripts in Eqs. (B7), (B9) and (B10). The value of subscript with bar goes with the value used in the summation, e.g.,

$$a_{\bar{M}} H^M V_M = a_1 H^1 V_1 + a_2 H^2 V_2 + a_3 H^3 V_3 \tag{B11}$$

REFERENCES

1. G. B. Olson, Overview: Science of Steel, in Innovations in Ultrahigh-Strength Steel Technology, eds. G. B. Olson, M. Azrin and E. S. Wright Thesis, Proc. 34th Sagamore Army Research Conf., 1990, pp. 3-66.

2. J. W. Christrian, The Theory of Transformation in Metals and Alloys.--Part I, Pergamon Press, 1975.

3. R. Kampmann and R. Wagner, Kinetics of Precipitation in Metastable Binary Alloys, Pergamon Press, New York, 1984, pp. 91-103.

4. T. Mura and N. Kinoshita, The Polynomial Eigenstrain Problem for an Anisotropic Ellipsoidal Inclusion, Phys. Stat. Sol. (a), 48 (1978), pp. 447-450.

5. R. J. Asaro and D. M. Barnett, The Non-uniform Transformation Strain Problem for an Anisotropic Ellipsoidal inclusion, J. Mech. Phys. Solids, 23 (1975), pp. 77-83.

6. Z. A. Moschovidis and T. Mura, Two-ellipsoidal Inhomogeneities by the Equivalent Inclusion Method, J. Appl. Mech., 42 (1975), pp. 847-852.

7. S. D. Gavazza and D. M. Barnett, The Elastic Interaction between a Screw Dislocation and a Spherical Inclusion, Int. J. Engng. Sci., 12 (1974), pp. 1025-1043.

8. J. R. Willis, M. R. Hayns and R. Bullough, The Dislocation Void Interaction, Proc. Roy. Soc., A329 (1972), pp. 121-126.

9. D. M. Barnett, On Nucleation of Coherent Precipitates Near Edge Dislocations, Scripa Metal., 5 (1971), pp. 261-266.

10. T. Mura, Continuous Distribution of Moving Dislocations, Phil. Mag., 8 (1963), pp. 843-857.

11. A. N. Stroh, Dislocations and Cracks in Anisotropic Elasticity, Phil. Mag., 3 (1958), pp. 625-646.

12. D. M. Barnett and J. Lothe, Synthesis of the Sextic and the Integral Formalism for Dislocations, Green's Function, and surface Waves in Anisotropic Elastic Solids, Physica Norveg., 7 (1973), pp. 13-19.

13. D. J. Bacon, D. M. Barnett and R. O. Scattergood, Anisotropic Continuum Theory of Lattice Defects, Progress in Materials Science, 23 (1979), pp. 51-262.

14. T. C. T. Ting, Some Identities And The Structure of N_1 in The Stroh Formalism of Anisotropic Elasticity, Qt. Appl. Math., XLVI (1988), pp. 109-120.

15. T. C. T. TING, Line Forces and Dislocations in Anisotropic Elastic Composite Wedges and Spaces, Phys. Stat. Sol.(b), 145 (1988), pp. 81-90.

16. T. C. T. Ting, Line Forces and Dislocations in Angularly Inhomogeneous Anisotropic Elastic Wedges and Spaces, Quart. J. Mech. Appl. Math., XLVII (1989), pp. 123-128.

17. J. S. Montgomery: Ph. D. Thesis, Northwe. ern University, 1990.

18. A. K. Head, The Energy of a Screw Dislocation in a Cubic Crystal, Phys. Stat. Sol., 5 (1964), pp. 51-54.

19. T. Mura, Micromechanics of Defects in Solids, Martinus Nijhoff, 1987.

20. J. D. Eshelby, The Determination of the Elastic field of an Ellipsoidal Inclusion, and Related Problems, Proc. Roy. Soc., A241 (1957), pp. 376-396.

21. J. D. Eshelby, Progress in Solid Mechanics, II (1961), pp. 89-140.

22. K. C. King, P. W. Voorhees, G. B. Olson and T. Mura, Solute Distribution around a Coherent Precipitate in a Multicompo:ent Alloy, Metall. Trans. A., to be published.

23. T. Mura and P. C. Cheng, The Elastic Field Outside an Ellipsoidal Inclusion, J. Appl. Mech., 44 (1977), pp. 591-594.

ACKNOWLEDGEMENT. We are grateful to Professor T. Mori for many helpful discussions during his visit under AFOSR support, to Professor D. M. Barnett for his sincere comments for this work, to Dr. Jonathan Montgomery for his determinations of the important structural and mechanical input parameters for the ferrite-M_2C system in AF1410. This research is sponsored by the Army Research Office under Grant DAAL03-89-K-0152 as part of the Steel Research Group program of the Materials Research Center of Northwestern University.

THERMAL STRESS IN A HALF SPACE WITH A CYLINDRICAL INHOMOGENEOUS INCLUSION

Hisao Hasegawa, Ruoh-huei Liarng, and Toshio Mura
Department of Civil Engineering
Northwestern University
Evanston, Illinois 60208-3109

The stress and displacement fields in an elastic half space subjected to a circular cylindrical inclusion with uniform temperature distribution are investigated. Using the Green's functions for axisymmetric body forces in elastic half space, one closed form solution is obtained for both interior and exterior elastic fields of the inclusion.

INTRODUCTION

The elastic fields caused by inclusions embedded in elastic half space has been a subject of interest in research fields such as surface science and geology. Many solutions for various eigenstrains can be found in Mura's book [1]. By using the Galerkin vector, Mindlin and Cheng [2] first obtained the solution of the thermoelastic stress field in the semi-infinite solid when a uniform dilatational thermal expansion is given inside a spherical inclusion. Seo and Mura [3] obtained the solution to the same problem, but due to an ellipsoidal inclusion, by using Green's functions found by Mindlin [4] for the semi-infinite isotropic medium. The elastic fields due to a cuboidal inclusion with uniform eigenstrains in a half space was obtained by Chiu [5] using the full space solutions of two cuboidal inclusions solved with specified initial strains that relieve the normal traction acting on the plane of symmetry. Yu and Sanday [6] proposed an alternate method for solving the axisymmetric elastic fields in the half space with an isotropic spheroidal inclusion. Their approach involves the application of the Hankel transformation method for the solution of prismatic dislocation loops and Eshelby's solution for ellipsoidal inclusions.

The solution presented in this paper is the result of a series of investigations by Hasegawa [7–9] on axisymmetric body force problems for semi-infinite elastic me-

Invited Paper: Dedicated to Bruno A. Boley and presented at the Sixty-Fifth Birthday of Bruno A. Boley Symposium, Winter Annual Meeting, American Society of Mechanical Engineers, Atlanta, Georgia, December 1–6, 1991.

The first author's current address is: Department of Mechanical Engineering, Meiji University, Kawasaki, Japan.

Journal of Thermal Stresses, 15:295–310, 1992
Copyright © 1992 by Hemisphere Publishing Corporation

dia. The Green's functions for axisymmetric body force in an elastic half space found by Hasegawa [9] is used to obtain the stress fields caused by a circular cylindrical inclusion. A single analytical solution is obtained for interior and exterior points of the inclusion.

FUNDAMENTAL EQUATIONS

Thermal changes in a body are accompanied by deformations in the relative portions of the body. Such deformations cannot proceed freely. In general, thermal stresses will be caused by constraint from the surrounding medium that prohibits the geometrically incompatible deformation. The strain components ε_{ij}^* in isotropic bodies due to the free thermal expansion are

$$\varepsilon_{ij}^* = \alpha T \delta_{ij} = \varepsilon^* \delta_{ij} \qquad i, j = 1, 2, 3 \tag{1}$$

where α is the coefficient of linear expansion, T is the temperature function, and δ_{ij} is the Kronecker delta.

For infinitesimal deformations considered in this work, the total strain ε_{ij} is regarded as the sum of elastic strain e_{ij} and thermal strain ε_{ij}^*, that is,

$$\varepsilon_{ij} = e_{ij} + \varepsilon_{ij}^* \tag{2}$$

The total strain must be compatible,

$$\varepsilon_{ij} = \frac{1}{2}(u_{i,j} + u_{j,i}) \tag{3}$$

where u_i are the displacement components and $u_{i,j} = \partial u_i / \partial x_j$. For an isotropic material, elastic strains are related to stresses σ_{ij} such that

$$e_{ij} = \frac{1}{2\mu}\left(\sigma_{ij} - \frac{\nu}{1+\nu}\sigma_{kk}\delta_{ij}\right) \tag{4}$$

It is assumed that the temperature changes are so small that the elastic moduli remain constant. Thus, the substitution of Eqs. (1) and (4) in Eq. (2) gives

$$\varepsilon_{ij} = \frac{1}{2\mu}\sigma_{ij} - \left[\frac{\nu}{2\mu(1+\nu)}\sigma_{kk} - \varepsilon^*\right]\delta_{ij} \tag{5}$$

and, solving for the σ_{ij}, it becomes

$$\sigma_{ij} = 2\mu\varepsilon_{ij} + \lambda\varepsilon_{kk}\delta_{ij} - (3\lambda + 2\mu)\varepsilon^*\delta_{ij} \tag{6}$$

where ν is the Poison's ratio and λ and μ are the Lame's constants. By the generalized Hooke's law, the stress components can be expressed as

$$\sigma_{ij} = C_{ijkl}(\varepsilon_{kl} - \delta_{kl}\varepsilon^*) \tag{6'}$$

The equilibrium equations under body force f are

$$\sigma_{ij,j} + f_i = 0 \tag{7}$$

When Eq. (6) is substituted into Eq. (7), it gives

$$(C_{ijkl}u_{k,l})_{,j} - (C_{ijkl}\delta_{kl}\varepsilon^*)_{,j} + f_i = 0 \tag{8}$$

If the inclusion is an inhomogeneity that has elastic moduli different than those of the matrix, it is assumed that the C_{ijkl} in the above Eq. (8) are piecewise continuous functions of x such that they are constant C_{ijkl} in the matrix and another constant C^*_{ijkl} in Ω. However, the inhomogeneous inclusion Ω can be simulated by an equivalent homogeneous inclusion by adding extra eigenstrain ε^{**}_{kl} called equivalent eigenstrains. They can be determined by

$$C^*_{ijkl}(u_{k,l} - \delta_{kl}\varepsilon^*) = C_{ijkl}(u_{k,l} - \delta_{kl}\varepsilon^* - \varepsilon^{**}_{kl}) \tag{9}$$

For isotropic materials, the equivalent eigenstrain can be written as $\varepsilon^{**}_{kl} = \delta_{kl}\varepsilon^{**}$. Equation (9) is simplified into

$$(3\lambda^* + 2\mu^*)(u_{k,k} - \varepsilon^*) = (3\lambda + 2\mu)(u_{k,k} - \varepsilon^* - \varepsilon^{**}) \tag{9'}$$

In this case, the equations of equilibrium (8) can be written as

$$C_{ijkl}u_{k,lj} - C_{ijkl}\delta_{kl}(\varepsilon^* + \varepsilon^{**})_{,j} + f_i = 0 \tag{8'}$$

Since $\varepsilon^* + \varepsilon^{**}$ is zero in the matrix and uniform in the inclusion, $(\varepsilon^* + \varepsilon^{**})_{,j}$ is the delta function defined on the boundary of Ω.

For an isotropic material, Eq. (8') becomes

$$\mu\nabla^2 u_i + (\mu + \lambda)\vartheta_{,i} = -f_i + (3\lambda + 2\mu)(\varepsilon^* + \varepsilon^{**})_{,i} \qquad i = 1, 2, 3 \tag{10}$$

where $\vartheta = \varepsilon_{kk} = u_{k,k}$ and $\varepsilon^*_j = \partial\varepsilon^*/\partial x_j$. When the matrix and the inhomogeneity have different thermal expansion coefficients, ε^*_j becomes the delta function on the boundary of Ω. The terms on the right-hand side of Eq. (10) can be treated as the effective body force components.

ELASTIC SOLUTIONS

If the Green's function $G_{ij}(\mathbf{x} - \mathbf{x}')$ is the displacement in x_i-direction at point x when a unit body force in x_j-direction is applied at point x' in an elastic medium, then the displacement components u_i in Eq. (8) are written as

$$u_i(\mathbf{x}) = -\int_{-\infty} G_{ij}(\mathbf{x} - \mathbf{x}')C_{jmnl}[\varepsilon^*_{mn}(\mathbf{x}') + \varepsilon^{**}_{mn}(\mathbf{x}')]_{,l}\, d\mathbf{x}'$$

or integrating by parts to get

$$u_i(\mathbf{x}) = -\int_{-\infty}^{\infty} G_{ij,j}(\mathbf{x} - \mathbf{x}')C_{jlmn}[\varepsilon^{*}_{mn}(\mathbf{x}') + \varepsilon^{**}_{mn}(\mathbf{x}')]\, d\mathbf{x}' \tag{11}$$

The corresponding stress components are

$$\sigma_{ij}(\mathbf{x}) = -C_{ijkl}\int_{-\infty}^{\infty} G_{kp,ql}(\mathbf{x} - \mathbf{x}')C_{pqmn}[\varepsilon^{*}_{mn}(\mathbf{x}') + \varepsilon^{**}_{mn}(\mathbf{x}')]\, d\mathbf{x}'$$

$$-C_{ijkl}[\varepsilon^{*}_{kl}(\mathbf{x}) + \varepsilon^{**}_{kl}(\mathbf{x})] \tag{12}$$

In this paper, a solid circular cylindrical homogeneous inclusion in the interior of an elastic half space, as shown in Fig. 1, is considered. Under the cylindrical coordinate system (r, θ, z), the surface $z = 0$ of the half space $(0 \le r < \infty, 0 \le z)$ satisfies the free boundary conditions

$$\sigma_z = \tau_{zr} = \tau_{z\theta} = 0 \tag{13}$$

and the uniform dilatational strains

$$\varepsilon^{*} = \varepsilon^{*}(r, z) = \varepsilon_0\{1 - S(r - c)\}\{S(z - b_1) - S(z - b_2)\} \qquad b_i > 0 \tag{14}$$

are distributed within the half space. Here $S(\ )$ is a Heaviside step function, ε_0 is the magnitude of eigenstrains, and c and $b = b_1 - b_2$ are the radius and the length

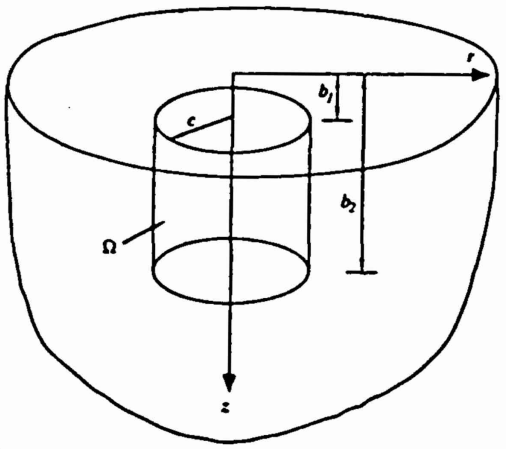


Fig. 1 A solid cylindrical inclusion in an elastic half space.

of the cylindrical inclusion, respectively. Neglecting the body force terms f_i, Eq. (10) now becomes

$$\mu\left(\nabla^2 - \frac{1}{r^2}\right)u_i + \mu\delta_{3i}\frac{u_3}{r^2} + (\lambda + \mu)[\nabla(\nabla \cdot \mathbf{U})]_i = (3\lambda + 2\mu)\varepsilon_{ij}^* \tag{15}$$

where U is a vector with components u_i, $i = 1, 2, 3$, corresponding to the displacements in the r-, θ-, and z-directions.

The general solutions can be simplified readily for the above problem. After considering the isotropy and axisymmetry properties, Eqs. (11) and (12) become

$$u_i(\mathbf{x}) = -(3\lambda + 2\mu)\int_\Omega G_{ik,k}(\mathbf{x} - \mathbf{x}')\varepsilon^*(\mathbf{x}')\,d\mathbf{x}' \tag{11'}$$

$$\sigma_{ij}(\mathbf{x}) = -(3\lambda + 2\mu)^2\int_\Omega G_{ik,kj}(\mathbf{x} - \mathbf{x}')\varepsilon^*(\mathbf{x}')\,d\mathbf{x}' - \sigma_{ij}^* \tag{12'}$$

where $\sigma_{ij}^* = 2\mu\varepsilon_{ij}^* + \lambda\delta_{ij}\varepsilon_{kk}^*$. It has been shown by Hasegawa [9] that the solution of the elastic fields in a semi-infinite medium caused by axisymmetric body forces is

$$u_i(\mathbf{x}) = -\int_0^\infty \Gamma_{ik}^H(\mathbf{x} - \mathbf{x}')F_k(\mathbf{x}')\,d\mathbf{x}' \tag{16}$$

$$\sigma_{ij}(\mathbf{x}) = -\int_0^\infty \Sigma_{ijk}^H(\mathbf{x} - \mathbf{x}')F_k(\mathbf{x}')\,d\mathbf{x}' - \sigma_{ij}^* \tag{17}$$

where $F_k(\mathbf{x}')$ are body forces in the x_k-direction and $\Gamma_{ik}^H(\mathbf{x} - \mathbf{x}')$ and $\Sigma_{ijk}^H(\mathbf{x} - \mathbf{x}')$, the Green's functions given by Hasegawa, denote the displacement and stress components, respectively, when an axisymmetric unit ring force in x_k-direction acts at a distance z' from the half space boundary along a circle of radius r'. The nonzero components of the Green's function Γ_{ik}^H can be expressed as follows:

$$\Gamma_{11}^H(\mathbf{x} - \mathbf{x}') = \frac{1}{\pi\mu(1 - \nu)}\int_0^\infty\int_0^\infty \alpha\bar{b}_1\left[\frac{2(1 - \nu)}{\alpha^2 + \beta^2} - \frac{\alpha^2}{(\alpha^2 + \beta^2)^2}\right]J_1(\alpha r)\cos(\beta z)\,d\alpha\,d\beta$$

$$+ \int_0^\infty (1 - 2\nu - \alpha z)\bar{P}_3 J_1(\alpha r)e^{-\alpha z}\,d\alpha \tag{18a}$$

$$\Gamma_{31}^H(\mathbf{x} - \mathbf{x}') = \frac{-1}{2\pi\mu(1 - \nu)}\int_0^\infty\int_0^\infty \bar{b}_1\frac{\alpha^2\beta}{(\alpha^2 + \beta^2)^2}J_0(\alpha r)\sin(\beta z)\,d\alpha\,d\beta$$

$$- \int_0^\infty (2 - 2\nu + \alpha z)\bar{P}_3 J_0(\alpha r)e^{-\alpha z}\,d\alpha \tag{18b}$$

$$\Gamma^{H}_{22}(\mathbf{x}-\mathbf{x}') = \frac{2}{\pi\mu}\int_0^\infty\int_0^\infty \bar{b}_2 \frac{\alpha}{\alpha^2+\beta^2} J_1(\alpha r)\cos(\beta z)\,d\alpha\,d\beta \tag{18c}$$

$$\Gamma^{H}_{13}(\mathbf{x}-\mathbf{x}') = \frac{1}{\pi\mu(1-\nu)}\int_0^\infty\int_0^\infty \bar{b}_3 \frac{\alpha^2\beta}{(\alpha^2+\beta^2)^2} J_1(\alpha r)\sin(\beta z)\,d\alpha\,d\beta$$
$$-\int_0^\infty (2-2\nu-\alpha z)\bar{P}_1 J_1(\alpha r)e^{-\alpha z}\,d\alpha \tag{18d}$$

$$\Gamma^{H}_{33}(\mathbf{x}-\mathbf{x}') = \frac{1}{\pi\mu(1-\nu)}\int_0^\infty\int_0^\infty \alpha\bar{b}_3\left[\frac{2(1-\nu)}{\alpha^2+\beta^2} - \frac{\beta^2}{(\alpha^2+\beta^2)^2}\right] J_0(\alpha r)\cos(\beta z)\,d\alpha\,d\beta$$
$$+\int_0^\infty (1-2\nu+\alpha z)\bar{P}_1 J_0(\alpha r)e^{-\alpha z}\,d\alpha \tag{18e}$$

where

$$\bar{b}_i = \int_0^\infty\int_0^\infty r b_i J_m(\alpha r)\cos(\beta z)\,dr\,dz \qquad m = 1-\delta_{i3} \tag{19a}$$

$$b_i = \frac{1}{2\pi r}\delta(r-r')\delta(z-z') \tag{19b}$$

$$\bar{P}_1 = \frac{2}{\pi(1-\nu)}\int_0^\infty \alpha\bar{b}_3\left[\frac{1-\nu}{\alpha^2+\beta^2} - \frac{\beta^2}{(\alpha^2+\beta^2)^2}\right] d\beta \tag{19c}$$

$$\bar{P}_3 = \frac{2}{\pi(1-\nu)}\int_0^\infty \alpha\bar{b}_1\left[\frac{1-\nu}{\alpha^2+\beta^2} - \frac{\alpha^2}{(\alpha^2+\beta^2)^2}\right] d\beta \tag{19d}$$

Here b_i are the axisymmetric unit body forces mentioned above, and J_m is the Bessel function, of the first kind of order m.

For the present case, body forces $Fk(\mathbf{x}')$ in Eqs. (16) and (17) can be substituted by the effective body forces $(3\lambda + 2\mu)[\varepsilon^*(\mathbf{x}')]_{,i}$ in Eq. (15). Thus,

$$u_i(\mathbf{x}) = -(3\lambda+2\mu)\int_\Omega \Gamma^{H}_{ik}(\mathbf{x}-\mathbf{x}')[\varepsilon^*(\mathbf{x}')]_{,k}\,d\mathbf{x}' \tag{20}$$

$$\sigma_{ij}(\mathbf{x}) = -(3\lambda+2\mu)\int_\Omega \Sigma^{H}_{ijk}(\mathbf{x}-\mathbf{x}')[\varepsilon^*(\mathbf{x}')]_{,k}\,d\mathbf{x}' - \sigma^*_{ij} \tag{21}$$

Recently, the authors [10] use the axisymmetric Green's functions to obtain so-

lutions due to axial eigenstrains given in a cylindrical inclusion. The same method is applied here to find solutions due to thermal expansions. Therefore, from Eqs. (14), (20), and (21) one obtains

$$u_i(r, z) = 2\pi\varepsilon_0(3\lambda + 2\mu)\left\{c\int_{b_1}^{b_2}\Gamma_{i1}^H(r, z, c, z')\,dz' + \int_0^c [\Gamma_{i3}^H(r, z, r', b_1) - \Gamma_{i3}^H(r, z, r', b_2)]r'\,dr'\right\} \quad (22)$$

$$\sigma_{ij}(r, z) = 2\pi\varepsilon_0(3\lambda + 2\mu)\left\{c\int_{b_1}^{b_2}\Sigma_{ij1}^H(r, z, c, z')\,dz' + \int_0^c [\Sigma_{ij3}^H(r, z, r', b_1) - \Sigma_{ij3}^H(r, z, r', b_2)]r'\,dr'\right\} - \sigma_{ij}^* \quad (23)$$

The integrals in Eq. (22) are performed by using integral formulas [11, 12], and the final results are

$$2\mu u_j = \frac{4\pi\mu(1+\nu)c\varepsilon_0}{(1-2\nu)D}\sum_{n=1}^{2}(-1)^n\left\{\sum_{i=1}^{2}[\bar{u}_j^1 + \bar{u}_j^3] + \bar{u}_j^1 + \bar{u}_j^3\right\} \quad (24)$$

with

$$\bar{u}_r^1 = (-1)^i z_i\left\{2(1-\nu)Q_{1/2}(x_i) + \frac{1-2\nu}{2cr}[(c^2 + r^2)Q_{-1/2}(x_i) - (c-r)^2 k_i \Pi(p, k_i)]\right\} \quad (25a)$$

$$\bar{u}_r^3 = z_i Q_{1/2}(x_i) \quad (25b)$$

$$\bar{u}_z^1 = (-1)^i\left\{rG_2(x_i) + \frac{c^2 - r^2 - z_i^2}{2c}Q_{-1/12}(x_i)\right\} \quad (25c)$$

$$\bar{u}_z^3 = (3-4\nu)rG_2(x_i) + \frac{(3-4\nu)(c^2-r^2) - z_i^2}{2c}Q_{-1/2}(x_i) + \frac{(1-2\nu)(c-r)z_i^2 k_i}{c(c+r)}\Pi(p, k_i) - \frac{(1-2\nu)\pi\sqrt{cr}|z_i|}{c}[1 + \mathrm{SGN}(c-r)] \quad (25d)$$

$$\bar{u}_r^1 = -\frac{\nu(1-2\nu)}{cr}\{-z_2(c-r)^2 k_2\Pi(p, k_2) + z_2(c^2 + r^2)Q_{-1/2}(x_2)\}$$

$$+ 2[b_n - \nu(3 - 2\nu)z_2]Q_{1/2}(x_2) \tag{25e}$$

$$\tilde{u}_r^3 = -\frac{(1-\nu)(1-2\nu)}{cr}[(c-r)^2 z_2 k_2 \Pi(p, k_2) - z_2(c^2 + r^2)Q_{-1/2}(x_2)]$$

$$+ \{2(2-\nu)(1-2\nu)z - 2(1-\nu)(1+2\nu)b_n\}Q_{1/2}(x_2)$$

$$- \frac{b_n z z_2}{cr(x_2^2 - 1)} G_1(x_2) \tag{25f}$$

$$\tilde{u}_z^1 = -8\nu(1-\nu)rG_2(x_2) - \frac{b_n z}{r}\left[Q_{1/2}(x_2) - \frac{x_2 - r/c}{x_2^2 - 1} G_1(x_2)\right]$$

$$- 2(1-\nu)(1-2\nu)\pi b_n \frac{\sqrt{cr}}{c}[1 + \mathrm{SGN}(c-r)]$$

$$+ \frac{2(1-2\nu)(c-r)z_2 k_2}{c(c+r)} \Pi(p, k_2)[(1-\nu)b_n - \nu z]$$

$$+ \frac{2}{c}[(1-\nu)b_n z_2 + \nu z z_2 - 2\nu(1-\nu)(c^2 - r^2)]Q_{-1/2}(x_2) \tag{25g}$$

$$\tilde{u}_z^3 = (1-2\nu)^2 r\left[2G_2(x_2) + \frac{c^2 - r^2}{cr} Q_{-1/2}(x_2)\right]$$

$$- (1-2\nu)\frac{z_2^2}{c}\left[\frac{2\nu(c-r)k_2}{c+r}\Pi(p, k_2) + Q_{-1/2}(x_2)\right]$$

$$+ 2\nu(1-2\nu)\frac{\pi\sqrt{cr}z_2}{c}[1 + \mathrm{SGN}(c-r)]$$

$$+ \frac{b_n z}{r}\left[Q_{1/2}(x_2) - \frac{x_2 - r/c}{x_2^2 - 1} G_1(x_2)\right] \tag{25h}$$

where

$$D = 8\pi^2\sqrt{cr}(1-\nu) \qquad z_1 = z - b_n \qquad z_2 = z + b_n \qquad x_i = \frac{r^2 + c^2 + z_i^2}{2cr}$$

$$p = \frac{4cr}{(c+r)^2} \qquad k_i^2 = \frac{4cr}{(c+r)^2 + z_i^2}$$

$$G_1(x_i) = x_i Q_{1/2}(x_i) - Q_{-1/2}(x_i) \qquad G_2(x_i) = x_i Q_{-1/2}(x_i) - Q_{1/2}(x_i)$$

and SGN$(c - r)$ is $+1$, 0, or -1 according to positive, zero, or negative value of $(c - r)$; $Q_n(x_i)$ is the Legendre function of the second kind of order n; $\Pi(p, k_i)$ is the complete elliptic integral of the third kind.

Equation (23) can be integrated in the same way to get

$$\sigma_{pq} = \frac{4\pi\mu(1+\nu)c\varepsilon_0}{(1-2\nu)D} \sum_{n=1}^{2} (-1)^n \left\{ \sum_{i=1}^{2} [\bar{\sigma}^1_{pq} + \bar{\sigma}^3_{pq}] + \bar{\sigma}^1_{pq} + \bar{\sigma}^3_{pq} \right\} \tag{26}$$

with

$$\bar{\sigma}^1_r = \frac{(-1)^i z_i}{2c} \left\{ \left[1 - \frac{(1-2\nu)c^2}{r^2} \right] Q_{-1/2}(x_i) - \frac{(3-4\nu)c}{r} Q_{1/2}(x_i) - \frac{c(x_i - r/c)}{r(x_i^2 - 1)} G_1(x_i) + \left[2(1-\nu)\frac{c-r}{c+r} + \frac{(1-2\nu)(c-r)^2}{r^2} \right] k_i \Pi(p, k_i) \right\} \tag{27a}$$

$$\bar{\sigma}^1_\theta = \frac{(-1)^i z_i}{2c} \left\{ \left[1 + \frac{(1-2\nu)c^2}{r^2} \right] Q_{-1/2}(x_i) + \frac{4(1-\nu)c}{r} Q_{1/2}(x_i) + \left[2\nu \frac{c-r}{c+r} - \frac{(1-2\nu)(c-r)^2}{r^2} \right] k_i \Pi(p, k_i) \right\} \tag{27b}$$

$$\bar{\sigma}^1_z = \frac{(-1)^i z_i}{2c} \left\{ -\frac{c}{r} \left[Q_{1/2}(x_i) - \frac{x_i - r/c}{x_i^2 - 1} G_1(x_i) \right] + 2\nu \left[Q_{-1/2}(x_i) + \frac{c-r}{c+r} k_i \Pi(p, k_i) \right] \right\} \tag{27c}$$

$$\bar{\tau}^1_{rz} = \frac{(-1)^i}{2} \left[2(1-2\nu) Q_{1/2}(x_i) + \frac{z_i^2}{cr(x_i^2 - 1)} G_1(x_i) \right] \tag{27d}$$

$$\bar{\sigma}^3_r = \frac{z_i}{2c} \left\{ -\frac{c}{r} \left[Q_{1/2}(x_i) + \frac{x_i - r/c}{x_i^2 - 1} G_1(x_i) \right] + 2\nu \left[Q_{-1/2}(x_i) + \frac{c-r}{c+r} k_i \Pi(p, k_i) \right] \right\} \tag{27e}$$

$$\bar{\sigma}^3_\theta = \frac{z_i}{c} \left\{ \frac{c}{r} Q_{1/2}(x_i) + \nu \left[Q_{-1/2}(x_i) + \frac{c-r}{c+r} k_i \Pi(p, k_i) \right] \right\} \tag{27f}$$

$$\bar{\sigma}^3_z = \frac{z_i}{2c} \left\{ -\frac{c}{r} \left[Q_{1/2}(x_i) - \frac{x_i - r/c}{x_i^2 - 1} G_1(x_i) \right] \right.$$

$$+ 2(1-\nu)\left[Q_{-1/2}(x_1) + \frac{c-r}{c+r}k_1\Pi(p,k_1)\right]\Bigg\} \tag{27g}$$

$$\bar{\tau}^3_{rz} = -\frac{1}{2}\left[2(1-2\nu)Q_{1/2}(x_1) - \frac{1}{x_1^2-1}\frac{z_1^2}{cr}G_1(x_1)\right] \tag{27h}$$

$$\begin{aligned}\bar{\sigma}^1_r = \frac{1}{c}\Bigg\{&-\left[2\nu - \nu(1-2\nu)\frac{c^2+r^2}{r^2}\right]z_2Q_{-1/2}(x_2)\\ &-\left[2\nu\frac{c-r}{c+r} + \frac{\nu(1-2\nu)(c-r)^2}{r^2}\right]z_2k_2\Pi(p,k_2)\\ &+\frac{2\nu c}{r}[2z + (1-2\nu)z_2]Q_{1/2}(x_2)\\ &-\frac{c}{r}\left[(b_n - 4b_n\nu + 2\nu z)Q_{1/2}(x_2) + (b_n - 2\nu z)\frac{x_2 - r/c}{x_2^2-1}G_1(x_2)\right]\\ &-\frac{b_n z z_2}{2r^2(x_2^2-1)}\left[3Q_{-1/2}(x_2) + \frac{r}{c}Q_{1/2}(x_2)\right]\\ &-\frac{4}{x_2^2-1}\left(G_1(x_2) + \frac{r}{c}G_2(x_2)\right) + 2G_1(x_2)\Bigg\}\end{aligned} \tag{27i}$$

$$\begin{aligned}\bar{\sigma}^1_\theta = \frac{2}{c}\Bigg\{&-z_2\nu\left[2\nu\frac{c-r}{c+r} - \frac{(1-2\nu)(c-r)^2}{2r^2}\right]k_2\Pi(p,k_2)\\ &-\frac{\nu z_2}{2}\left[(1+2\nu) + (1-2\nu)\frac{c^2}{r^2}\right]Q_{-1/2}(x_2)\\ &+\frac{c}{r}[(1-\nu)b_n - 2\nu z - \nu(1-2\nu)z_2]Q_{1/2}(x_2)\\ &+\frac{b_n c}{r(x_2^2-1)}\left[\frac{zz_2}{2cr} - \nu(x_2 - r/c)\right]\Bigg\}\end{aligned} \tag{27j}$$

$$\begin{aligned}\bar{\sigma}^1_z = \frac{1}{c}\Bigg\{&\frac{(b_n + 2\nu z)c}{r}\left[Q_{1/2}(x_2) - \frac{x_2 - r/c}{x_2^2-1}G_1(x_2)\right]\\ &-2\nu z_2\left[Q_{-1/2}(x_2) + \frac{c-r}{c+r}k_2\Pi(p,k_2)\right]\end{aligned}$$

$$+\frac{b_n z z_2}{2r^2(x_2^2-1)}\left[3Q_{-1/2}(x_2)+\frac{r}{c}Q_{1/2}(x_2)\right.$$

$$\left.-\frac{4}{x_2^2-1}\left(G_1(x_2)+\frac{r}{c}G_2(x_2)\right)\right]\Bigg\} \tag{27k}$$

$$\bar{\tau}_{rz}^1=\frac{z}{cr}\left\{\frac{b_n-2\nu z_2}{x_2^2-1}G_1(x_2)-\frac{b_n}{x_2^2-1}\left[\frac{z_2^2}{2cr}Q_{1/2}(x_2)-\frac{2z_2^2}{cr(x_2^2-1)}G_2(x_2)\right]\right\} \tag{27l}$$

$$\bar{\sigma}_r^3=\frac{2}{r}\left\{-\frac{b_n z z_2}{c^2(x_2^2-1)^2}G_2(x_2)\right.$$

$$+\left[\frac{3b_n z z_2}{4cr(x_2^2-1)}+\frac{rz_2(1-2\nu)}{c}\left(\frac{1+\nu}{2}-\frac{c^2(1-\nu)}{2r^2}\right)\right]Q_{-1/2}(x_2)$$

$$+\left[\frac{b_n z z_2}{4c^2(x_2^2-1)}-\frac{(1-2\nu)(3-2\nu)z}{2}+\nu(1-2\nu)b_n\right]Q_{1/2}(x_2)$$

$$+\frac{rz_2(1-2\nu)}{c}\left[\frac{c-r}{c+r}+\frac{(1-\nu)(c-r)^2}{2r^2}\right]k_2\Pi(p,k_2)$$

$$+\frac{1}{x_2^2-1}\left[\frac{b_n z z_2}{2cr}\left(1-\frac{2}{x_2^2-1}\right)\right.$$

$$\left.\left.-\frac{(1-2\nu)z-2b_n}{2}(x_2-r/c)\right]G_1(x_2)\right\} \tag{27m}$$

$$\bar{\sigma}_\theta^3=-\frac{2}{r}\left\{\frac{1}{x_2^2-1}\left[\frac{b_n z z_2}{2cr}-b_n\nu(x_2-r/c)\right]G_1(x_2)\right.$$

$$-\frac{z_2(1-2\nu)}{2c}\left[2\nu r+(1-\nu)\frac{c^2+r^2}{r}\right]Q_{-1/2}(x_2)$$

$$+\frac{z_2}{2c}(c-r)(1-2\nu)\left[-\frac{2\nu r}{c+r}+(1-\nu)\frac{c-r}{r}\right]k_2\Pi(p,k_2)$$

$$\left.-[(1-2\nu)(2-\nu)z-b_n(1+2\nu-2\nu^2)]Q_{1/2}(x_2)\right\} \tag{27n}$$

$$\bar{\sigma}_z^3=\frac{z}{r}\left\{\frac{1}{x_2^2-1}\left[\frac{2b_n z_2}{cr(x_2^2-1)}+(1-2\nu)(x_2-r/c)\right]G_1(x_2)\right.$$

$$+\frac{2b_n z_2}{c^2(x_2^2-1)^2}G_2(x_2)-\frac{3b_n z_2}{2cr(x_2^2-1)}Q_{-1/2}(x_2)$$

$$-\left[\frac{b_n z_2}{2c^2(x_2^2-1)}+1-2\nu\right]Q_{1/2}(x_2)\Bigg\} \tag{27o}$$

$$\tilde{\tau}_{rz}^{33}=\frac{1}{cr(x_2^2-1)}[(1-2\nu)zz_2-b_n(z+z_2)]G_1(x_2)-\frac{2b_n zz_2^2}{c^2r^2(x_2^2-1)^2}G_2(x_2)$$

$$+\left[\frac{b_n zz_2^2}{2c^2r^2(x_2^2-1)}+2(1-2\nu)\right]Q_{1/2}(x_2) \tag{27p}$$

Equations (24) and (26) satisfy the fundamental equations of elasticity (15) subject to the boundary conditions in Eq. (13) through the semi-infinite domain.

DISCUSSION AND RESULTS

Numerical calculations for displacement and stress fields have been performed for a homogeneous cylindrical inclusion with given dilatational eigenstrains. The Poisson's ratio of the material is assumed to be 0.3; the length and radius of the inclusion are both 1.0. The distance from the center plane of the inclusion to the elastic free surface, which is called the depth of the inclusion, is x_0.

Figure 2 shows the effect of inclusion depth on displacements on the free surface. It is evident that as the depth of the inclusion increases, the magnitude of the surface displacements decreases.

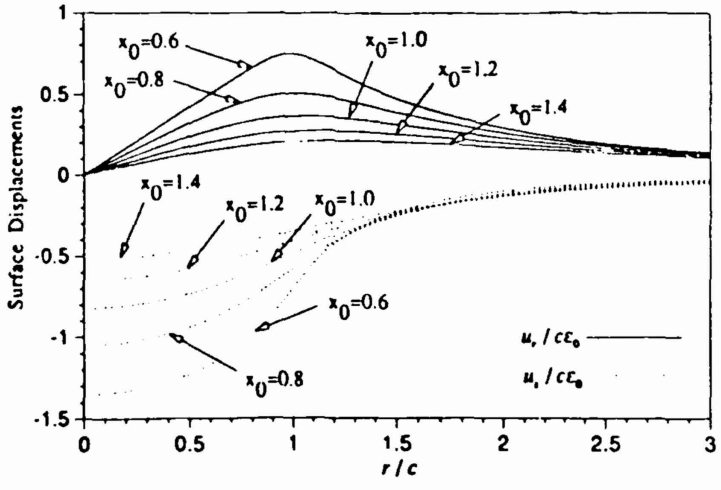


Fig. 2 Effect of the inclusion depth (x_0) on the surface displacements.

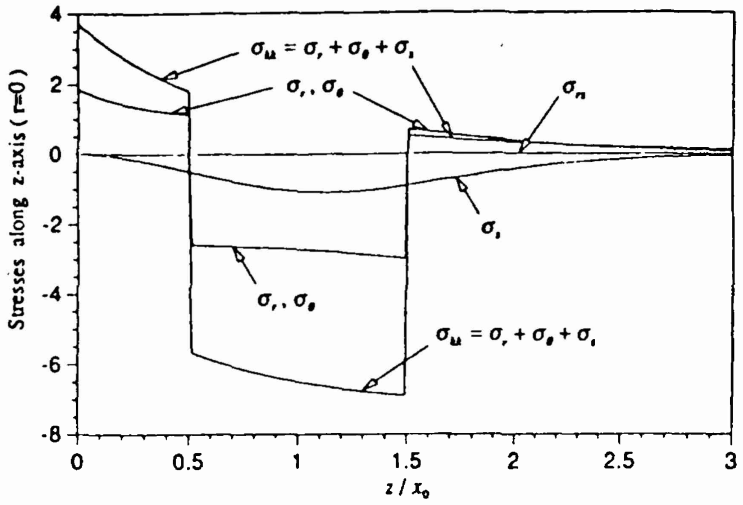


Fig. 3 Variation of stresses along z-axis ($r = 0$).

Figures 3 to 8 show the distributions of stresses due to an inclusion with depth $x_0 = 1$. As expected, all of the stress components are negative for interior points. Normal stress components are continuous while the other stress components change signs across the inclusion boundary.

Figures 3 and 4 illustrate the variation of all the nonzero stress components along z-axis and along the center plane of this inclusion. It is observed that σ_r has the

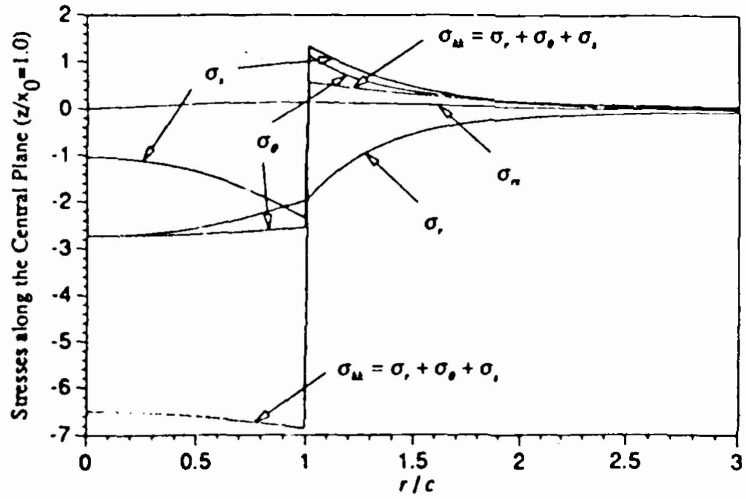


Fig. 4 Variation of stresses along r-direction on the central plane of the inclusion.

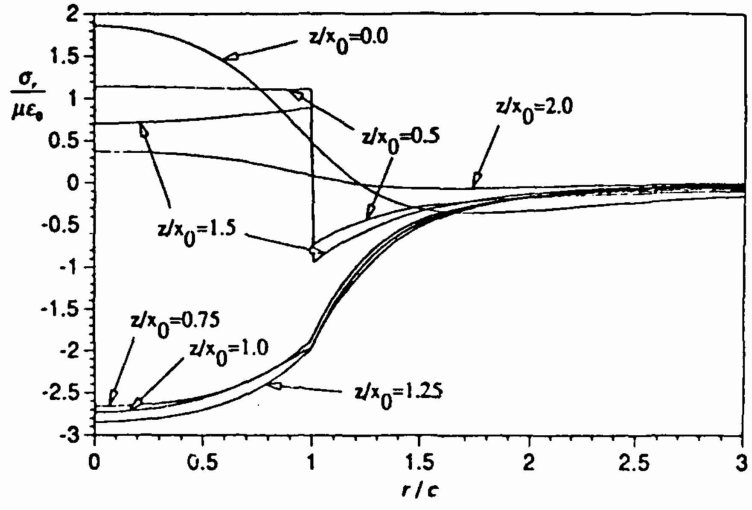


Fig. 5 Variation of σ_r along r-direction on different depth z/x_0.

smallest magnitude and σ_r and σ_θ are almost of the same value inside the inclusion. This result is not surprising if one considers the constraint of a half space on an embedded inclusion.

Although the stress distributions are not uniform in general, it is worth to note in Figs. 7 and 8 that the hydrostatic stress is nearly constant in the inclusion. Therefore, the elastic strain energy for the present case can be approximated by $W^* = -\frac{1}{2} V\sigma_{kk}\varepsilon_0$, where V is the volume of the cylindrical inclusion.

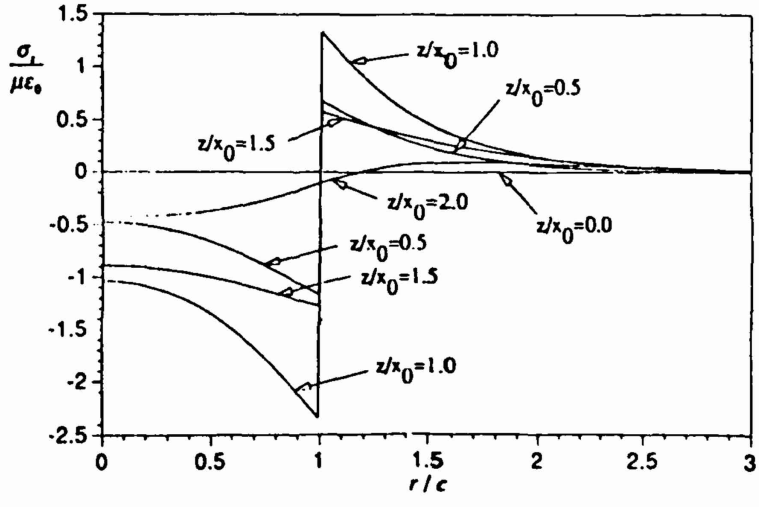


Fig. 6 Variation of σ_z along r-direction on different depth z/x_0.

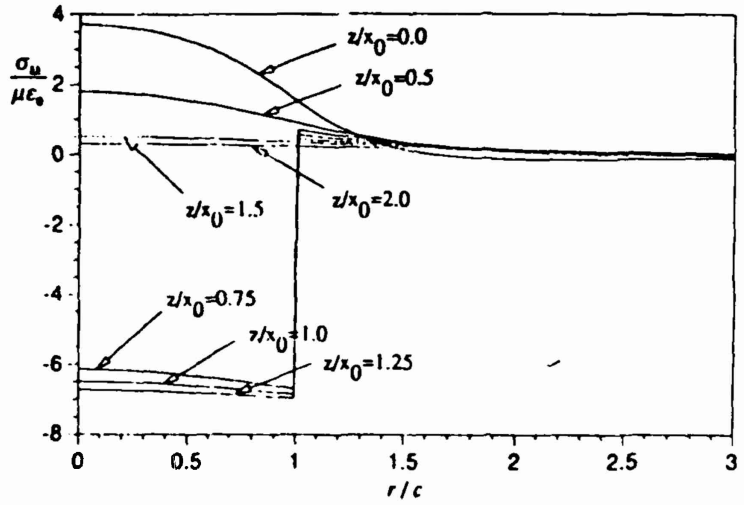


Fig. 7 Variation of σ_M along r-direction on different depth z/x_0.

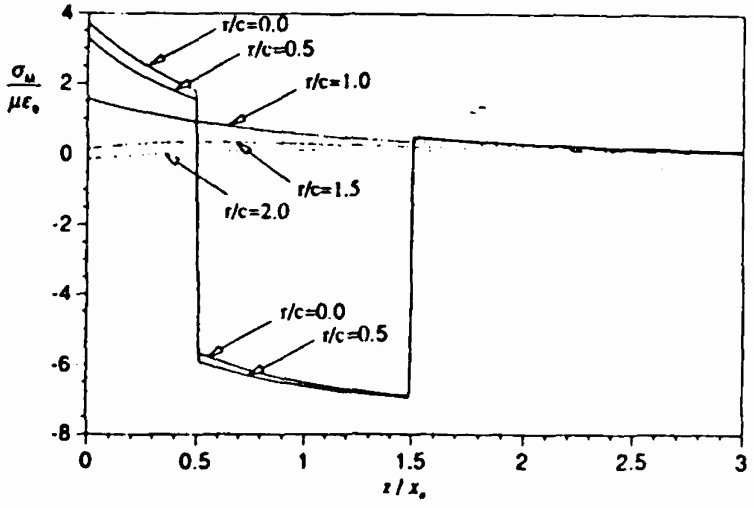


Fig. 8 Variation of σ_M along z-direction on different radius r/c.

CONCLUSIONS

In this paper, exact solutions in closed forms were shown for thermal stress fields produced by a circular cylindrical inclusion with uniform temperature in an elastic half space. The solution was easily obtained by using the stress fields due to a circular cylindrical inclusion with uniform axial eigenstrain in an elastic half space.

ACKNOWLEDGMENT

This research work was supported mainly by the Army Research Office under contract number DAAL03-K-0512 and was partially supported by AFOSR-89-0269.

REFERENCES

1. T. Mura, *Micromechanics of Defects in Solids*, Martinus-Nijhoff, Dordrecht, 1982.
2. R. D. Mindlin and D. H. Cheng, Thermoelastic Stress, in The Semi-Infinite Solid, *J. Appl. Phys.*, vol. 21, pp. 931–933, 1950.
3. K. Seo and T. Mura, The Elastic Field in a Half Space Due to Ellipsoidal Inclusions with Uniform Dilatational Eigenstrains, *ASME J. Appl. Mech.*, vol. 46, pp. 568–572, 1979.
4. R. D. Mindlin, Force at a Point in the Interior of a Semi-Infinite Solid, *Proc. First Midwestern Conf. on Solid Mechanics*, pp. 55–59, 1953.
5. Y. P. Chiu, On the Stress Field and Surface Deformation in a Half Space with a Cuboidal Zone in which Initial Strains are Uniform, *ASME J. Appl. Mech.*, vol. 45, pp. 302–306, 1978.
6. H. Y. Yu and S. C. Sanday, Axisymmetric Inclusion in a Half Space, *ASME J. Appl. Mech.*, vol. 57, pp. 74–77, 1990.
7. H. Hasegawa, An Extension of Love's Solution for the Axisymmetric Problems of Elasticity, *Bull. JSME*, vol. 18, pp. 484–492, 1975.
8. H. Hasegawa, Axisymmetric Body Force Problems of an Elastic Half Space. *Bull. JSME*, vol. 19, pp. 1262–1269, 1976.
9. H. Hasegawa, Green's Functions for Axisymmetric Body Force Problems of an Elastic Half Space and Their Application, *Bull. JSME*, vol. 27, pp. 1829–1835, 1984.
10. H. Hasegawa, V.-G. Lee, and T. Mura, The Stress Fields Caused by a Circular Cylindrical Inclusion in an Elastic Half Space, *ASME J. Appl. Mech.*, in press.
11. A. Erdelyi, *Tables of Integral Transforms*, vol. 1, 2, McGraw-Hill, New York, 1945.
12. G. Eason, B. Noble and I. N. Sneddon, On Certain Integrals of Lipschitz-Hankel Type Involving Products of Bessel Functions, *Philo. Trans. Roy. Soc. London Ser. A*, vol. 247, pp. 529–551, 1955.

Received November 11, 1991

M_2C CARBIDE PRECIPITATION IN AF1410

J.S. Montgomery and G.B. Olson

U.S. Army Materials Technology Laboratory
and
Northwestern University

ABSTRACT

M_2C carbide precipitation was investigated in a martensitic Co-Ni steel, AF1410. Results of TEM (from both thin foils and extraction replicas) and X-ray diffraction were combined with results of collaborative SANS and APFIM studies to determine phase fractions, compositions, and lattice parameters throughout precipitation, including estimation of carbide initial critical nucleus properties. The composition dependence of the M_2C lattice parameters was modelled to predict the composition-dependent transformation eigenstrains for coherent precipitation; this was input into collaborative numerical calculations of both the coherent carbide elastic self energy and the dislocation interaction energy during heterogeneous precipitation.

The observed overall precipitation behavior is consistent with theoretically-predicted behavior at high supersaturations where nucleation and coarsening compete such that the average particle size remains close to the critical size as supersaturation drops. However, the coarsening in this system follows a $t^{1/5}$ rate law consistent with heterogeneous precipitation on dislocations. Initial precipitation appears to be coherent, the carbides tending toward a rod shape with major axis oriented along the minimum principal strain direction. At initial nucleation, particles are Fe-rich and C-deficient, diminishing the transformation eigenstrains to a near invariant-line-strain condition. The observed relation between carbide volume fraction and the shape-dependent capillarity parameter $\partial S/\partial V$ implies a coherency loss transition in AF1410 reached at 8hr tempering at 510°C.

The precipitation in AF1410 at 510°C exhibits a "renucleation" phenomenon in which a second stage of nucleation occurs beyond the precipitation half-completion time (1-2hrs). It appears that the carbide composition during precipitation follows a trajectory of increasing interfacial energy and nearly constant volume driving force. This may contribute to the renucleation phenomenon, but the computed barrier for heterogeneous nucleation on the dislocations is at this point an order of magnitude too high. An alternative possibility is that renucleation may represent autocatalytic heterogeneous nucleation in the stress field of coherent carbides, once they have grown to sufficient size to act as potent nucleation sites.

INTRODUCTION

Cobalt-Nickel Secondary Hardening Steels

Research by Speich et al. [1, 2] has elucidated steel compositions with a unique combination of strength and toughness. These steels contain 10 wt% nickel to lower the ductile-to brittle transition temperature to well below room temperature, and to ensure high hardenability. Molybdenum additions increase hardenability, retard temper embrittlement, and, in combination with carbon, promote secondary hardening reactions in which alloy carbides are formed [3, 4]. Chromium is generally added to increase hardenability and to enhance the secondary hardening response. The role of cobalt is least clearly understood, but it is thought [1, 2] to (a) retard the recovery of the dislocation substructure, (b) provide a finer dispersion of M_2C, and (c) provide a small amount of solid solution strengthening. The finer precipitate dispersion may arise because (a) heterogeneous nucleation on dislocations accelerates nucleation at low temperatures in an unrecovered matrix, (b) cobalt may decrease the solid solubility of the alloy carbide [5] and (c) since cobalt raises the activity of carbon in ferrite [6, 7, 8], this increases the supersaturation and nucleation rate. In addition to raising the activity of carbon in solution, Goldschmidt [9] proposes that cementite dissolves cobalt but is rendered progressively less stable (i.e., raising its free energy), Co_3C being an entirely unstable carbide. Grujicic [10], using the Thermo-Calc software and an early cobalt database, found that cobalt has an almost negligible effect on the driving force for precipitation of M_2C. However, there seems to be a number of experimental examples where cobalt significantly increases the driving force for other precipitation reactions. In addition to retarding the formation of austenite, it has been reported that Co in maraging steels has the effect of increasing the supersaturation of Mo [11], or equivalently, lowering the solubility of Mo in the matrix [12], accelerating the precipitation of Mo-containing intermetallics.

Chandhok, Hirth and Dulis [6, 7, 8] also propose that cobalt may decrease the carbide-martensite interfacial energy which would enhance nucleation, and following nucleation, the growing carbide rejects cobalt into the matrix at the carbide-martensite interface. This cobalt-rich zone further increases the carbon activity near the interface, decreasing the activity gradient into the growing particles, thereby decreasing the diffusion flux of carbon, and decreasing the rate of growth. There is also evidence [13, 14, 15, 16] for Fe-Co(-Ni) short-range ordering in these steels This will decrease the growth and coarsening rates by reducing the substitutional diffusivities through correlation effects Additionally, Decker [17] asserts that cobalt may accentuate the initial segregation of Mo to the dislocation strain fields, which would speed the precipitation of M_2C and thereby cause a fine dispersion. The toughness of these alloys is primarily due to the fineness of the carbides, the low impurity level, and the slightly overaged structure which nearly eliminates the embrittling cementite phase [1, 2]. The primary goal in the design of these alloys is to maintain an extremely fine carbide dispersion while simultaneously eliminating cementite.

The nominal compositions and mechanical properties of two commercial controlled-recovery secondary-hardening steels—HY180 and AF1410—are shown in table I, along with 300M (the classic epsilon-carbide strengthened UHS steel) and a 300-grade maraging steel. Because of the extreme toughness of AF1410, it is important now to look into alloys of similar matrix composition, but with higher carbon and secondary-hardening element contents to increase the secondary-hardening response. Keeping the alloy car-

bides as fine as possible at completion of precipitation should contribute greatly to the strength with minimal loss of toughness.

The goal of modification of these steels is improved strength with minimal loss of toughness. Control of precipitation processes is essential to achieving higher strength while maintaining the microstructural basis of high toughness. Atom-probe field-ion microscopy (APFIM) has been used to study precipitation of M_2C in AF1410 [18, 19, 20, 21, 22], giving carbide compositions as a function of tempering time at 510°C, as well as rough sizes and shapes of the carbides. However, crystallographic parameters and interfacial features cannot be readily obtained with this technique, and carbide coherency loss has to be inferred from a morphology change. Determining the coherency loss mechanism(s) for these carbides is important, since, as coherency decreases, the interfacial energy increases, increasing the coarsening rate and thus decreasing the strength and toughness of the steel. Coherency loss should therefore be delayed at least until precipitation is complete and all cementite is dissolved.

Thermodynamics of Carbide Precipitation

Thermo-Calc™ is a quantitative metallurgical thermochemistry computer program developed by the Physical Metallurgy division of the Royal Institute of Technology (KTH) in Stockholm. The facilities of Thermo-Calc allow one to tabulate thermodynamic data, calculate the heat of chemical reactions and their driving force, evaluate equilibria for chemical systems and phase transformations and calculate various types of multicomponent phase diagrams. It is important to many problems in the chemical and metallurgical industries to know the equilibrium conditions and to understand how the equilibrium can be affected by various external factors. Thermo-Calc is able to provide this important information. Although Thermo-Calc was initially developed for the calculation of strict chemical equilibria, it can also be used to calculate constrained, or metastable, equilibria. The calculation of metastable equilibria is far more interesting and useful from an alloy and heat treatment development point of view. An example of metastable equilibrium is a para-equilibrium, where the precipitating phase has the same composition of its metal sublattice as the parent phase. Thus Thermo-Calc can be used as an alloy design tool. Because it can calculate constrained equilibria (such as para-equilibrium) and the driving forces for various phase transformations, the composition and heat-treatment of a particular alloy with particular requirements can be calculated which gives the required phase transformations. The result of the phase transformations gives the desired microstructure, and through structure-property relationships, the desired properties are obtained.

Theory of Homogeneous Precipitation

The present state of the theory of homogeneous precipitation has been recently assessed by Kampmann and Wagner [23, 24]. Precipitation in supersaturated metastable alloys has been usually subdivided into three distinct stages (I-III). In the first stage (I), nucleation of the precipitating phase takes place. These nuclei result from spatially localized composition fluctuations which occur statistically within the supersaturated matrix. In stage II, diffusional growth of a precipitate occurs by solute depletion of the surrounding matrix, without competing with the growth of any other particles. This solute depletion decreases the driving force (supersaturation) for nucleation. Stage III is characterized by particle coarsening, in which the particle size distribution coarsens by the growth of larger particle at the expense of smaller particles, which dissolve. The distinction between a growth stage (II) and a coarsening stage (III) is somewhat arbitrary, and is made only to mark two special periods during which certain approximations can be made so the complex diffusion problem can be solved analytically.

Nucleation: In this paper, the formation of stable nuclei will be treated within the framework of classical nucleation theory, i.e., the droplet model is used in all stages of precipitation [25]. Following Russell [26], the nucleation rate is given by

$$J = \exp\left[\frac{-t_w}{t}\right] Z\beta^* N_e \exp\left[\frac{-\delta W^*}{kT}\right] \qquad (1),$$

where $\delta W^* = \frac{4\pi r^{*2}\gamma}{3}$ is the work of formation of a critical nucleus with radius r^* containing n^* solute atoms; γ is the interfacial energy, $Z = \left[\delta G^*/3\pi kTn^{*2}\right]^{1/2}$ is the Zeldovitch factor, $\beta^* = D\bar{C}/\lambda_{at}^2$ is the rate at which solute atoms from the matrix of mean concentration $\bar{C}$ join the critical nucleus D is the effective diffusivity, N_0 the number of atomic sites per unit volume, t_w the incubation period and λ_{at} the atomic jump width. For the nucleation of multicomponent precipitates, an effective $(DC)_{eff}$ (from coarsening theory) can be used.

Growth: A nucleated, stable, spherical particle of radius r and solute concentration C_p embedded in a supersaturated matrix (of solute concentration $\bar{C}(t)$ far away from the precipitate) will grow at a rate

$$v(r) = \frac{dr}{dt} = \frac{\bar{C}(t) - C_r}{C_p - C_r}\frac{D}{r} \qquad (2),$$

where C_r is the solute concentration at the interphase boundary. Assuming a monodispersive system, $C_r = C_e = \bar{C}(t\rightarrow\infty)$, and $\bar{C}(t) = C_0 = \bar{C}(t=0)$, integration of (2) yields

$$r(t) = \left[2\frac{C_0 - C_e}{C_p - C_e}\right]\sqrt{Dt} \qquad (3),$$

giving parabolic growth behavior.

Coarsening: Due to the Gibbs-Thomson effect, one must deal with a particle size distribution f(r,t), rather than with precipitates of uniform size. In this case, C_r depends on r according to

$$C_r = C_e \exp\left[\frac{2\gamma V_m}{RT}\frac{1}{r}\right] \qquad (4),$$

in which V_m is the molar volume and R is the gas constant The growth rate v is still given by equation (2). However, because of equation (4), particles will either grow (v>0) or dissolve (v<0) depending on whether $r>r^*$ or $r<r^*$, with

$$r^* = \frac{-2\gamma}{\Delta g} \qquad (5)$$

For the dilute solution case,

$$\Delta g = \frac{-RT}{V_m}\ln\frac{\bar{C}}{C_e} \qquad (6)$$

Lifschitz and Slyozov [27] and Wagner [28] (LSW) calculated the time evolution of the mean radius $\bar{r}(t)$ and the number density $N_V(t)$ on the basis of equation (2) and the continuity equation

$$\frac{\partial f}{\partial t} + \frac{\partial}{\partial r}\left[f\frac{\partial r}{\partial t}\right] = 0 \qquad (7).$$

However, certain approximations had to be made to solve the equations of motion analytically: (1) the precipitated volume fraction f_V = const., i.e., the precipitation is close to completion, and (2), equation (4) was used in its linearized version

$$C_r = C_e\left[1 + \frac{2\gamma V_m}{RT}\frac{1}{r}\right] \qquad (8).$$

With these approximations, the LSW theory yields in the asymptotic limit ($t \to \infty$) for volume diffusion-controlled coarsening

$$\bar{r}^3(t) - \bar{r}_0^3 = \frac{8}{9}\frac{\gamma V_m}{RT}\frac{DC_e}{C_p - C_e}(t - t_0) \qquad (9).$$

Behavior at High Supersaturations

The splitting up of the course of precipitation into three distinct regimes is rather artificial. In reality, particularly during the early stages of precipitation in alloys of high supersaturation, all these processes will overlap and the precipitation kinetics will be more complicated. In 1967 Kampmann and Kahlweit [29] considered precipitation as a continuous race between the sizes of the nucleus and of the precipitates, figure I [29]. Particles which nucleate at different times t will only continue to grow as long as their size remains above a critical size $r^*(t)$. The critical size increases with time because, as precipitation occurs, the supersaturation of the matrix drops, which lowers the driving force for precipitation. Thus if a particle does not grow fast enough, it will become subcritical and dissolve. Kampmann and Kahlweit point out that if one could quantitatively describe this race, then he could predict the outcome of the precipitation reaction. In 1980, Langer and Schwartz [30] treated this problem theoretically for droplet formation and growth in near-critical fluids (LS-model). They modified the continuity equation (7) to include nucleation, which becomes

$$\frac{\partial f}{\partial t} + \frac{\partial}{\partial r}\left[f\frac{\partial r}{\partial t}\right] = j(r) \qquad (10),$$

where $j(r)$ is a distributed source of droplets such that

$$J = \int_{r^*}^{\infty} j(r)\,dr \qquad (11).$$

Knowing the properties that such a function must have, they assumed an "apparent" particle distribution function in which subcritical particles were ignored, and from which the coarsening rate at long times approached that from LSW theory. In addition, they too used the linearized version of the Gibbs-Thomson equation (8). Langer and Schwartz found that systems with low supersaturations exhibit three-stage behavior, i.e., the kinetics could be approximated by nucleation, growth and coarsening stages. Systems with higher supersaturations show mixed kinetic behavior.

Wendt [31, 32] Haasen [33], and Wendt and Haasen [34] modified the theory (MLS-model) in such a way that it can be applied for the description of the kinetics of precipitate formation and growth in metastable alloys of high degrees of supersaturation. The authors compared the results of the model to experimental atom probe field ion microscope (APFIM) data for Ni-14 at% Al aging at 550°C, figure II [34]. In spite of using the linearized version of the Gibbs-Thomson equation (8), they obtained good agreement with theory and experiment. In Kampmann and Wagner's [23, 24] version of the MLS-model, the non-linearized version (equation (4)) was used, but they point out that the MLS theory is still based on the same assumptions as the original LS theory. In particular, the explicit form of $f(r,t)$ is not accounted for and the long-time coarsening behavior is assumed to match the LSW results, i.e., is described by equation (9). Kampmann and Wagner [23, 24] have therefore devised an algorithm, termed the numerical model (N-model), which describes accurately the entire course of precipitation within the framework of existing nucleation and growth theories. Accurate is meant in the sense that relative to the LS- and MLS-models, fewer simplifying assumptions enter this algorithm; in particular, the time evolution of $f(r,t)$ is computed with minimal approximations. The authors then applied both the MLS- and the N-models to the Cu-1.9 at% Ti system. For this system, aging at 350°C, they found that the MLS-model provides a rather good survey of the general course of precipitation. However, due to the simplifying assumptions made, it does not predict the precipitation kinetics with the same accuracy as the N-model. Results of these models were compared with experimental data obtained from an AP/FIM study [35], figure III. The N-model fits the experimental data points quite well for $\gamma = 0.067$ J/m^2 and $D = 2.5 \times 10^{-15}$ cm^2/sec. In contrast, poor agreement is obtained with $\gamma = 0.071$ J/m^2, reflecting the degree of precision with which γ could be determined by fitting to precipitation kinetics.

The present theory has been developed for homogeneous, low-misfit precipitation only. Necessary modifications to this theory for the precipitation of M_2C in steel are discussed in the next sub-sections.

Multicomponent Coarsening

Because the M in M_2C may contain several elements, one must also consider how this alters the diffusion-controlled growth and coarsening of the carbides. Lee [36, 37] has adapted the Björklund et al. [38] model of cementite multicomponent coarsening, along with the work of Speich and Oriani [39] on the precipitate shape effect, to apply to the case of M_2C. In this theory, the coarsening rate of the carbide minor radius is given by

$$\bar{r}^3 - \bar{r}_0^3 = \frac{4}{9}K_r(t - t_0) \qquad (12).$$

where the coarsening rate constant

$$K_r = \frac{2\gamma V_m}{RT\ln(2\beta)}\left[\sum_{M_i}(k_{M_i} - k_{Fe})(k_{M_i} - 1)\frac{C_e}{D_{M_i}}\right]^{-1} \qquad (13).$$

and β is the aspect ratio (l/r) of the carbide, k_i is the partitioning coefficient $C_p^{M_i}/\bar{C}(t)$, and D_M is the diffusivity of metal i in ferrite. The inverse of the terms within the summation are analogous to an electrical resistance Examination of this inverse form reveals that the total resistance is a linear summation of each resistance step.

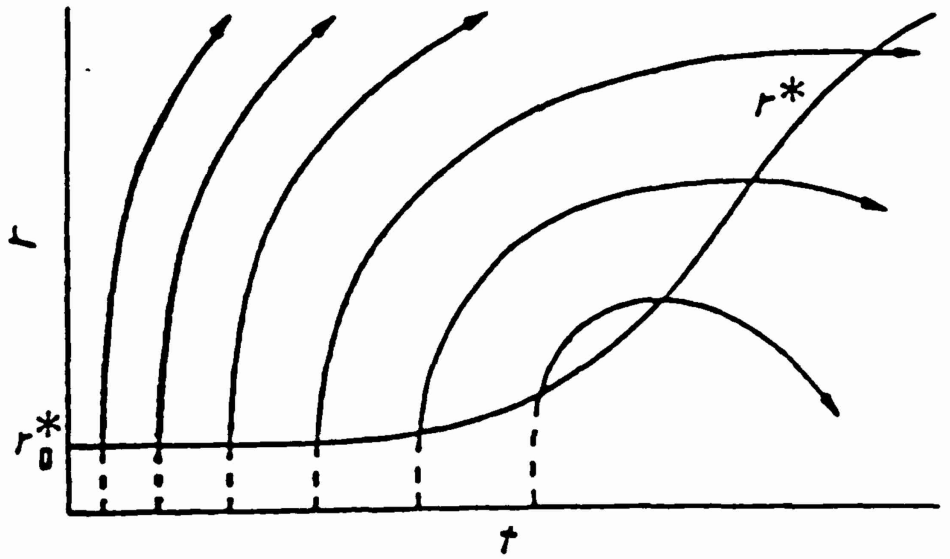


Figure I. Sizes of the critical nucleus r^* and of the particles r as a function of time (schematic). (From reference [29].)

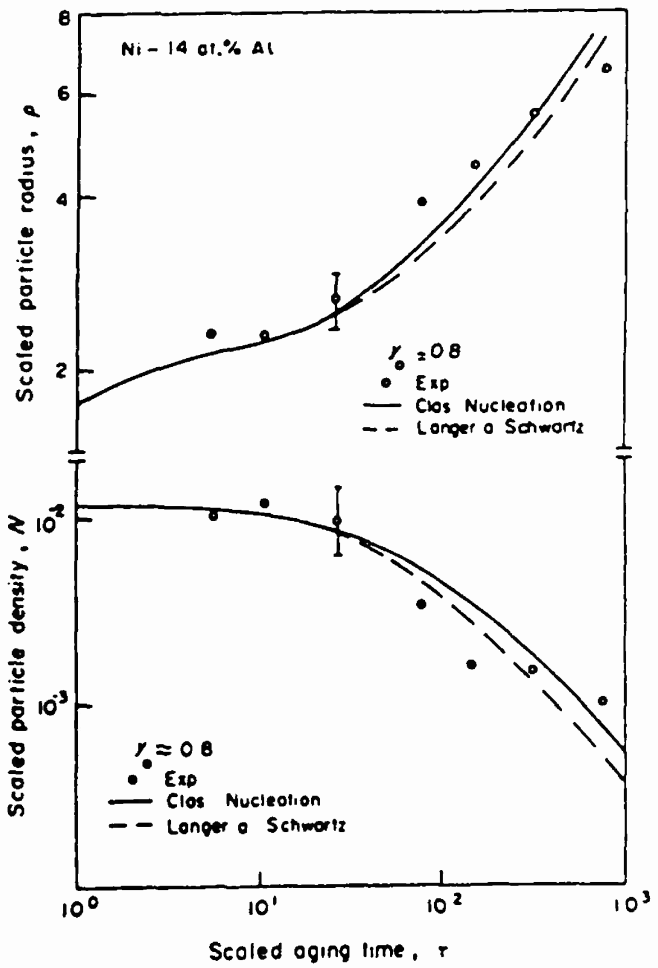
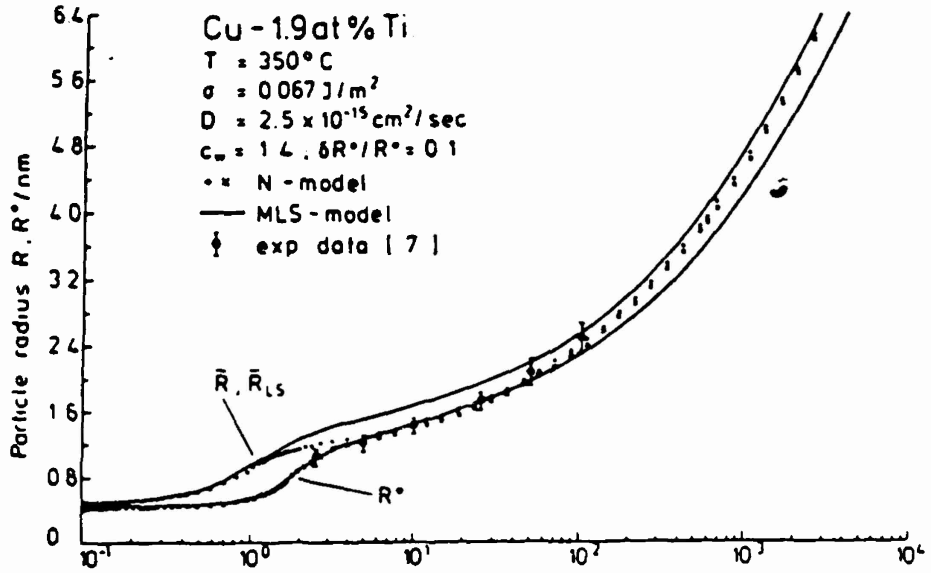


Figure II. Variation of the scaled particle density with scaled aging time for Ni-14 at% Al at 550°C. (From reference [34].)



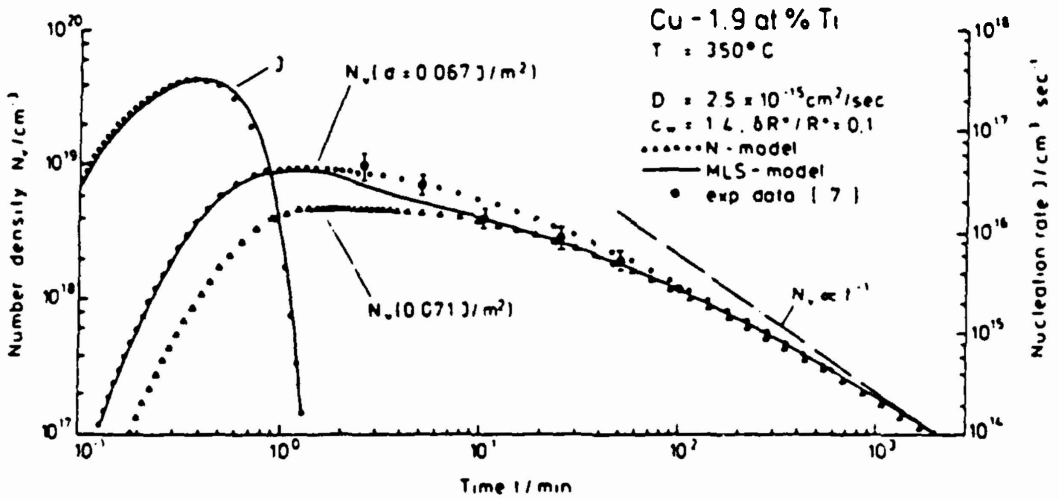


Figure III. Variation of the particle radius and of the particle density with aging time for Cu-1.9 at% Ti at 350°C. (From reference [35].)

which corresponds to a series-type connection of resistance. Thus coarsening occurs through series-type diffusion with the slowest-diffusing element controlling the coarsening rate. Current research by Kuehmann [40], using a more fundamental approach to this problem has shown very similar results, that is, that the coarsening rate constant is proportional to the concentration-weighted average of the diffusivities, analogous to resistors in series.

Once the carbon level is chosen for the alloy, there is an additional degree of freedom in selecting the ratio of M to C. As was determined by Olson et al. [41], and further refined by Grujicic [10], alloys whose compositions are "balanced" with respect to the stoichiometry of the precipitate will have the lowest coarsening rate of the precipitate. Therefore an alloy with 0.25 wt% C (1.16 at% C) should have 4 wt% Mo (2.33 at% Mo) to give the slowest coarsening of Mo_2C.

Heterogeneous Precipitation with High Coherency Strain

The overall free energy change on precipitation is given by

$$\Delta G_{TOT} = \Delta G_{CHE} + \Delta G_{SUR} + \Delta G_{STR} + \Delta G_{INT} \qquad (14)$$

where ΔG_{CHE} is the chemical free energy change (negative for precipitation), ΔG_{SUR} is the free energy associated with the interphase boundary (positive), ΔG_{STR} is the self-energy of the precipitate due to its strain field (positive), and ΔG_{INT} is the interaction energy due to the strain field of the precipitate interacting with the stress field of a point, line or planar defect (typically negative). In the preceding analyses, ΔG_{SUR} was taken for a spherical precipitate with uniform interfacial energy γ, the value of which was found by fitting the precipitation kinetics. Also in the preceding analyses, ΔG_{STR} (apart from its modification of C_e) and ΔG_{INT} were neglected. This is a good approximation for coherent precipitates of small misfit which nucleate, grow and coarsen homogeneously. However, in the subject system, the M_2C may be partially coherent, and it may have a heterogeneous nature at some or all phases of precipitation.

The free energy associated with a semicoherent interphase boundary is

$$\Delta G_{SUR} = \int_A \gamma_{elas} \cdot dA + \int_A \gamma_{chem} \cdot dA \qquad (15),$$

where γ_{elas} and γ_{chem} are the elastic and chemical contributions to the interfacial energy, respectively. Olson and Cohen [42], who followed the method of Hirth and Lothe [43], calculated the contribution to the energy per unit area for a pure edge "misfit" dislocation array with Burgers vector b_y as

$$\gamma(b_y) = \frac{\mu b_y^2}{4\pi D_b(1-\nu)}\left[\frac{2\pi b}{D_b\alpha_c} - \frac{\pi b}{D_b\alpha_c}\coth\frac{\pi b}{D_b\alpha_c} - \ln\left(2\sinh\frac{\pi b}{D_b\alpha_c}\right)\right] \qquad (16),$$

where D_b is the periodic spacing of the dislocations, b is the total Burgers vector of the anticoherency dislocations, and α_c is a core-energy parameter taken between 1 and 2 for metals.

The strain energy of a coherent ellipsoidal inclusion was calculated by Eshelby [44, 45] using a set of imaginary cutting, straining and welding operations. The total strain energy in the nucleus and the matrix may then be found from

$$\Delta G_{STR} = -\frac{1}{2}\int_V (\sigma_{ij}^T - \sigma_{ij}^C)\varepsilon_{ij}^T dV \qquad (17),$$

where σ_{ij}^T and σ_{ij}^C are the stresses related to the stress-free and constrained particle strains, and ε_{ij}^T is the strain of the stress-free transformation.

If the alloy carbides do indeed nucleate on dislocations, there will be an interaction energy ΔG_{INT} tending to favor precipitation. The interaction energy of the strain field ε_{ij}^T of a precipitate with the stress field $\sigma_{ij}^{\perp}$ of a dislocation is given by [43]

$$\Delta G_{INT} = \int_V \sigma_{ij}^{\perp}\varepsilon_{ij}^T dV \qquad (18).$$

If, following nucleation, the precipitates are associated with dislocations, either by remaining in proximity or moving to proximity, then they may grow and coarsen heterogeneously. In a field-ion microscopic study of Mo_2C coarsening in Fe by Davies and Ralph [46], they found that their precipitate size data are consistent with the theory of bulk-diffusion controlled coarsening, and that the precipitates vary in shape during the initial stages of coarsening. They also state that it is probable that the precipitates nucleate on dislocations, with the caveat that at the tempering temperature, the dislocations are able to move easily since recrystallization occurs on overaging. The dislocations could therefore move the short distances necessary to associate themselves with the precipitates, and hence the observation of well-developed precipitates on dislocations does not prove that nucleation occurred at these sites.

The precipitation rate of M_2C for the compositions of interest is controlled by the slower diffusing species—M. For the case of heterogeneous growth and coarsening, there will be one of two rate-limiting steps: (1) diffusion of M along the dislocations, so-called dislocation pipe diffusion, or (2) diffusion of M through the matrix before it gets to the dislocation, so-called collector line diffusion.

Table II summarizes the cases of precipitate coarsening that have been considered. For the collector line theory, Ham in the referenced paper [48] really was deriving a theory of stress-assisted precipitation on dislocations. However, if we let the stress interaction go to zero, we are left with what is ostensibly a collector line theory—bulk diffusion to the dislocation line is the rate-limiting step. (It is surprising that this case has received so little attention.) In a study of precipitation of $MgZn_x$ in Al-Zn-Mg by Allen and Vander Sande [52], they found precipitates that coarsened on dislocation lines with a time exponent of 1/5 or 2/9. The precision of the data was insufficient to discriminate between the two, but by looking at precipitation at different temperatures, they could develop Arrhenius plots and find the activation energy for precipitation. The activation energy found was in good agreement with that for bulk diffusion of Mg and Zn in Al, not pipe diffusion. Therefore, the collector line mechanism is operating in this system.

Evidence that the collector line phenomenon is active in controlled-recovery secondary-hardening steels comes from two studies: (1) Murphy and Whiteman [53] in a study of the kinetics of Mo_2C precipitation in tempered martensite, found that the character of the precipitation changed abruptly

after the matrix had recovered. Thin foil work indicated that the initial carbides were precipitating on dislocations, however, the activation energy for precipitation was in agreement with that for bulk diffusion of Mo. (2) Lee [36, 37], who investigated M_2C carbide coarsening in AF1410, also found the activation energy for coarsening to be in agreement with that for bulk diffusion. Work by Davenport [54], followed by Speich et al. [1, 2], has indicated that these carbides precipitate along dislocation lines in these steels.

Carbide Structures and Properties

Transition metal carbides have been reviewed very well by Nagakura and Oketani [55], and there are a few good books on the subject, most notably Goldschmidt [9]. Carbides generally have wide regions of solid solubility, with their properties continuous across the single-phase region. We are more interested in how the lattice parameter changes with composition, since this will affect a precipitate particle's elastic energy and coherency. Carbide lattice parameters are a function of their composition, and generally this is linear. This has been demonstrated most clearly in MC (NaCl-type) mixed carbides, but there has been some work done on mixed M_2C carbides. These have been: $(V,Cr)_2C$ [56], $(W,Cr)_2C$ [57], $(Mo,V)_2C$ [58], and $(W,Ta)_2C$ [59]

There are seven ways for carbon to order within the M_2C carbides [55]. The conditions for this ordering have been considered by Hiraga and Hirabayashi [60]. When carbon orders, it usually distorts the (nominally HCP) lattice slightly, and leads to a different (commonly orthorhombic) unit cell. The crystallographic axes chosen for a carbide will depend on its space group. In order to compare and mix the carbides, it is necessary to choose a common unit cell, and convert the lattice parameters to it. The most convenient one seems to be the one chosen by Taylor [61, 62], which is an orthorhombic unit cell with its c-axis parallel to the c-axis of an equivalent hexagonal unit cell. The seven M_2C carbide subtypes are shown in table III with the scheme for converting their unit cells to this common one.

To quantify the degree of orthorhombic distortion of a carbide unit cell relative to HCP, we will use the parameter

$$\omega = \frac{b_c^{orth}}{a_c^{orth}\sqrt{3}} \qquad [19],$$

which is equal to one for a purely hexagonal unit cell. When V_2C and Nb_2C order, it distorts the HCP arrangement of metal atoms into an orthorhombic unit cell, with $\omega = 1.0110$ and 1.0141, respectively [60, 63, 64]. The mixed carbide $(V,Cr)_2C$ has a small orthorhombic distortion ($\omega = 1.0086$) [56]. The "η-" [65, 66] or "ε'-" [61, 62] iron carbide, which we here denote "Fe_2C," is the ordered form of ε-carbide and also has a small orthorhombic distortion ($\omega = 0.9577$); this phase was identified by electron diffraction. In Mo_2C, this carbon ordering does not distort the metal HCP lattice ($\omega = 1$), and since carbon does not scatter X-rays very well, this was not discovered until 1963 [67], by neutron diffraction.

The Young's modulus of Mo_2C has been reported in a number of studies [68, 69, 70, 71, 72, 73], as 217-228 GPa. Russian literature invariably quotes a value from one study by Neshpor and Samsonov [74], which is far too high (534 GPa); the value that appeared in this paper was, in fact, an estimate based on an empirical correlation, rather than an experimental measurement. Any other elastic properties are very hard to come by, even ν. Here, ν was estimated from data on the MC (NaCl) carbides [73, 75, 76, 77, 78, 79] to be 0.19. This low value for ν indicates a high bulk modulus to shear modulus ratio, which is typical for covalent solids. Diamond has a Poisson's ratio of 0.068. Data on how the elastic constants change with composition do not exist for M_2C, as they do for MC. The microhardness of Mo_2C is usually reported as 1500-2000 kg/mm^2. The most recent, thorough study on this was by Vahldiek et al. [80], where they determined that the average random hardness of as-grown crystals was 1520 kg/mm^2. For MC carbides it has been shown that their hardness and modulus generally increase with increasing carbon content, although they may have a peak somewhat under stoichiometry [81, 82, 83, 84]. The plastic deformation of M_2C carbides has been investigated [73, 80, 85], and it has been found that the primary slip system is $(0001)\langle 2\bar{1}\bar{1}0\rangle$ or slip along the basal plane. Secondary slip occurs on $\{10\bar{1}0\}\langle 2\bar{1}\bar{1}0\rangle$ (prismatic slip), while the twinning system is $\{10\bar{1}2\}[0001]$.

Carbides in Steels

Carbides (and nitrides) in steels have been comprehensively reviewed by Jack and Jack [86]. The iron-based carbides of interest in this study are epsilon (ε) carbide and theta (θ) carbide or cementite. Epsilon carbide precipitates during the first stage of tempering, between 100° and 200°C, or during the quench. (For a review of the tempering of steel, see Speich and Leslie [87].) Carbides that precipitate during the quench are termed autotempered carbides. Cementite precipitates during the third stage of tempering (250-450°C), or, if the steel has a high enough M_S, during the quench. The second stage of tempering corresponds to the decomposition of retained austenite. During the fourth stage (500-700°C), "alloy carbides" precipitate. These are carbides that are not iron-based, and may be MC, M_2C, M_7C_3, $M_{23}C_6$, M_6C, or others. This stage of tempering is also called secondary hardening, because the precipitation of these alloy carbides gives rise to substantial hardening.

The alloy carbides in steels, just as when they are isolated, can have variable compositions. The results of several studies of alloy carbide precipitation have shown that the composition of the carbides is related to the composition of the alloy [88, 89, 90, 91]. For example, as the Cr/Mo ratio of the alloy is increased, the Cr/Mo ratio of the carbide precipitated will also increase. This is, of course, in keeping with LeChatlier's principle. Thus, the properties in general, and the lattice parameters in particular, of the precipitating carbide can be altered by altering the alloy chemistry. This will have an effect on the carbides' state of coherency.

Two previous atom-probe field-ion microscopy studies of carbides in steels have shown that alloy carbides in the early stages of precipitation are significantly carbon-deficient and iron-enriched. Youle et al. [92] found this effect but did not quantify it. Stiller et al. [93] determined the composition of M_2C carbides in a high speed steel (2.26C-0.41Si-0.30Mn-4.2Cr-7.0Mo-6.7W-10.3Co-6.4V) tempered at 560°C for 1hr as $(Cr_{0.32}Mo_{0.31}Fe_{0.23}V_{0.09}W_{0.05})_2C_{0.66}$. After 24hr at this temperature the carbides had the composition $(Cr_{0.49}Mo_{0.31}Fe_{0.09}V_{0.02}W_{0.08})_2C_{0.87}$.

In a study of Mo_2C precipitation in a 3.5Mo-0.22C steel, Davenport [54] found that in addition to the dislocations inherited from the martensite,the cementite-martensite interfaces acted as potent nucleation sites for the carbides. He proposed that the growth of a particular variant of the alloy carbide morphology was favored because of interfacial

energy interaction. This variant lay parallel to the cementite habit plane and eventually absorbed the adjacent carbides, including those in the matrix. This resulted in the alloy carbides having a non-random dispersion in the overaged state that was related to the prior cementite positions, which was termed a "footprint" morphology.

Carbide Crystallography and Kinematics

A general approach to the crystallography and kinematics of phase transformations has been recently put forward by Olson and Cohen [42]. In any theory of crystalline interfacial structure for a coherent particle, it is necessary to establish a lattice correspondence which relates the identity of lattice planes and directions in the two crystal structures which meet at the interface. This correspondence then defines a lattice deformation which is an affine transformation describing the homogeneous distortion of a unit cell of one structure to that of the other. In matrix notation, a lattice deformation $\tilde{S}$ can be factored into a pure strain $\tilde{B}$ and a rigid body rotation $\tilde{R}$;

$$\tilde{S} = \tilde{R}\tilde{B} \qquad (20).$$

When one or both of the crystal structures involves a basis, additional inhomogeneous atom displacements termed shuffles may occur within the unit cell which, as such, do not contribute to the distortion of lattice vectors.

Once the lattice deformation has produced the correct structure of the transformation product, any further deformation must be lattice invariant, which produces a change of shape without altering the lattice. A particle can then reduce its coherency by a lattice-invariant deformation $\tilde{P}$. This can occur by any of the usual mechanisms of conventional plastic deformation in crystals, such as the glide and climb of crystal lattice dislocations or mechanical twinning, and will be subject to the usual constraints of crystal plasticity. Macroscopic (long-range) cancellation of a component of the homogeneous lattice deformation is most effectively accomplished by a uniform periodic array of lattice dislocations or twins [42]. *The result of all these deformations* is the particle's macroscopic shape change $\tilde{E}$, expressed by

$$\tilde{E} = \tilde{R}\tilde{B}\tilde{P} \qquad (21),$$

where $\tilde{E}$ is the macroscopic shape change, $\tilde{R}$ is the rigid-body rotation, $\tilde{B}$ is the lattice deformation, and $\tilde{P}$ is the inhomogeneous lattice-invariant deformation.

A lattice deformation can be visualized by considering how a general distortion deforms a sphere of unit radius. The general pure strain $\tilde{B}$ distorts the sphere into an ellipsoid with three unequal semi-axes. When at least one of the semi-axes is greater than unity and at least one other is less than unity, the sphere and the ellipsoid intersect, defining a right elliptic "Bain" cone with its apex at the origin. The total lattice deformation $\tilde{R}\tilde{B}$ can then be an invariant-line strain (ILS) which leaves a particular direction undistorted and unrotated. Combining the lattice deformation with an appropriate $\tilde{P}$ in the form of a simple shear can then make $\tilde{E}$ an invariant-plane strain (IPS) which is a deformation leaving a particular plane macroscopically undistorted and unrotated. Adopting this plane as the habit of a plate-shaped semicoherent particle minimizes its strain energy. Several mathematical procedures have been developed to analyze the crystallography of semicoherent IPS transformations [94, 95, 96].

In generalizing these concepts, Olson and Cohen [42] have discussed three principles governing the orientation relations and morphology of transformation products:

Principle 1: The rigid-body rotation accompanying the transformation of an enclosed particle will minimize rotations of directions of maximum dimension.

Principle 2: A transformed particle which minimizes strain energy will maximize its dimensions in directions of minimum distortion.

Principle 3: A particle which minimizes surface energy will adopt a morphology which maximizes the coincidence of lattice sites in its interface.

In a study of aging phenomena in ferrous martensites, Taylor [61] observed the precipitation of orthorhombic ε'-carbide as plates via high resolution TEM. This carbide has the same crystal structure as Mo_2C, but different lattice parameters. These plates exhibited an orientation relationship with the matrix analogous to that proposed by Pitsch and Schrader [97] for hexagonal ε-carbide in ferrite, namely,

$$\begin{matrix}(001)_\varepsilon \,//\, (011)_\alpha \\ [100]_\varepsilon \,//\, [100]_\alpha\end{matrix}$$

Jack [98] also postulated an orientation relationship between ε-carbide and *martensite*, which was subsequently confirmed by Wells [99],

$$\begin{matrix}(0001)_\varepsilon \,//\, (011)_\alpha \\ (10\bar{1}1)_\varepsilon \,//\, (011)_\alpha \\ [11\bar{2}0]_\varepsilon \ 5°16' \text{ from } [100]_\alpha\end{matrix}$$

This orientation relationship differs from the Pitsch and Schrader relationship by a rotation of only 5°16' about $[011]_\alpha$ or $[0001]_\varepsilon$. The inability to image Kikuchi bands in ferrous martensites precluded accurate specimen orientation, so that Taylor was unable to discriminate between the two.

Taylor found that the ε'-carbides exhibit extensive faulting on their "basal" plane that appears to be an internal accomodation mechanism necessary to achieve an IPS which minimizes the total strain energy. The transformation strain of the semicoherent precipitate was analyzed as an IPS with inhomogeneous shear $\tilde{P}$ on $\{011\}_\alpha$ (the type of plane from which the carbide basal plane is derived). A BCC→orthorhombic lattice deformation was adopted, and a computerized version of the procedure developed by Bowles and MacKenzie [94] (originally to analyze the crystallography of the martensite transformation in steels) was used. Figure IV [61] shows a cubic [100] stereogram depicting the Bain cone for the BCC→ε'-carbide lattice deformation in Fe-25Ni-0.4C. The intersection of the internal shear plane and the cone defines two possible invariant lines (x_i). The predicted habit plane normal corresponding to the $[3\bar{1}1]$ invariant line (and $[2\bar{1}\bar{1}]$ invariant normal) is designated by "$P_1(x_2, n_2)$," and is close to the observed (102) habit. The predicted orientation relationship was also consistent with electron diffraction patterns.

The lattice correspondence used by Taylor can be stated formally by the matrix expression

$$\vec{b} = [bCo]\vec{o} \qquad (22),$$

where $\vec{b}$ is a vector in the parent BCC lattice, $\vec{o}$ is a vector of the product orthorhombic lattice, and $[bCo]$ is a 3X3 matrix

which describes the lattice correspondence, namely,

$$[bCo] = \begin{bmatrix} 1 & 0 & 0 \\ 0 & 1 & 1 \\ 0 & \bar{1} & 1 \end{bmatrix} \quad (23).$$

The crystal structure of hexagonal carbides is shown in figure V [55]. This structure can be seen to be an HCP structure of metal atoms with carbon atoms in octahedral interstices. One-third to one-half of the octahedral sites are occupied by carbon atoms, depending on the chemical composition. For example, the composition of ε-carbide varies from Fe_3C to Fe_2C. In order to compare the principal strains of the coherent lattice deformation, all possible M_2C carbides were taken from the literature (primarily from the JCPDS card file [100]) and converted to a common orthorhombic unit cell, table IV. Principal strains defined by

$$\varepsilon_1 = \frac{a_c^{orth}}{a_\alpha} - 1 \quad (24a)$$

$$\varepsilon_2 = \frac{b_c^{orth}}{a_\alpha\sqrt{2}} - 1 \quad (24b)$$

$$\varepsilon_3 = \frac{c_c^{orth}}{a_\alpha\sqrt{2}} - 1 \quad (24c)$$

were then evaluated using $a_\alpha = 2.870$Å for the high Ni-Co alloys of interest here.

Starting with Mo_2C, one can see that the carbide can reduce its transformation strains by becoming carbon-deficient (adding C vacancies), and by substitution by other metals; "mixed" M_2C carbides exhibit lattice parameters between those of their pure components. For Fe_2C and Cr_2C, ε_1 actually becomes negative, satisfying the condition for an invariant line strain.

When Mo_2C precipitates in a ferritic matrix it assumes the morphology of rods or needles [101, 102]. Using Transmission Electron Microscopy (TEM), the orientation relationship and habit direction of Mo_2C in ferrite was determined in 1966 by Dyson et al. [103]. Referring the carbide to an HCP lattice, they found the orientation relationship is best represented as:

$$\begin{matrix} (0001)_c \,//\, (011)_\alpha \\ [2\bar{1}\bar{1}0]_c \,//\, [100]_\alpha \end{matrix}$$

which is identical to that postulated by Pitsch and Schrader [97] for ε-carbide in ferrite. With respect to the (orthorhombic) coherent lattice deformation, this relationship corresponds to nonrotation of the principal axes. A stereographic projection for this relationship is shown in figure VI. Dyson et al. also found that the habit direction of the Mo_2C needles is perpendicular to $(2\bar{1}\bar{1}0)_c$, which is parallel to one of the cubic cell edges of ferrite, viz., $[100]_\alpha$. This direction coincides with the principal axis of smallest strain (ε_1) of the coherent BCC→orthorhombic lattice deformation ("Principle 2" discussed earlier). Tanino et al. [104] also reported the Pitsch and Schrader orientation relationship, as well as the $[100]_\alpha$ habit direction. A figure for the arrangement of Mo and Fe atoms on the $(0001)_c \,//\, (011)_\alpha$ plane, consistent with the lattice correspondence of equations [1.19], is shown in figure VII [88], illustrating the relatively good matching along $[2\bar{1}\bar{1}0]_c \,//\, [100]_\alpha$, corresponding to ε_1. In addition, Tanino et al. interpreted features within overaged Mo_2C needles with an average spacing of 30Å as Mouré fringes. This spacing is in good agreement with the value calculated from the difference in the interplanar spacings of $(2\bar{1}\bar{1}0)_c$ and $(002)_\alpha$. They also showed a TEM micrograph of a 7.3Mo-0.17C steel that exhibited diffraction contrast due to the coherency strain around under-aged Mo_2C precipitates.

However, Davenport [54], in a study of secondary-hardening steels, interpreted similar features with 60Å spacing within both overaged Mo_2C and W_2C carbides not as Moiré fringes, but as interfacial dislocations. This was because the fringes were resolved in dark field micrographs taken from the carbide reflections only. Davenport also tried to duplicate the result of Tanino et al. of coherent under-aged Mo_2C precipitates without success in his 3.5Mo-0.22C steel, so an 8.2Mo-0.22C steel was made. On quenching this steel from 1300°C, up to ~30% δ-ferrite was observed in the martensite. Due to preferential electropolishing, the apparent density of this phase was increased in thin foils to such a degree that the martensite structure was only occasionally observed. The δ-ferrite was relatively defect-free and after tempering for a short time, e.g. 3 minutes at 700°C, a fine dispersion of Mo_2C needles lying along the cube directions was resolved. These needles were seen to exhibit extensive streaking in diffraction patterns. It was concluded that the results of Tanino et al. concerning the nature of the Mo_2C-ferrite interface were drawn from observations on δ-ferrite.

Taylor found in his analysis [61] that as ε_1 approaches 0, the invariant line (figure IV) moves closer to [100], shrinking the Bain cone, and moving the habit plane towards (001). For the case where $\varepsilon_1 \geq 0$, an IPS solution based on a single lattice-invariant shear is no longer possible. This corresponds to the case of Mo_2C with the Pitsch-Schrader orientation relationship. However, an invariant-line strain (ILS) or near-invariant line strain may still be realizable, dependent upon the operation of an appropriate inhomogeneous lattice-invariant deformation $\tilde{P}$, which would result in the observed rod-shaped particles along [100]. The expected behavior is illustrated in figure VIII. Figure VIIIa shows a fully coherent ellipsoidal particle, edge-on to the basal plane $(0001)_c \,//\, (011)_\alpha$, along with the macroscopic shape change ellipse. Figure VIIIb shows an ILS semicoherent particle in the same orientation. For the fully coherent case, the interfacial energy is a minimum, and because there is a minimum misfit along $[100]_\alpha$, the particle maximizes its dimension in this direction (Principle 2). Here the macroscopic shape change ellipse does not intersect the unit sphere. For the ILS case, because of the coherency loss associated with the internal accomodation deformations pictured, the ellipse just touches the unit sphere at two points, defining a line (and so an ILS) along $[100]_\alpha$.

PURPOSE AND PLAN OF STUDY

Designers of critical structural components are currently limited by the performance of ultrahigh-strength steels. Performance for these steels is gaged by their strength/toughness combinations.

Controlled-recovery secondary-hardening steels are a class of ultrahigh-strength steels which exhibit outstanding combinations of strength and toughness. The primary strengthening mechanism in this class of steels is the precipi-

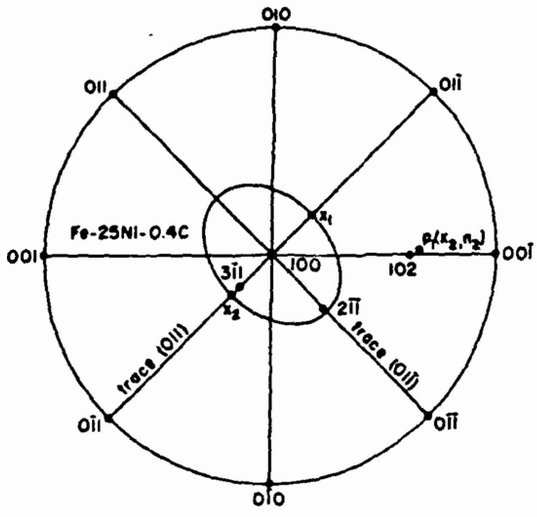


Figure IV. Cubic [100] stereogram depicting the Bain cone for the BCC→ε'-carbide lattice deformation in Fe-25Ni-0.4C. (After reference [61].)

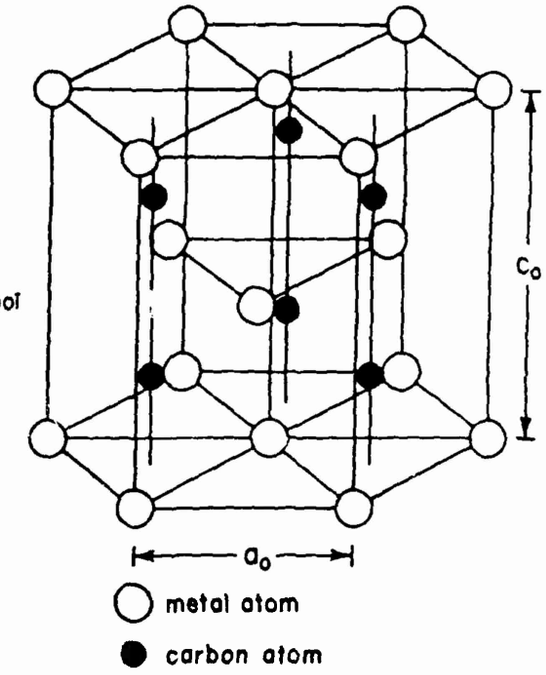


Figure V. Crystal structure of M_2C hexagonal carbides. (After reference [55].)

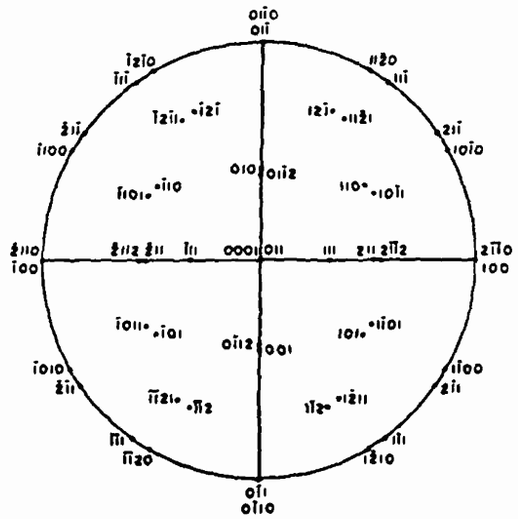


Figure VI. Stereographic projection of M_2C in ferrite based on the Pitsch-Schrader orientation relationship. (After reference [97].)

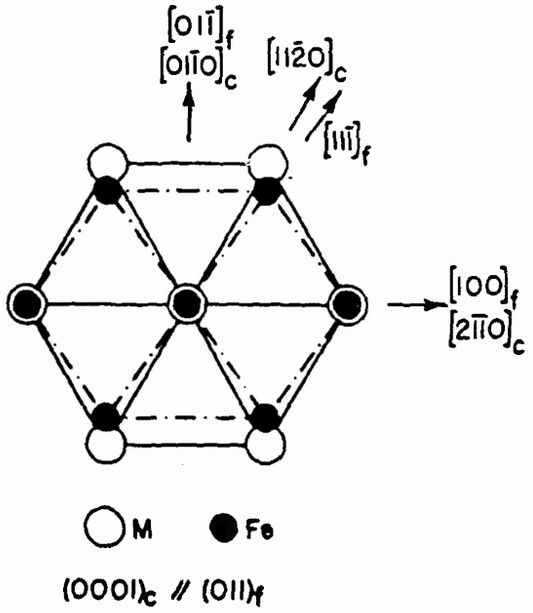


Figure VII. Orientation relationship between M_2C precipitates and ferrite matrix. (After reference [88].)

tation of M_2C carbides. In order to further improve the properties, the precipitation kinetics and kinematics need to be completely characterized. These steels have been developed semi-empirically, and thus precise knowledge of their microstructural evolution is lacking.

The ultimate goal of this research is to develop a predictive precipitation model to assist in the design of new alloys within this class of steel.

The class of steels investigated are in general, and AF1410 in particular, highly complex alloys whose chemistry and processing have been empirically optimized. These are not model systems in which fundamental materials science phenomena can be conveniently investigated, as, say in Ni-7%Al or Al-4%Cu. The reasons are legion:

- There are many components and many phases
- The alloys are not homogeneous
- There is short-range ordering of the matrix
- The carbon in the M_2C carbide can also order
- The carbon source for M_2C precipitation are the transition (iron) carbides ε and θ which have variable composition
- M_2C is itself a transition phase and also has variable composition
- The precipitation is heterogeneous primarily along dislocation lines
- Austenite precipitation is concurrent with M_2C precipitation.
- Much is happening simultaneously: M_2C is precipitating while its composition is changing, and the composition of the phase that is its carbon source is also changing. At later stages, recovery of the matrix occurs, and the stable (equilibrium) carbide precipitates.

Not only are these steels not model alloys, but it seems to be impossible to design a model alloy where one can examine one phenomenon without interference—it seems necessary to have everything occur simultaneously. The high degree of interaction in these alloys appears to be necessary for them to "work."

In spite of these difficulties, however, there is much we can learn from the study of these alloys. AF1410 has been extensively researched by these and other authors, so that many of the precipitation parameters are known. As outlined in the introduction, the theory of precipitation is fairly well-developed, but it is not quite up to the predictive level needed for alloy design. Thus, this paper represents a first-order explanation for the phenomena we observe in the subject steels. In the process, we will identify those aspects which need to be quantified more precisely to allow a predictive precipitation model for alloy design.

EXPERIMENTAL PROCEDURES

Material

Originally, commercial AF1410 steel was supplied by Carpenter Technology Corporation as 12.7mm (0.5in) square bar, austenitized (830°C/1.5hr), oil quenched, and deep-freeze-treated (-75°C/ 1hr). This material was used for the carbon extraction replicas and preliminary APFIM work. Later, we received the rest of the AF1410 from this heat (K89605) in as-rotary-forged 11.5cm (4.5in) round bar. This material was used for all other work. The composition of the alloy used in this study is shown in table V, while some of the properties of this alloy are listed in table VI.

There were two austenitizing (solutionizing) temperatures used for this material. The first, 830°C, or "commercial" solutionizing, temperature was used to duplicate material which has had much research performed on it (as above). However, other specimens were given a different 1000°C, or "complete" solutionizing, treatment. This temperature was chosen to ensure complete dissolution of all the carbide phases. Within this paper, "AF1410-830" will refer to AF1410 solutionized at 830°C, while "AF1410-1000" will refer to that solutionized at 1000°C.

By increasing the solutionizing temperature just 55°C, Gore [105, 106] found a dramatic change in the number of types of precipitates in AF1410, table VII. The M_3C phase in these lists is autotempered cementite. For the commercial solutionizing temperature (830°C), there is a long list of undissolved precipitates (found from carbon extraction replicas), while for the higher solutionizing temperature (885°C), the list becomes very short. For the complete solutionizing temperature (1000°C) the only item on the list should be autotempered cementite. The presence of a smaller number of phases makes it much easier to analyze the alloy with various techniques (TEM, SANS, XRD, APFIM), but it makes it less applicable to the condition in which the alloy is actually used; thus the two solutionizing temperatures.

Heat Treatment

For metallography, microhardness, carbon extraction replicas, and X-ray diffraction, where the preferred form is flat, polished, and about one square centimeter in area, the heat treatment procedure was as follows. Material in the as-received (AR) condition was cut into bars ~1.5cm (5/8in) square. AF1410 does not quench crack, so it can be sliced from a large block after austenitization. This steel is quite prone to decarburization (even with as little as 0.16 wt% carbon) so the heat treatment must be carefully planned to ensure no decarburization in the material being examined.

To obtain properly heat-treated material with no decarburization, smaller specimens are encapsulated in evacuated tubes of quartz or Vycor™ for austenitizing and Pyrex™ for tempering. Larger specimens (ones that will not fit into 25mm OD quartz/Vycor/Pyrex tube) are wrapped in 0.05mm (0.002in) stainless steel foil. Before any heat treatment, the specimen and its glass or stainless steel wrapper is carefully cleaned of oxides, grease, fingerprints, etc.

Once the AR material was sliced into ~3x15x15mm (~1/8x5/8x5/8in) platelets, they were marked with a vibro-engraver, cleaned of oxide and grease, and encapsulated in quartz or Vycor using a mechanical pump vacuum {<13Pa (<100 mtorr)}. No inert gas backfill was used, nor was any getter (Ti, Ta, etc.) used. The encapsulated specimens were quenched from the austenitizing temperature by breaking the tube over a bucket of quench oil, the specimens falling into the oil, which was then stirred.

The tempering temperature used throughout this study is 510°C (950°F), because of the extensive work done on AF1410 tempered at 510°C. Specimens of the alloy were tempered at 510°C for 5min to 1000hr. For times between 5min and 1hr, a neutral salt bath was used, or they were coated with an anti-decarburization coating (30min-1hr only). For times between 1 and 1000hr, specimens were cleaned and encapsulated in Pyrex under mechanical pump vacuum, no backfill, no getter (as before). Specimens were water quenched from the tempering temperature either by dropping the exposed specimens (short times), or the Pyrex-encapsulated specimens (long times), into a bucket of room-temperature water. Thermal shock would break the Pyrex

TABLE I. NOMINAL COMPOSITIONS AND PROPERTIES OF COMMERCIAL ULTRAHIGH-STRENGTH STEELS

Alloy	Composition (wt%)							Properties	
	C	Si/Co	Ni	Mo	Cr	Ti	Al	YS MPa (ksi)	K_{IC} (ksi√in)
300M	0.40	1.6Si	1.8	0.3	0.8	-	-	1585 (230)	55 (60)
18Ni300	0.03	9Co	18	5	-	0.65	0.10	1860 (270)	82 (90)
AF1410	0.16	14Co	10	1	2	-	-	1515 (220)	164 (180)
AerMet100	0.23	13.4Co	11.1	1.2	3.1	-	-	1725 (250)	91 (100)

TABLE II. THEORIES OF HETEROGENEOUS PRECIPITATE COARSENING

Heterogeneity	Diffusion Limited By	Time Exponent	References
none	bulk	1/3	[27, 28]
dislocation	dislocation ("pipe")	1/5	[47]
dislocation	bulk ("collector line")	2/9	[48]
grain boundary	grain boundary	1/4	[49]
grain boundary	bulk ("collector plate")	lengthening: 1/4 thickening: 1/2	[50,51]

TABLE III. M_2C UNIT CELL INTERCONVERSION

Subtype	Space Group	System	a_c^{orth}	b_c^{orth}	c_c^{orth}
L'3	$P6_3/mmc$	HEX	a	a√3	c
ε-Ni_3C	$R\bar{3}C$	TRIG	a/√3	a	c
ε-Fe_3N	$P6_322$	HEX	a/√3	a	c
ε-Fe_2N	P312	HEX	a/√3	a	c
C6	$P\bar{3}m1$	HEX	a	a√3	c
Co_2N	Pnnm	ORTH	c	a	b
ξ-Fe_2N	Pbcn	ORTH	b/2	c	a

TABLE IV. M_2C LATTICE PARAMETERS AND TRANSFORMATIONSTRAINS (a_α = 2.870Å)

Carbide	a_c (Å)	b_c (Å)	c_c (Å)	ε_1	ε_2	ε_3
ε'-Fe_2C	2.831	4.696	4.345	-0.014	0.157	0.071
Cr_2C	2.835	4.910	4.460	-0.012	0.210	0.099
$(Cr,V)_2C$	2.868	5.008	4.530	-0.001	0.234	0.116
$(Cr,Mo)_2C$	2.890	5.007	4.560	0.007	0.233	0.124
V_2C	2.904	5.030	4.579	0.012	0.239	0.128
W_2C	2.997	5.191	4.728	0.044	0.279	0.165
$Mo_2C_{0.9}$	3.002	5.200	4.725	0.046	0.281	0.164
Mo_2C	3.012	5.218	4.735	0.050	0.286	0.167

TABLE V. COMPOSITION OF THE ALLOY USED IN THIS STUDY (wt%)

	C	Co	Ni	Cr	Mo	Fe
AF1410	0.163	14.24	10.21	2.10	1.03	bal.

TABLE VI. PROPERTIES OF AF1410

Property	Value
E	203 GPa
ν	0.295
A_{C1}	627-629°C
A_{C3}	822-828°C
M_S	335-338°C
M_F	160-177°C

and cause a good water quench.

For an extra margin of safety, the fully heat-treated specimens were then surface ground from one side, to remove any possible decarburization, recarburization or contamination. In all cases at least 0.25mm was ground off, but for longer-tempered specimens, more material was removed usually at least 0.50mm). The specimens were then normally mounted in Bakelite and metallographically ground and polished.

Microhardness Measurements

Vickers microhardness (VHN) of fully heat-treated and surface ground platelets was used because many measurements can be taken on one specimen, and the variation gave a better indication of the specimen's heterogeneity. Specimens were mounted in Bakelite and polished through six micron diamond. A 1000 gm load was used; ten measurements were taken in a line centered on the specimen and indentations were spaced 1-2 mm apart. The mean and the variance of these ten measurements was then taken.

Transmission Electron Microscopy

A Philips EM400T Transmission Electron Microscope was used primarily, with some of the work performed on several JEOL 200CX microscopes. 3mm discs were either punched out of pre-thinned sheet or sliced from 3mm diameter rods, finish-ground with 600 grit paper to <0.025mm, and electropolished with 5% perchloric acid plus 1% glycerol in methanol at -50°C (±5°C), 25VDC. Chromic-acetic acid solutions were tried without success.

It was found that an oxide film would rapidly form (within a few hours, even under vacuum) on the surface of thinned foils that only sometimes could be removed by ion milling. This film gave Moiré fringe contrast starting at carbides, then proceeding to patches in the matrix, and finally covering the entire surface with fringes. This oxide film seemed to be quite similar to the film reported by Taylor [61] on Fe-15Ni-1C, and that reported by Heckmus and Stubbe [107]. To permit easier viewing of more carbides as well as measurement of their lattice parameters, carbon extraction replicas were used. Between 10 and 20 carbides were measured for each tempering treatment. The sizes and shapes of the carbides were spot-cross-checked between the two techniques.

For most of this work, specimens were mounted in Bakelite, ground and polished through 6 micron diamond, and a thin layer of carbon evaporated onto the surface. This carbon layer was stripped with 5% bromine in methanol at -20°C (±10°C), given successive washes in methanol and collected on 400 mesh copper grids. Later work has employed an electrolytic 5% HCl in methanol solution operated at 5VDC, room temperature, for etching and stripping. For lattice parameter work, 50-100Å of reagent grade aluminum was evaporated onto the replica to provide an internal calibration which resulted in reducing the error in the d-spacings to ±0.01Å. It was found that using a separate (external) standard gave inaccurate results, even with extreme care.

X-ray Diffraction

Polished specimens were broken out of the Bakelite mounts and centered in a Picker X-ray diffractometer equipped with a Cr rotating anode source, diffracted beam monochromater and scintillation detector. The intensity vs. 2θ scan was digitally read into an IBM PC™-compatible computer, which simplified data analysis. For austenite and cementite volume fraction determinations, the intensities of the peaks were found from (1) subtracting the background: five data points on either side of the peak, far from the peak were used to fit a linear least-squares fit line to the background; (2) this background was then subtracted from the peak and (3), the peak was integrated using Simpson's rule. The peak intensity ratios were used in the direct comparison method [108] to determine the volume fractions of austenite and cementite.

For austenite, only one peak from each phase (austenite 220 and ferrite 200) was used, and the R-factor used was derived from calibration with NBS Standard Reference Material #485.

$$\frac{f_V^\gamma}{f_V^\alpha} = R_{\gamma 220 \alpha 200}\left[\frac{I_{\gamma 220}}{I_{\alpha 200}}\right] \qquad (25a),$$

where f_V are the volume fractions of the phases i, I_i are the integrated peak intensities, and R_{ij} are the R-factors relating intensity to volume fraction. At longer tempering times (larger volume fraction precipitated austenite), the intensity of the γ peaks were sufficiently intense so as to allow a lattice parameter determination.

$$\frac{f_V^\theta}{f_V^\alpha} = R_{\theta\alpha 110}\left[\frac{I_\theta}{I_{\alpha 110}}\right] \qquad (25b),$$

$$\frac{f_V^\theta}{f_V^\alpha} = R_{\theta\alpha 200}\left[\frac{I_\theta}{I_{\alpha 200}}\right] \qquad (25c).$$

The cementite peaks used were (121), (210) and (002). These are intense enough, and close enough together, that they can be integrated as one peak. This integrated cementite peak (I_θ) was compared against the (110) and (200) ferrite peaks ($I_{\alpha 110}$, $I_{\alpha 200}$). The R-factors were initially calculated using the direct comparison method described in Cullity [108]. Later on, R-factors were obtained by assuming para-equilibrium exists at a tempering time of thirty minutes, and calibrating the measured volume fraction of cementite with that calculated using Thermo-Calc. These calibrated R-factors were found to be about 40% lower than the calculated ones. Giamei and Freise [109] found that as the volume fraction of cementite became small, the R-factors changed significantly, justifying the use of the calibrated R-factors. Because the material is slightly textured, the volume fractions found from each of these R-factors were generally different, and these were plotted as separate data, rather than averaging them.

Cementite has a great many diffraction peaks. However, most of the more intense ones are too close to ferrite, austenite, or M_2C peaks, and therefore cannot be used. The use of MoK_α radiation would be preferable to the CrK_α used, as the shorter wavelength would allow access to more peaks, some of which would not interfere with the peaks from other phases. Because the intensity of the cementite peaks used is so low, very slow scans (2000 sec/deg 2θ) over large values of 2θ (10 deg) gave very long experimental runs (6hr), which really pushes the assumption of beam stability. Therefore, the ferrite peaks were run twice, before *and after* the cementite peaks, and the intensities of these (ferrite) peaks were averaged. These intensities generally did not vary much: less than 2%. However, it would be preferable to use a beam intensity monitor so as to not rely so much on the assumed stability of the beam during these long runs.

For the "precision" lattice parameter measurements, narrower incident-beam and receiving slits were used. For the Nelson-Reilly-Taylor-Sinclair (NRTS) [108] extrapolation routine, only peaks with 2θ angles between 90° and 180° are used; the only ferrite peaks available in this range (using CrK_α radiation) are the 200 (~106° 2θ) and the 211 (~156° 2θ) peaks. It would be much more preferable if four or more peaks could be used (leading to greater precision); this would necessitate the use of MoK_α radiation. The a_α's determined from the two peak positions were extrapolated to $2\theta = 180°$ to find the most precise value of the lattice parameter.

RESULTS

Microhardness Measurements

As an introduction to the isothermal tempering behavior of AF1410, Vickers microhardness of the specimens used for XRD and SANS experiments is plotted vs. tempering time at 510°C in figure IX. Data for both solutionizing temperatures are shown. There are two unusual features in these tempering curves: (1) the 830°C-solutioned material is overall harder than the 1000°C-solutioned material, especially at shorter times. In terms of the amount of precipitating M_2C, one would expect the other steel to be harder. (2) There is a precipitous drop in hardness at 8hr. This is reproducible for these specimens. However, when duplicate specimens ("DUP1" and "DUP2") were heat-treated and tested, they had the effect of smoothing out the hardness curves, but there is still a noticeable drop at 8hr. The data points for these later specimens are shown as smaller, filled symbols.

Thin Foils of AF1410

In the 1hr condition, the carbides are just barely observable as 20-60Å particles, seen primarily on dislocations. The dislocation density is extremely high. After 5hr, the carbides are more easily observed as 150Å ellipsoids. The dislocation density is still very high, but consists of more regularly-spaced networks. After 16hr, the carbides have not coarsened greatly and are still about 200Å long. There are patches of dislocation-free areas. In the 100hr condition, the carbides have coarsened to about 300Å in length, and the matrix appears fully recovered.

The orientation relationship of the carbides with the matrix was not systematically determined, but the observed diffraction patterns were consistent with the Pitsch-Schrader orientation (figure V).

The width-wise type of fringes in the carbides reported by Tanino et al. [104] and Davenport [54] were not observed in the AF1410 M_2C carbides, nor was the presence of any "footprint" morphology of the M_2C carbides. Other fringes attributed to an oxide surface layer were, however, observed. The presence of this tenacious oxide film was one reason for the move to the use of carbon extraction replicas.

Carbon Extraction Replicas

Figure X shows the length of the M_2C carbides as a function of tempering time at 510°C for AF1410. The triangles are data from a preliminary FIM investigation by Liddle et al. [21], and the connecting line is dashed because of problems with local magnification at these sizes. The circles are from the present extraction replica results. The data overlap nicely in the 3-16hr region. At the far right-hand side (>100hr) is a reference slope of 1/3 from LSW coarsening theory [27, 28].

Individual carbides from steels with various tempering conditions were carefully examined for signs of internal faulting, so as to identify an inhomogeneous lattice-invariant deformation for the near-ILS transformation, vis-á-vis Taylor [61]. In no case was such faulting observed, within the resolution of the technique used.

The M_2C carbide lattice parameters are shown in table VIII for AF1410, tempered at 510°C for 1 to 196hr. The spacings shown are good to ±0.01Å, as these were arrived at by using an internal calibration standard described in the previous section. The a'_c parameter here is the a-parameter of the carbides assuming an hexagonal crystal structure with no orthorhombic distortion ($\omega = 1$).

The AF1410/1hr carbide lattice parameters could not be determined because of diffuseness of the rings, probably due to a composition range of the carbides and/or a size effect, giving a range of lattice parameters. For AF1410, a'_c is constant at 2.88Å until 16hr, where there is an upward shift. At 100hr and beyond a'_c is constant at 2.90Å.

Figure XI is a composite figure showing the M_2C carbide length, aspect ratio β, lattice parameters and alloy microhardness as a function of tempering time at 510°C. From FIM observations [18, 19, 20, 21, 22], it is believed that the aspect ratio starts off at about 1, which is reasonable for a particle minimizing its interfacial area, and there seems to be an upward trend in aspect ratio. The 0.02Å shift in the a'_c lattice parameter is shown graphically near the bottom of the figure.

X-ray Diffraction

The R-factor that was found by calibration with NBS SRM 485 was used in equation (25a):

$$\frac{f_V^\gamma}{f_V^\alpha} = 0.290\left[\frac{I_{\gamma 220}}{I_{\alpha 200}}\right] \qquad (26a),$$

to find the volume fraction of austenite as a function of tempering time for AF1410 given each of the solutionizing temperatures. This is shown in figure XII. Data marked "HML" is from the thesis of Lee [37]. Tempering times below one hour gave negligible austenite volume fractions. The lattice parameter of the austenite precipitated was found to be fairly constant at 3.588 ± 0.002Å.

Using calculated R-values,

$$\frac{f_V^\theta}{f_V^\alpha} = 1.84\left[\frac{I_\theta}{I_{\alpha 110}}\right] \qquad (26b),$$

$$\frac{f_V^\theta}{f_V^\alpha} = 0.40\left[\frac{I_\theta}{I_{\alpha 200}}\right] \qquad (26c),$$

figure XIII was obtained: the cementite volume fractions as a function of tempering time in AF1410. The amount of cementite present at 100hr is not insignificant relative to that at 5min, and suggests that it can never be totally eliminated. The cementite peak-to-background ratios of all the samples examined were below 1.4, so noise has a significant effect on the scatter of the data. Allen's SANS M_2C volume fraction measurements [110] are also plotted on this figure, using the first-order calibration scheme described in the following section.

Figure XIV shows the matrix lattice parameter, also

as a function of tempering time, for both the 830°C and 1000°C-solutioned material. The drop is very small for the precision of the measurement—the use of Mo radiation would probably give at least one more significant digit. The drop in lattice parameter is due to Cr and Mo coming out of solid solution and precipitating as M_2C carbide. There is a significant drop at 30min for the 830°C material and at 2hr for the 1000°C material. This would indicate faster precipitation kinetics of the lower-temperature solutionized material.

Results of Collaborative Studies

Microanalysis

In their theses, Haidemenopoulos [15] and Carinci [19] determined the composition of austenite in AF1410 tempered at 510°C for 8hr. Haidemenopoulos used a VG HB5 STEM, while Carinci used a VG FIM-100 APFIM. Additionally, Haidemenopoulos used Thermo-Calc to calculate the equilibrium composition at this tempering temperature, table IX. Their results qualitatively agree, except with regard to the most important element—Ni. This element is the primary determiner of the stability of the austenite. It is expected that the actual, average austenite composition lies between these two measurements.

Using the atom probe, Carinci [18, 19] measured the composition of the M_2C carbides in AF1410 at selected tempering times. Later, using the same equipment, Olson et al. [22] expanded on these measurements to include more carbides and a broader range of times. Figure XV shows these compositions, averaged over the number of ions analyzed.

Microstructure

Allen et al. [110], has performed extensive small angle neutron scattering (SANS) experiments and analysis on AF1410 with both solutionizing temperatures (830 and 1000°C), tempered from 15min to 100hr. Because of the many carbides sampled with this technique, it is believed to be the most accurate. This SANS data (size, number density and volume fraction) was therefore used preferentially over APFIM and TEM data for the analyses in this paper. However, the shape of the carbides (aspect ratio) could not be determined by this technique, so TEM data was relied upon to calculate equivalent sphere diameters. Figure XVI shows the equivalent sphere diameters, number densities and volume fractions of M_2C. It is seen that, during precipitation, the log carbide size versus log time is nearly linear instead of sigmoidal. This suppression of a growth regime is what is predicted by the Langer-Schwartz theory for systems with high supersaturation. There appears to be a small blip, away from linearity, at 1hr, which suggests a small amount of growth at this time.

Figure XVII shows how the size distributions change with tempering time. A curious feature of both sets of curves is that the distributions appear to go backwards between two aging times. That is, the population of carbides do not completely monotonically increase in size. This happens between 1 and 2hr for both AF1410-830 and AF1410-1000. The number density of carbides continues to increase in this time interval, so the carbides are not shrinking or dissolving. The only explanation for this is that there is a burst of nucleation between 1 and 2hr ("renucleation") which pumps up the size distribution from the lower end. The conditions that make this possible are considered in the discussion section.

ANALYSIS

Qualitative Discussion of AF1410

Accelerated precipitation kinetics

From Davenport's isothermal tempering studies of a 3.5Mo-0.22C steel [54], it is estimated that this steel reaches peak hardness at 510°C after 220hr. Speich's work on 10Ni-8Co-2Cr-1Mo-xC steels [1, 2] showed that these steels reached peak hardness after about one hour at 510°C. The AF1410-830 in this study reached peak hardness at 510°C after about one hour, while AF1410-1000 reached it between 1 and 2hr. Other experimental 0.25C Co-Ni-Cr-Mo steels examined by the authors have all reached peak hardness after about 10hr [111]. As stated in the introduction, Co has the effect of retarding dislocation recovery, and of raising the activity of carbon in solution, providing a greater driving force for precipitation.

At the earliest times investigated (1hr), the precipitates were observed on dislocations. However, because the dislocations have some mobility at the tempering temperature (510°C), they could have moved the short distance required to associate themselves with the precipitates. This distance is given by

$$s = \frac{1}{2}\left[\frac{1}{N_V}\right]^{1/3} \qquad (27),$$

where N_V is the number of particles per unit volume. If we use the maximum value of N_V, found after tempering 2hr by Allen et al. [110], of $3.6 \times 10^{17}/cm^3$, s is about 70Å.

From energetic considerations, it is more probable that the carbides are heterogeneously nucleated on dislocations. The contention that all the M_2C carbides are associated with dislocations is supported by work by Speich et al. [1, 2] on a 10Ni-8Co-2Cr-1Mo-0.12C steel (HY180). At peak hardness, they observed a dislocation spacing λ of 400Å and a carbide spacing along these dislocations s_L of 100Å. The number density of these carbides is

$$N_V^{HY180} = N_L L_V = \frac{L_V}{s_L} = \frac{3}{\lambda^2 s_L} = \frac{1.9 \times 10^{17}}{cm^3} \qquad (28).$$

This steel had 0.12 wt% C, while AF1410 has 0.16 wt% C. The two alloys both have 2Cr-1Mo. Therefore, assuming all other things remain equal, the number density of carbides at peak hardness in AF1410 should be increased over that in HY180 by a factor of 0.16/0.12. This gives $N_V^{AF1410} = 2.5 \times 10^{17}/cm^3$. The number density of AF1410-1000 was measured by Allen [110] using SANS as $1.3 \times 10^{17}/cm^3$ at 1hr and $3.6 \times 10^{17}/cm^3$ at 2hr. (This steel exhibits peak hardness between these two tempering times.) The agreement is very good.

Thus, as observed by Davenport [54], Speich et al. [1, 2], and corroborated by the thin foil work of this study, nucleation/growth/coarsening (precipitation) of M_2C in these steels is heterogeneous, on dislocations. The high dislocation density inherited from the martensitic transformation is able to persist at the high tempering (secondary hardening) temperatures because of the effect of Co. Assuming that this is the only effect of cobalt, the spacing of carbides along the dislocations (s_L) will remain constant between two hypothetical alloys, one with cobalt and the other without. However, because the original high dislocation density of the martensite is retained during precipitation, there will be a greater number density of carbides overall. Also, since the dislocation density is higher, the average distance between dislocations (λ) will be smaller, so that the solute that eventually goes into the precipitate has to travel a shorter distance. The time it takes for solute to diffuse a certain distance is proportional to the square of that distance. Therefore, if this dis-

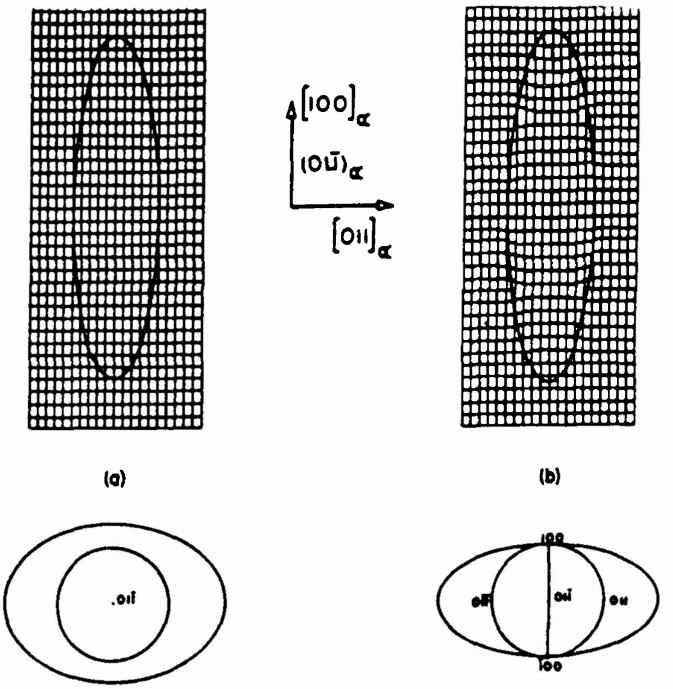


Figure VIII. Ellipsoidal carbide particles edge-on to the basal plane, with associated deformation ellipses. (a) Fully coherent case, (b) semicoherent ILS case.

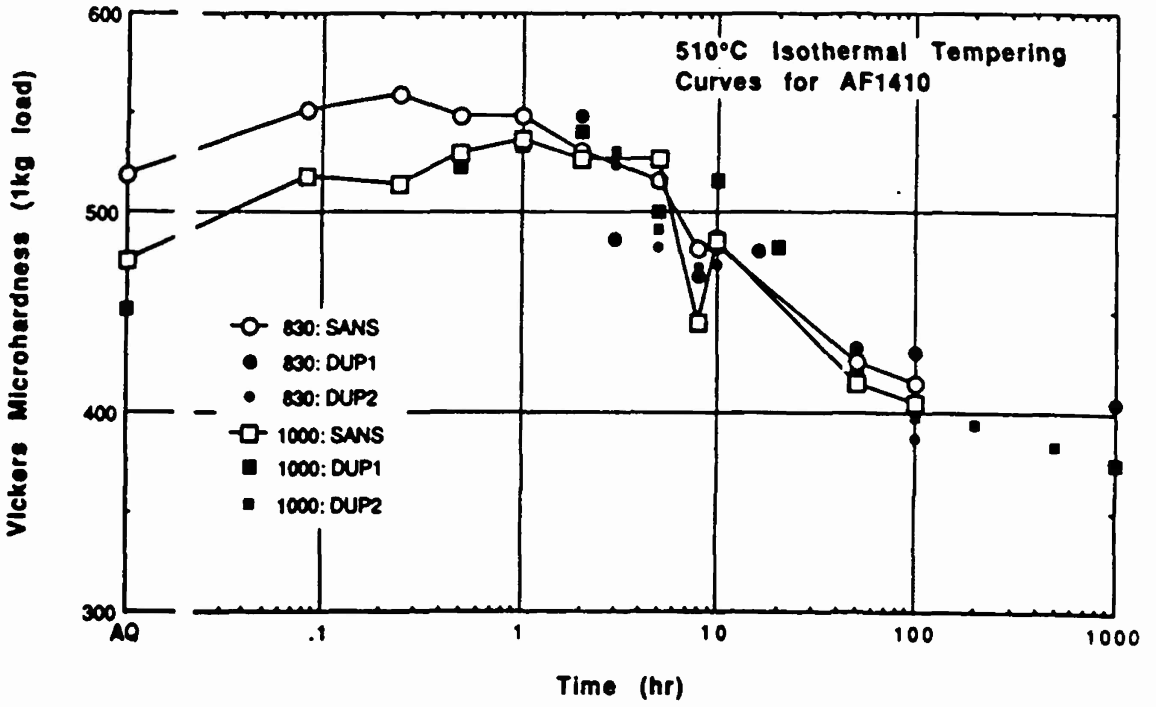


Figure IX. Vickers microhardness of AF1410 for the two solutionizing temperatures as a function of tempering time (SANS specimens and duplicate specimens).

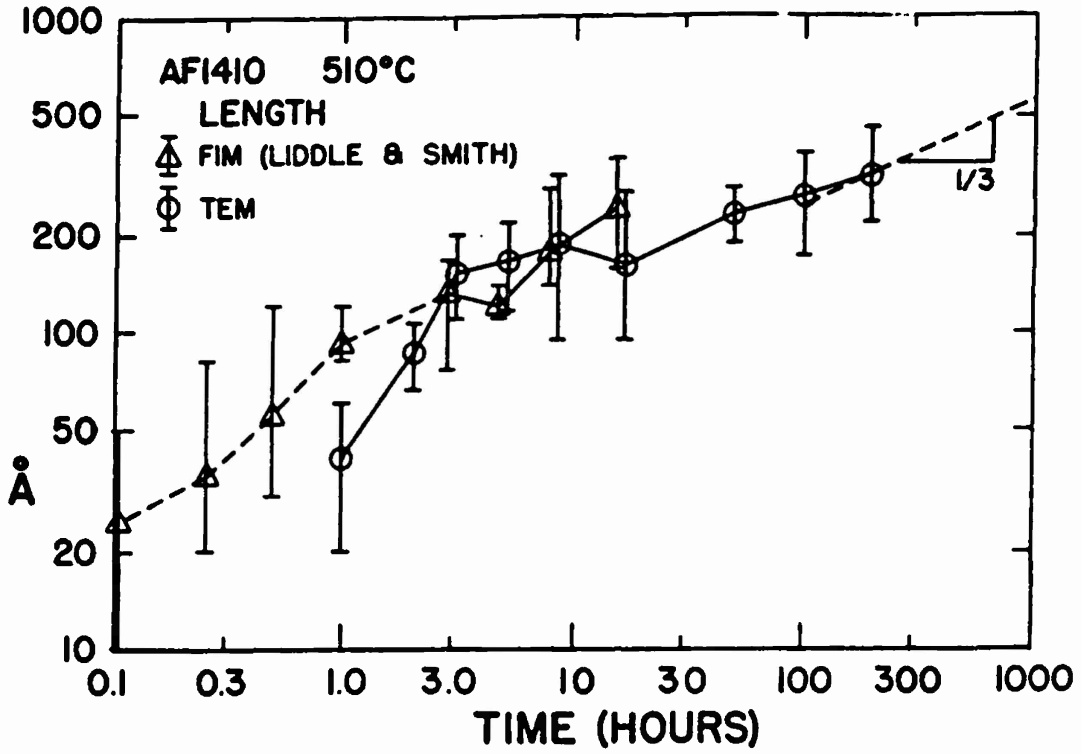


Figure X. Length of M_2C carbides extracted from AF1410 as a function of tempering time at 510°C.

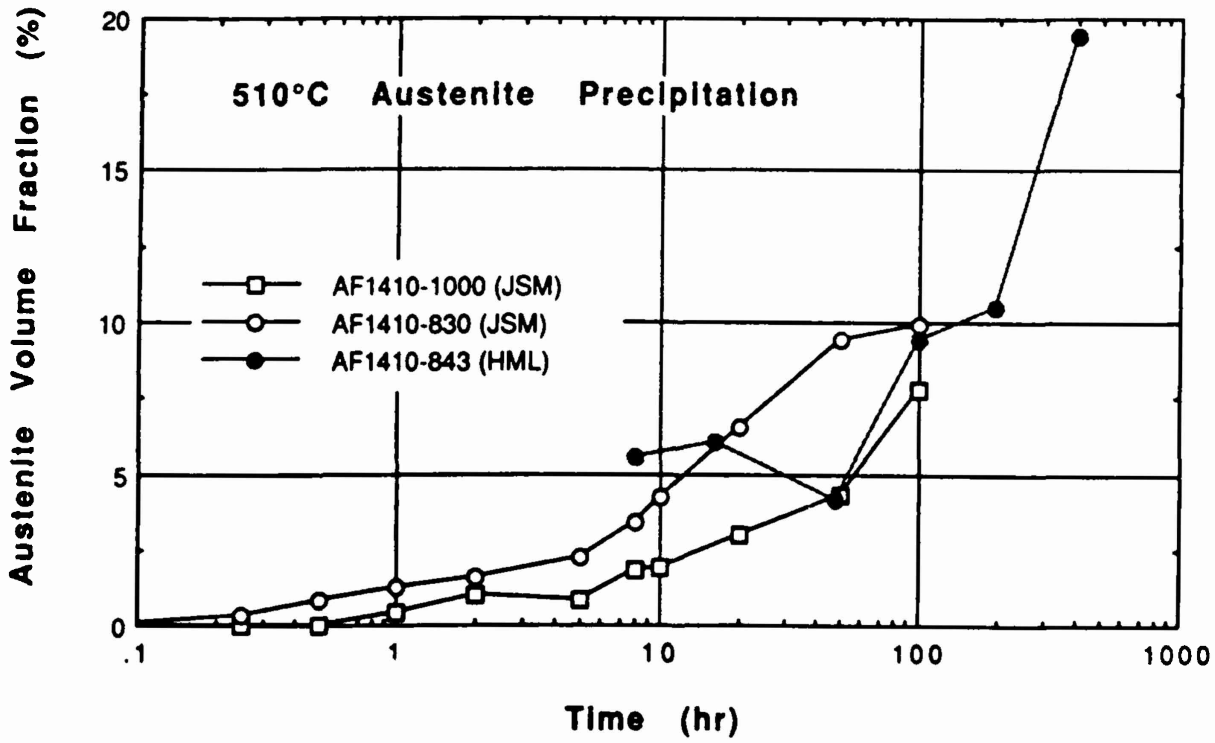


Figure XII. Austenite volume fractions (from XRD) as a function of tempering time at 510°C. Data marked "HML" are from Lee [37].

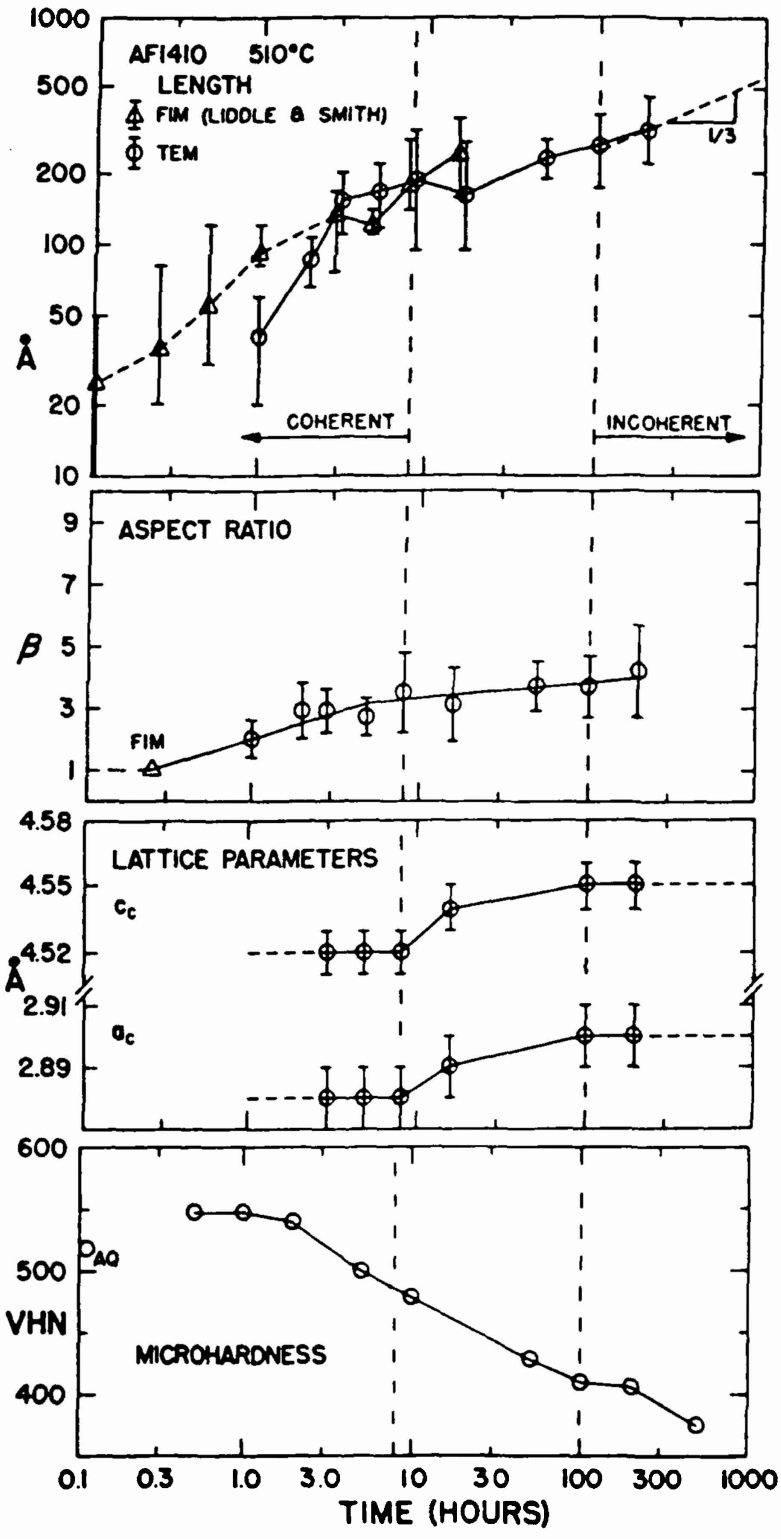


Figure XI. Length, aspect ratio, and lattice parameters of M_2C carbides extracted from AF1410-830, and microhardness of the alloy as a function of tempering time at 510°C.

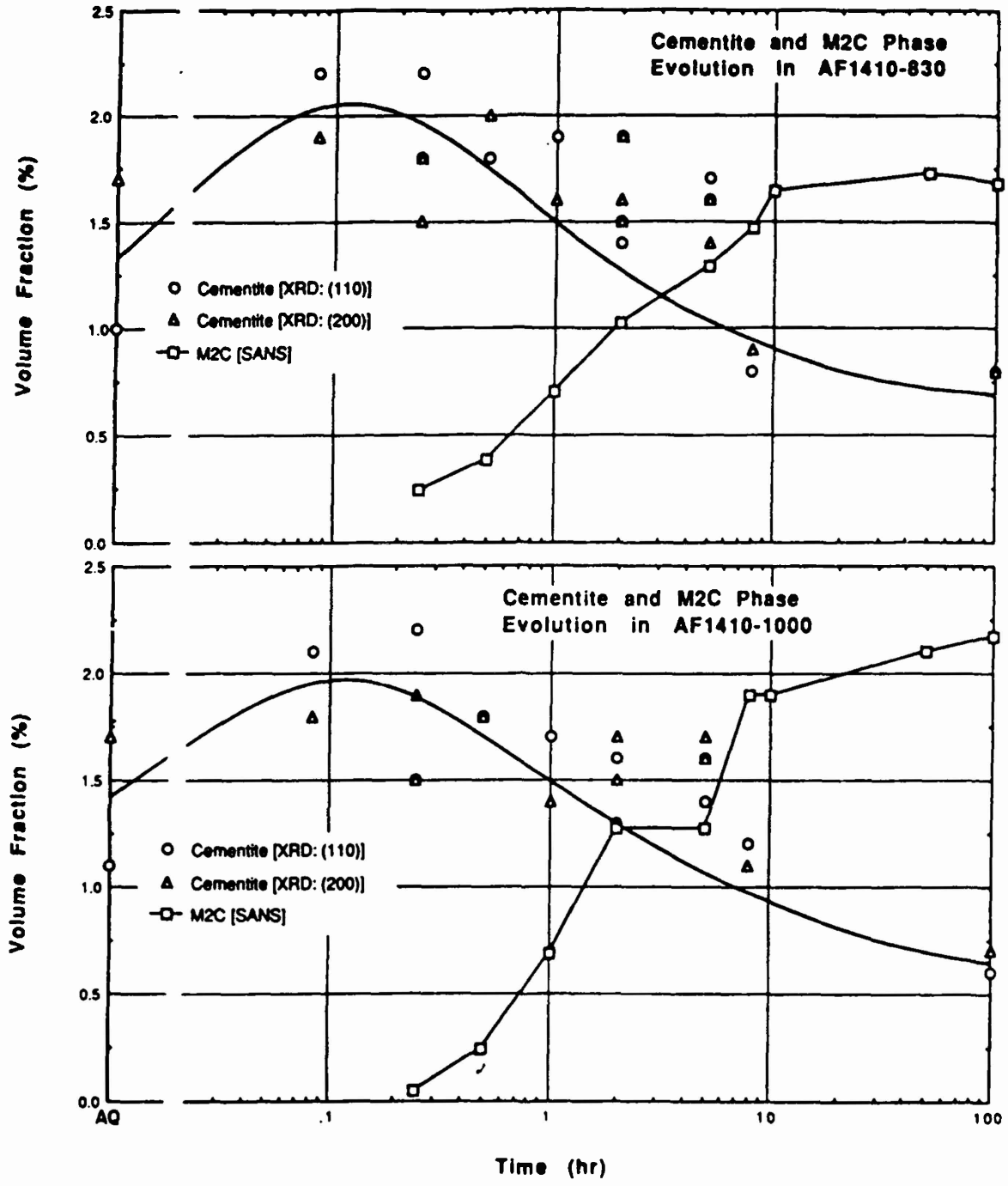


Figure XIII. M_3C (from XRD, using calculated R-values) and M_2C (from SANS, using a first-order calibration) volume fractions as a function of tempering time for AF1410-830 and AF1410-1000. The ferrite diffraction peak used is indicated as either (110) or (200).

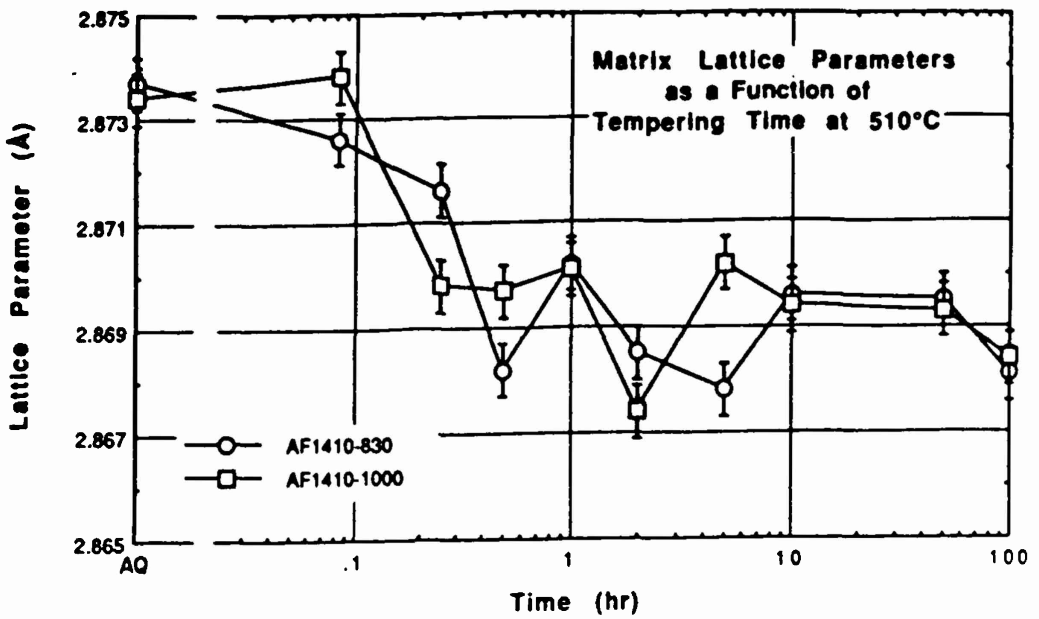


Figure XIV. Matrix lattice parameters (from XRD) as a function of tempering time of AF1410-830 and AF1410-1000.

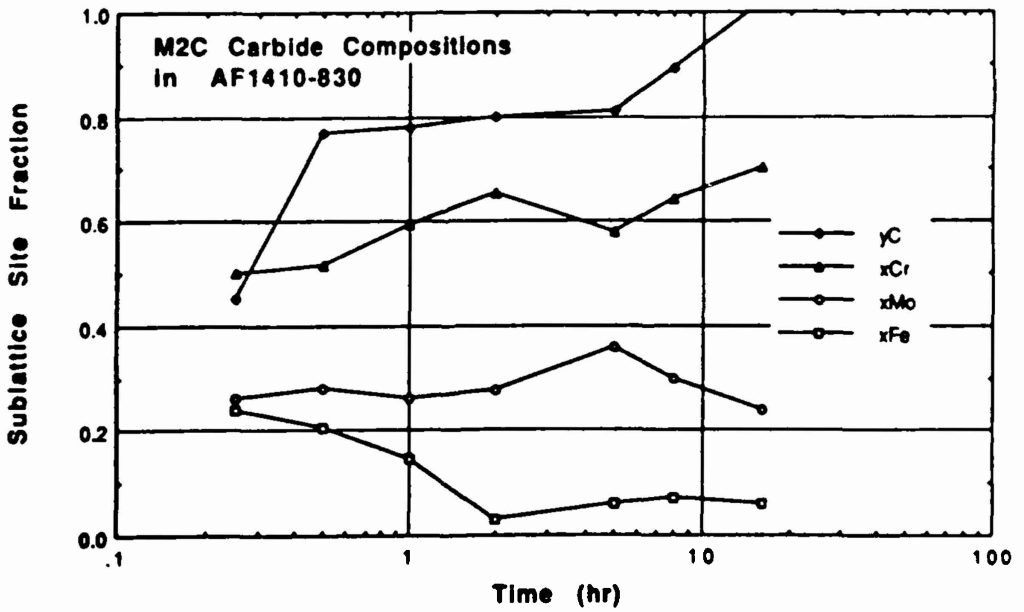


Figure XV. Measured composition of M_2C in AF1410 tempered at 510°C using APFIM. (From references [18, 22].)

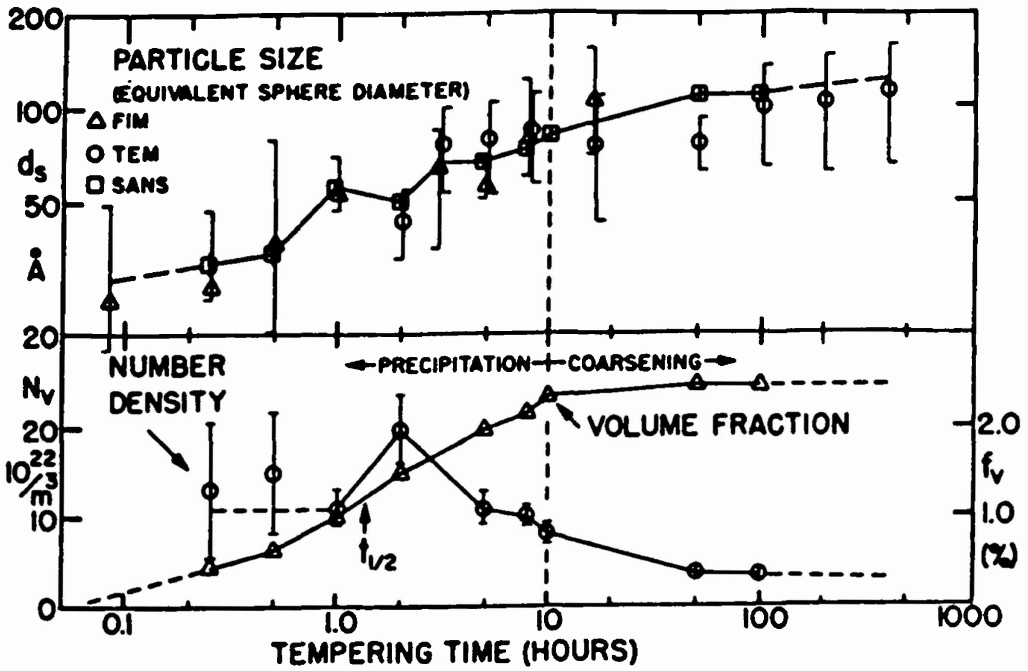


Figure XVI. M_2C carbide equivalent sphere diameter, number density, and volume fraction in AF1410 as a function of tempering time at 510°C. (From reference [110].) Data marked "FIM" are from a preliminary study by Liddle [21].

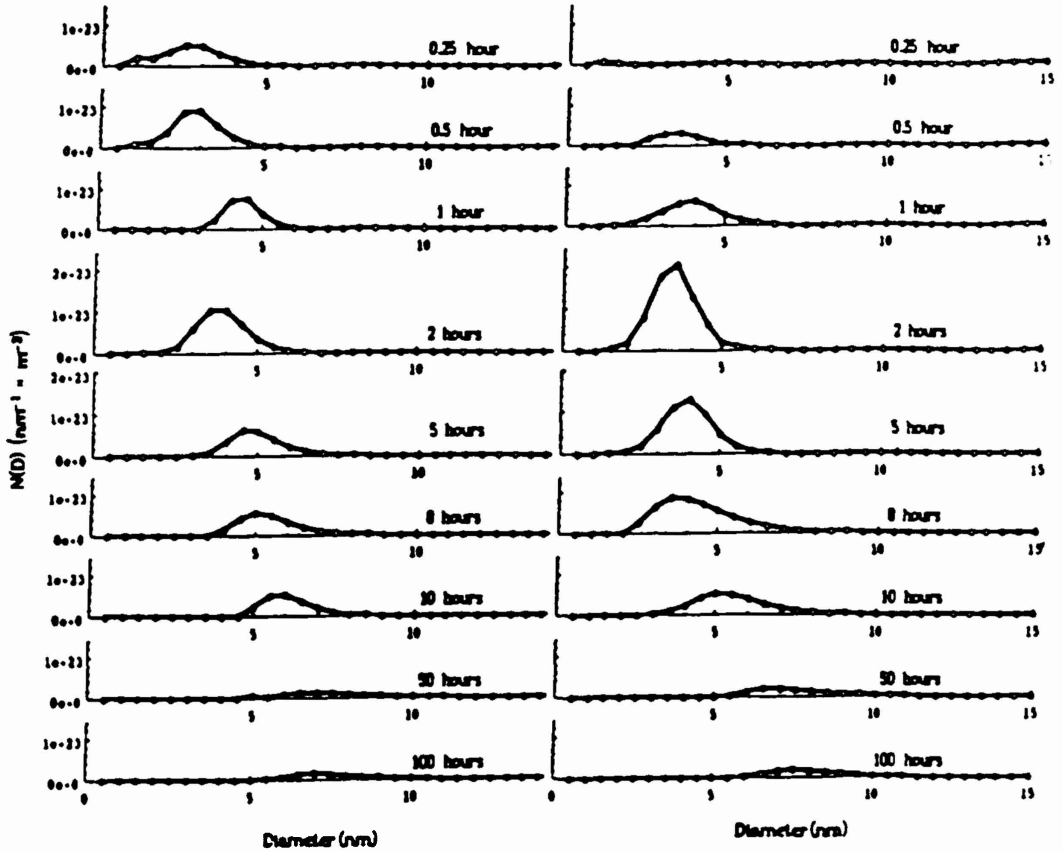


Figure XVII. Carbide size distributions as a function of tempering time at 510°C of AF1410-830 and AF1410-1000. (From reference [110].)

tance is reduced by a factor of 14.8, this gives the required 220X acceleration in kinetics. The dislocation density is

$$L_V = \frac{3}{\lambda^2} \quad (29),$$

so that to reduce λ by a factor of 14.8, L_V must be increased by a factor of 220. This increase is easily obtained by the retardation of dislocation recovery. Thus, overall, the kinetics are accelerated by the same factor as the increase in dislocation density. In this analysis we have ignored the effect Co will have on the driving force for precipitation. This may have a significant effect on the nucleation rate because of the exponential dependence on driving force. Since cobalt increases the driving force, this will increase the nucleation rate and speed precipitation.

The presence of the high dislocation density in the unrecovered martensite does not necessarily increase the rate of solute transport to the growing precipitate, but it will alter the coarsening time exponent. This is because the mass transport through the bulk is usually the rate-limiting step. The time it takes for the solute to diffuse through the bulk (lattice) to the dislocations is

$$t_{bulk} = \frac{(\lambda/2)^2}{D_{bulk}} \quad (30),$$

while the time it takes for the solute to diffuse down the dislocation "pipe" to the precipitates is

$$t_{pipe} = \frac{(s_L/2)^2}{D_{pipe}} \quad (31).$$

The step that takes the longest is the rate-controlling step. Thus when

$$\frac{\lambda^2}{D_{bulk}} > \frac{s_L^2}{D_{pipe}} \quad (32),$$

bulk diffusion controls, and vice versa. Rearranging this yields

$$\frac{D_{pipe}}{D_{bulk}} > \frac{s_L^2}{\lambda^2} \quad (33).$$

In a steel almost identical to AF1410, Speich [1, 2] observed $\lambda = 400$Å and $s_L = 100$Å. This gives $s_L^2/\lambda^2 = 0.06$. Since D_{pipe}/D_{bulk} is always much larger than one, diffusion through the bulk will control the mass transport of solute. Thus the precipitation kinetics are accelerated by the high dislocation density during precipitation not because of pipe diffusion, but rather by the higher volume density of nucleation sites. Again, the effect of Co on the driving force may also have a significant contribution.

Averaging the available microhardness data on AF1410-830 and AF1410-1000, shows AF1410-830 to be initially harder, then at later times, AF1410-1000 takes over. The explanation here is that initially they both have about the same volume fractions of M_2C, but AF1410-830 has the smaller grain size, making it harder. At the "complete solutionizing" temperature, there is undoubtedly some grain growth occurring. This is because the grain-boundary pinning precipitates, MC carbides in this case, are dissolved. Because of the Hall-Petch effect, all other things being equal, the smaller-grained material will be stronger. At later tempering times, AF1410-1000 is able to precipitate out a greater volume fraction of M_2C because more was put into solution during austenization. Therefore, AF1410-1000 ends up slightly harder. This contention is supported by the SANS data: the number density of M_2C of AF1410-1000 begins to exceed that of AF1410-830 between one and two hours.

Schmidt and Gore [112] observed the same phenomenon in AF1410 over an even narrower range of solutionizing temperatures (815-885°C), except that initially harder material remained harder at all tempering times. They measured the prior austenite grain size and found some grain growth, but not enough to explain the magnitude of the hardness differences. Their explanation was that the higher solutionizing temperature dissolves more of the excess ($M_{23}C_6$, M_6C) carbides, increasing the amount of Cr in solution. Referencing Speich [1], they stated that this will increase the coarsening rate of the carbides, and so lower the alloy's hardness. However, if this were the case, the higher-solutioned material should have earlier peak hardness, instead of the observed parallel hardness curves. There is another explanation for this phenomenon. It is agreed that the differences in grain size probably cannot account for the differences in the hardnesses of their steels. They noted that there was more autotempering in the higher-solutioned material because of the increased Cr in solution raising M_S, but could not use this as an explanation because the hardness differences persisted even after the cementite is substantially dissolved. Because there is more Cr in solution in the higher-solutioned material, the precipitating M_2C will also have more Cr dissolved in it. Although the magnitude of this effect is unknown at this time, the Cr/Mo ratio of the carbides will determine the strength of the obstacle to dislocation movement.

High Supersaturation and $t^{1/5}$ Coarsening

All of the alloys studied fall into the high supersaturation regime as defined by the Langer-Schwartz theory [30]. The supersaturation is high when

$$y = \left[\frac{kT}{\delta W^*}\right]^{1/2} \geq 0.3 \quad (34)$$

δW^* can be found by rearranging the nucleation rate equation (1) to yield

$$\delta W^* = -kT \ln\left[\frac{J}{Z\beta^* N_0}\right] \quad (35).$$

The nucleation rate J was estimated from $\Delta N_V/\Delta t$ and Z was estimated to range between 1/2 and 1/200. β^* was estimated from the multicomponent coarsening rate constants found by Lee [36, 37], adjusted to take into account the higher concentration of solute. The nucleation site density N_0 was estimated assuming that a possible site was on a dislocation with a site spacing b along the dislocation.

Computed estimates of y in table X indicate y is between 0.312 and 0.637. Thus the alloy is in the high supersaturation regime. This is consistent with the suppression of the growth regime as seen in the r(t) curve of figure XVI.

Excluding the "growth" data point at 1hr of Allen's SANS M_2C sizes vs. log time and taking a least-squares fit, we obtain a time exponent of 1/5.2 for AF1410-830 and 1/5.4 for AF1410-1000. This is acceptably close to that found from coarsening theories in which diffusion is limited

by dislocation pipe diffusion (1/5) and by bulk diffusion to dislocations (collector line) (2/9).

Lattice Parameters as a Function of Composition

M_2C carbide

The effect of V, Cr, Fe, Nb, Mo, Ta, W and C on the lattice parameters of M_2C was found from an extremely wide range of sources [9, 55-60, 65, 67, 71-73, 82-84, 100, 113-125]. As discussed in the introduction, carbides of mixed composition generally exhibit lattice parameters which are the rule-of-mixtures (Vegard's Law) values, using the parameters and the site fractions of their pure components.

Effect of Cr: Pure Cr_2C seems to have been synthesized only once, by Lux and Eberle [117], which indicates that its existence is questionable. Instead of using their lattice parameters (a_c = 2.79Å, c_c = 4.46Å), data from the mixed carbide $(Cr,Mo)_2C$ [57] was extrapolated to pure Cr_2C to obtain its lattice parameters (a_c =2.835Å, c_c = 4.460Å). This value is not far from the value found from extrapolating data from $(V,Cr)_2C$ [56] to pure Cr_2C (orthorhombic: a_c^{ORTH} = 2.821Å, b_c^{ORTH} = 4.883Å, c_c^{ORTH} = 4.401Å) and then converting to an hexagonal unit cell (a_c = 2.819Å, c_c = 4.401Å).

Effect of Fe: Data on the effect of Fe on the lattice parameters of M_2C does not exist; and there is little data on orthorhombic Fe_2C. This is the ordered carbide investigated by Hirotsu et al. [65, 66] (their η-carbide) and Taylor et al. [61, 62] (their ε'-carbide). This set of papers has the a, b, and c orthorhombic lattice parameters as a function of alloy Ni content. These data were plotted and extrapolated to zero alloy Ni content. The orthorhombic unit cell was then converted to an equivalent hexagonal unit cell as described in the introduction

Effect of C: This is the most difficult effect to assess, as there is very little reliable data on it. The best single paper on this is by Rudy et al. [119]. All the data that exists were used to come up with something that has at least one-digit accuracy. The overall equations are:

$$a_c = 2.904X_V + 2.835X_{Cr} + 2.771X_{Fe} + 3.103X_{Nb} + 3.012X_{Mo} + 3.103X_{Ta} + 2.997X_W - 0.1Y_{V_a}\ \text{Å} \quad (36a),$$

$$c_c = 4.579X_V + 4.460X_{Cr} + 4.345X_{Fe} + 4.938X_{Nb} + 4.735X_{Mo} + 4.937X_{Ta} + 4.728X_W - 0.1Y_{V_a}\ \text{Å} \quad (36b),$$

where X_i are the site fractions of the metal sublattice, and Y_{V_a} is the site fraction of vacancies on the carbon sublattice.

BCC matrix

From data in the appendix of [126] (not published in [127]), taking a least squares fit, we obtain

$$a_\alpha = 2.8543\text{Å} + 4.9\text{E-}4\text{Å/at\% Co} + 5.2\text{E-}4\text{Å/at\% Ni} + 13.9\text{E-}4\text{Å/at\% Cr} + 36.7\text{E-}4\text{Å/at\% Mo} + 64.1\text{E-}4\text{Å/at\% C} \quad (37).$$

The effect of C was obtained from data in Roberts [128]. Carbon imparts a tetragonality to the lattice, which at low at% C is imperceptible. The least-squares fit to the a and c tetragonal lattice parameters as a function of carbon content was converted to an equivalent cubic unit cell using equal unit cell volumes.

M_2C Composition Trajectories

Similar to previous APFIM studies of alloy carbide compositions [92, 93], M_2C carbides in AF1410 start out with compositions far from equilibrium. The compositions of the carbides that were used in the mass balance calculations were based on APFIM data [18, 19, 22], and "assessed" with the available lattice parameter measurements. Thus the composition of the carbides is seen as moving monotonically from that of the initial carbides formed to that of the equilibrium composition. Figure XVIII shows the measured M_2C composition trajectories versus log time, along with the lines for the "assessed" compositions.

To obtain an estimate of the initial critical nucleus size and composition, these variables were plotted vs. volume fraction M_2C precipitated, as seen in figure XIX. This then was extrapolated to zero volume fraction to obtain information about the initial critical nucleus, table XI.

Thus, at initial nucleation, it is seen from this table that there is at least one negative eigenstrain and at least one positive eigenstrain: this is a necessary condition for a near invariant-line strain transformation. We see that carbide parameters can be plotted against the volume fraction precipitated, and this can be extrapolated to zero volume fraction to examine the initial nucleation regime. Similarly, to examine coherent equilibrium in the absence of capillarity, the carbide compositions can be plotted versus the capillarity parameter $\partial S/\partial V$.

For a sphere, $V = 4\pi r^3/3$, $S = 4\pi r^2$, and $\partial S/\partial V = 2/r$. For an ellipsoid of revolution with an aspect ratio of β and minor radius r, $V = 4\pi\beta r^3/3$. The surface area is more complicated, and the approximate analytical solution has been found by Johnson and Cahn [129]. Converting their solution into the variables used in this paper, we arrive at

$$S = 4\pi r^2 g(\beta) \quad (38),$$

where

$$g(\beta) = \frac{1}{4}\left[\frac{\beta(1+\beta)}{2}\right]^{2/3} \cdot \left\{2 + \frac{8(4-\beta)^2}{9(1+\beta)} \frac{\text{TANH}^{-1}\left(\left[\frac{(\beta-1)(\beta+3)}{(\beta+1)^2}\right]^{1/2}\right)}{\left[(\beta-1)(\beta+3)\right]^{1/3}}\right\} \quad (39).$$

$\partial S/\partial V$ is found as

$$\frac{\partial S}{\partial V} = \frac{2}{r} f(\beta) \quad (40),$$

where

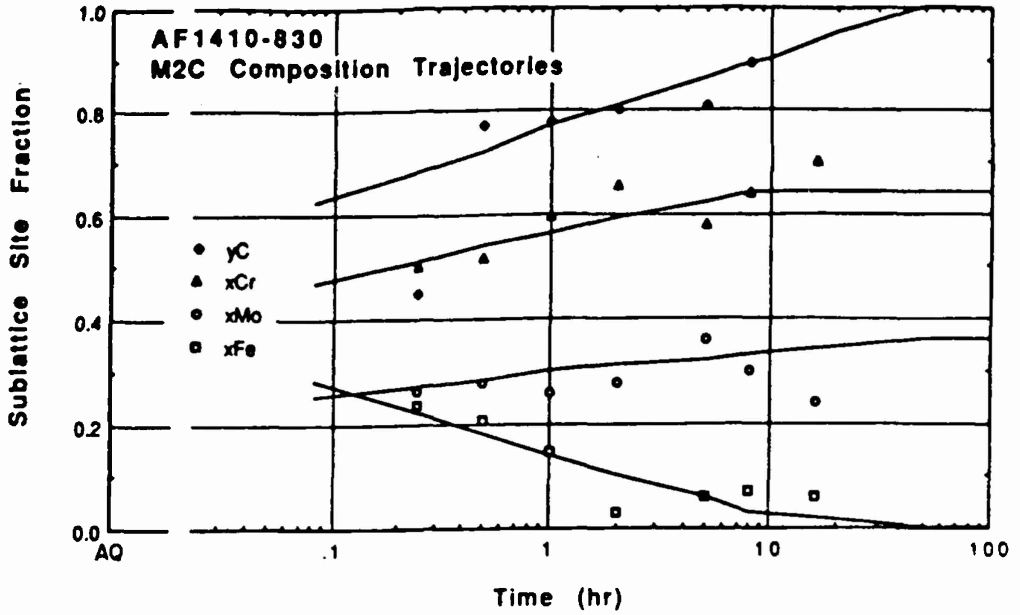


Figure XVIII. Measured M_2C compositions in AF1410-830 vs. log tempering time (data are from [22]). "Assessed" compositions are shown as solid lines.

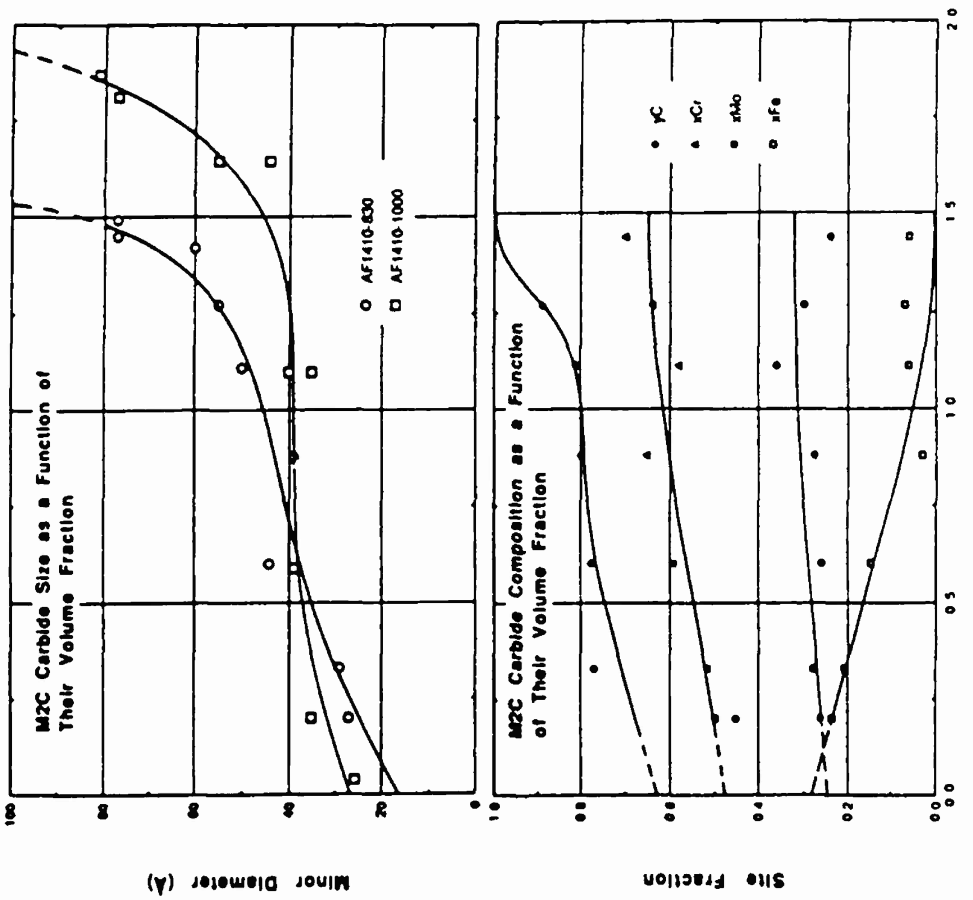


Figure XIX. Size and composition of M_2C carbides in AF1410-830 vs their volume fraction. Extrapolation to zero volume fraction indicates initial nucleation

$$f(\beta) = \left[\frac{1+\beta}{8}\right]\left[\frac{2}{\beta(1+\beta)}\right]^{1/3} \cdot \left\{2 + \frac{8(4-\beta)^2}{9(1+\beta)} \frac{\text{TANH}^{-1}\left\{\left[\frac{(\beta-1)(\beta+3)}{(\beta+1)^2}\right]^{1/2}\right\}}{\left[(\beta-1)(\beta+3)\right]^{1/3}}\right\} \quad (41).$$

Figure XX plots M_2C size and composition vs. the capillarity parameter $\partial S/\partial V$. Extrapolating these to $\partial S/\partial V = 0$ ($r \rightarrow \infty$) indicates coherent equilibrium in the absence of capillarity. Any breaks in these curves should indicate coherency loss.

Mass Balance Calculations

At this point it seems appropriate to discuss the rationale behind the remainder of this paper. For the alloy AF1410-830, we wish to determine the free energies related to the precipitation of M_2C as a function of tempering time at 510°C, as described by equation (14):

$$\Delta G_{TOT} = \Delta G_{CHE} + \Delta G_{SUR} + \Delta G_{STR} + \Delta G_{INT} \quad (14).$$

Of these energies, one of the most elusive is the chemical driving force, ΔG_{CHE}. The principal input in the determination of this free energy is the composition and volume fractions of all the phases present as a function of time. These will be found by the use of a mass balance. Conceptually, this is quite straightforward: all the atoms initially present in the alloy have to be accounted for at each step in time. The compositions and/or volume fractions of some phases have been measured directly. Where they have not, they must be determined indirectly, but at all times, all atoms must be accounted for. Figure XXI is a block diagram outlining the mass balance calculations described in this section.

The SANS volume fractions of Allen et al. [110] were calibrated as follows. The 1000°C material at 100hr was assumed to have the maximum theoretical volume fraction M_2C precipitated. The maximum volume fraction M_2C precipitated is found from a mass balance: all the carbon (0.16 wt%), all the molybdenum (1.03 wt%), and the balance chromium (0.80 wt%) goes to make stoichiometric $(Mo,Cr)_2C$. The resultant weight of carbide per unit weight of matrix is then obtained.

To convert this into volume fraction, we need to know the densities of this $(Mo,Cr)_2C$ and the solute-depleted matrix:

$$f_v^{ppt} = \frac{\frac{\text{carbide wt}}{\text{carbide density}}}{\frac{\text{matrix wt}}{\text{matrix density}} + \frac{\text{carbide wt}}{\text{carbide density}}} \times 100\% \quad (42).$$

Initially, we will assume that these are the only phases present—this will be close enough for our purposes (the first iteration). Since the compositions of both precipitate and matrix are known, their densities can be readily determined from a combination of the atomic weights of the atoms present in the phases and their lattice parameters found from equations (36)-(37) Doing this, 2.17% was obtained for the maximum theoretical volume fraction of M_2C. This then serves as a calibration for the SANS measurement of volume fraction: we will assume that this maximum volume fraction precipitated occurs in the 1000°C-solutioned material tempered for 100hr. Thus the SANS volume fractions arrived at by Allen et al. [110] must be multiplied by 2.17/3.22 ≈ 0.674. We then assume that in the 830°C-solutioned material tempered for 50hr, the difference between the volume fraction of M_2C actually precipitated and the maximum theoretical possible represents the carbon that is tied up in undissolved ("excess") carbides. We assume these to be stoichiometric $M_{23}C_6$, with composition $(Cr_{0.6}Fe_{0.3}Mo_{0.1})_{23}C_6$. This composition was estimated using the Thermo-Calc [130] software, and the volume fraction of this phase is calculated to be 0.66%.

There is carbon in solution in the matrix; this is determined by the composition of the cementite that it is in equilibrium with. From studies on the precipitation of cementite by Eldis and Sherman [131, 132, 133, 134] who determined an apparent activation energy, we assumed para-equilibrium exists at 30min, and asymptotically approaching equilibrium as in figure XXII. The para-equilibrium and equilibrium calculations were performed by Ghosh [135] using the Thermo-Calc software. The initial slope of the curve was found by first calibrating the volume fractions of cementite found by X-ray diffraction at this time (30min) to the para-equilibrium amount, and since we know how much carbon is in the other phases, then by mass balance, the carbon that is not in M_2C, $M_{23}C_6$, or cementite is in solution in the matrix.

The remaining carbon, that is, the carbon not in the matrix, M_2C or $M_{23}C_6$, is assumed to be in stoichiometric Fe_3C. The cementite found in an APFIM study of Fe-Ni-C [136] was determined to be stoichiometric within the accuracy of the technique. That cementite has only Fe on its metal sublattice is an approximation: the actual cementite formed will have a variable composition, but because f_v^θ is small, this is minor and will not affect the final results of the analysis.

At this point we have the necessary information to fill in table XII for the five phases of interest. The composition of the precipitated austenite was estimated from STEM [15, 16] and APFIM [18, 19] measurements, and was assumed to remain constant at 75Fe-15Ni-10Co (at%). This assumption is supported by the fact that the measured lattice parameter of the precipitated austenite remained constant.

Because there was found to be residual cementite present at long times (0.41%, by XRD), the maximum theoretical volume fraction of M_2C had to be recalculated, and the SANS volume fractions had to be recalibrated. The other phase compositions and volume fractions were then recalculated. It is felt that a third iteration would not result in any significant changes.

The end result of these mass balance calculations is shown in the following figures. Figure XXIII shows the matrix composition trajectories, while figure XXIV shows the matrix lattice parameters calculated from composition using equation (37), along with those measured using X-ray diffraction. Figure XXV illustrates the evolution of the volume fractions of cementite, M_2C and austenite, and figure XXVI compares the calculated volume fractions of cementite with those measured by X-ray diffraction.

The ultimate use of these mass balance calculations is the tracking of the phases' composition and volume fraction, and the calculation of the driving force for precipitation of M_2C (ΔG_{CHE}).

Elastic Energy Calculations

The last two free energies in equation (14) are the strain energy (ΔG_{STR}) and the interaction energy (ΔG_{INT}).

Mass Balance Calculations Block Diagram

(1) Calculate the maximum theoretical volume fraction of M_2C, assuming all C, Mo, balance Cr makes $(Mo,Cr)_2C$, and that α, M_2C are the only phases present.

↓

(2) Use this to calibrate the SANS measurement of $f_V^{M_2C}$ in AF1410-1000 at 1000hr, then rescale the other SANS measurements.

↓

(3) Calculate the maximum theoretical volume fraction of M_2C in AF1410-830, assuming that any excess carbon is in $M_{23}C_6$ of a certain composition.

↓

(4) Using the "assessed" M_2C compositions, SANS $f_V^{M_2C}$, XRD f_V^{α}, etc., calculate the compositions and volume fractions of the other phases at all times.

↓

(5) Using these phase compositions and volume fractions, use Thermo-Calc to calculate para-equilibrium with respect to cementite.

↓

(6) Assume that this para-equilibrium exists at 30min, then calibrate XRD f_V^{α}, and rescale other XRD f_V^{α} measurements.

↓

(7) By mass balance, at all times, carbon not in cementite, M_2C or $M_{23}C_6$ is in the matrix.

↓

(8) Recalculate the maximum theoretical volume fraction of M_2C, recalibrate SANS $f_V^{M_2C}$, recalculate other phase compositions and volume fractions.

↓

(9) Use Thermo-Calc to calculate the chemical driving force for M_2C precipitation at all times.

Figure XXI. Block diagram of the mass balance calculations for AF1410-830.

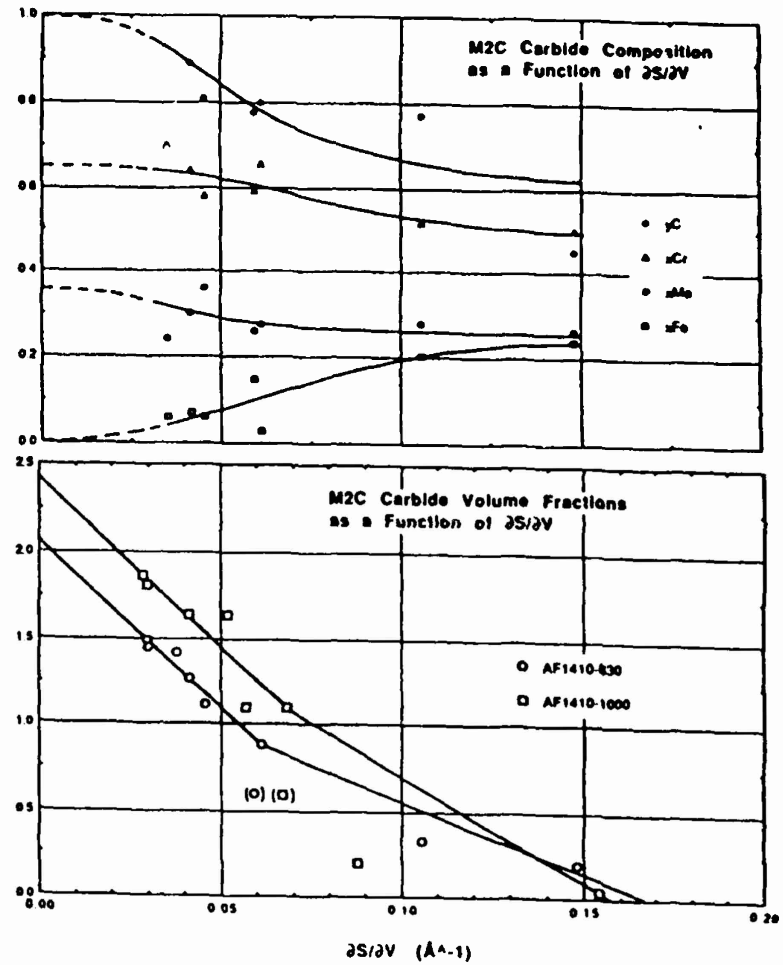


Figure XX. Composition of M_2C carbides in AF1410-830, and volume fraction of M_2C carbides in AF1410-830 and AF1410-1000 vs. $\partial S/\partial V$. Extapolation to zero $\partial S/\partial V$ indicates equilibrium. Data points in parentheses correspond to the "growth blips" on the $d_S(t)$ curves.

TABLE VII. PRECIPITATES FOUND IN AS-QUENCHED AF1410

830°C Solutionizing		885°C Solutionizing	
Particle Type	Size Range (nm)	Particle Type	Size Range (nm)
$(Fe,Ni,Co)_3C$	50-100 rods	$(Fe,Ni,Co)_3C$	40-230 rods
$(Ti,Mo)_x(C,N)$	10-180	$(Ti,Mo)_x(C,N)$	20-35
$(Cr,Fe,Mo)_{23}C_6$	50-125		
$(Fe,Cr,Mo)_{23}C_6$	75-105		
$(Mo,Cr)_xC$	30-65		
$(Mo,Fe)_xC$	40-50		
Mo_xC	5-10		

TABLE VIII. M_2C CARBIDE LATTICE PARAMETERS (Å)

	1	3	5	8	16	100	196
a_c	----	2.88	2.88	2.88	2.89	2.90	2.90
c_c	----	4.52	4.52	4.52	4.54	4.55	4.55

TABLE IX. AUSTENITE COMPOSITIONS IN AF1410 TEMPERED AT 510°C FOR 8hr (wt%)

Element	STEM (Haidemenopolous)	APFIM (Carinci)	Thermo-Calc (equilibrium)
Fe	69.0	55.8	56.2
Co	13.2	9.5	4.1
Ni	14.0	29.4	38.5
Cr	2.8	3.1	1.0
Mo	1.0	1.9	0.2
C	---	0.3	<0.1

TABLE X. CALCULATION OF THE NUCLEATION BARRIER HEIGHT

Variable	Maximum δW^*	Minimum δW^*
$J = \partial N_V/\partial t$ (1/m^{3}sec)	1.0×10^{19}	2.5×10^{19}
Z	1/2	1/200
β^* (1/sec)	7.8×10^{-3}	7.8×10^{-4}
N_0 (1/cm^3)	7.5×10^{19}	7.5×10^{18}
δW^* (J)	1.11×10^{-19}	2.66×10^{-20}
y	0.312	0.637

TABLE XI. INITIAL CRITICAL NUCLEUS PARAMETERS

Size (minor radius, Å)	12
X_{Cr}	0.47
X_{Mo}	0.25
X_{Fe}	0.28
Y_C	0.62
a_c (Å)	2.8233
c_c (Å)	4.4586
ε_1	-0.0172
ε_2	0.2037
ε_3	0.0975

TABLE XII. MASS BALANCE CALCULATIONS

Phase	Volume Fraction	Composition
Austenite	X-ray diffraction	STEM/APFIM
M_2C	SANS	APFIM
$M_{23}C_6$	Approx. const. as above	$(Cr_{0.6}Fe_{0.3}Mo_{0.1})_{23}C_6$
Cementite	Calculated from bal. C	Fe_3C assumed
Martensite	Balance	Balance

These comprise the elastic energy of the precipitating M_2C carbide. Based on the analysis of the previous sections, three cases for the elastic energy of a coherent M_2C carbide were considered [137]:

- Case 1: $\beta = 1$, initial nucleation, composition found by plotting carbide composition vs. volume fraction precipitated and extrapolating to (almost) zero volume fraction
- Case 2: $\beta = 2$, half completion time (between 1 and 2hr)
- Case 3: $\beta = 3$, 8hr temper

For each of these cases, the composition of the carbide was given either directly by APFIM and/or STEM, or indirectly by interpolating or extrapolating. With these compositions, the lattice parameters of the carbides could be determined by use of the previously-determined formula relating composition to lattice parameter. Then, with the lattice parameter of the carbide and that of the matrix (found from precision lattice parameter measurements), the eigenstrains could be found for each case, using equations (24). These were the eigenstrains King used in his elastic energy calculations, table XIII. The elastic constants used were taken from Simmons [138] for α-Fe at room temperature:

Matrix: $C_{11} = 220.3$ GPa
$C_{12} = 124.8$ GPa
$C_{44} = 112.0$ GPa

Carbide: $E = 250$ GPa
$\nu = 0.19$

First, the self energy of a carbide (Δg_{STR}) was calculated. Then, the interaction energy (Δg_{INT}) was found by first taking a carbide of fixed size, shape and eigenstrains, and finding the position around a pure screw dislocation that minimized the elastic energy. (Because the strain field around a coherent carbide particle is primarily dilatation, the interaction will be the weakest for a screw dislocation, since the stress field is pure shear. However, a screw dislocation was chosen because this is the character that is most often observed in ferrous lath martensites.) This position was held constant and the carbide was allowed to grow out from the dislocation (at constant shape); the interaction energy was calculated as a function of size for each of the three cases. The interaction energy $\rightarrow 0$ as size $\rightarrow \infty$, so that the elastic energy approaches the self energy when the carbide becomes large. The tabulated numerical data of King [137] was found to fit a function of the form

$$\Delta g_{INT} = - \frac{10^4 \text{ J/cm}^3}{A_{INT} + r B_{INT}} \qquad (43),$$

where r is the carbide minor radius (d/2). In all cases, the correlation coefficient of the fitted line was better than 0.99. This variable interaction energy has an effect on the total free energy similar to a negative surface energy. The results are presented in table XIV.

The self energy found by King represents an upper bound to this energy, as it is based on linear elasticity. The transformation strains are much larger than can be accommodated by this theory, and future work should address the anharmonic elastic constants of the matrix and carbide. Any refinement of these calculations will lower the self energies. The measured M_2C composition trajectory for AF1410 shows much smaller departures from the incoherent equilibrium compositions compared to coherent thermodynamic prediction when the full computed self energy is used. An analysis by Ghosh [135] indicates reasonable agreement with observed X_{Cr} and X_{Mo} when the self energy is reduced by a factor of 1/4 to 1/2. A factor of $\alpha = 1/2$ is employed in the current analysis. This factor is near the minimum correction needed for coherent precipitation to be thermodynamically possible in this system.

Nucleation

The chemical driving force ΔG_{CHE} for the precipitation of M_2C of the "assessed" composition from a matrix of the calculated composition was calculated using Thermo-Calc [135] (figure XXVII). Note that $-\Delta g_{CHE}$ increases from 5 to 30min despite the dropping supersaturation. This is primarily because the driving force is a very strong function of the carbide and matrix carbon contents. The carbon content of the carbides is increasing faster than the carbon content of the matrix is dropping. The values for the three cases are presented in table XV.

The surface energy for a carbide particle was found from

$$\Delta G_{SUR} = \gamma S = \gamma 4 \pi r^2 g(\beta) \qquad (44),$$

where $g(\beta)$ is the ellipsoid shape function defined by (39). We may now use the nucleation rate equation (1) since, from Langer-Schwartz theory, it applies to all systems with high supersaturation: at all times, the average particle is near-critical. The volume energy terms were then combined with the surface energy terms to give the total free energy of a precipitating M_2C carbide for the three cases. The surface energy γ was adjusted so that the critical nucleus size matches a size 10% smaller than the observed M_2C precipitate size. This is because we are assuming the average observed size is slightly supercritical; this assumption is supported by the work of Wendt and Haasen [34].

The parameters for homogeneous nucleation were found by using the surface energies from the calculation for heterogeneous precipitation, and setting the interaction energy to zero. Then

$$\left[\frac{\partial \Delta G_{TOT}^{homog}}{\partial V} \right]_{r^*_{homog}} = 0 \qquad (45)$$

and

$$\delta W^*_{homog} = \left[\Delta G_{TOT}^{homog} \right]_{r = r^*_{homog}} \qquad (46).$$

There is no solution for Case 3 above because the self energy is greater than the available chemical driving force. This may indicate coherency loss: an incoherent precipitate will have negligible self energy.

Comparing the barrier height found from the total free energy calculations for Case 2 (table XVI: 9.5×10^{-19}J) with those found from the nucleation rate equation (table X: 1.11×10^{-19} to 2.66×10^{-20}J), it is seen that the former is about an order of magnitude too high to account for the observed nucleation rate. A possible mechanism (borrowed from martensite nucleation theory) that will bring this barrier down is autocatalysis. Here, when the range of the stress field of a carbide gets to be sufficiently large, it will interact with the strain field of a nucleating carbide embryo nearby, lowering its elastic energy. The requirements of this mechanism are currently being studied by King [139]. The fact that the carbides must become larger for this mechanism to occur is consistent with the observation of renucleation. This possibility is explored further in the next section.

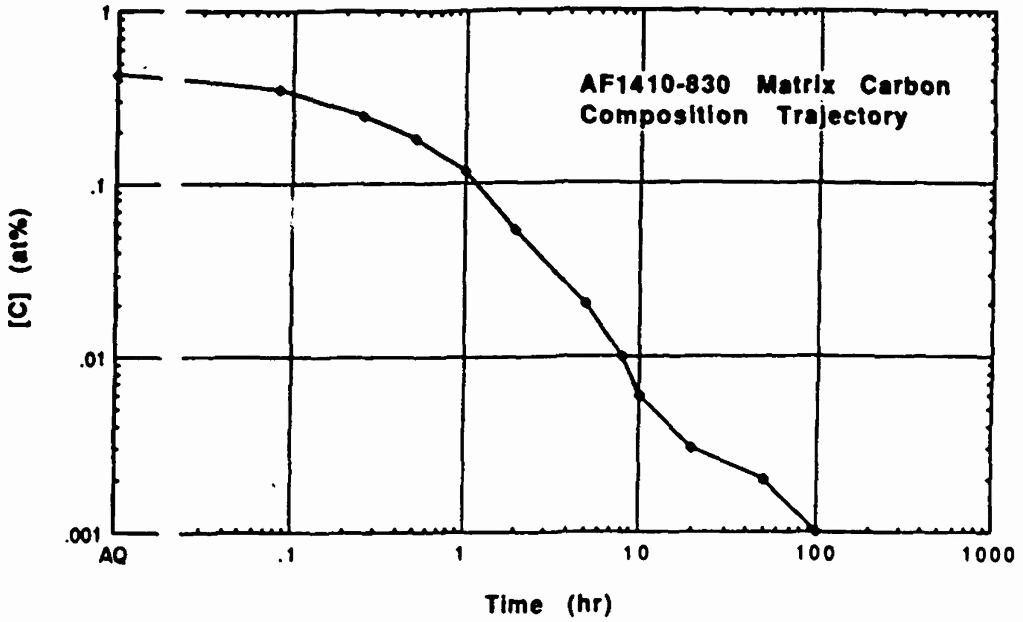


Figure XXII. Matrix carbon content of AF1410-830 vs. log tempering time, calculated from mass balance.

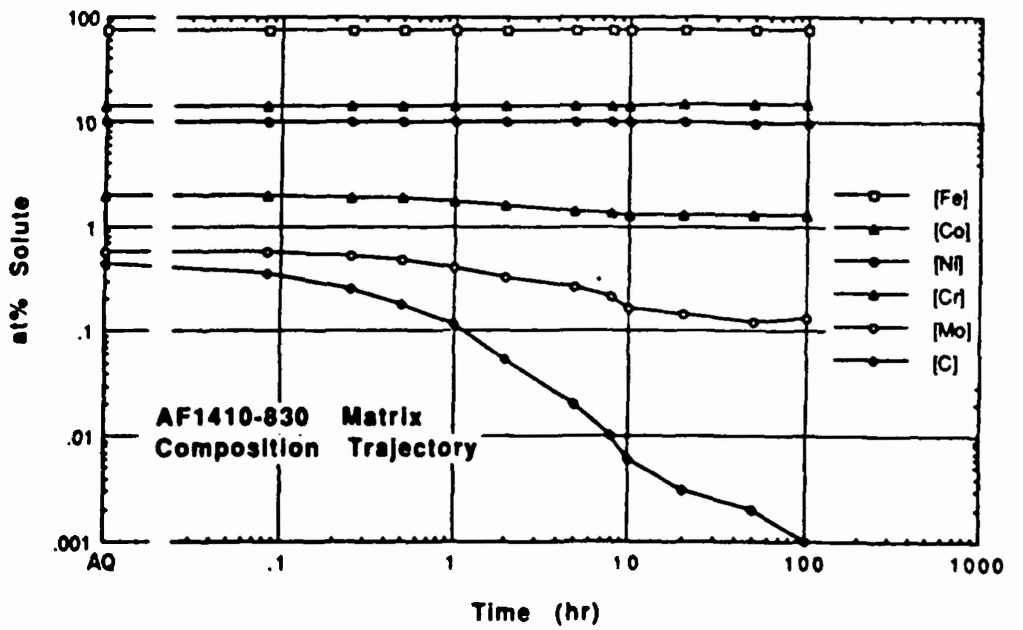


Figure XXIII. Matrix composition trajectory of AF1410-830, calculated from mass balance.

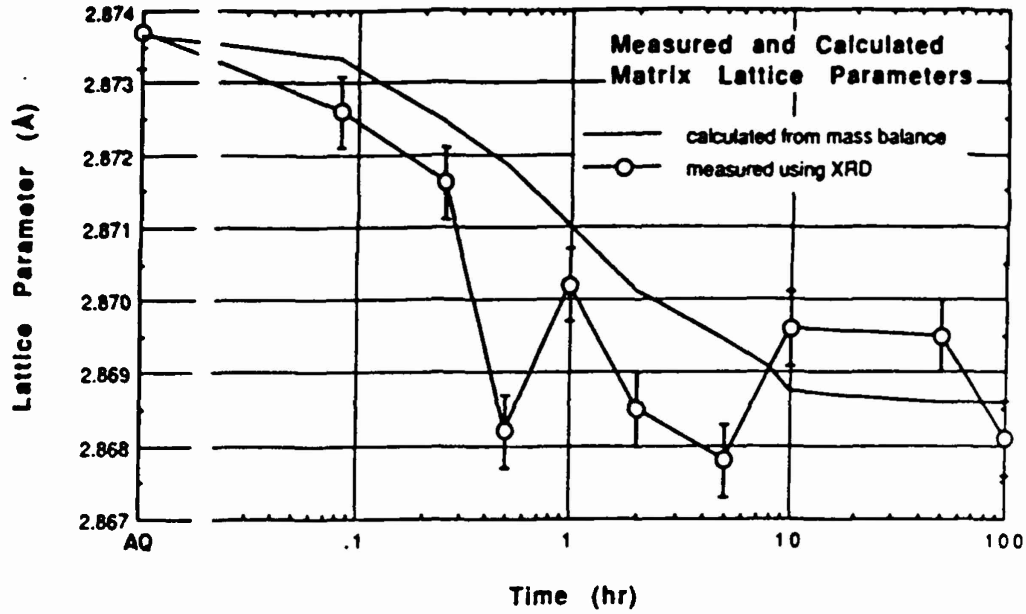


Figure XXIV. Measured (from XRD) and calculated (from mass balance) matrix lattice parameters.

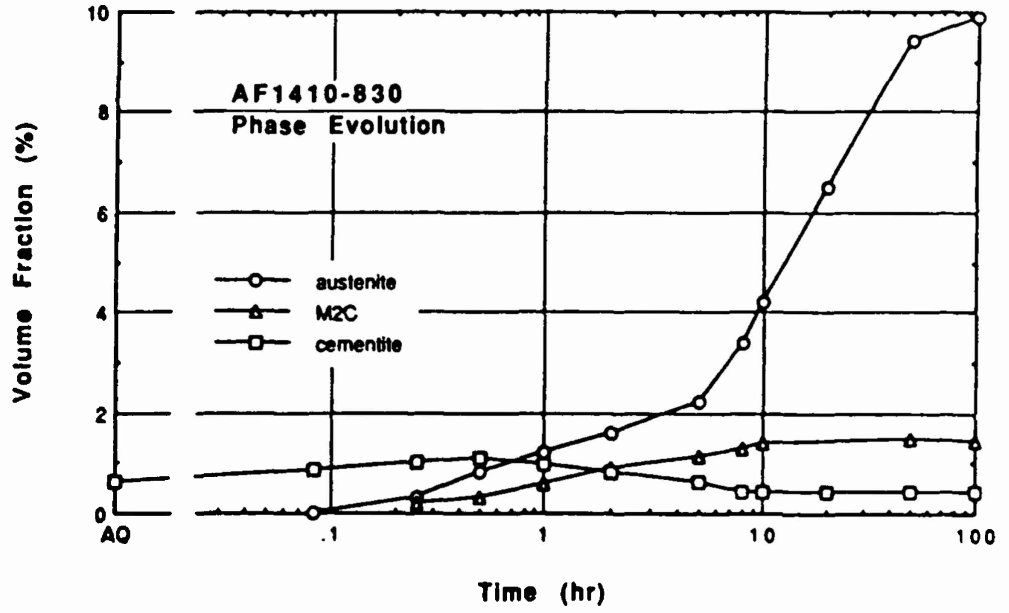


Figure XXV. Phase evolution of AF1410-830: volume fractions of cementite, M_2C and austenite.

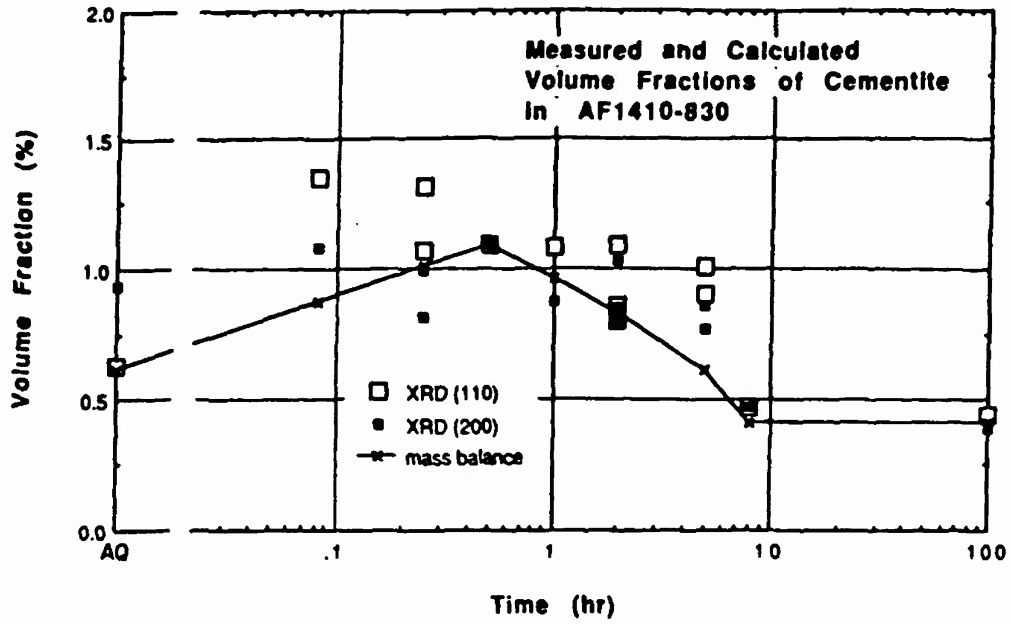


Figure XXVI. Measured (from XRD, using calibrated R-values) and calculated (from mass balance) volume fractions of cementite.

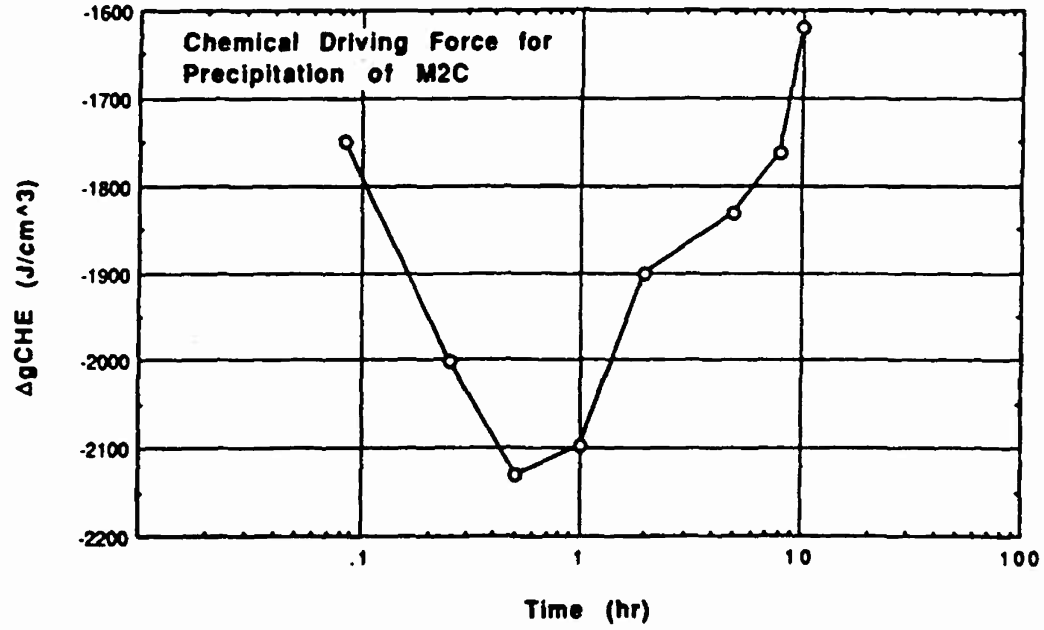


Figure XXVII. Chemical driving force for precipitation of M_2C in AF1410-830 as a function of tempering time at 510°C.

TABLE XIII. ELASTIC ENERGY CASES CONSIDERED

Case →	1	2	3
f_V^{M2C} (%theo. max.)	0%	59%	85%
β	1.0	2.0	3.0
X_{Cr}	0.47	0.59	0.64
X_{Mo}	0.25	0.31	0.33
X_{Fe}	0.28	0.10	0.03
Y_C	0.62	0.81	0.89
a_α (Å)	2.8726	2.8685	2.8690
a_c (Å)	2.8233	2.8645	2.8805
c_c (Å)	4.4586	4.5148	4.5363
ε_1	-0.0172	-0.0009	0.0040
ε_2	0.2037	0.2237	0.2297
ε_3	0.0975	0.1130	0.1180

TABLE XIV. RESULTS OF THE ELASTIC ENERGY CALCULATIONS

Case →	1	2	3
Δg_{STR} (J/cm^3)	3496	3704	3619
A_{INT}	3.9436	5.8261	4.0122
B_{INT} (Å^{-1})	3.2183	3.6220	4.4109

TABLE XV. CHEMICAL DRIVING FORCES

Case →	1	2	3
Matrix Composition (at%)			
[C]	0.345	0.054	0.010
[Mo]	0.558	0.328	0.208
[Cr]	1.962	1.546	1.322
[Ni]	10.020	10.001	9.904
[Co]	13.919	14.079	14.161
[Fe]	73.196	73.992	74.396
M_2C Composition			
X_{Cr}	0.47	0.59	0.64
X_{Mo}	0.25	0.31	0.33
X_{Fe}	0.28	0.10	0.03
Y_C	0.62	0.81	0.89
Δg_{CHE} (J/cm^3)	-1750	-1900	-1760

TABLE XVI. RESULTS OF THE TOTAL FREE ENERGY CALCULATIONS

Case →	1	2	3
Carbide Critical Radius (Å)	10.8	15.3	24.3
Surface Energy γ (mJ/m^2)	99	190	---
Barrier Height, δW^* (J)	7.7×10^{-20}	9.5×10^{-19}	---
Homog. Critical Radius (Å)	998	52	---
Homog. Barrier (J)	2.0×10^{-18}	2.8×10^{-17}	---

DISCUSSION

Precipitation Energetics

Because the initial critical nucleus has at least one positive transformation eigenstrain and at least one negative, the possibility of a near-ILS transformation exists. However, because of the magnitudes of the transformation strains and the complexity of the matrix, the possible operating inhomogeneous lattice-invariant deformation is extremely difficult to determine directly with any known technique.

Between Cases 1 and 2 (initial nucleation and the half-completion time), it is seen that the surface energy of the carbides (table XVI) is increasing. From APFIM measurements, it is also seen that the composition of the carbides changes significantly with respect to carbon and iron (table XIII). Bond-mismatch theories of the (chemical) surface energy usually give it as a function of the difference between the compositions of the carbide and the matrix. The form that γ should take in the present case considered is then:

$$\gamma = \sum_i A_i \Delta X_i^2 + \sum_j B_j \Delta Y_j^2 \qquad (47),$$

where ΔX_i and ΔY_j are the differences in compositions on the metal and interstitial (carbon) sublattices respectively, viewing the carbide as an interstitial alloy. Therefore, there will be composition-dependent capillarity, and this will increase with tempering time. The surface energy γ generally is the last parameter found in many studies of nucleation and coarsening, and the present work is no exception. In order to determine the parameters A_i and B_j in the above equation for these multicomponent alloys and carbides, several alloys will have to be analyzed with the same level of intensity as AF1410 in this work. However, it is expected that carbon and iron will have the largest effect, since the concentration differences of these elements are the greatest between the carbide and matrix. Looked at another way, these are the elements that are rejected the most strongly from the two phases: carbon form the matrix, and iron from the carbide; thus (alluding to bond-mismatch theory) these will be the ones that are the most anomalous and so will have the most impact on the surface energy

During precipitation, the supersaturation is dropping, the carbide site fraction carbon is increasing, the surface energy is increasing, and because the carbides are larger, the dislocation interaction energy (per volume of carbide) is decreasing. The carbides have several degrees of freedom in minimizing their free energy. The increasing site fraction carbon increases both the interfacial energy and the self energy, while greatly increasing the chemical driving force. The composition of the metal sites will have less of an effect on the interfacial energy than the carbon site fraction: the difference between the concentration of the metal in the carbide and in the matrix is much less than the difference between the concentration of carbon in the carbide and the matrix.

With regard to the precipitation energetics, it seems like the carbides do a lot of balancing. They balance off their site fraction carbon with the carbon in solution in the matrix to maintain a chemical driving force for precipitation; and they seem to alter their site fractions of Fe, Cr and Mo to balance off the chemical driving force with elastic energy. Evidently, interactions, and the promotion of coherency, are important: we can't simplify the alloy to examine each phenomenon separately, since this would reduce the number of degrees of freedom available to the alloy. The important interactions are: carbides↔dislocations, composition↔driving force, and composition↔coarsening. We need a material of this complexity to give us these synergistic effects.

"Renucleation"

From the SANS number density data of Allen [110] (figure XVII), it appears as if there is a second burst of nucleation between one and two hours in AF1410-830. We have been calling this phenomenon "renucleation." Although this phenomenon is beyond the level of current theory, there are a number of reasons why this may occur.

During the first 30 minutes, the supersaturation is dropping, but the chemical driving force is increasing because of the changing carbide compositions. The chemical driving force decreases after 30min, but it is still greater than that for initial nucleation until about 8hr tempering time. This keeps up the driving force for the carbides, but what may be providing an extra kick is the autocatalytic effect.

At initial nucleation, when the critical size of the carbides is small, the stress field of the dislocations provide highly potent nucleation sites. Later, as tempering proceeds and the critical size of the carbides increases, this potency decreases because the interaction energy decreases (per volume of carbide) with increasing carbide size (equation(43)). These larger but still coherent carbides develop longer-range stress fields, and this can produce highly potent nucleation sites in the vicinity of existing carbides. This phenomenon is termed autocatalysis, and has a significant impact on the nucleation of martensite. Autocatalytic nucleation may resolve the 10x discrepancy in δW^* at half-completion time. If so, it is then important to maintain coherency to sufficient size for the autocatalytic effect.

Role of Heterogeneous Precipitation

Nucleation

Comparing $\delta W^*_{heterog}$ and δW^*_{homog} (table XVI) shows us that the interaction energy is necessary for the coherent nucleation of M_2C. Thus there is an absence of the "footprint" morphology in AF1410. Homogeneous incoherent nucleation, if it weren't bypassed, would occur as Davenport observed: on cementite-martensite interfaces. The Mo_2C in Davenport's simpler Mo-C steel exhibited a "footprint" morphology, in which cementite precipitated fully and coarsened, then served as the carbon source for the precipitating Mo_2C. There was some initial precipitation of Mo_2C along dislocation lines, but the Mo_2C precipitated preferentially on the cementite-martensite interfaces and this morphology dominated at longer tempering times. When the cementite was finally dissolved, the Mo_2C exhibited a "footprint" of the cementite's prior position. AF1410 does not exhibit this phenomenon because cementite does not have a chance to coarsen to this degree. Because the precipitation kinetics of M_2C are accelerated by the effects of cobalt (dislocation recovery resistance and enhancement of driving force), the available carbon is used up (dissolving the cementite) before the incoherent precipitation of M_2C on the cementite-martensite interfaces can occur. Because cobalt destabilizes cementite, it may also slow its precipitation. In AF1410, cementite precipitation is not bypassed by M_2C precipitation, but it does not survive long enough to coarsen. The tail end of cementite precipitation may be cut off by M_2C precipitation, since there was a detectable volume fraction of M_2C even at 15min tempering time.

Growth/coarsening

The log carbide size as a function of log tempering time is nearly linear. Aside from a small blip at 1hr, the growth regime appears to be completely suppressed. This is

consistent with the Langer-Schwartz theory of precipitation at high supersaturations. However, the time exponent is very close to 1/5. Wendt and Haasen, and Kampmann and Wagner who were involved in the experimental verification of the L-S model and its derivatives, all see the precipitates jump immediately into $t^{1/3}$ size functionality. All of their systems were homogeneous nucleation, growth and coarsening—the steels studied in this study may be exhibiting L-S behavior, with nucleation occurring during the dropping supersaturation, but with $t^{1/5}$ kinetics because of the heterogeneous nature of the precipitation.

Carbide Coherency and Coherency Loss

Carbide Coherency

The work in this study does not provide direct evidence that the carbides nucleate coherently. In fact when one first looks at this system and the magnitude of the eigenstrains, it seems unlikely that the carbides would ever be coherent. However, circumstantial evidence for coherent nucleation follows from the observation by Tanino et al. [104] of double lobe contrast (indicating a coherent precipitate) from Mo_2C carbides in what Davenport [54] claims to be a predominantly δ-ferritic steel. These carbides were up to about 0.1 μm long. Davenport did not observe double lobe contrast from Mo_2C carbides in his martensitic 3.5Mo-0.22C steel, and concluded from this that they are not coherent. However, because the strain field of the dislocations overlap with that of the precipitate, double-lobe contrast may not be observable for a coherent precipitate in this case. Because of the interaction energy between the strain fields of the carbide and dislocation, it seems even more likely that carbides in a matrix with a high dislocation density (martensitic) would be coherent, compared to the same carbides in δ-ferrite. Coherent carbides will have a stronger interaction with the dislocations.

Therefore, we know from Tanino et al. [104] and Davenport [54] that Mo_2C carbides precipitating in δ-ferrite are coherent. For a steel of the carbon content investigated, the "tetragonality" of the martensite is negligible, so there is no difference in the crystallography and kinematics of Mo_2C carbide precipitation between these two phases. The carbides precipitating in AF1410 are "mixed" M_2C carbides which have substantially lower transformation strains (table IV) and so are even more likely to be coherent. Further support for coherency of the carbides is provided by the direction of the change in carbide lattice parameter: it increases (towards that calculated for incoherent equilibrium) as the carbides become larger.

Coherency Loss

Because of the magnitude of the transformation strains, it is expected that the carbides lose their coherency at some point within the 1000hr time frame investigated. From FIM observations, Liddle et al. [21] used an apparent change in the carbides' morphology (aspect ratio) to signify a loss of coherency. In the present work, no such abrupt change in particle morphology was observed, nor was any carbide internal faulting. The carbides generally had a wide range of aspect ratios in any particular heat treatment, and there was a general upward trend as tempering times increased. Because of the large ranges of β, and the specimen size examined, any discontinuities in β in figure XI do not appear to be significant.

Besides the footprint morphology, another phenomenon that Davenport observed that was not seen in the investigated steels was the presence of fringe contrast widthwise in the carbides. He interpreted these fringes as anticoherency (or misfit) dislocations, however, image simulation is really needed to make this determination. These fringes occurred in carbides larger than about 0.1 μm long.

If we say that the final carbide lattice parameters correspond to the incoherent state, then we can say that the carbides lose coherency at 100hr. However, there is a variety of evidence that points to 8hr as the point at which carbides undergo some degree of coherency loss. Because $\partial S/\partial V$ is a capillarity variable, any discontinuities in carbide data plotted as a function of this variable should indicate an abrupt change in the interfacial energy. The only phenomenon that can cause this abrupt change is a coherency loss. These discontinuities occur at about 8hr tempering time. Consistent with this observation is the "no solution" for Case 3 in table XVI. Recall that Case 3 was for 8hr tempering, and that there was no solution because the self energy was greater than the available chemical driving force. An incoherent precipitate will have negligible self energy. Additionally, there is a significant, reproducible drop in the microhardness at 8hr. Coherent carbides may be stronger obstacles to the movement of dislocations than carbides that have experienced some degree of coherency loss, all other things remaining the same.

SUMMARY

M_2C carbide precipitation and associated secondary hardening behavior were investigated in a martensitic Co-Ni steel, AF1410. Results of transmission electron microscopy (from both thin foils and extraction replicas) and X-ray diffraction were combined with results of collaborative SANS and APFIM studies to define phase fractions, compositions, and lattice parameters throughout precipitation, including estimation of carbide initial critical nucleus properties by extrapolating to zero volume fraction. Phase compositions were used to compute precipitation chemical driving forces employing the Thermo-Calc thermochemical software and database. Combining new experimental data and available literature data, the composition dependence of the M_2C lattice parameters was modelled to predict the composition-dependent transformation eigenstrains for coherent precipitation; this was input into collaborative numerical calculations of both the coherent carbide elastic self energy and the dislocation interaction energy during heterogeneous precipitation.

The observed overall precipitation behavior is consistent with theoretically-predicted behavior at very high supersaturations where nucleation and coarsening compete such that the average particle size remains close to the critical size as supersaturation drops. All the steels studied in this paper were in the regime of high supersaturation as defined by Langer and Schwartz. This is consistent with the observed nearly-linear log d vs. log t curve for AF1410. However, instead of $t^{1/3}$, the carbides exhibited a $t^{1/5}$ size functionality, consistent with heterogeneous precipitation on dislocations. M_2C alloy carbides precipitating from an iron-base matrix tend to have all positive transformation strains. Initial precipitation appears to be coherent, the carbides tending toward a rod shape with major axis oriented along the minimum principal strain direction. This morphology evidently is adopted to reduce the carbides' elastic energy. At initial nucleation, particles are Fe-rich and C-deficient, diminishing the transformation eigenstrains to a near-invariant-line strain condition. Nucleation of M_2C in AF1410 is heterogeneous, along dislocation lines. This heterogeneous nucleation reduces the barrier height δW^*, and the incubation time. Acceleration of M_2C precipitation precludes the existence of

a "footprint" morphology on prior cementite positions.

Interpreting the average particle size as near critical size throughout precipitation, the observed relation between carbide volume fraction and the shape-dependent capillarity parameter $\partial S/\partial V$ implies a coherency loss transition in AF1410 corresponding to a critical particle length of 164Å and diameter of 50Å (reached at 8hr tempering at 510°C). This conclusion is supported by observations on lattice parameter shifts, insufficient chemical driving force available to overcome a coherent carbide's self energy, and discontinuities in the microhardness curves. Linear elastic calculations of the coherent carbide elastic self energy are interpreted as an upper bound, the thermodynamics of this system indicating that the energy should be reduced by at least a factor of 1/2. Any refinement of these linear elastic calculations will lower the self energy. Employing such a self energy correction factor, the computed dislocation interaction energy for coherent nucleation on a screw dislocation gives excellent agreement with the observed initial nucleation rate and critical nucleus size for a carbide coherent interfacial energy of 99mJ/m^2.

The precipitation in AF1410 at 510°C shows a "renucleation" phenomenon in which a second stage of nucleation occurs beyond the precipitation half-completion time (1-2hrs). The particles at this point exhibit a composition favoring a higher precipitation driving force despite the reduced supersaturation, but the observed critical size indicates a higher interfacial energy of 190mJ/m^2. Thus the surface energy of the carbides increases with tempering time, consistent with it being a function of $(\Delta X_i)^2$, $(\Delta Y_i)^2$. It appears that the carbide composition during precipitation follows a trajectory of increasing interfacial energy and nearly constant volume driving force. This may contribute to the renucleation phenomenon, but the computed barrier for heterogeneous nucleation on the dislocations is at this point an order of magnitude too high. An alternative possibility is that renucleation may represent autocatalytic heterogeneous nucleation in the stress field of coherent carbides, once they have grown to sufficient size to act as potent nucleation sites. Autocatalysis will further reduce the nucleation barrier height. The renucleation phenomenon appears to be very important to the maintenance of a fine particle size at longer tempering times in order to achieve high fracture toughness at high strength.

A predictive model of M_2C carbide precipitation in this steel will require an accurate determination of the amount of carbon in solution in the matrix, as well as the dependence of the surface energy on compositional difference between the matrix and carbide. Control of observed coupled precipitation and renucleation phenomena offers the potential for design of alloy compositions capable of more efficiently achieving higher strength levels at a given alloy carbon content.

ACKNOWLEDGEMENTS

The authors gratefully acknowledge Andrew Allen, Kwang-Un King, Gautam Ghosh and Charles Kuehmann for their collaboration on this research. The CarTech Corporation, through Raymond Hemphill, kindly supplied the materials for this paper. Research at Northwestern University was sponsored by the Army Research Office, and J.S. Montgomery was supported by MTL.

REFERENCES AND NOTES

1. G.R. Speich, D.S. Dabkowski and L.F. Porter, "Strength and Toughness of Fe-10Ni Alloys Containing C, Cr, Mo, and Co," Met. Trans., Vol. 4, 1973, pp. 303-314.
2. G.R. Speich, "Secondary Hardening Ultrahigh-Strength Steels," Innovations in Ultrahigh-Strength Steel Technology (34th Sagamore Army Materials Research Conference Proceedings), G.B. Olson, et al., eds., U.S. Government Printing Office, Washington, DC, 1990, pp. 89-111.
3. K. Kuo, "Carbides in Chromium, Molybdenum, and Tungsten Steels," JISI, Vol. 173, 1953, pp. 363-375.
4. K. Kuo, "Carbide Precipitation, Secondary Hardening, and Red Hardness of High-Speed Steel," JISI, Vol. 174, 1953, pp. 223-228.
5. S. Floreen and G.R. Speich, "Some Observations on the Strength and Toughness of Maraging Steels," Trans. ASM, Vol. 57, 1964, pp. 714-726.
6. V.K. Chandhok, J.P. Hirth and E.J. Dulis, "Effect of Cobalt on Carbon Activity and Diffusivity in Steel," Trans. AIME, Vol. 224, 1962, pp. 858-864.
7. J.P. Hirth, E.J. Dulis and V.K. Chandhok, "The Contribution of Cobalt to the Tempering Resistance and Hot Hardness of Tool Steels and Cobalt Replacement," Strength of Metals and Alloys (ICSMA 6), R.C. Gifkins, ed., Pergamon Press, New York, NY, 1983, pp. 185-191.
8. V.K. Chandhok, J.P. Hirth and E.J. Dulis, "Effect of Cobalt on Tempering Tool and Alloy Steels," Trans. ASM, Vol. 56, 1963, pp. 677-692.
9. H. J. Goldschmidt, Interstitial Alloys, Plenum Press, New York, NY, 1967.
10. M. Grujicic, "Design of M_2C Carbides for Secondary Hardening," Innovations in Ultrahigh-Strength Steel Technology (34th Sagamore Army Materials Research Conference Proceedings), G.B. Olson, et al., eds., U.S. Government Printing Office, Washington, DC, 1990, pp. 223-237.
11. D.T. Peters and C.R. Cupp, "The Kinetics of Aging Reactions in 18 Pct Ni Maraging Steels," Trans AIME, Vol. 236, 1966, pp. 1420-1429.
12. W. Sha, A. Cerezo and G.D.W. Smith, "A Field-Ion Microscopy and Atom Probe Study of Ageing Behaviour of a Co-Bearing Maraging Steel," Coll. de Physique, Supp. 11, Vol. 50, 1989, pp. 407-412.
13. D. Coutsouradis, et al., "Role of Cobalt in the Strengthening Mechanisms in the AFC-77 Steel," *(Technical Report AFML-TR-66-243)* National Center of Metallurgical Research, Liege, Belgium.
14. I. Aslinidis, "Softening and Recovery Resistance in Fe, Fe-Co, Fe-Al, Fe-Ni, and Fe-Ni-Co Alloys," Ph.D. Thesis, MIT Dept. of Mat. Sci. and Eng'g., 1989.
15. G.N. Haidemenopoulos, "Dispersed-Phase Transformation Toughening in Ultrahigh-Strength Steels," Ph.D. Thesis, MIT Dept. of Mat. Sci. and Eng'g., 1988.
16. G.N. Haidemenopoulos, G.B. Olson and M. Cohen, "Dispersed-Phase Transformation Toughening in Ultrahigh-Strength Steels," Innovations in Ultrahigh-Strength Steel Technology (34th Sagamore Army Materials Research Conference Proceedings), G.B. Olson, et al., eds., U.S. Government Printing Office, Washington, DC, 1990, pp. 549-593.
17. R.F. Decker, "Alloy Design, Using Second Phases," Met. Trans., Vol. 4, 1973, pp. 2495-2518.
18. G.M. Carinci, et al., "AP/FIM Study of Multicomponent M_2C Precipitation," Innovations in Ultrahigh-Strength Steel Technology (34th Sagamore Army Materials Research Conference Proceedings), G.B. Olson, et al., eds., U.S. Government Printing Office, Washington, DC, 1990, pp. 179-

208.
19. G.M. Carinci, "Precipitation of Multicomponent Carbides in Co-Ni Martensitic Steels," Ph.D. Thesis, MIT Dept. of Mat. Sci. and Eng'g., 1989.
20. Li Chang, G.D.W. Smith and G.B. Olson, "Ageing and Tempering of Ferrous Martensites," J. de Physique Supp., Vol. 47, No. 3, 1986, pp. 265-273.
21. J.A. Liddle, G.D.W. Smith and G.B. Olson, "Alloy Carbide Precipitation in a High Cobalt-Nickel Secondary Hardening Steel," J. de Physique Supp., Vol. 47, No. 11, 1986, pp. 223-231.
22. G.B. Olson, T.J. Kinkus and J.S. Montgomery, "APFIM Study of Multicomponent M_2C Carbide Precipitation in AF1410 Steel," Surf. Sci., in press, pp. .
23. R. Kampmann and R. Wagner, "Kinetics of Precipitation in Metastable Binary Alloys," Decomposition of Alloys: the early stages (Proceedings of the 2nd Acta-Scripta Metallurgica Conference), P. Haasen, et al., eds., Pergamon Press, New York, NY, 1984, pp. 91-103.
24. R. Wagner and R. Kampmann, "Solid State Precipitation at High Supersaturations," Innovations in Ultrahigh-Strength Steel Technology (34th Sagamore Army Materials Research Conference Proceedings), G.B. Olson, et al., eds., U.S. Government Printing Office, Washington, DC, 1990, pp. 209-221.
25. J.W. Christian, The Theory of Transformations in Metals and Alloys, Pergamon Press, Oxford, UK, 1965.
26. K.C. Russell, "Nucleation in Solids," Phase Transformations, H.I Aaronson, ed., ASM, Metals Park, OH, 1970, pp. 219-268.
27. I.M. Lifschitz and V.V. Slyozov, "The Kinetics of Precipitation from Supersaturated Solid Solutions," J. Phys. Chem. Solids, Vol. 19, 1961, pp. 35-50.
28. C. Wagner, "Theorie der Alterung von Niederschlägen durch Umlösen," Z. Elektrochem, Vol. 65, 1961, pp. 581-591.
29. L. Kampmann and M. Kahlweit, "Zur Theorie von Fällungen," Ber. Bunsen. Phys. Chem, Vol. 71, 1967, pp. 78-87.
30. J.S. Langer and A.J. Schwartz, "Kinetics of Nucleation in Near-Critical Fluids," Phys. Rev. A, Vol. 21, 1980, pp. 948-958.
31. H. Wendt, "Nucleation, Growth and Coarsening in Highly Supersaturated Solid Solutions," D.Ing. Thesis, Göttingen, 1981.
32. H. Wendt, "Early Decomposition Stages in a Ni-Al Alloy," Proceedings of an International Conference on Solid-Solid Phase Transformations, H.I. Aaronson, et al., eds., TMS-AIME, Warrendale, PA, 1982, pp. 445-449.
33. P. Haasen, "Early Stages of the Decomposition of Alloys," Ber. Bunsen. Phys. Chem., Vol. 87, 1983, pp. 201-207.
34. H. Wendt and P. Haasen, "Nucleation and Growth of γ'-Precipitates in Ni-14 at.% Al," Acta Met., Vol. 31, 1983, pp. 1649.
35. L. von Alvensleben and R. Wagner, "FIM-AP Studies of Early Stage Decomposition in Cu-Ti Alloys," Decomposition of Alloys: the early stages (Proceedings of the 2nd Acta-Scripta Metallurgica Conference), P. Haasen, et al., eds., Pergamon Press, New York, NY, 1985, pp. 143-148.
36. H.M. Lee, S.M. Allen and M. Grujicic, "Stability and Coarsening Resistance of M_2C Carbides in Secondary Hardening Steels," Innovations in Ultrahigh-Strength Steel Technology (34th Sagamore Army Materials Research Conference Proceedings), G.B. Olson, et al., eds., U.S. Government Printing Office, Washington, DC, 1990, pp. 127-146.
37. H.M. Lee, "Stability and Coarsening Resistance of M_2C Carbides in the Secondary Hardening Reaction," Ph.D. Thesis, MIT Dept. of Mat. Sci. and Eng'g., 1989.
38. S. Björklund, L.F. Donaghey and M. Hillert, "The Effect of Alloying Elements on the Rate of Ostwald Ripening of Cementite in Steel," Acta Met., Vol. 20, 1972, pp. 867-874.
39. G.R. Speich and R.A. Oriani, "The Rate of Coarsening of Copper Precipitate in an Alpha-Iron Matrix," Trans. AIME, Vol. 233, 1965, pp. 623-631.
40. C.J. Kuehmann, *research in progress*, 1990. .
41. G.B. Olson, et al., "Grain-Coarsening Resistance and the Stability of Second-Phase Dispersions in Rapidly Solidified Steels," Rapidly Solidified Amorphous and Crystalline Alloys (Proceedings of the MRS, #8), B.H. Kear, et al., eds., North-Holland, New York, NY, 1982, pp. 355-362.
42. G.B. Olson and Morris Cohen, "Dislocation Theory of Martensitic Transformations," Dislocations in Solids, F.R.N. Nabarro, ed., North-Holland, Amsterdam, ND, 1986, pp. 319-404.
43. J.P. Hirth and J. Lothe, Theory of Dislocations, McGraw-Hill, New York, NY, 1968.
44. J.D. Eshelby, "The Determination of the Elastic Field of an Ellipsoidal Inclusion and Related Problems," Proc. Roy. Soc., Vol. A241, 1957, pp. 376-396.
45. J.D. Eshelby, "Elastic Inclusions and Inhomogeneities," Progress in Solid Mechanics, I.N. Sneddon, et al., Vol. 2, North-Holland, Amsterdam, ND, 1961, 89-140.
46. D.M. Davies and B. Ralph, "Field-Ion Microscopic Study of Quenched and Tempered Fe-Mo-C," JISI, Vol. 210, 1972, pp. 262-266.
47. H. Kreye, "Einfluß von Versetzungen auf die Umlösung von Teilchen," Z. Metallkunde, Vol. 61, 1970, pp. 108-112.
48. F.S. Ham, "Stress-Assisted Precipitation on Dislocations," J. Appl. Phys., Vol. 30, 1959, pp. 915-926.
49. A.J. Ardell, "On The Coarsening of Grain Boundary Precipitates," Acta Met., Vol. 20, 1972, pp. 601-609.
50. H.B. Aaron and H.I. Aaronson, "Growth of Grain Boundary Precipitates in Al-4% Cu by Interfacial Diffusion," Acta Met., Vol. 16, 1968, pp. 789-798.
51. A.D. Brailsford and H.B. Aaron, "Growth of Grain-Boundary Precipitates," J. Appl. Phys., Vol. 40, No. 4, 1969, pp. 1702-1710.
52. R.M. Allen and J.B. Vander Sande, "A High Resolution Transmission Electron Microscope Study of Early Stage Precipitation on Dislocation Lines in Al-Zn-Mg," Met. Trans., Vol. 9A, 1978, pp. 1251-1258.
53. S. Murphy and J.A. Whiteman, "The Kinetics of Mo_2C Precipitation in Tempered Martensite," Met. Sci. J., Vol. 4, 1970, pp. 58-62.
54. A.T. Davenport, "Precipitation in Some Pure Secondary Hardening Steels," D.Phil. Thesis, University of Sheffield, Faculty of Metallurgy, 1968.
55. S. Nagakura and S. Oketani, "Structure of Transition Metal Carbides," ISI Jap., Vol. 8, 1968, pp. 265-294.
56. H. Rassärts, R. Kieffer and H. Nowotny, "Der Dreistoff: Vanadin-Chrom-Kohlenstoff," Monatsh.

Chem., Vol. 96, 1965, pp. 1536-1542.
57. P. Stecher, F. Benesovsky and H. Nowotny, "Untersuchungen im System Chrom-Wolfram-Kohlenstoff," Planseeber. Pulvermet., Vol. 12, 1964, pp. 89-95.
58. E. Rudy, E. Rudy and F. Benesovsky, "Untersuchungen im System Vanadin-Molybdän-Kohlenstoff," Planseeber. Pulvermet., Vol. 10, 1962, pp. 42-64.
59. E. Rudy, E. Rudy and F. Benesovsky, "Untersuchungen im System Tantal-Wolfram-Kohlenstoff," Monatsh. Chem., Vol. 93, 1962, pp. 1176-1195.
60. K. Hiraga and M. Hirabayashi, "The Formation of Varieties of Carbon Ordering in Pseudobinary Compounds of V_2C, Nb_2C and Ta_2C," J. Appl. Cryst., Vol. 13, 1980, pp. 17-23.
61. K.A. Taylor, "Aging Phenomena in Ferrous Martensites," Ph.D. Thesis, MIT Dept. of Mat. Sci. and Eng'g., 1985.
62. K.A. Taylor, et al., "Carbide Precipitation during Stage I Tempering of Fe-Ni-C Martensites," Met. Trans., Vol. 20A, 1989, pp. 2749-2765.
63. E. Rudy, St. Windisch and C.E. Brukl, "Revision of the Vanadium-Carbon and Niobium-Carbon Systems," Planseeber. Pulvermet., Vol. 16, 1968, pp. 3-33.
64. K. Yvon, W. Rieger and H. Nowotny, "Die Kristallstruktur von V_2C," Monatsh. Chem., Vol. 97, 1966, pp. 689-694.
65. Y. Hirotsu and S. Nagakura, "Crystal Structure and Morphology of the Carbide Precipitated from Martensitic High Carbon Steel During the First Stage of Tempering," Acta Met., Vol. 20, 1972, pp. 645-655.
66. Y. Hirotsu, et al., "Electron Microscopy and Diffraction Study of the Carbide Precipitated from Martensitic Low and High Nickel Steels at the First Stage of Tempering," Trans. JIM, Vol. 17, 1976, pp. 503-513.
67. E. Parthé and V. Sadagopan, "The Structure of Dimolybdenum Carbide by Neutron Diffraction Technique," Acta Cryst., Vol. 16, 1963, pp. 202-205.
68. W. Köster and W. Rauscher, "Beziehungen zwischen dem Elastizitätsmodul von Zweistofflegierungen und ihrem Aufbau," Z. Metallkunde, Vol. 39, 1948, pp. 111-120.
69. J.F. Lynch, et al., Engineering Properties of Selected Ceramic Materials, ACerS, Inc., Columbus, OH, 1966.
70. J.F. Lynch, "Engineering Properties of Selected Ceramic Materials," *(Technical Report AFML-TR-66-52)* Air Force Materials Laboratory, .
71. Peter T.B. Shaffer, Materials Index, Plenum Press, New York, NY, 1964.
72. J.R. Hague, et al., Refractory Ceramics for Aerospace, ACerS, Inc., Columbus, OH, 1964.
73. Louis E. Toth, Transition Metal Carbides and Nitrides, Academic Press, New York, NY, 1971.
74. V.S. Neshpor and G.V. Samsonov, "On The Brittleness of Metal-Like Compounds," Fiz. Metal. Metalloved., Vol. 4, No. 1, 1957, pp. 181-183.
75. D.J. Rowcliffe and G.E. Hollox, "Hardness Anisotropy, Deformation Mechanisms and Brittle-to-Ductile Transition in Carbides," J. Mater. Sci., Vol. 6, 1971, pp. 1270-1276.
76. R.H.J. Hannink and M.J. Murray, "Elastic Moduli Measurements of some Cubic Transition Metal Carbides and Alloyed Carbides," J. Mater. Sci., Vol. 9, 1974, pp. 223-228.
77. R.W. Bartlett and C.W. Smith, "Elastic Constants of Tantalum Monocarbide, $TaC_{0.90}$," J.Appl. Phys., Vol. 38, 1967, pp. 5428-5429.
78. R. Chang and L.J. Graham, "Low temperature Elastic Properties of ZrC and TiC," J. Appl. Phys., Vol. 37, 1966, pp. 3778-3783.
79. Y. Kumashiro, et al., "The Elastic Constants of TiC, VC, and NbC Single Crystals," Proc. Sixth Int'l Conf. on Internal Friction and Ultrasonic Attenuation in Solids, R.R. Hasiguti, ed., University of Tokyo Press, Tokyo, 1977, pp. 395-399.
80. F.W. Vahldiek, S.A. Mersol and C.T. Lynch, "Microhardness Anisotropy, Slip, and Twinning in Mo_2C Single Crystals," Trans. AIME, Vol. 236, 1966, pp. 1490-1496.
81. I.M. Vinitskii, "Relation between the Properties of Monocarbides of Groups IV-V Transition Metals and Their Carbon Content," Poroshk. Metall., No. 6 (114), 1972, pp. 76-82.
82. G.V. Samsonov, et al., "Certain Properties of Nb_2C and V_2C in the Region of Homogeneity," Neorg. Mater., Vol. 11, No. 1, 1975, pp. 62-65.
83. G. Santoro, "Variation of Some Properties of Tantalum Carbide with Carbon Content," Trans. AIME, Vol. 227, 1963, pp. 1361-1368.
84. L. Ramqvist, "Variation of Hardness, Resistivity and Lattice Parameter with Carbon Content of Group 5b Metal Carbides," Jernkont. Ann., Vol. 152, 1968, pp. 465-475.
85. G. Orange, et al., "Systémes de Glissement de l'Hémicarbure de Tungsténe á Température Ambiante," Mater. Sci. and Eng'g., Vol. 34, 1978, pp. 291-294.
86. D.H. Jack and K.H. Jack, "Carbides and Nitrides in Steels," Mater. Sci. and Eng'g., Vol. 11, 1973, pp. 1-27.
87. G.R. Speich and W.C. Leslie, "Tempering of Steel," Met. Trans., Vol. 3, 1972, pp. 1043-1054.
88. H. Morikawa, H. Komatsu and M. Tanino, "Effect of Chromium upon Coherency Between M_2C Precipitates and α-Iron Matrix in 0.1C-10Ni-8Co-1Mo-Cr Steels," (Jap.) J. of EM, Vol. 22, 1973, pp. 99-101.
89. F.K. Naumann, et al., "Die Änderung des Mikrogefüges von warmfesten Stählen durch Zeitstandbeanspruchung," Arch. Eisenh., Vol. 42, 1971, pp. 439-447.
90. T. Nishimura, "Effect of Chromium Contents on the Isothermal Tempering Characteristics of 3Mo-Cr Type Steels," J. Jap. Inst. Met., Vol. 32, 1968, pp. 708-713.
91. J. Pilling and N. Ridley, "Tempering of 2.25Cr-1Mo Low Carbon Steels," Met. Trans., Vol. 13A, 1982, pp. 557-563.
92. A. Youle, P.J. Turner and B. Ralph, "A Preliminary Field-Ion Atom-Probe Investigation of Competitive Carbide Formation in Ferritic Steels," J. Microscopy, Vol. 101, 1974, pp. 1-8.
93. K. Stiller, et al., "High Resolution Microanalytical Study of Precipitation in a Powder Metallurgical High Speed Steel," Acta Met., Vol. 32, 1984, pp. 1457-1467.
94. J.S. Bowles and J.K. MacKenzie, "The Crystallography of Martensite Transformations I, II, III," Acta Met., Vol. 2, 1954, pp. 129-137, 138-147, 224-234.
95. R. Bullough and B.A. Bilby, "Continuous Distributions of Dislocations: Surface Dislocations and the Crystallography of Martensitic Transformations," Proc. Roy. Soc., Vol. B69, 1956, pp. 1276-

1286.
96. M.S. Wechsler, D.S. Lieberman and T.A. Read, "On the Theory of the Formation of Martensite," Trans. AIME, Vol. 197, 1953, pp. 1503-1515.
97. W. Pitsch and A. Schrader, "Die Ausscheidungsform des ε-Karbides im Ferrit und im Martensit beim Anlassen," Arch. Eisenh., Vol. 29, 1958, pp. 715-721.
98. K.H. Jack, "Structural Transformations in the Tempering of High-Carbon Martensitic Steels," JISI, Vol. 169, 1951, pp. 26-36.
99. M.G.H. Wells, "An Electron Transmission Study of the Tempering of Martensite in an Fe-Ni-C Alloy," Acta Met., Vol. 12, 1964, pp. 389-399.
100. Powder Diffraction File, Joint Commitee for Powder Diffraction Standards, Swarthmore, PA, 1988.
101. D. Raynor, J.A. Whiteman and R.W.K. Honeycombe, "Precipitation of Molybdenum and Vanadium Carbides in High-Purity Iron Alloys," JISI, Vol. 204, 1966, pp. 349-354.
102. D. Raynor, J.A. Whiteman and R.W.K. Honeycombe, "In-Situ Transformation of Fe_3C to Mo_2C in Iron-Molybdenum-Carbon Alloys," JISI, Vol. 204, 1966, pp. 1114-1116.
103. D.J. Dyson, et al., "The Orientation Relationship and Growth Direction of Mo_2C in Ferrite," Acta Met., Vol. 14, 1966, pp. 867-875.
104. M. Tanino, T. Nishida and K. Aoki, "Orientation Relationship and Coherency between Mo_2C and the Ferrite Matrix," JISI, Vol. 205, 1967, pp. 874-875.
105. M.J. Gore, G.B. Olson and M. Cohen, "Grain-Refining Dispersions and Properties in Ultrahigh-Strength Steels," Innovations in Ultrahigh-Strength Steel Technology (34th Sagamore Army Materials Research Conference Proceedings), G.B. Olson, et al., eds., U.S. Government Printing Office, Washington, DC, 1990, pp. 425-441.
106. M.J. Gore, "Grain-Refining Dispersions and Mechanical Properties in Ultrahigh-Strength Steels," Ph.D. Thesis, MIT Dept. of Mat. Sci. and Eng'g., 1988.
107. G. Heckmus and J. Stubbe, "Untersuchungen von feinen Ausscheidungen im Stahl 10 CrMo 9 10 mit der Elektronenbeugung und Röntgenmikroanalyse," Arch. Eisenh., Vol. 45, 1974, pp. 551-557.
108. B.D. Cullity, Elements of X-ray Diffraction, Addison-Wesley, Reading, MA, 1978.
109. A.F. Giamei and E.J. Freise, "Optimization of X-Ray Diffraction Quantitative Analysis," Trans. AIME, Vol. 239, 1967, pp. 1676-1685.
110. A.J. Allen, D. Gauvillet and J.R. Weertman, "Small Angle Neutron Scattering Studies of Carbide Precipitation in Ultrahigh-Strength Steels," Acta Met., in press.
111. J.S. Montgomery, "M_2C Carbide Precipitation in Martensitic Cobalt-Nickel Steels," Ph.D. Thesis, Northwestern University, 1990.
112. M. Schmidt and M.J. Gore, "Solution Treatment Effects in AF1410 Steel," Innovations in Ultrahigh-Strength Steel Technology (34th Sagamore Army Materials Research Conference Proceedings), G.B. Olson, et al., eds., U.S. Government Printing Office, Washington, DC, 1990, pp. 407-424.
113. A.L. Bowman, "The Variation of Lattice Parameter with Carbon Content of Tantalum Carbide," J. Phys. Chem., Vol. 65, 1961, pp. 1596-1598.
114. A.L. Bowman, "The Crystal Structures of V_2C and Ta_2C," Acta Cryst., Vol. 19, 1965, pp. 6-9.
115. D.M. Johnson and J.F. Lynch, "Critical Surveys of Data Sources: Ceramics," *(Data Survey STP 396-2)* National Bureau of Standards, December, 1975.
116. T.Ya. Kosolapova, Carbides, Plenum Press, New York, NY, 1968, translated 1971 .
117. H. Lux and L. Eberle, "Zur Kenntnis der Chrom(II)-Salze und des Chrom(II)-oxids, III," Chem. Ber., Vol. 94, 1961, pp. 1562-1571.
118. H. Nowotny and R. Kieffer, "Röntgenographische Untersuchungen von Karbidsystemen," Metallforschung, Vol. 2, 1947, pp. 247-265.
119. E. Rudy, et al., "The Constitution of Binary Molybdenum-Carbon Alloys," Trans. AIME, Vol. 239, 1967, pp. 1247-1267.
120. G.V. Samsonov, Properties Index, Plenum Press, NewYork, NY, 1964.
121. G.V. Samsonov, High Temperature Inorganic Compounds, US Dept. of Commerce, Springfield, VA, 1965, translated 1971 .
122. G.V. Samsonov, Refractory Carbides, Consultants Bureau, New York, NY, 1970, translated 1974 .
123. G.V. Samsonov and I.M. Vinitskii, Handbook of Refractory Compounds, Plenum Press, New York, NY, 1976, translated 1980 .
124. Paul Schwarztkopf and Richard Kieffer, Refractory Hard Metals, MacMillan, New York, NY, 1953.
125. Edmund K. Storms, The Refractory Carbides, Academic Press, New York, NY, 1967.
126. E.P. Abrahamson and S.L. Lopata, "The Lattice Parameters and Solubility Limits of Alpha Iron as Affected by Some Binary Transition-Element Additions," *(Technical Report AMRA TR 66-25)* U.S. Army Materials Research Agency, 1966.
127. E.P. Abrahamson and S.L. Lopata, "The Latuce Parameters and Solubility Limits of Alpha Iron as Affected by Some Binary Transition-Element Additions," Trans. AIME, Vol. 236, 1966, pp. 76-87.
128. C.S. Roberts, "Effect of Carbon on the Volume Fractions and Lattice Parameters of Retained Austenite and Martensite," JOM, Vol. 5, 1953, pp. 203-204.
129. W.C. Johnson and J.W. Cahn, "Elastically-Induced Shape Bifurcations of Inclusions," Acta Met., Vol. 32, 1984, pp. 1925-1933.
130. B. Jansson, "Thermo-Calc: A Databank for Equilibrium and Phase Diagram Calculations," Ph.D. Thesis, KTH, Stockholm, Sweden, 1984.
131. A.M. Sherman, "The Structure and Aging of Martensite," Ph.D. Thesis, MIT Dept. of Mat. Sci. and Eng'g., 1972.
132. G.T. Eldis, "Ausforming and Tempering of High-Alloy Steels," Thesis, MIT Dept. of Mat. Sci. and Eng'g., 1971.
133. G.B. Olson and M. Cohen, "Early Stages of Aging and Tempering of Ferrous Martensites," Met. Trans., Vol. 14A, 1983, pp. 1057-1065.
134 A.M. Sherman, G.T. Eldis and M. Cohen, "The Aging and Tempering of Iron-Nickel-Carbon Martensites," Met. Trans., Vol. 14A, 1983, pp. 995-1005.
135. G. Ghosh, *research in progress*, 1990.
136. M.K. Miller, et al., "An Atom Probe Study of the Aging of Iron-Nickel-Carbon Martensite," Met. Trans., Vol. 14A, 1983, pp. 1021-1024.
137. K.-U. King, "The Eigenstrain Method: Extension to Lattice Theory and Applications to Coherent Precipitation," Ph.D. Thesis, NU Dept. of Civ. Eng'g., 1990.
138. G. Simmons and H. Wang, Single Crystal Elastic Constants and Calculated Aggregate Properties, A Handbook, MIT Press, Cambridge, MA, 1971.
139. K.-U. King, *research in progress*, 1990.

Scripta METALLURGICA et MATERIALIA | Vol. 29, pp. 1135-1140, 1993 Printed in the U.S.A. | Pergamon Press Ltd.
All rights reserved

OSTWALD RIPENING IN MULTICOMPONENT ALLOYS.

A.Umantsev and G.B.Olson
Dept of Materials Science and Engineering, Northwestern University, Evanston, Illinois 60208 - 3108

(Received June 6, 1993)
(Revised July 28, 1993)

The widespread use of second-phase dispersions in materials has stimulated the intensive study of the diffusion processes occurring in them at the last stage of a first-order phase transformation, termed Ostwald ripening or coarsening. As a result of the large surface area, the mixture is not in thermodynamic equilibrium. Relaxation of such a system is characterized by an increase in the scale size of the second phase and a decrease in the total energy. Significant progress in the theory of coarsening in a dilute binary mixture was made by Lifshitz and Slyozov (LS) [1] and Wagner [2], who developed a method of treating an ensemble of particles and made quantitative predictions of the long time behavior of the average particle size, particle number density, and supersaturation of a coarsening system. An interesting variant of this approach has recently been made by Marqusee and Ross (MR) [3], which employs the scaling concept for the asymptotic time dependence of the average particle size and size distribution function. Recently Calderon *et.al.* [4] relaxed the restriction of the dilute solution and derived the rate constant of the coarsening process in an arbitrary binary alloy.

The first attempt to treat a ternary alloy was made by Bhattacharyya and Russell [5] who approximated the coarsening rate in terms of the smallest product of the diffusivity and concentration amidst all the species involved. Bjorklund *et. al.* [6] took a more rigorous approach which, however, was based on an incorrect assumption of equal activities for each component in both phases. Chaix and Allibert [7] considered a model for Ostwald ripening of a two phase ternary system in the case of negligible solubility of one of the components in the precipitating phase. Based on the first-order expansion of the chemical potentials this model predicts serious deviations from LS theory when applying to nonic ternary system. More recently Kuehmann and Voorhees [8] analyzed the behavior of a ternary alloy without any restrictions on solution thermodynamics. They showed that the presence of the third component alters composition trajectories of species in the particle and matrix, because local equilibrium now provides insufficient constraints for them to be determined. Slyozov and Sagalovich [9-11] considered precipitation of stoichiometric compounds with different stoichiometric ratios from a dilute multicomponent solution, and showed that in the first-order approximation, the different phases are independent and can be described by decoupled systems of equations analogous to the two-phase case. Lee *et.al.* [12], studying precipitation hardening in steels, considered coarsening of M_2C carbides of nonstoichiometric composition in a dilute iron-based alloy, utilizing the approach of [6].

In what follows, we analyze the coarsening process of an ensemble of particles, precipitating from a *multicomponent alloy of arbitrary composition*. We utilize the method of expansion of chemical potentials, which enables us to describe the coarsening rate through partial derivatives of the chemical potential, with respect to the mole fractions of different components. The latter can be easily calculated numerically, with the help of modern computer database programs such as ThermoCalc [13]. In the present study the multicomponent interactions for diffusion are not considered, which implies rather special properties of the matrix of mobility coefficients. The full problem which takes into account off-diagonal diffusion coefficients is under study and will be described elsewhere.

Coarsening Rate

Consider the precipitate phase β as an ensemble of spherical particles of composition $\{X_j^\beta(R), j=1,...,n\}$ and radius R, characterized by the particle radius distribution function $f(R,t)$. These particles are surrounded by the matrix phase α of composition $\{X_j^\alpha, j=1,...,n\}$, where n is an arbitrary number of components of an alloy. Coarsening can be described as the process of growth or dissolution of particles by incorporation of mass into them and causes an associated decrease in the matrix composition field. Redistribution of species in the latter satisfies the Fickian law:

$$\frac{\partial X_j^\alpha}{\partial t} = -\nabla J_j^\alpha, \quad J_j^\alpha = -D_j \nabla X_j^\alpha \tag{1}$$

where composition $\{X_j^\alpha\}$ is given in mole fractions; the flux J_j^α has the meaning of a partial volume of the component j, transported across unit area in unit time and has the units of length per time; D_j is the intrinsic diffusivity. The requirement of flux conservation on the interface of a particle of radius R yields the first boundary condition:

0956-716X/93 $6.00 + .00
Copyright (c) 1993 Pergamon Press Ltd.

$$[X_j^\beta(R) - X_j^\alpha(R)]\frac{dR}{dt} = -J_j^\alpha(R) \quad (2)$$

where the flux into the phase β is ignored. Since coarsening predominantly occurs after a nearly equilibrium state has formed, the concentration gradients, which are responsible for the diffusive growth of particles, are small. Therefore, the composition field in the matrix can be approximated by the solution of the quasisteady diffusion equation, i.e. Eq.(1) with $\partial X_j^\alpha/\partial t = 0$. Thus the flux of the component j on the spherical surface of radius R is expressed as:

$$J_j^\alpha(R) = \frac{D_j}{R}[X_j^\alpha(R) - X_j^\alpha(\infty)] \quad (3)$$

where $X_j^\alpha(\infty)$ is the mole fraction of the species j in the matrix far from the particle (mean field composition). Combining Eqs. (2) and (3) one can derive that growth or dissolution of a particle in a multicomponent alloy is described by a set of rate equations:

$$[X_j^\beta(R) - X_j^\alpha(R)]\frac{dR}{dt} = \frac{D_j}{R}[X_j^\alpha(\infty) - X_j^\alpha(R)] \quad (4)$$

In the case of coarsening when the diffusion rates are very small, there is enough time for the conditions of local equilibrium to establish at the interface. They can be obtained by equating the chemical potentials of each component in both phases. To simplify the mathematical treatment, we introduce a composition "vector" space $\mathbf{X}=\{X_j, j=1,...,n\}$ of the dimension n and define a "vector" of the chemical potentials $\mu=\{\mu_j, j=1,...,n\}$ in this space. Then the conditions of local equilibrium take the form:

$$\mu_R^\beta[\mathbf{X}^\beta(R)] = \mu^\alpha[\mathbf{X}^\alpha(R)] \quad (5)$$

Here μ^α is a vector of chemical potentials of the bulk matrix phase and μ_R^β of the precipitate particle of the radius R which, due to the Gibbs-Thompson effect, relates to the chemical potential of the bulk precipitate phase as [14]:

$$\mu_R^\beta[\mathbf{X}^\beta(R)] = \mu^\beta[\mathbf{X}^\beta(R)] + \frac{2\sigma}{R}\bar{\mathbf{V}}^\beta \quad (6)$$

where $\bar{\mathbf{V}}^\beta = \{\bar{V}_i^\beta, i=1,...,n\}$ is the "vector" of partial molar volumes $\bar{V}_i^\beta$ of the species in the precipitate phase.

The condition of global (complete) equilibrium, which implies a flat interface between the α-phase (matrix) and β-phase (precipitate), is expressed as follows:

$$\mu^\beta(\bar{\mathbf{X}}^\beta) = \mu^\alpha(\bar{\mathbf{X}}^\alpha) \quad (7)$$

In the composition space $\{\mathbf{X}\}$, this condition determines hypersurfaces of equilibrium, the composition tie lines and the equilibrium partition coefficients of components: $k_i = \bar{X}_i^\beta/\bar{X}_i^\alpha$. In a multicomponent alloy, the equilibrium mole fractions $\bar{\mathbf{X}}^{\alpha,\beta}$ are no longer given functions of temperature and pressure *only* as it is for a binary solution. Instead, they are also functions of the overall composition of the system $\mathbf{X}^0$.

As the composition change due to the Gibbs-Thompson effect is small, we assume that *everywhere* in the matrix $|X_j^\alpha - \bar{X}_j^\alpha| << 1$. This enables us to expand the chemical potentials of components in the matrix phase in a Taylor series about the equilibrium reference state $\bar{\mathbf{X}}^\alpha$ and restrict the series to the first order terms:

$$\mu_i^\alpha(\mathbf{X}^\alpha) = \mu_i^\alpha(\bar{\mathbf{X}}^\alpha) + \sum_{j=2}^{n} \mu_{i,j}^\alpha (X_j^\alpha - \bar{X}_j^\alpha) \quad (8)$$

where $\mathbf{M}^\alpha = (\mu_{i,j}^\alpha) = (\partial\mu_i^\alpha(\bar{\mathbf{X}}^\alpha)/\partial X_j)_{X_k}$ is a nonsymmetric matrix of interaction coefficients whose (i,j)th element characterizes the influence of a component j on the chemical potential of a component i (see Appendix).

Coarsening is a late stage of structural evolution when the precipitate phase is close to its equilibrium constitution. Therefore, we shall assume that the composition of all precipitate particles is homogeneous and at equilibrium:

$$\mathbf{X}^\beta = \bar{\mathbf{X}}^\beta \quad (9)$$

Taking into account Eqs. (5–9) and matrix multiplication rules, the conditions of local equilibrium become:

$$\mathbf{M}^\alpha[\mathbf{X}^\alpha(R) - \bar{\mathbf{X}}^\alpha] = \frac{2\sigma}{R}\bar{\mathbf{V}}^\beta \quad (10)$$

The next element of the coarsening theory is mass conservation. Assuming that there are no external sources of components, the mass conservation constraint can be written as:

$$X_j^0 = (1-\varphi)\, X_j^\alpha(\infty) + \varphi X_j^\beta(R), \qquad \varphi(t) = (4\pi/3 V_m^\beta)\int_0^\infty R^3 f\ (R,t)\, dR \tag{11}$$

where φ is the volume fraction and $V_m^\beta = \bar{X}^\beta \cdot \bar{V}^\beta$ is the molar volume of the precipitate phase ($\cdot$ designates the dot product of vectors). If nucleation has ceased, and if fluctuations in the system are negligible, then the equation of motion for f is:

$$\frac{df}{dt} + \frac{\partial}{\partial R}(f\,\frac{dR}{dt}) = 0 \tag{12}$$

Solution of the system of equations (4),(11),(12) for each species leads to an apparent component dependent rate of particle growth, which is not correct. Interactions between species, introduced into this model through the multicomponent Gibbs fre. energy, eliminate this ambiguity and the system of equations (4),(11),(12) can be transvected into a component independent form.

To implement this, we subtract $\bar{X}_j^\alpha$ from both sides of Eq.(11) and multiply both sides of Eq.(4) by $\bar{X}_i^\beta \mu_{i,j}^\alpha / D_j$ and Eq(11) by $\bar{X}_i^\beta \mu_{i,j}^\alpha$. Then, summing over i and j and applying Eqs.(8-12) yields the generalized rate equation:

$$[\Phi - A(R)]\frac{dR}{dt} = \frac{1}{R}[\Delta(t) - \frac{2\sigma V_m^\beta}{R}] \tag{13}$$

and mass conservation constraint:

$$\Delta_0 = (1-\varphi)\,\Delta(t) + \varphi\Gamma \tag{14}$$

The cumulative supersaturation of an alloy is a scalar

$$\Delta(t) = \sum_{i=1}^{n} \bar{X}_i^\beta\{\mu_i^\alpha[X^\alpha(\infty)] - \mu_i^\alpha[\bar{X}^\alpha]\} = \bar{X}^\beta \cdot \{\mu^\alpha[X^\alpha(\infty)] - \mu^\alpha[\bar{X}^\alpha]\} \tag{15}$$

which contains contributions from each species, weighted with respect to the particle composition and represents a thermodynamic driving force for precipitation. For a particle to grow, the supersaturation should be positive and a particle radius should be larger than the critical radius $R_c = 2\sigma V_m^\beta/\Delta(t)$. It is interesting to note that the critical particle is not only in local but in global, though unstable, equilibrium with a matrix which is basically the reason for coarsening. However, for the coarsening to proceed, the matrix may not necessarily be supersaturated with respect to *all* of the components, which yields the chemical potential increase of *some* components during the transformation.

In the limit of a small transformation fraction φ the overall composition vector X^0 is in a small vicinity of the vector of equilibrium solubilities of the matrix $\bar{X}^\alpha$, see Eq.(11). Thus the scalar

$$\Delta_0 = \sum_{i=1}^{n} \bar{X}_i^\beta[\mu_i^\alpha(X^0) - \mu_i^\alpha(\bar{X}^\alpha)] = \bar{X}^\beta \cdot [\mu^\alpha(X^0) - \mu^\alpha(\bar{X}^\alpha)] \tag{16}$$

represents the initial cumulative supersaturation of the matrix prior to precipitation transformation.

The time-independent scalar quadratic form

$$\Gamma = \sum_{j=2}^{n}\sum_{i=1}^{n} \bar{X}_i^\beta \mu_{i,j}^\alpha (\bar{X}_j^\beta - \bar{X}_j^\alpha) = \sum_{j=2}^{n}\sum_{i=2}^{n} (\bar{X}_i^\beta - \bar{X}_i^\alpha) G_{m,ij}^\alpha (\bar{X}_j^\beta - \bar{X}_j^\alpha) = (\bar{X}^\beta - \bar{X}^\alpha)\, G_2^\alpha\, (\bar{X}^\beta - \bar{X}^\alpha) \tag{17}$$

characterizes binary and *ternary(1-i-j) interactions* in the system at equilibrium. Eq.(A8) was applied to the equilibrium solubilities of the matrix $\bar{X}^\alpha$ and precipitate $\bar{X}^\beta$ phases and $G_2^\alpha = (G_{m,ij}^\alpha) = (\partial^2 G_m^\alpha(\bar{X}^\alpha)/\partial X_i \partial X$ is the symmetric matrix of the second order partial derivatives of the molar Gibbs free energy of the α-phase (see Appendix). Eventually after a long-term coarsening regime the majority phase will find itself in a composition state $\bar{X}^\alpha$ which is necessarily outside of the spinodal region if the latter exists. This ensures the stability of this state which mathematically can be expressed as positive definiteness of the matrix G_2^α[14]. Thus the quadratic form Γ is always positive or null regardless of the vector $(\bar{X}^\beta - \bar{X}^\alpha)$. This enables us to see, Eq.(14), that as the cumulative supersaturation of an alloy decreases with time the volume fraction of the minority phase tends to its limiting value $\bar{\varphi} = \Delta_0/\Gamma$.

The scalar parameter Φ, defined as follows,

$$\Phi = \sum_{j=2}^{n}\sum_{i=1}^{n} \bar{X}_i^\beta \frac{\mu_{ij}^\alpha}{D_j} (\bar{X}_j^\beta - \bar{X}_j^\alpha) = \sum_{j=2}^{n}\sum_{i=2}^{n} (\bar{X}_i^\beta - \bar{X}_i^\alpha) \frac{G_{m,ij}^\alpha}{D_j} (\bar{X}_j^\beta - \bar{X}_j^\alpha) \tag{18}$$

characterizes the coarsening resistance of a material and depends upon diffusion mobilities and thermodynamic

ir ..actions between species. It can either be dominated by the slowest diffusing component if its diffusivity is much less than that of the remaining ones, or if all species have diffusivities near a weighted average $\bar{D}$, then $\Phi = \Gamma/\bar{D}$. The term $A(R) = \sum_{j=2}^{n} \sum_{i=1}^{n} \bar{X}_i^{\beta}\mu_{ij}^{\alpha}[X_j^{\alpha}(R) - \bar{X}_j^{\alpha}]/D_j \approx 2\sigma V_m^{\beta}/\bar{D}R$ originates from the difference in composition at the flat and curved interfaces of the matrix and vanishes asymptotically for large particles.

The problem of coarsening of a multicomponent alloy is described by Eqs.(12–14), which are of the same type as that for the binary case and, hence, can be analyzed by the asymptotic method either of LS [1] or MR [3] for the case of a small volume fraction of the precipitate phase, viz $\Delta_0 << \Gamma$. For the average particle size $\bar{R}(t)$, supersaturation $\Delta(t)$, and the number of precipitate particles $N(t)$, this yields:

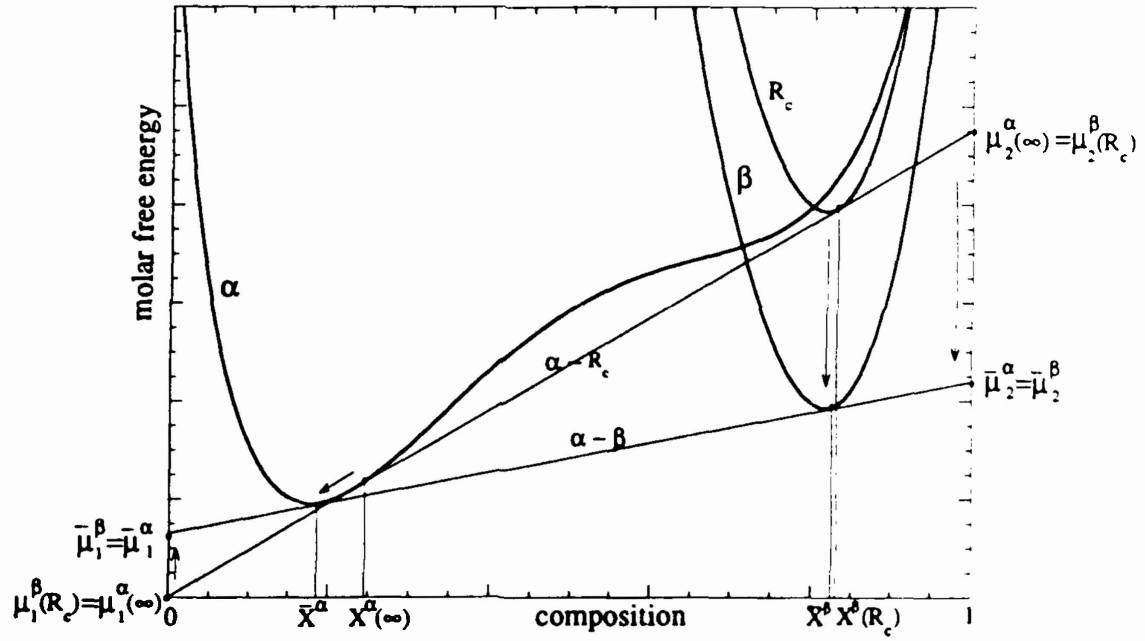
$$\bar{R}^3(t) = (2/3)^2 Kt + O(1), \quad K = 2\sigma V_m^{\beta}/\Phi \tag{19}$$

$$\Delta(t) = (3\sigma V_m^{\beta})^{2/3}\, \Phi^{1/3}\, t^{-1/3} + O(t^{-2/3}) \tag{20}$$

$$N(t) = (3\bar{\varphi}\Phi/4\pi\sigma)t^{-1} + O(t^{-4/3}) \tag{21}$$

For a binary alloy, expression (15) takes the form:

$$\Delta^b(t) = \bar{X}_1^{\beta}\{\mu_1^{\alpha}[X^{\alpha}(\infty)] - \mu_1^{\alpha}[\bar{X}^{\alpha}]\} + \bar{X}_2^{\beta}\{\mu_2^{\alpha}[X^{\alpha}(\infty)] - \mu_2^{\alpha}[\bar{X}^{\alpha}]\}$$



The above Figure represents the molar free-energy curves of the bulk matrix α, precipitate β phases and that of the precipitate particle of the critical radius R_C as functions of composition of a binary alloy X. The common tangent construction between bulk phases (α–β line) and matrix/critical particle (α–R_C line) reflects global equilibria existing in the system and helps to elucidate the thermodynamics of coarsening. Representative points of the matrix and particles move in the directions designated by arrows in the Figure, the chemical potential of the solute atoms distant from precipitate particles decreases, but the chemical potential of the solvent increases, leading to an overall decrease of supersaturation $\Delta^b(t)$. Note that the variation of composition in the particle is much smaller than in the matrix. For the coarsening resistance, Eq.(18) yields $\Phi^b = G_{m\,22}^{\alpha}(\bar{X}_2^{\beta} - \bar{X}_2^{\alpha})^2/D$ and one can recover from Eq. (19) the expression for the rate constant, which coincides with that of [4], obtained without the assumption of Eq.(9). This occurs because the deviation of the particle composition from the equilibrium one, due to the Gibbs-Thompson effect, is of the order of 1/R. It constitutes a small correction to the difference of equilibrium solubilities $(\bar{X}_j^{\beta} - \bar{X}_j^{\alpha})$ in the left-hand side of Eq. (4). Together with A(R), Eq.(13), this correction vanishes asymptotically, but may affect initial stages of coarsening when the average particle size is small, significantly retarding the rate of transformation. In the case of

ternary alloys, Eqs. (18) and (19) yield a rate constant identical to that of [8].

Now we shall analyze the influence of the solution thermodynamics on the coarsening rate of an alloy. By virtue of linear dependence of the coarsening resistance on the Gibbs free energy function for any real solution, Eq.(18), one can write the latter as a superposition of contributions $\Phi = \Phi^{id} + \Phi^{E}$, which result from the entropy of mixing Φ^{id} and interactions between species in the solution Φ^{E}. Using Eq.(A.7) and the expression for the molar Gibbs free energy of an ideal solution $G_m^{id} = \sum_{i=1}^{n} X_i\mu_i^* + R_gT\sum_{i=1}^{n} X_i\ln X_i$ where μ_i^* is the chemical potential of a pure component and R_g is the gas constant [14], the partial derivatives of the free energy can be written as follows:

$$\frac{G_{m,ij}^{id,\alpha}}{R_gT} = \frac{1}{\bar{X}_1^{\alpha}} + \frac{\delta_{ij}}{\bar{X}_i^{\alpha}}, \qquad i>1, j>1 \tag{22}$$

For the coarsening resistance, this yields the expression:

$$\Phi^{id} = R_gT\sum_{i=2}^{n}\frac{\bar{X}_i^{\alpha}}{D_i}(k_i-1)(k_i-k_1) \tag{23}$$

The same expression can be derived in the dilute solution limit: $\Phi^{dl} = \Phi^{id}$, because $\mu_{i,j}^{dl} = \mu_{i,j}^{id} = R_gT(\delta_{ij} - \delta_{i1})/X_i$. In this case the rate constant K, Eq.(19), is identical to that obtained by Lee *et. al.* [12] with the help of an inappropriate assumption of equal activities in both phases at equilibrium. This coincidence is a result of the relative unimportance of the thermodynamics of the precipitate phase for the process of coarsening. For a binary alloy to recover the LS result from Eq.(23), one also has to make an assumption of a rather special phase diagram with negligible solubility of the solvent in the precipitating phase $\bar{X}_2^{\beta}\approx 1$. For a regular substitutional multicomponent solution of the matrix phase $G_m^{E} = (Z/2)\sum_{i=1}^{n}\sum_{j=1}^{n}(1-\delta_{ij})\,\omega_{ij}X_iX_j$, where Z is the coordination number, $\omega_{ij} = u_{ij} - \frac{1}{2}(u_{ii}+u_{jj})$, and u_{ij} is the bonding energy between species *i* and *j* [14]. Then, from Eqs.(18) and (A.7) for the excess quantity of the coarsening resistance for a multicomponent regular solution, we deduce

$$\Phi^{E} = Z\sum_{j=2}^{n}\sum_{i=2}^{n}(\bar{X}_i^{\beta} - \bar{X}_i^{\alpha})\frac{\Omega_{ij}}{D_j}(\bar{X}_j^{\beta} - \bar{X}_j^{\alpha}), \qquad \Omega_{ij} = \omega_{ij} - \omega_{1i} - \omega_{1j} = u_{ij} - u_{1i} - u_{1j} + u_{11} \tag{24}$$

Adding Eqs.(23) and (24) one can obtain the expression for the coarsening resistance of a binary regular solution:

$$\Phi^{b,r} = (R_gT - Z\omega_{12}\bar{X}_1^{\alpha}\bar{X}_2^{\alpha})\,\bar{X}_2^{\alpha}(k_2-1)(k_2-k_1)/D \tag{25}$$

The explicit effect of ω_{12} interactions appearing in Eq.(25) is dominated by an opposite sign effect on the solubility $\bar{X}_2^{\alpha}$. In the case of pure solute precipitation out of a binary regular solution, $\bar{X}_2^{\beta}\approx 1$, the coarsening resistance can be expressed as : $\Phi^{b,r} \approx \Phi^{b,id}\exp[Z\omega_{12}(1-\bar{X}_2^{\alpha,id})^2/R_gT]$.

To estimate the coarsening rate of a real multicomponent alloy, one can find the matrix M^{α} or G_2^{α} which may be obtained using modern computer databases. The analytical form of Eq.(18) also offers qualitative insights into possible solute interaction mechanisms of coarsening resistance. For instance, in the case of a fast diffusing interstitial solute which does not contribute significantly to Φ of Eq.(18) through its diagonal terms ($\mu_{i,i}^{\alpha}$), a significant contribution to coarsening can arise from its cross terms ($\mu_{i,j}^{\alpha}$) with a slower diffusing solute. An example may be the interaction of C and other alloying elements in the coarsening of carbides in steels.

Acknowledgment

We are thankful to C. Kuehmann and P. Voorhees for helpful discussion. This research was supported by ARO under Grant DAAL03-K-0152 as part of the Steel Research Group program.

Appendix

Interaction coefficients.

In this section the properties of the matrix of interaction coefficients ($\mu_{i,j}$) will be described in application to a multicomponent system. The Gibbs - Duhem equation of a multicomponent system takes the form:

$$\sum_{i=1}^{n} X_i d\mu_i = 0 \tag{A.1}$$

where, according to the definition, mole fractions X_j obey the constraint:

$$\sum_{j=1}^{n} X_j = 1 \tag{A.2}$$

Expanding chemical potentials about the equilibrium composition, Eq.(8), and taking into account Eq.(A.2) the Gibbs - Duhem equation becomes:

$$\sum_{i=1}^{n} X_i \sum_{j=2}^{n} \mu_{i,j} \Delta X_j = \sum_{j=2}^{n} (\sum_{i=1}^{n} X_i \mu_{i,j}) \Delta X_j = 0$$

where ΔX_j, j=2,...,n are arbitrary perturbations of mole fractions of the species. This identity is possible only if all the coefficients in front of perturbations ΔX_j vanish. Hence, for all species j:

$$\sum_{i=1}^{n} X_i \mu_{i,j} \equiv 0 \tag{A.3}$$

As it is well known

$$\mu_j = \begin{cases} G_m - \sum_{k=2}^{n} X_k \frac{\partial G_m}{\partial X_k}, & i=1 \\ \frac{\partial G_m}{\partial X_j} + \mu_1, & i>1 \end{cases} \tag{A.4}$$

where G_m is the molar Gibbs free energy of the system. It is advantageous to introduce a matrix $x_{i,j}$ as

$$x_{i,j} \equiv (\frac{\partial X_i}{\partial X_j})_{X_k} = \begin{cases} 0, & j=1 \\ -1, & i=1, j>1 \\ \delta_{ij}, & i>1, j>1 \end{cases} \tag{A.5}$$

where δ_{ij} is Kronecker's symbol ($\delta_{ij}=0$ for $i \neq j$ and $\delta_{ij}=1$ for i=j). Then from Eqs.(A.4,5) we obtain the expression for the matrix of interaction coefficients:

$$\mu_{i,j} = \begin{cases} 0, & j=1 \\ -\sum_{k=2}^{n} X_k G_{m,kj}, & i=1, j>1 \\ \mu_{1,j} + G_{m\ ij}, & i>1, j>1 \end{cases} \tag{A.6}$$

where the matrix of partial derivatives of the free energy is determined as follows:

$$G_{m,ij} \equiv \frac{\partial^2 G_m(X)}{\partial X_j dX_i}, \quad i>1 \text{ and } j>1 \tag{A.7}$$

Consider two points of a composition space: **X** and **Y**, which belong either to the same phase field of an equilibrium phase diagram or different ones. Applying Eqs. (A.3,6,7), one can derive the relation:

$$\sum_{i=1}^{n} Y_i \mu_{i,j}(X) = \sum_{i=1}^{n} (Y_i - X_i) \mu_{i,j}(X) = \sum_{i=2}^{n} (Y_i - X_i) G_{m,ij}(X) \tag{A.8}$$

which is a direct consequence of the Gibbs-Duhem equation. This relation is used in Eqs.(17) and (18) to convert from a nonsymmetric matrix of interaction coefficients ($\mu_{i,j}$) to a symmetric matrix ($G_{m,ij}$).

References

1. I.M. Lifshitz and V.V. Slyozov, *J. Phys. Chem. Solids* **15**, 35 (1961)
2. C. Wagner, *Z. Electrochem.* **65**, 581 (1961)
3. J.A. Marqusee and J. Ross, *J. Chem. Phys.* **79**, 373 (1983)
4. H.A. Calderon, P.W. Voorhees, J.L.Murray, G. Kostorz, *Acta metall.* To be published.
5. S.K. Bhattacharyya and K.C. Russell, *Metal. Trans.* **3**, 2195, (1972)
6. S. Bjorklund, L.F. Donaghey and M. Hillert, *Acta metall.* **20**, 867 91972)
7. J.M. Chaix and C.H. Allibert, *Acta metall.* **34**, 1593 (1986)
8. C. Kuehmann and P.W. Voorhees, Preprint.
9. V.V. Slyozov and V.V. Sagalovich, *Sov. Phys. Solid State.* **17**, 974 (1975)
10. V.V. Slyozov and V.V. Sagalovich, *J. Phys. Chem. Solids* **38**, 943 (1977)
11. V.V. Slyozov and V.V. Sagalovich, *Sov. Phys. Usp.* **30**, 23 (1987)
12. H.M. Lee, S.M. Allen and M. Grujicic, *Metal. Trans. A* , **22A**, 2863 (1991)
13. B. Sundman, B. Jansson, and J.O. Anderson, *Calphad*, **9**, 153 (1985)
14. C.H.P. Lupis *Chemical Thermodynamics of Materials.* Elsevier, North-Holland (1983).